The Effects of Fuel Volatility and Operating Conditions on Sprays from Pressure-Swirl Fuel Injectors

by

Brad A. VanDerWege

B.S., Mechanical Engineering (1994)
University of Michigan, Ann Arbor

M.S., Mechanical Engineering (1996)
Massachusetts Institute of Technology

SUBMITTED TO THE DEPARTMENT OF MECHANICAL ENGINEERING
IN PARTIAL FULFILLMENT OF THE REQUIREMENTS FOR THE DEGREE OF

DOCTOR OF PHILOSOPHY
AT THE
MASSACHUSETTS INSTITUTE OF TECHNOLOGY

June 1999

Signature of Author_____
Department of Mechanical Engineering
June 1999

Certified by_____
Simone Hochgreb
Associate Professor of Mechanical Engineering
Thesis Supervisor

Accepted by_____
Ain A. Sonin
Chairman, Departmental Graduate Committee

The Effects of Fuel Volatility and Operating Conditions on Sprays from Pressure-Swirl Fuel Injectors

by

Brad A. VanDerWege

Submitted to the Department of Mechanical Engineering
on May 7, 1999 in Partial Fulfillment of the Requirements
for the Degree of Doctor of Philosophy.

ABSTRACT

Optimal design of modern direct injection gasoline engines depends heavily on the fuel spray. Most of the studies published regarding these fuel sprays involve cold bench tests or motored optical engines, neglecting the roles of the fuel volatility and temperature. This study, therefore, was designed to describe changes in the spray properties due to fuel volatility and operating conditions using a firing optically-accessible engine. Planar laser-induced fluorescence and planar Mie scattering imaging experiments were performed to show changes in the spray structure, including its radial and axial penetration. Phase-Doppler particle analysis experiments were included to track the droplet diameter and velocity at various points throughout the spray. A computational fluid dynamics model was also used to study the physics leading to the observed changes.

The results show that the spray structure changes with not only ambient gas density, which is often measured, but also fuel temperature and volatility. The mean droplet diameter was found to decrease substantially with increasing fuel temperature and decreasing ambient density. Under conditions of low potential for vaporization, the observed trends agree with published correlations for pressure-swirl atomizers. As ambient density decreases and fuel temperature increases, the volatile ends of multi-component fuels evaporate quickly, producing a vapor core along the axis of the spray. Beyond a certain point, evaporation is violent enough to cause additional breakup of the droplets. A fit to this volatility-induced breakup data provides an additional correlation for determining the mean diameter of volatile sprays. Coincident with the volatility-induced breakup trend is an increase in the initial cone angle of the spray. However, the reduced droplet diameter and rapid vapor generation under these superheated conditions result in a narrow spray with increased axial penetration.

In the process of performing these experiments, insights were found regarding the operation of these diagnostics in high-density sprays.

Thesis Supervisor: Simone Hochgreb
Associate Professor of Mechanical Engineering

ACKNOWLEDGMENTS

Without the hard work and dedication of my thesis advisor, Professor Simone Hochgreb, this work would not have been possible. In addition, the advice of my thesis committee, Professors John Heywood, John Lienhard V, and Daniel Nocera, and the members of the MIT Engine and Fuels Research Consortium has made a profound impact on this work.

I believe that neither this project nor much of anything else would have been accomplished around the Sloan Lab without the expertise of Nancy Cook, Brian Corkum, Pete Menard, and Professor Wai Cheng. At the same time, I often wonder if anything in the entire department would function without the unending knowledge of Leslie Regan.

A special thanks to Frank Zhao and the AETG at DaimlerChrysler for the opportunity to use their spray model—especially to Todd Lounsberry for showing me through FIRE and allowing me to take over his office for weeks at a time.

I would like to thank Mike Shelby for setting up the most unique of engines, as well as the engine controller, the dyno, the excimer, the camera, and half of everything else in the test cell. But more so, I would like to thank him, as well as Mark Dawson, Robert Meyer, Chris O'Brien, Dave Kayes, Helen Liu, and Micha Wiegel for their occasional advice and continual friendship.

The following people helped me to varying amounts with my work, but more than anything they made the Sloan Automotive Lab a much more pleasant and interesting place: Mike Bush, Gatis Bazbauers, Alan Shihedeh, John Fox, Mike Norris, J.R. Linna, Bouke Nordiz, Vincent Frotier, Pete Hinze, Sangmeoung Han, Haissam Haidar, Wolf Bauer, Wole Akinyemi, Norman Peralta, Steve Casey, Carlos Herrera, Denis Artzner, Benoist Thirouard, Ertan Yilmaz, Jim Cowart, Cornelius O'Sullivan, Matt Rublewski, Marcus Megerle, Conner McNally, Brian Hallgren, Gary Landsberg, and David Schmidt.

And in those rare, but precious, times when I wasn't in the lab, the following people helped make Boston home: Katrina Harris, Natasha Winters, Jennifer Ward, Maya Farhoud, Greg DaRe, Peter Madden, Patrisha Hersh, Adriana Laverne, and The Protestant Student Community: John Wuestneck, Jennifer Lane, Kevin Day, Paulo Oliveira, John McKay, and Susanna Mierau. They were aided, though, by the following establishments: The Field, The Sunset, CBC, The Muddy, and The Border.

While experimental apparatus are fickle and degrees are never sure until the thesis is signed, the love and support of my family was always available and never in doubt.

This work has been sponsored by the Department of Energy, contract number DE-AC04-94AL85000. Additional support from Zexel, Inc. (S. Takeshita) and the MIT Engine and Fuels Consortium is gratefully acknowledged. I would also like to thank the National Science Foundation for their support through a Graduate Research Fellowship.

TABLE OF CONTENTS

LIST OF TABLES

LIST OF FIGURES

NOMENCLATURE

Acronyms:

ATDCI	after top-dead-center in the intake stroke
ASOI	after start of injection
BDC	bottom-dead-center
DI	direct injection
DISI	direct-injection spark-ignition
EVC	exhaust valve closing
EVO	exhaust valve opening
FBP	final boiling point
IBP	initial boiling point
ICCD	intensified charge-couple device
IVC	intake valve closing
IVO	intake valve opening
LDV	laser-Doppler volicimeter
PDPA	phase-Doppler particle analysis
PLIF	planar laser-induced fluorescence
PMT	photo-multiplier tube
RMS	root mean square
SMD	Sauter mean diameter
TDC	top-dead-center

Symbols:

A, B, C	Antoine vapor pressure correlation constants
A_{12}, A_{21}	van Laar activity coefficient correlation constants
A_0	orifice area
C_D	coefficient of discharge
d_o	diameter of orifice
DV_{90}	diameter at which 90% of liquid is contained in smaller droplets
Fo	Fourier number
I	light intensity
I_{DC}	intensity related to camera dark charge
I_L	laser sheet intensity
K_i	equilibrium constant for species i
m	mass flow rate
P	total pressure
P_A	ambient pressure

P_i	partial pressure of species i
P_{VAP}	vapor pressure
R	radial distance
T	temperature
T_{10}	temperature at which 10% of liquid will evaporate
T_A	ambient temperature
T_{BP}	bubble point temperature
T_f	fuel temperature
T_{inj}	fuel injector mean temperature
T_{TC}	thermocouple measured temperature
x_i	mole fraction of species i in the liquid
y_i	mole fraction of species i in the vapor
Z	axial distance
α	thermal diffusivity
ϕ	fluorescence yield
γ_i	activity coefficient of species i
ΔP_L	differential pressure across injector
ΔT	superheat temperature
μ_L	liquid viscosity
Π	normalized excess vapor pressure
ρ_A	ambient density
ρ_L	liquid density
σ	surface tension

CHAPTER 1

INTRODUCTION

1.1 MOTIVATION

As the environmental concerns over automotive carbon dioxide production heighten and government regulations of fuel economy become stricter, automotive companies are continually researching new technologies to improve the efficiency automotive propulsion systems. While a great deal of hype has recently surrounded zero-emissions concepts such as fuel cells and electric vehicles, the internal combustion engine remains the primary propulsion source for the automotive industry for the foreseeable future. One internal combustion engine technology that has recently been receiving substantial attention is the direct-injection spark-ignition (DISI) engine. The potential benefits associated with DISI engines in both fuel economy and transient fuel management have been highlighted in several recent publications, and reinforced by the introduction of several engine models into the international market [1-5]. While DISI engine designs have existed for some time [6, 7], the renewed interest in the technology has been encouraged by advances in high-pressure fuel injection technology as well as sophisticated electronic control techniques.

By injecting the fuel directly into the combustion chamber, the amount and distribution of the fuel can be more carefully controlled. Potential emissions and fuel economy benefits are possible through the better fuel metering during cold starts and transients. However, the primary fuel-economy benefits come from the ability to control the distribution of the fuel. By concentrating the fuel around the spark plug, a stratified mixture is produced in which the combustion chamber overall is fuel-lean, but the region around the spark plug is rich enough to burn. Since the load can then be controlled by the amount of fuel introduced, throttling losses can be reduced at low load. Stratified operation also reduces heat loss to the combustion

chamber walls. The ability to control the initial distribution of fuel is also useful with a homogeneous charge. By evaporating the fuel in the charge air, the charge temperature is reduced. This decrease in temperature can increase the volumetric efficiency of the engine by increasing the charge density, and it can increase knock resistance. The high compression ratio possible because of the higher knock resistance improves fuel efficiency as well. However, achieving all of the fuel economy benefits while managing hydrocarbon and nitric oxide emissions, especially under stratified operation, requires a thorough understanding of the processes involved in the vaporization and distribution of the injected fuel.

The successful operation of modern DISI engines depends on matching a combustion chamber shape and in-cylinder flow field with the spray shape and momentum to enable complete air utilization during full load homogeneous operation and provide a well contained pocket of combustible mixture during part-load, stratified charge operation. Pressure-swirl injectors are often considered the best design for providing appropriate spray characteristics for both of these operating regimes [8]. This study focuses on the fuel distribution during the injection period, which is not strongly influenced by the specific design of a particular combustion chamber shape or flow field.

1.2 Background

1.2.1 Direct-Injection Spark-Ignition Engines

While nearly all spark-ignition engines produced today utilize fuel injection into the intake port, designs for fuel injection directly into the combustion chamber have been studied for decades. In the 1970's an extensive amount of research was performed on stratified charge engines [7]. Some designs, such as the Honda CVCC, involved two sources of fuel to produce a rich mixture in a prechamber. Designs that injected all of the fuel into the combustion chamber included the MAN-FM, the Texaco TCCS, and the Ford PROCO [7, 8]. Both the MAN-FM and

Texaco TCCS systems operated in a late-injection, stratified-charge mode only, resulting in a smoke-limited maximum torque [7]. The Ford PROCO design improved air utilization by injecting earlier in the compression stroke at higher load to produce a more homogeneous mixture [7, 9]. However, these systems still suffered from the limited flexibility and relatively poor atomization of their diesel-based fuel injection systems [8]. In addition, the Texaco TCCS and Ford PROCO designs involved a close coupling of the fuel spray and the spark plugs to achieve stratification. This design, however, was associated with spark plug fouling and high hydrocarbon and soot emissions [5].

Modern DISI engine designs, on the other hand, utilize the combustion chamber geometry along with the charge motion and the momentum of the spray to transport the fuel to the spark plug for stratified operation. Designs involving in-cylinder swirl [2] and tumble [5, 10] have been proposed. This design philosophy and the flexibility introduced by the use of electronically controlled injectors, are often quoted as the primary reasons for the resurgence in DISI research.

The flexibility of the electronic injection systems is thoroughly utilized, as well, with as many as five different injection strategies being employed. 1) For low-load, stratified-charge operation, injection is typically from mid-stroke to late in the compression stroke [2, 5, 10]. This timing allows less time for mixing, generating a stratified charge. 2) For high-load operation and high-speed operation, injection is during the intake stroke, allowing sufficient mixing time to generate a homogeneous mixture [2, 5, 10]. The resulting high air utilization keeps maximum output near (or above) that of current port-fuel-injected engines. 3) In some designs, to smooth the transition between early and late injection, a two-stage injection is used, in which fuel is injected in both the intake and compression strokes to produce as semi-stratified charge [10]. 4) A dual-injection strategy has also been proposed to reduce knocking tendency [11, 12]. The first injection produces a homogeneous lean mixture cooling the charge to increase volumetric efficiency. The lean end gasses and the additional cooling provided by the second injection

reduce the knocking tendency. 5) A secondary injection during the expansion stroke has also been proposed to increase exhaust gas temperatures to reduce catalyst light-off times [12]. Obviously, with such a large array of goals for the injector and the wide variety of conditions under which it must operate, a thorough understanding of the injection process is needed.

The fuel economy advantage of the DISI engine under stratified-charge conditions over a standard port-fuel-injected engine can be as much as 40% for the lowest speed and load conditions [5]. Under more normal driving conditions, the advantage is still 15 to 20% [2, 5]. At the same time, full-load performance, when running under homogeneous conditions, can be improved 8 to 12% [5, 10]. Using the dual-injection strategy to reduce knocking tendencies, an additional 9% improvement in torque can be gained at low speeds [12]. Obtaining these advantages while controlling exhaust emissions, though, has remained a challenge. Engine out emissions of hydrocarbons (HC) and oxides of nitrogen (NOx) are higher than for a port-injected engine at low load, but the addition of exhaust gas recirculation (EGR) substantially improves both. The primary emissions disadvantage of the DISI engine is that, under stratified-charge operation, the overall fuel-lean mixture prevents the three-way catalyst from reducing NOx. Two types of lean-NOx catalysts have been developed: the NOx trap catalyst and the selective reduction catalyst. Unfortunately, the selective-reduction catalyst exhibits a relatively low conversion efficiency and the trap-type catalyst is highly sensitive to sulfur poisoning [12].

Until the catalyst concerns are resolved, stratified-charge engines are typically not considered for production in the United States. However, the advantages of DISI engines in fueling control, maximum output, and knock resistance may lead to the introduction of stoichiometric-only designs.

1.2.2 Pressure-Swirl Sprays

The requirements on the fuel system in a DISI engine are much more demanding than for a port-injected engine. The DISI fuel injection system must be able to: provide a higher level of

atomization with a low penetration rate, deliver the fuel in a shorter amount of time, resist deposit formation, and operate effectively at higher temperatures and ambient pressures [8]. Due to the relatively short time available for the fuel spray to evaporate in a DISI engine, the Sauter mean diameter of the droplets should be in the range of 15 to 25 μm [8]. Pressure-swirl injectors are generally believed to be the best available technology to satisfy these requirements [8, 13]. Pressure-swirl atomizers operate by providing significant angular velocity to the liquid. The fluid is introduced into a swirl chamber either trangentially or helically to provide angular momentum. The chamber contracts near the exit orifice, increasing the angular velocity of the fluid. As the fluid exits the orifice it spreads out into a hollow cone, the angle of which is determined by the ratio of tangential to axial velocities. This liquid sheet thins as it expands, quickly breaking up. The resulting spray has a hollow-cone structure.

Measurements of the sprays are typically one of three types: imaging, droplet size measurements, or mass-flux measurements with a patternator. A number of imaging experiments have been performed involving either laser sheet Mie scattering [14, 15] or planar laser-induced fluorescence [13, 16]. These experiments are typically designed to measure the distribution of the fuel spray in terms of its axial penetration rate and width as a function of ambient pressure or injection timing [1, 14]. The sprays are found to decrease in width and axial penetration as the ambient pressure is increased. In addition, the pre-spray is often observed to have poor atomization and a high penetration velocity, resulting in piston or wall wetting [15]. Droplet mean diameters are typically measured by the laser diffraction method [17, 18] or phase-Doppler particle analysis (PDPA) [13, 14, 19], and are typically measured as a function of injection pressure, spray cone angle, or location within the spray. The mean droplet diameter is found to monotonically decrease with increasing injection pressure [8], but the behavior with cone angle appears to be more complicated [17]. Experiments with the transient patternator at the University of Wisconsin [20, 21], offer temporally and spatially resolved mass flux values.

These mass flux measurements have been used to compare injection systems by providing cross-sections of liquid mass distribution in sprays.

While the injection system in a DISI engine needs to operate in a wide range of operating conditions, the only operating condition changed in most of these studies is the ambient pressure. Even then, most studies use ambient pressures only above atmospheric. Granted, the DISI engine gains its largest advantages under unthrottled, late-injection conditions, in which the ambient pressure at the time of injection is above atmospheric, but the engine must run effectively and cleanly under all conditions to be commercially viable. This includes high-speed, low-load conditions, under which the engine is throttled, resulting in sub-atmospheric ambient pressures. In addition, most motored engine and spray bench tests purposefully minimize evaporation of the fluid for safety reasons. This means using a low-volatility solvent at room temperature, which neglects the effects of temperature or volatility on the spray. One exception is the work done by Davy, *et al.* [22], in which a warm engine was fired with gasoline. However, the temperature was apparently not varied or reported.

1.2.3 Flash Boiling

The role of volatility in the atomization of liquid injection has been studied in a number of ways. Early works focussed on the simplified case of a superheated liquid jet [23, 24]. This work showed that the atomization of the jet was greatly enhanced when the fluid was sufficiently superheated, but the superheat required to shatter the jet depended on the surface quality of the orifice and the Weber number of the jet [23]. This breakup mechanism is often suggested as a mechanism for producing small droplet sizes from simple, low-pressure injectors systems [25, 26].

The effect of flash boiling on standard fuel injectors has also been studied. Studying a plain orifice injector, Oza and Sinnamon [27] defined two regimes of flash boiling. They defined an internal-flashing regime, in which bubbles are formed inside the injector orifice

leading to the ejection of a two-phase flow. In this regime, the spray was shown expand rapidly upon exiting the injector. In their external-flashing regime, an intact liquid jet leaves the orifice, but is quickly shattered by rapid bubble growth.

Senda and coworkers [28-30] measured spray angle, breakup length, and SMD of a pintle-type injector with decreasing ambient pressure. They measured a non-monotonic change in all three properties as flash boiling was initiated. As ambient pressure decreased, the spray at first narrowed giving a longer breakup length and poorer atomization followed by a reversal to wider cone angles with shorter breakup lengths and better atomization. A similar two-stage transition has been observed for pintle injectors in a port injected engine [31]. Senda and coworkers went on to develop a model of the bubble formation and the resulting breakup of the spray. While bubble growth models have existed for some time [23, 27], defining the point of origin and number of bubble nuclei has proved elusive. They proceeded by assuming that the bubble nuclei were formed in a vena contracta at the entrance of the injector orifice. The number of nuclei was estimated from microscopic photographs of the flow. Finally, breakup was assumed to occur when the bubbles filled the liquid sheet, assuming no coalescence of bubbles. The resulting number of droplets was twice the number of bubbles. However, the difficulty in applying this model to other injection systems lies in the need to know the pressure history of the fluid and the nucleation properties.

1.3 OBJECTIVES

The objective of this work is to determine the effects of engine operating conditions and fuel volatility on the structure and atomization of sprays from pressure-swirl fuel injectors. As described above, the behavior of the fuel spray is vital in the performance of DISI engines. While changes in the spray with increased ambient pressure and injection timing have been reported, little information was available about pressure dependence at sub-atmospheric pressure, as well as temperature dependence and the effect of volatile fuels. This study, therefore, focuses

on sprays of volatile fuels under a range of temperatures and ambient pressures representative of DISI engines operating with early injection. Changes in the spray were studied using laser-sheet imaging, optical droplet sizing, and a computational fluid dynamics model of the spray.

CHAPTER 2
EXPERIMENTAL SETUP

2.1 INTRODUCTION

The experimental setup was designed to provide the fuel spray with an environment consistent with early injection strategies while allowing access for optical diagnostics. To accomplish this, an optically-accessible research engine was modified for direction injection operation. With optical access from three sides, laser sheet imaging was easily set up to provide information of the spray structure. Both planar laser-induced fluorescence (PLIF) and planar Mie scattering images were taken to emphasize different aspects of the spray. Optical access was also required for the phase-Doppler particle analysis (PDPA) measurements of droplet diameter and velocity.

2.2 APPARATUS

2.2.1 Optical Engine

Experiments were conducted in a 'single-cylinder' engine that has been extensively modified for optical access. The engine has a square cross section, which allows complete optical access through two opposed quartz side walls and a 75.6 mm x 72.6 mm viewing area through a third quartz window (Fig. 2.1). The third window was added to allow the fluorescence to be viewed at 90 degrees from the path of the laser light. The windows were sealed with a gaskets cut out of sheet silicone rubber. The seals were attached to the windows using high-temperature RTV. This allowed easier assembly and increased seal life. At high load, blow-by gasses in the corners burned the silicone window seals, resulting in a seal life of only a few minutes. To extend the seal life, high-load tests were run with retarded spark timing (TDC).

Dimensions and specifications for the engine are given in Table 2.1. The compression ratio for the engine was 8:1, which is significantly lower than that of the several prototype DI

engines currently operating at 11-12:1, since sealing the optical engine becomes progressively more difficult as the peak pressures increase. The piston seals are three rows of spring-loaded graphite bars, which overlap in the corners. Graphite provides a fairly good, lubrication-free seal, but it did leave some residue on the windows, especially at TDC position. The flat head and piston surfaces allow excellent optical access. The injectors are installed in a hole previously used for the spark plug. The existing spark-plug thread is appropriate for the Chrysler injector, but an adapter was required for the Zexel injectors. Drawings of the Zexel injector adapter as well as of the modifications for the third window can be found in [32].

The current setup was not designed for stratified operation via flow or geometry coupling. Therefore, in tests performed with late injection timings (90° BTDC) firing was sporadic or non-existent.

The head temperatures quoted when using the Zexel injector were taken by a thermocouple imbedded in the injector adapter about 2 mm from the injector tip. Head temperatures quoted when using the Chrysler injector were taken by a thermocouple on the back side of the head surface (which is about 4 mm thick) about 20 mm from the injector axis. The temperature typically quoted with the Chrysler injector is from a thermocouple bonded to the side of the injector body.

Spark and fuel injection control was performed by a PC with an I/O board running LabView software. Details of this engine control system can be found in [32]. Since the engine is uncooled, the temperature rose throughout an experiment. To minimize this effect in the imaging experiments, the engine controller was designed with a skip-fire function. When activated, this allowed the engine to be fired for a selected number of cycles with the imaging system being activated on a selected cycle in that series. Between series of fired cycles, the engine was motored, minimizing temperature increase. The skip-fire strategy was typically run with ten cycles fired before an image was taken to get reasonable residual properties for the cycle of interest.

To control the engine speed, the engine was connected to an AC electric motor with a variable-frequency drive. While the motor has the ability to absorb energy, this was not found necessary. The engine has such significant friction that even at 0.9 bar load the motor was drawing over 2.5 kW to maintain 1000 rpm.

2.2.2 Fuel Injectors

Two pressure-swirl fuel injectors, designed for direct-injection use, were used in this study. They were supplied by Zexel, Inc. (HFI-2.1: 960040-2330; #664167) and DaimlerChrysler (formerly Chrysler). The injector from Chrysler is a prototype developed for their direct-injection two-stroke engine project in the early 1990's. Both injectors have 60° nominal cone angles, were supplied with fuel at 5 MPa, and were electrically driven by hardware supplied with each unit.

Pressure-swirl atomizers operate by imparting significant angular momentum to the fluid as it enters the swirl chamber. Figure 2.2 shows a schematic of the fluid flow. The diameter decreases at the exit of the swirl chamber, causing an increase in the angular velocity. The angular velocity in the orifice is often high enough to produce a gap at the centerline of the flow that is filled with air from below. This air core is generally believed to be at roughly atmospheric pressure. As the flow exits the orifice, it is no longer confined, so it spreads out into a conical sheet. The cone angle depends on the ratio of the angular and axial velocities of the fluid. As the liquid sheet spreads out, it thins, becoming unstable and breaking up into ligaments and then droplets.

Entrainment of air by the high velocity spray causes a low-pressure zone in the core of the spray. The spray generates a large-scale gas flow radially inward at the base of the spray and axially downward in the core of the spray cone. At high ambient densities, the entrainment has a stronger effect, resulting in significantly reduced radial penetration.

2.2.3 Fuel System

Since the direct-injection fuel system requires significantly higher fuel pressures than port-fuel-injection systems (5 MPa versus 0.3 MPa) a standard automotive fuel pump was not sufficient. In this setup, a hydraulic accumulator and high-pressure nitrogen supply were used to generate the high fuel pressure. Figure 2.3 shows a schematic of the fuel system. The accumulator separates the fuel from the high-pressure nitrogen via a teflon-sealed piston to prevent excessive absorption of gas in the fuel. This precaution was taken even though a test in which air was purposefully introduced into the fuel side of the accumulator showed no obvious effects on the spray. This system has several advantages over a high-pressure pump: the pressure can be varied over a wide range, the components are relatively inexpensive, the accumulator has few wetted parts to flush when changing fuels, and there are no lubricity requirements on the fuel.

The original system used a bladder-type accumulator with a Buna-N bladder. Material compatibility problems were found with the Buna-N and the ketones used as fluorescent tracers in the fuel. First, the iso-octane/acetone mixtures used for fluorescence studies, which were clear when put into the accumulator, became yellow upon removal. Iso-octane contaminated in a similar manner showed significant fluorescence, while none was expected. This fluorescent contaminent was apparently either a compound leached out of the bladder or a product of the decomposition or dissolution of the Buna-N. Second, Buna-N was shown to swell significantly in the presence of acetone (approx. 16% for an iso-octane/acetone mixture). A noticeable amount of acetone could also be smelled in the nitrogen released from the gas side of the accumulator. These two points suggest that the bladder absorbed and was permeable to acetone, which resulted in an unknown concentration of dopant remaining in the fuel. Concerns were also raised about possible mechanical failure of the bladder due to contact with the ketone.

To alleviate these concerns, the bladder accumulator was replaced by a piston-type hydraulic accumulator (Tobul 3AT30-2-S). This accumulator was equipped with specially-ordered teflon-encapsulated Viton seals to prevent attack by the ketone-doped fuel mixtures.

The fuel filling procedure was intended to remove any pockets of air in the fuel system as it is filled. The fuel filling procedure began with evacuation of the nitrogen side of the accumulator through the bleed valve. Then the liquid side of the accumulator was evacuated using a liquid trap to protect the vacuum pump. With the main filling valve closed, the vacuum valve was switched to draw the fuel into the filling tube. The vacuum valve was then switched back to vacuum to remove the air in the filling tube. With the vacuum valve switched back to the fuel reservoir, the main filling valve was opened to allow the fuel to be drawn in. Once all of the fuel entered, the main filling valve was closed tightly, and the bleed valve was opened to release the vacuum.

2.2.4 Fuels

The fuels used in this study were intended to simulate volatility aspects of commercial gasoline. All of the fuel components used are listed in Table 2.2. Amoco Indolene High Octane Motor Fuel III (brand code 15211) is a multi-component petroleum product formulated like gasoline which has been tested to meet restrictions on a number of properties. This fuel was used for the PDPA tests as well as selected PLIF and Mie scattering tests. The five single-component hydrocarbons were used in a mixed fuel described in Section 3.7.1. Iso-octane (2,2,4-trimethylpentane) and 2-methylbutane were also used in other PLIF and Mie scattering tests. The four ketones were used as fluorescent dopants in fuel mixtures, as discussed in Sec. 2.3.3.2.

2.3 DIAGNOSTICS

2.3.1 Diagnostic Strategy

The diagnostics used in this work to study the behavior and structure of the fuel spray fall into two classes of optical diagnostics: planar imaging and optical drop sizing. The use of these diagnostics not only takes advantage of the engine's optical access, but also avoids some of its inherent limitations. The unorthodox shape of the combustion chamber and relatively poor piston sealing make combustion studies unrealistic. In addition, unknown cylinder flows make fuel flow less meaningful when the injection-induced flows are no longer dominant. For these reasons, this study focused on the fuel spray itself. Consequences of the observations made here on engine operation are left to studies involving more-realistic geometries.

Planar imaging was accomplished by both planar laser-induced fluorescence (PLIF) and planar Mie scattering. Optical drop sizing was accomplished by phase-Doppler particle analysis (PDPA). These diagnostics are widely used for spray measurements. This selection of diagnostics complemented each other very well since the imaging experiments gave a clear view of the distribution of the fuel in the spray, and the PDPA provided detailed information at a particular point in the spray.

PLIF allows imaging of particular fluorescent compounds in the fuel. This was utilized in this study by adding fluorescent dopants with varied volatility. Therefore, the images represent the distributions of lighter or heavier components of the fuel. One limitation of PLIF, though, is that the signal does not distinguish between liquid and vapor—the fluorescent compound is detected in both phases. This ambiguity was minimized by using a low-volatility dopant. Additional information regarding phase was added by the planar Mie scattering experiments. Light is elastically scattered by the droplet and not by the vapor. The images, therefore, represent distributions of the liquid droplets only. The droplet-diameter dependence of

Mie scattering also allowed estimates of changes in the mean droplet diameter to be made from comparisons with the PLIF.

In spite of the ease of signal detection, it is very difficult to make either of these imaging techniques quantitative. To obtain quantitative results, PDPA was used to measurement droplet diameter, velocity, and timing at multiple points throughout the spray.

2.3.2 Imaging System

A digital CCD camera was used to record the images for the PLIF and Planar Mie-scattering experiments. The camera used was a Princeton Instruments gated-intensified-CCD camera (576SE ICCD detector and ST138 controller). The CCD array has 384 rows and 576 columns of pixels. To minimize dark charge, the CCD array was cooled by a Peltier-effect thermoelectric cooler. The minimum temperature is about –35 °C, but the cooler was run at 0 °C for earlier tests and 20 °C for later tests. The hot junction of the cooler was then cooled with water. To prevent water condensation on the array, the camera was purged constantly with dry nitrogen.

Exposure times of the camera were controlled by gating the intensifier. Gating effectively uses the intensifier as a shutter by turning the gain on and off electronically. With intensifier gating, exposure times from under 5 nanoseconds to several seconds can be achieved. Typical exposure times used were 0.1 to 5 μs for PLIF, 0.5 to 10 μs for Mie scattering, and 50 to 100 μs for focussing in ambient light. The gain setting for the intensifier was typically set to 90% of full scale. The camera manual is not specific about voltages corresponding to gain settings.

The lens used on the camera was a 60 mm, f/2.8 Nikkor camera lens. This lens contains glass optics, which prevents detection of scattered UV laser radiation in the PLIF tests. This was verified with a UV-blocking filter. The spatial resolution of the system ranged from about 200 μm to 70 μm, depending on the setup. The intensifier also causes some blurring which reduces

the effective resolution. Because the droplets the sprays used here are typically under 50 μm, individual droplets cannot be distinguished by this system.

2.3.3 Planar Laser-Induced Fluorescence

2.3.3.1 Theory

Laser-induced fluorescence is achieved through the excitation of a fluorescent compound and the subsequent observation of its spontaneous emission. When a molecule of the fluorescent compound absorbs a photon of the exciting laser radiation, it is raised to a higher-energy-level electronic state. Some fraction of the excited molecules then relaxes to an intermediate energy level, emitting a photon of radiation at a lower energy (longer wavelength) than the exciting laser. The absorption spectra of the relatively small molecules of interest for doping gasoline are typically in the ultraviolet region. Although this requires an ultraviolet-capable laser and sheet-forming optics, standard collection optics can be used since the fluorescence is typically in the visible range.

The number of molecules emitting the fluorescent photons is a fraction of the number excited, so that the intensity of the fluorescence is approximately proportional to the mass of dopant excited. The proportionality constant between the number of photons emitted to those absorbed, called the quantum yield, typically depends on temperature and is affected by collisional quenching by oxygen or other molecules. Table 2.3 lists the uncertainties associated with the PLIF signal, their estimated magnitude, and possible corrective measures. Most of the images presented in this work are uncorrected. Therefore, image intensities, in general, cannot be compared between sets of images. An exception is in Section 3.7, where corrective measures were taken to calibrate the images.

2.3.3.2 Fluorescent Dopants

The effectiveness of PLIF as a diagnostic is highly dependent on the choice of fluorescent dopant. For this study some of the main considerations were: absorption spectra overlapping the wavelengths of available lasers, fluorescence in the visible range, high quantum yield, minimal oxygen quenching, low temperature dependence, and co-evaporation with gasoline. Heavy, aromatic compounds in gasoline will fluoresce readily, but since the identity and concentrations of these compounds are not well known and may vary from batch to batch, the intensity of gasoline fluorescence is not considered a quantitative diagnostic [33]. Gasoline fluorescence is used, though, in some of the tests in this work to avoid concerns related to the appropriateness of volatility characteristics of formulated test fuels. Since the fluorescing compounds in gasoline generally have high boiling points, these images represent the distribution of heavy ends of the fuel.

In order to allow mapping of more volatile fractions of the fuel in a semi-quantitative manner, a fluorescent dopant is used in a non-fluorescing base fuel. The base fuels used are either iso-octane or a blend of five hydrocarbons described in Section 3.7.1. The dopants most often considered for engine work are carbonyl compounds [34, 35]. These include both aldehydes and ketones. These groups both exhibit ultraviolet absorption spectra and visible emission spectra and offer a range of volatilities suitable for gasoline tracing [35, 36]. Ketones have the added advantages of having a stronger signal, weaker pressure dependence [35], as well as being generally more easier/less toxic to handle than aldehydes.

Four ketones were used in this study. Acetone (T_B = 56 °C) was used to simulate the light ends of gasoline. The middle of the distillation curve is represented by 3-pentanone (T_B = 102 °C). The heavy ends of gasoline are represented by cyclohexanone (T_B = 155 °C). In some tests, 2-butanone (methylethylketone, MEK; T_B = 80 °C) was used as an intermediate between acetone and 3-pentanone. The fluorescence yields of the three straight-chain ketones were very

similar, while that for cyclohexanone was about a factor of two higher (see Sec. 3.7.2.2). A summary of fuel components is given in Section 2.2.4.

2.3.3.3 Laser System

The laser used to excite the ketone dopants was a XeCl excimer laser (Lambda Physik Compex 102; 308 nm). The excimer is a pulsed laser with a pulse duration of 10-50 ns. The peak pulse energy is quoted at 200 mJ, and the maximum repetition rate is 20 Hz.

The beam exits the laser in a rectangular shape having dimensions of 23 mm tall by 7 mm wide. For the early, close-up images, the beam was shaped by a pair of cylindrical lenses (focal length 157 mm and 52 mm) and a slit, changing the beam dimensions to 23 mm high by 0.5 mm thick. Approximately 20% of the 70 mJ pulse energy emitted by the laser was actually transmitted to the test volume, limited mainly by attenuation by the slit. For the wide-field-of-view images, to avoid the loss at the slit, the beam was focussed horizontally with a single cylindrical lens. A schematic of this optical setup is shown in Figure 2.4. The sheet-thinning lens has a long focal length (1047 mm) to minimize thickness variation across the combustion chamber. The resulting laser sheet was about 0.5 mm thick. The beam was also expanded vertically with a cylindrical lens (157 mm) to extend over the entire stroke. A 100 mJ pulse energy was used for these tests.

Aligning the optics was relatively easy since almost any target placed in the laser beam fluoresces brightly.

2.3.3.4 System Timing

Timing of the PLIF system was controlled by a pulse generator purchased with the imaging system (Princeton Instruments PG200). This pulse generator has a high voltage output to control the camera intensifier gate, as well as two TTL-level outputs. Figure 2.5 is a schematic of the PLIF wiring connections. The input to the PLIF system was typically a trigger signal from the engine controller synchronized with the injection signal. The changes made to

the engine-controller skip-fire algorithm to facilitate this timing are described in Appendix 1. If the PG200 was not receiving an inhibit signal from the camera controller (ST138), it began timing from the rising edge of the injection signal. After prescribed delays, the PG200 triggered the camera controller to activate the CCD array, the laser, and then gated the camera intensifier. The data cable from the image computer to the PG200 allowed preset timing programs to be loaded. A sample PG200 program for the timing of movie images is shown in Appendix 2.

The LIF signal was found to reach the camera approximately 3.7 μs after the laser trigger. Since the timing of the laser pulse varied, the intensifier gate duration (0.1 μs) was made significantly longer than the LIF signal (on the order of tens of nanoseconds).

2.3.4 Planar Mie Scattering

2.3.4.1 Theory

The scattering experiments performed in this work, while referred to as Mie scattering, are analyzed under the assumption that they are in the limit of geometric scattering. When the size of the scattering particles is of the order of the wavelength of the light, the wave nature of the light is important. Scattering in the limit of particles much smaller than the light wavelength is termed Rayleigh scattering. In this limit, the light wave interacts with the entire particle. In the opposite extreme, in which the particle is much larger than the wavelength of the light, geometric optics and ray theory apply. This is based on ray-tracing concepts such as reflection and refraction, and is sometimes referred to as geometric scattering. Mie theory allows calculations anywhere between these two extremes.

For the larger droplets in the sprays of interest here, geometric scattering is a good approximation. Even for the smallest droplets observed (about 5 μm compared to 0.5 μm laser wavelength), the variation from the geometric scattering solution is oscillatory in droplet diameter [37]. This means that for the broad droplet size distributions observed, these variations should cancel out.

A geometric scattering calculation to determine the dependence of the scattering intensity on the droplet diameter is shown in Appendix 5. The calculation shows that the scattered light intensity is proportional to the total droplet surface area. The scattering image intensity, therefore, is proportional to the volume of liquid present, and inversely proportional to the size of the droplets in which it is contained. Since the PDPA results (Chapter 4) show that the mean droplet size does not vary by more than about 20% within a spray, variations in the image intensity represent the distribution of liquid mass in the spray.

On the other hand, mean droplet sizes vary by nearly a factor of three between operating conditions. Assuming that the total amount of fuel injected was constant, the mean scattering intensity was then inversely proportional to the droplet diameter. This fact was used to estimate changes in droplet diameter in Sections 3.1.3 and 4.6.1.

2.3.4.2 Laser System

The planar Mie-scattering experiments were performed with an argon-ion laser (Coherent Innova-90) capable of 2.0 W at 514.5 nm. The same laser was used with the Phase-Doppler Particle Analysis system. The light output is visible (green) and continuous.

The beam exiting the laser was roughly 5 mm in diameter with a Gaussian intensity profile. The early experiments used a cylindrical lens to increase the height of the beam. The beam was then passed through the same thickness-reducing lens-pair and slit used in the early PLIF experiments. The later Mie-scattering experiments used an optical setup similar to the later PLIF experiments. The same height-increasing cylindrical lens was used in all Mie-scattering experiments. To reduce the variation in intensity across the beam, it was over-expanded vertically to allow the use of only the center portion of the beam. The thickness-decreasing lens had the same long focal-length (1047 mm) used in the PLIF experiments. This later setup allowed a much larger fraction of the beam to be used. This fact, combined with higher laser power used, allowed much higher laser intensity in the sheet.

2.3.4.3 System Timing

Timing for Mie scattering experiments was very similar to that for the PLIF experiments (see section 2.3.3.4). Since the argon-ion laser is continuous, no laser trigger signal is needed. In addition, for the Mie scattering experiments, the intensity of the image varies with the gate duration of the intensifier. To minimize blurring, the Mie scattering images were taken with the aperture fully open (f/2.8) so that the shortest possible intensifier gate duration could be used. In the early experiments where the laser intensity in the sheet was low, the intensifier gate duration was as long as 10 μs, which resulted in significant blurring of the images. The modifications to the laser sheet (see Section 2.3.4.2) allowed gate durations as short as 0.5 μs.

2.3.5 Phase-Doppler Particle Analysis

2.3.5.1 Theory

The operation of the Phase Doppler Particle Analyzer (PDPA; Aerometrics, Inc.) is similar to a conventional Laser Doppler Velocimeter (LDV) with the addition of multiple detectors to determine the droplet diameter. A schematic of the PDPA operation is shown in Figure 2.6. A laser beam is split into two and sent through a fiber-optic cable to the transmitter. The transmitter crosses the two beams at the measurement location. A droplet passing through the beam crossing scatters light, creating a fringe pattern in the far-field [38]. The receiver collects some of this scattered light onto three detectors. As the fringes move past the detectors, they produce identical signals with a phase shift. An LDV would use one of these signals to determine the droplet velocity component in the plane of the laser beams. The PDPA, in addition, uses the phase shift between the signals to determine the droplet diameter. A detailed description of the diagnostic development and signal processing is given by Bachalo and Houser [39].

The beam splitting is performed by a rotating grating that is also used to introduce a frequency shift [40]. The main purpose of this frequency shift is to remove the ambiguity in the direction of the velocity.

Each time a burst of scattered light fringes is detected, the PDPA system calculates the velocity and diameter. Checks are performed on the data to ensure consistency. If no problems are found, the system records the time and any external inputs along with the velocity and diameter.

2.3.5.2 PDPA Hardware

The PDPA hardware used in this study was mid-1980's vintage equipment (DIG4) produced by Aerometrics, Inc. Component model and serial numbers are supplied in Table 2.4. The system components are shown schematically in Figure 2.7.

Laser light was supplied by a Coherent Innova 90-4 argon-ion laser. For use with the PDPA, the laser was set to produce 1.0 W of light at 514.5 nm (maximum was about 2 W). The exit aperture of the laser was set to a diameter of 2.37 mm (setting 5). The laser beam is directed into the frequency shift unit. Inside, the beam is split in two, with a frequency shift added. The frequency-shift motor is driven by the MOTOR CONTROLLER unit. The two beams are directed into fiber-optic cables, which lead to the TRANSMITTER. In the TRANSMITTER, the two beams are separated and then focussed onto the measurement location. Scattered light from the droplets is captured by the RECEIVER. The RECEIVER focuses the light onto a slit, which is used to set the size of the probe volume. The light passing through the slit is focused into three fiber-optic cables, which lead to three photo-multiplier tubes (PMTs) in the PHOTODETECTOR UNIT. Signals from the PMTs are processed in the PDPA PROCESSOR by counter-type electronics, and then sent to the interface card in the computer. An external input was supplied by an additional interface card (UniBoard). A counter with a reset was connected to the external input to process timing information. The computer was a standard Pentium PC, although locating a PC with sufficient

slots and room for the large interface cards proved somewhat challenging. The software was level 5.22 supplied by Aerometrics.

All operation of the system is done through the computer, with the exception of supplying power to the PMTs.

2.3.5.3 System Setup

The setup of the PDPA system is quite flexible—allowing for a wide range of droplet diameters, velocities, and densities. The pressure-swirl injectors used here produce very dense sprays of small droplets, and due to the transient nature of the injection, a wide range of velocities were observed as well. These conditions represented challenges for the PDPA system, and therefore, required a careful setup. A summary of the setup parameters is shown in Table 2.5.

Of the scattering angles the system is set up to use, 30° was chosen because it provides the strongest signal and was practical for the optical engine setup. Questions were raised about the effect of the orientation of the optical-engine windows on the results, but tests using three different orientations (normal to the transmitter, normal to the receiver, and 15° from the normal of each) showed no significant difference. The most practical setup for accessing the desired measurement points was taken: both the transmitter and receiver 15° from the window normal, as depicted in Fig. 2.7.

The small droplet sizes required a larger angle between the crossing laser beams. This was accomplished by using the beam expander to increase the beam separation to 40 mm, and using a shorter focal length lens on the transmitter (250 mm versus 498 mm). This allowed for measurement of droplet diameters down to 0.6 μm. Since the usable diameter range covers a factor of 35, a typical diameter range was 1 to 35 μm.

Usable signals are produced with the PDPA when only one droplet is in the sample volume at a time. This becomes less likely as the spray density increases. To minimize this

problem with the high-density used here, the sample volume was made as small as possible. The high beam incidence angle, required for measuring small droplets, decreased the sample volume. Additionally, reducing the receiver slit width from 100 μm to 50 μm cut the sample volume in half.

Reducing the PMT voltage also reduced the sample volume by requiring droplets to be closer to the axis of the Gaussian beam to be detected. The PMT voltage was initially selected to result in a limited number of saturations, which is one of the suggested guidelines. It was later discovered that this results in a large number of false readings under certain conditions. These false readings could not be validated when diameter collection was turned on, resulting in very low validation rates (8 to 10%). Initial suspicion of these readings resulted from significant differences between the velocity histograms with the diameter collection turned on or off. When the diameter collection was turned off and nearly all of the readings were recorded, significantly more droplets were observed in the middle of the velocity range. Subsequent tests showed that these droplet readings were in the middle of the range regardless of the range selected by decreasing the frequency shift, while other droplet readings moved in the appropriate manner. Whether these false readings were the result of multiple droplets in the sample volume or large amounts of scattered light from outside the sample volume (see Sec. 4.2) is unknown. The false readings were mostly removed, though, by decreasing the PMT voltage, which reduced the sample volume and the detection of scattered light. The PMT voltage used, 370 V, was a balance between these false readings and leaving too many of the smallest droplets undetected.

With the optical setup defined by the considerations described above, two of the available velocity ranges encompassed most of the velocities observed. The higher range, which was used most often, covered 14.5 to 64.3 m/s. Using the maximum frequency shift of 16.4 m/s, the resulting measurement range was –2.0 to 47.9 m/s. This provided a good range, except for tests at the periphery of the spray, where there are a significant number of droplets with negative velocity. In these cases, the next-lower velocity range was used (7.2 to 28.3 m/s). In this range,

the frequency shift only changes the lower bound of the range. For most of the tests conducted with this range, some the droplets exceeded the maximum velocity. To minimize any bias of the mean velocity, the minimum velocity was often chosen to cut off roughly the same number of droplets. A typical resulting velocity range for this setting was –4.8 to 28.3 m/s.

The validation rate of droplet measurements ranged from about 30 to 60%. The higher validation rates generally occurred in sprays with large mean droplet sizes (low spray density). The most common droplet-rejection errors were phase-ratio-under and over (KU and KO). These errors occur when the difference between the two independent phase measurements is too large. The operation manual suggests that these errors occur from multiple particles in the sample volume or noisy signals, both of which can be caused by the high spray density. Additionally, a large number of diameter-over errors were observed, despite the fact that the diameter histogram generally trailed off significantly before the end of the range. The fact that the diameter-over errors scaled with the phase-ratio-under and over errors suggests that they were also errors due to the high spray density, which were falsely interpreted.

The external input of the PDPA system was set up to record the time since the start of injection. For each droplet reading, the external-input board recorded a 12-bit value from an external source. To record the time since injection, a counter with a reset was used to provide the 12-bit signal. The input to the counter was generated by a signal generator. The reset was connected to a pulse generator that was triggered by the start of the injection signal from the engine controller. The signal generator was generally set to 33.3 kHz to provide as fine a resolution as possible while still covering the entire cycle. This setting resulted in a temporal resolution of 30 μs.

Since the third window in the optical engine was not needed for the PDPA tests, it was replaced by a solid steel wall. Also, since the PDPA can record data continuously, the skip-fire function of the engine controller was not used.

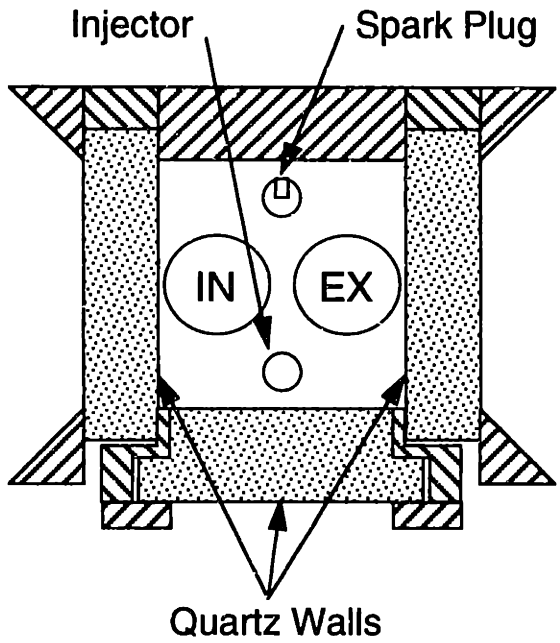

Figure 2.1: Schematic of the optical engine. Horizontal cross section

Table 2.1: Optical engine

Parameter	**Description**
Cross section	82.6 x 82.6 mm
Stroke	114.3 mm
Displacement	0.77 liter
Number of valves	2
Head geometry	flat
Piston geometry	flat
Compression ratio	8:1
Connecting rod length	254 mm
Valve timing:	
IVO	5 °BTC
IVC	55 °ABC
EVO	48 °BBC
EVC	12 °ATC

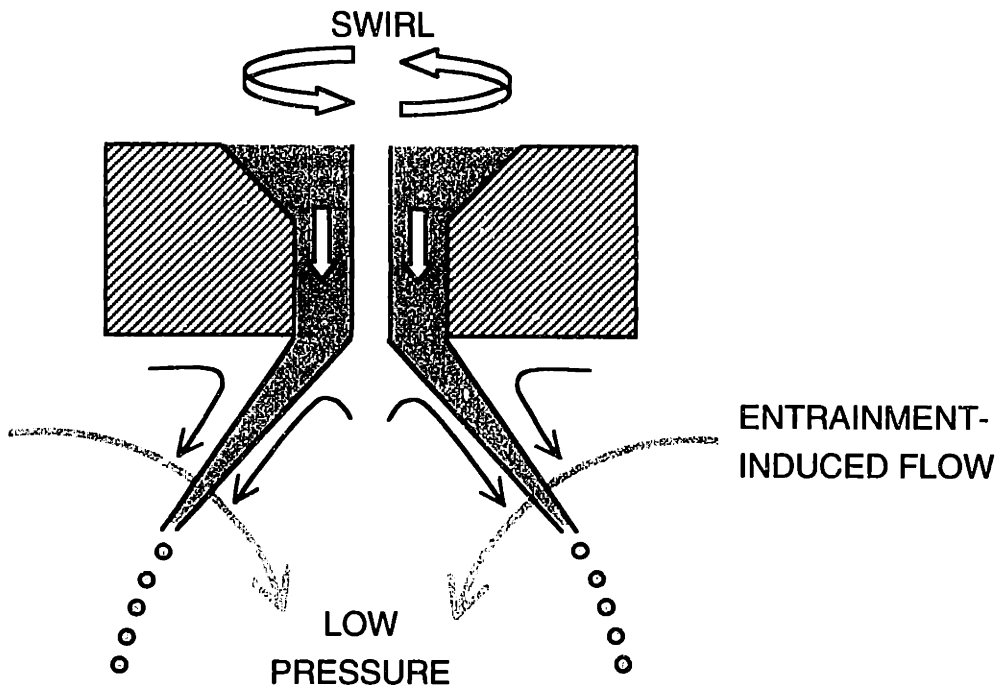

Figure 2.2: Schematic of pressure-swirl injector spray.

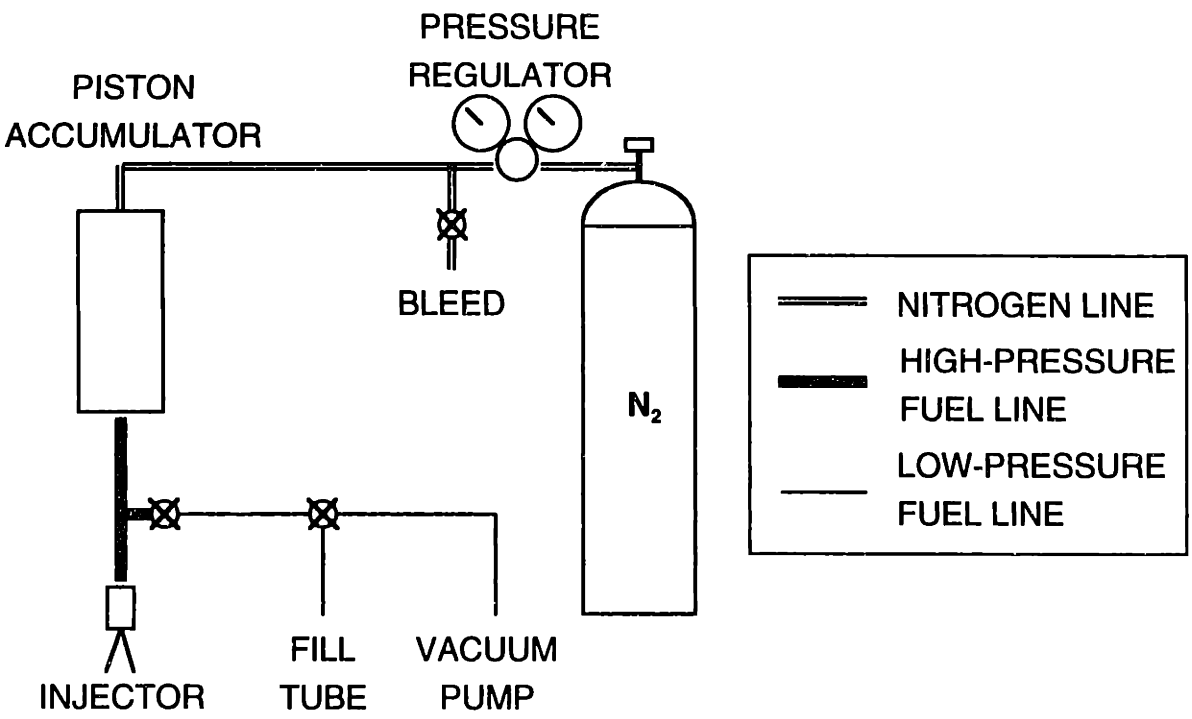

Figure 2.3: Schematic of fuel system.

Table 2.2: Fuel components.

Fuel Species	Boiling Point (°C)	Source	Purity
indolene	30 to 197	Amoco	(15211)
2-methylbutane	30	EM Science	95%
cyclopentane	50	Aldrich	75+%
2,2,4-trimethylpentane	99	J.T. Baker	95%
isopropylbenzene	154	Aldrich	98%
1,3-diisopropylbenzene	203	Aldrich	96%
acetone	56	Mallinckrodt	99.5%
2-butanone	80	Mallinckrodt	99.5%
3-pentanone	102	Aldrich	98%
cyclohexanone	155	Aldrich	99.8%

Table 2.3: PLIF error estimation

	QUANTITY	VARIATION	UNCERTAINTY	ERROR*	CORRECTION
1	beam intensity	constant	±6 mJ shot to shot	±6%	Laser energy meter or reference cell.
2	laser sheet width	constant	±100 μm		Careful control of focussing.
3	laser sheet non-uniformity	15% due to beam expansion	(absorption error in calibration)	15% (±5%)	Calibration test with homogeneous acetone vapor in combustion chamber.
4	laser scattering		unknown but significant	fluorescence of material not in laser sheet	Careful analysis for conditions in which this is prominent
5	absorption of laser		unknown		Compare two sides of spray cone for estimation of severity
6	temperature	70 K in head temperature (400 K during compression)	±30 K due to heat transfer and vaporization	±4% acetone (13%/100K) ±9% 3-pent. (30%/100K)	Difficult to determine–less significant with 266 nm excitation
7	pressure (in air)	0.07 MPa with intake press. (0.5 MPa compression)	±0.01 MPa	0.1% acetone (12%/MPa) 0% 3-pent	Negligible during intake stroke.
8	re-absorption of fluorescence		small		Overlap of emission and absorption spectra are negligible
9	dirty windows		unknown	significant— can be complete loss of signal	New piston seals help
10	camera lens aperture	f/2.8 to f/32	small	factor of 128 (±5%)	Need reference cell for fine correction
11	camera dark charge & background	constant w/ noise	750/65636 ±200/65536	1±0.3%	Subtract background / decrease cooler temperature

* Temperature and pressure dependencies from [Fujikawa].

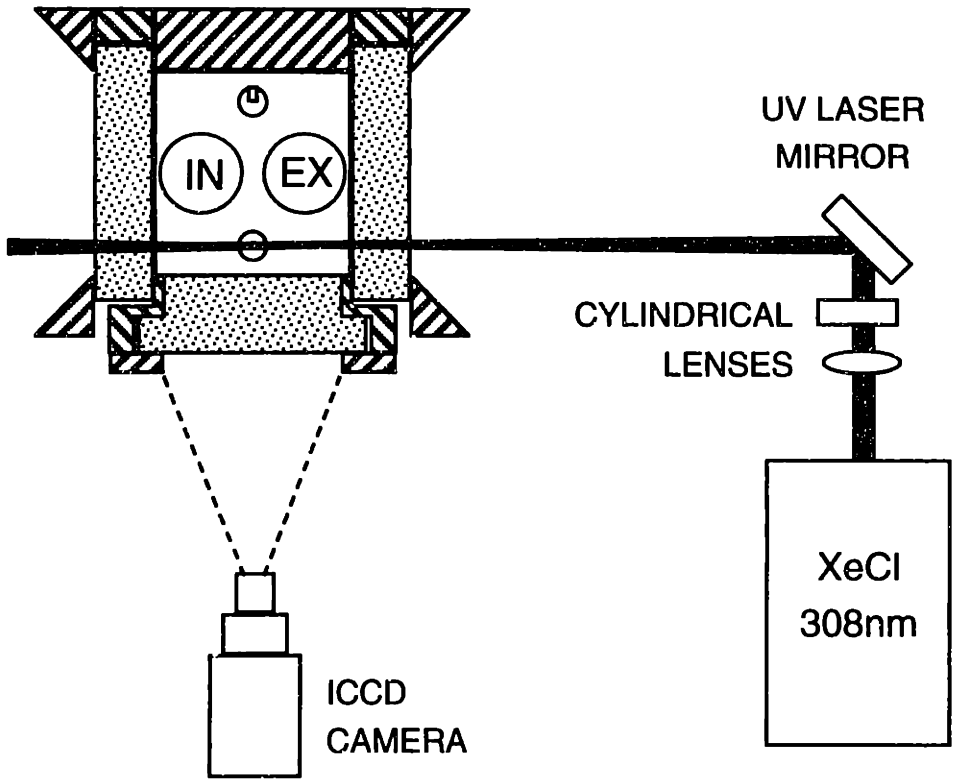

Figure 2.4: Schematic of PLIF optical setup (second setup–without slit).

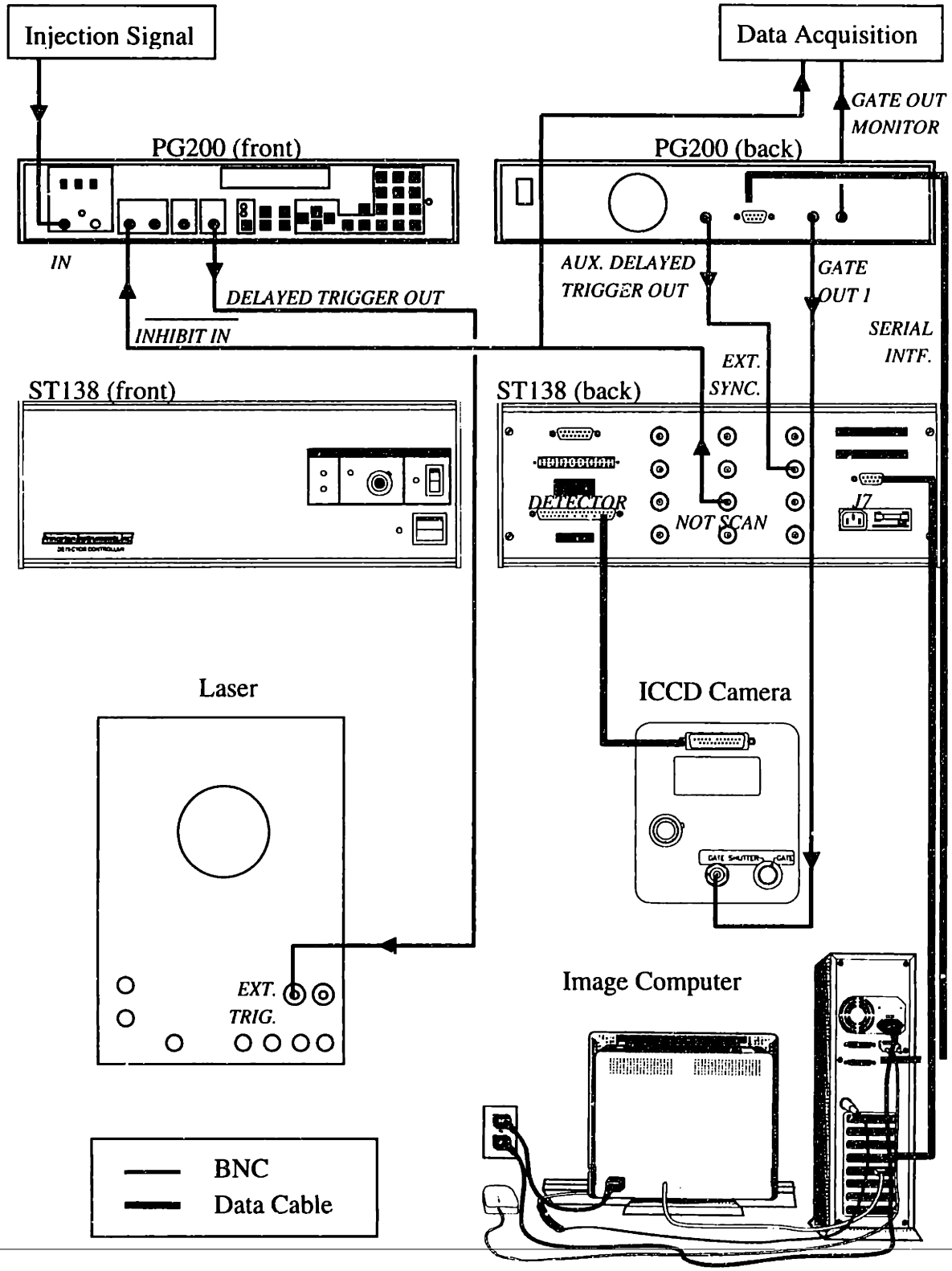

Figure 2.5: PLIF equipment electrical connections.

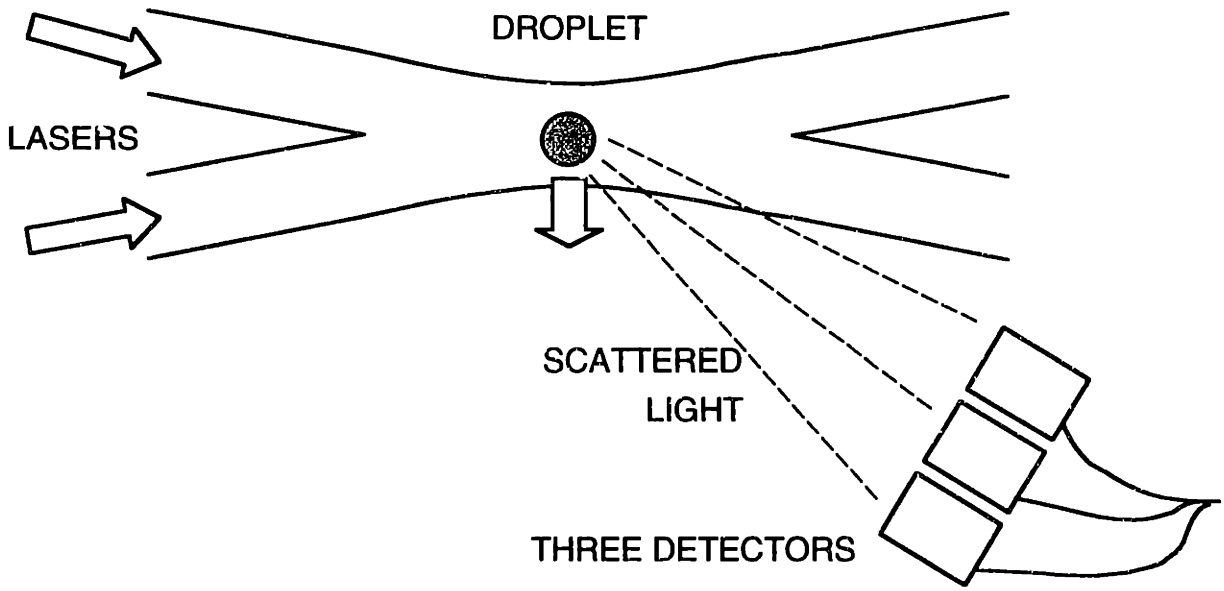

Figure 2.6: Schematic of PDPA operation.

Table 2.4: PDPA Hardware.

Part Name	Model No.	Serial No.
Motor Controller MI	MCB7100•3	249
Transmitter	XMT•1104	011
Receiver	RCV•2104	020
Photodetector Unit	RCM2100	012
PDPA Processor	PDP•3100•5	294

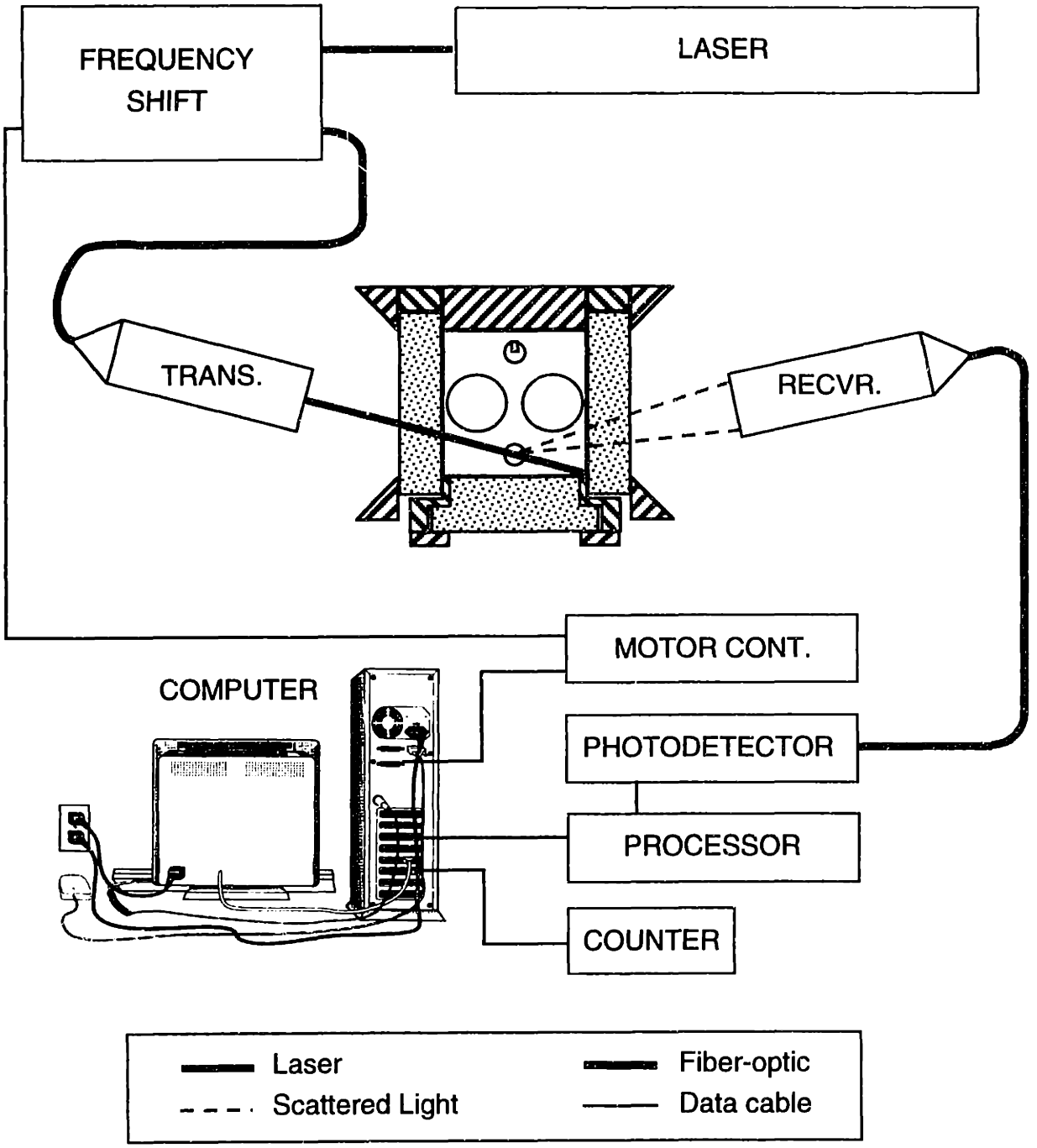

Figure 2.7: Schematic of PDPA system. Top view of engine.

Table 2.5: PDPA Setup Parameters.

Parameter	Value
Scattering angle	30°
Beam spacing	40 mm
Transmitter focal length	250 mm
Receiver focal length	250 mm
Receiver slit width	50 μm
PMT voltage	370 V
Sync. timing resolution	30 μs

CHAPTER 3

IMAGING RESULTS

3.1 Initial Observations

3.1.1 Engine Warm-up

The earliest observations of flash boiling with this apparatus were made by Shelby [32]. Since the optical engine is uncooled, it warmed up quickly during a test. Initially, the head temperature was not measured. However, during longer tests it was noticed that the spray image changed from the beginning to the end of the tests (Figure 3.1). To study these observations, a thermocouple was added to the injector adapter, and tests were performed allowing the engine to heat without changing any of the operating conditions. Tests showed that the head temperature could approach 100 °C in 90 seconds. Figure 3.1a was taken at the beginning of the test, when the head temperature was about 35 °C. After 75 seconds of running, with the head approaching 90 °C, Figure 3.1b was taken. These tests were performed with a vertical laser sheet, acetone-doped iso-octane as the fuel, and an intake pressure somewhat below 0.5 bar. The intake pressure was not known precisely during operation due to an increase in the engine speed when firing was initiated. The increased engine speed with a fixed throttle position resulted in a lower intake pressure. The cold image appears as two well-defined lines, representing a slice through the expected hollow-cone structure. As the engine warmed, though, there was a gradual transition to the cylindrical structure shown in the second image. The peak intensity was no longer at the periphery of the spray but along the centerline. If one defines the structure of the spray by considering a horizontal intensity profile, a transition between hollow cone and filled cone occurred when the intensity at the edges of the spray is no higher than at the centerline.

The temperature sensitivity of the images was repeated with a less volatile dopant: 3-pentanone (T_B = 102 °C) and no transition was observed. A second set of images exhibiting this difference is shown in Figure 3.2. The images were produced using a horizontal laser sheet cutting through the spray 15 mm below the head. The images of the fluorescence were taken at an oblique angle, resulting in ellipsoidal rings for the hollow-cone spray. The right edge of the images is missing due to the proximity of the combustion chamber wall. These images also show no transition for the 3-pentanone dopant, and a gradual filling of the cone for the acetone-doped spray.

The spray image transitions observed with the acetone dopant were tentatively explained as the result of the very fast evaporation of the light dopant from the spray, which was then drawn to the axis of the spray cone by the induced gas flows. While this is consistent with the observations, there was little other evidence to support it. In addition, there were other concerns including the possibility of an effect due to nitrogen absorption in the fuel. The focus of the present work, therefore, has been to understand the effect of ambient conditions and fuel volatility on the structure of pressure-swirl sprays.

3.1.2 Pressure and Temperature

Initial attempts to recreate the transition that Shelby observed proved unsuccessful. The operating conditions that he had recorded were used: a ten-to-one mixture of iso-octane and acetone, start of injection at 60 °ATDCI, a head temperature of 90 °C, and 0.5 bar intake pressure. However, at these conditions no transition was observed. Two things were known to have changed since Shelby used the apparatus to perform his tests. First, the method of timing the camera changed. A sweep of camera timings, though, discovered nothing. Second, a bladder-type hydraulic accumulator had been added to the fuel system. If the transition had been due to nitrogen absorption in the fuel, the addition of the accumulator would have prevented it. A test with air purposely added to the fuel side of the bladder, though, showed no effect.

However, the accumulator was found to have one other possible effect. When unused fuel was removed from the accumulator, it had been yellowed apparently due to interaction of the ketone dopants with the Buna-N bladder material. Since the compound that yellowed the fuel fluoresces, concerns were raised that this fluorescence may mask the acetone fluorescence. Replacement of the bladder-type accumulator with a piston-type accumulator, though, had no effect. The explanation for this discrepancy comes from another change to the apparatus that had no apparent connection. Between these and the original tests, the dynamometer had been replaced. The original unit was a DC motor. Due to the significant friction in the engine, no power absorption is required. When the initial experiments were taken, the intake pressure was set and then the injection was started to begin firing. However, since the old motor was not speed-controlled, the torque added from firing caused the engine speed to increase, thereby lowering the intake pressure. The replacement dynamometer was an AC motor with a frequency controller. The controller corrects for load changes, keeping a constant speed. The intake pressure, therefore, remained at its motored value. Tests run at lower intake pressure were able to recreate the transition at high temperature. Figure 3.3 shows that the transition from hollow cone to filled cone was intensified as the intake pressure was decreased from 0.5 bar to 0.3 bar.

Repeating these test with a wider range of pressures, Figure 3.4 shows a small transition at 0.6 bar and none at 0.9 bar.

3.1.3 Mie Scattering

Since the PLIF experiments discussed in the previous sections were sensitive to the dopant in either liquid or vapor form, some ambiguity existed as to whether the evaporation of the acetone affected the spray structure. The PLIF results could be explained by either vaporization of the acetone dopant into the core of the spray or the disruption of the entire spray with transport of acetone-containing droplets into the center of the spray. To investigate this issue, planar Mie scattering tests were performed. While the PLIF signal is sensitive to both the

liquid and vapor phases, the Mie scattering signal is only sensitive to the presence of liquid droplets. The expectation was that if the evaporation of the acetone had little effect on the rest of the spray, the Mie scattering images would not change. Figure 3.5 clearly shows that this is not the case. Both signals show the same transition to a filled cone structure. The cold Mie scattering image showed a well-defined hollow-cone structure much like the PLIF. There was some blurring in the Mie scattering images, though, due to the relatively long camera gate (10 μs). The hot Mie scattering image, like the hot PLIF image, shows a filled distribution with decreased radial penetration. These results initially suggested that the evaporation of the acetone was causing droplet breakup, and the resulting smaller droplets were more easily entrained by the induced gas flows and drawn into the core of the spray cone. More recent analyses, as discussed in Sec. 3.2, showed that, while the mean droplet diameter was reduced, the apparent change in structure of the Mie scattering images can be explained by the multiple scattering of the laser sheet.

An analysis of the change in scattering intensity of the PLIF and Mie signals was performed to estimate the reduction in droplet size. This technique has been proposed by other investigators [41] as a possible method. For a fixed liquid volume crossed by the laser sheet, the scattering intensity is roughly inversely proportional to the droplet diameter (see Appendix 5), while the PLIF intensity should be constant. In the present case however, changes in both images can occur due to changes in the spray distribution. If the spray is more concentrated near its axis, the laser sheet passes through a larger fraction of the total spray. This would cause a higher integrated image intensity for the hot cases in both the PLIF and Mie images. To correct for the increased mass in the laser sheet, the increase in intensity of the Mie scattering images was corrected with the increase in intensity of the PLIF images. The integrated image intensity for the PLIF images (averaged over 10 frames) increases from cold to hot by 17%. Increased fluorescence yield can account for an 8% increase [34]. The remaining 8% (1.08 x 1.08 = 1.17) was attributed to the spray redistribution. In contrast, the increase in integrated image intensity

for the Mie scattering images from the cold to the hot case was 91%. Assuming that redistribution causes an 8% increase in mass in this case as well, a 77% increase is due to the scattering efficiency (1.08 x 1.77 = 1.91). This suggests a roughly 44% reduction in mean droplet diameter (1 / 1.77 = 0.56). This result is in fair agreement with the 34% reduction later measured by the PDPA for the Chrysler injector between the same operating conditions (a comparison with Mie scattering form the Chrysler injector is discussed in Sec. 4.6.1). These results are considered only approximate due to changes in the fluorescence yield of the acetone as it is converted to vapor and mixed with air and the effects of multiple scattering.

3.2 Spray Optical Scattering

3.2.1 Introduction

Since both the PLIF and Mie scattering images shown above exhibit a similar transition to a solid-cone structure, the original explanation was similar for both. The transition of the Mie scattering images suggested that fluid droplets were being drawn to the core of the spray cone, presumably due to stronger gas-flow effects on the smaller droplets. The PLIF experiments could then show either liquid or vapor acetone being drawn to the core of the spray cone. The main disagreement with this theory arose from the results of the PDPA analysis (see Sec. 4.3.3). The PDPA data showed very few droplets in the core of the spray. Since this was in direct opposition to the theory held for the imaging results, further work was done to determine the cause of the discrepancy. The most likely explanation was that one of the diagnostics was not operating as expected in the core of the spray. As outlined in the following sections and in Sec. 4.2, neither the PDPA nor the laser sheet imaging could obtain correct results at the core of the spray. All of the diagnostics suffered from the high degree of scattering in the dense sprays.

3.2.2 Off-Axis Spray Images

The theory proposed as to how scattering could affect the planar imaging diagnostics is related to illumination of unintended parts of the spray. Parts of the spray not directly illuminated by the laser sheet appear in the region of the image associated with the core of the spray. To estimate this effect, a set of images was taken from an angle close to the plane of the laser sheet (Figure 3.6). In the absence of scattering effects, the sheet of the hollow-cone spray directly illuminated by the laser would appear from this angle as two lines at a narrow angle to each other, representing the near and far intersections of the spray cone and the laser sheet. Other parts of the spray, illuminated by scattering, appear outside this narrow region. The camera was positioned as close to the laser sheet as possible without blocking it. A diffuser was placed behind the engine to gauge the intensity of the laser light after passing through the spray. The resulting images are shown in Figure 3.7. The two vertical lines near the spray are due to fluorescence off the window surfaces as the laser sheet enters and exits the combustion chamber, at least partially due to fuel wetting the windows. The darker line farther to the right is the laser sheet striking the diffuser. Note that the timings between images are not uniform.

Figure 3.7a shows the expected distribution of fuel as the spray develops for the cold case: the two lines representing the near and far sides of the spray cone are most apparent at 1400 μs ASOI. Near the injector tip though, significant intensity is seen to the sides of these two lines where laser light has been scattered out of the path of the laser sheet. However, since over most the spray length only the spray in the laser sheet is illuminated, scattering is relatively insignificant under these conditions. This is also evident in the intensity of the laser light striking the diffuser. The laser sheet is relatively undisturbed by the development of the spray due to scattering. The observed reduction in the laser sheet intensity, at 2000 μs ASOI, is due to impingement of the spray on the near window. This impingement on the windows explains why the fluorescence off the windows is always stronger in the cold case. This liquid fuel on the cold windows can be swept back and forth by the piston seals before it evaporates completely.

The images from the hot case (Fig. 3.7b), on the other hand, show significant scattering. First, the observed spray projections are too wide to represent only the portion of the spray aligned with the laser sheet. In the absence of scatter, one would expect to observe two lines spaced even more closely than in the cold case due to the decreased width of the hot spray. Even more remarkable, though, is the drastic decrease in the intensity of the laser light striking the diffuser. Almost no light remains after passing through the spray. This results in part from the increased absorption of light due to the denser spray, but chiefly from the intense scattering from the small droplets in the hot spray. The spray density, and therefore light scattering, is higher for the more compact spray, which has a mean droplet diameter about 35% smaller (see PDPA results Sec. 4.6.3) at the high temperature than under cold conditions. Light extinction by the spray is further studied in the following section.

3.2.3 Laser Sheet Extinction

As shown in the previous section, extinction of the laser sheet is a sensitive gauge of scattering in the spray. The set of tests presented here for measuring the profile of the PLIF laser sheet was intended to observe small-angle scattering as well as extinction. The setup for these tests is shown schematically in Figure 3.8. Since the laser beam expands horizontally and vertically after leaving the engine, the scale of the resulting images is not known precisely. Images of the laser sheet profile were taken both with and without the spray present. One pair of images is shown in Figure 3.9. They represent the laser sheet cross-section that passed roughly 5 to 30 mm below the injector tip. Without the spray, the laser sheet intensity profile is approximately Gaussian across and nearly uniform along the sheet. When the spray is present, the laser sheet projection is irregular and its average intensity is decreased dramatically. Moreover, the width of the intensity profile is wider relative to the peak than without the spray, due to light scattered away from the laser sheet at small angles. Plotted in Figure 3.10 are the intensity profiles of the laser sheet with and without the spray averaged over ten frames and the

height of the image for a cold spray at atmospheric pressure. The light extinction, defined as the percentage reduction in intensity relative to the undisturbed beam, is about 85% at the centerline.

3.2.4 White Light Extinction

Another way to determine whether hot sprays have a hollow or solid-cone structure was to examine the profile of light extinction across the spray. A hollow cone spray should exhibit less extinction at the centerline than at the edges due to the shorter path length through the spray. This mechanism is illustrated in Figure 3.11. Consider, for example a signal which is proportional to mass (such as extinction for a fixed droplet diameter distribution). For a hollow cone distribution and uniform illumination by a sheet crossing horizontally through the cone, the signal observed on a plane parallel to the axis of the cone would be the signal integrated over a chord perpendicular to each position on the projected plane. For uniform extinction in an optically thin medium, the intensity obtained would be equal to the incident intensity minus the integrated extinction through the corresponding chord. If the extinction is proportional to the total mass of material through the cross-section, this would be the complement of the integrated profile or $(I_0(x)-I(x))$, with $I_0(x)$ representing the incident light intensity in the absence of the spray and $I(x)$ is the measured intensity.

Integrated profiles for possible distributions around a circular geometry, so-called Abel Transforms, are shown in Figure 3.12. Starting from profile A, which shows the cross-section of a hollow-cone profile, its projection is represented by profile B. If profile B were the cross-sectional profile, a partially-filled cone, its projection would be the top-hat profile in C. For a top-hat cross-section, a solid cone, the projection would be profile D.

The experiments performed to measure the extinction profile involved back-lighting the spray with white light. Figure 3.13 shows a schematic of the setup. A diffuser, behind the spray from the point of view of the camera, is illuminated by a slide projector. A sample image of the spray is shown in Figure 3.14. Sample intensity profiles are given in Figure 3.15. The sprays for

these tests were made with 2-methylbutane, which is transparent to visible light. The reduction in transmission, therefore, is entirely due to scattering. Two profiles each from a cold and hot spray were used to calculate the extinction profiles, using the following equation.

$$\varepsilon = \frac{I_0 - I}{I_0 - I_{DC}} \tag{3.1}$$

Here, I_0 is the local intensity without the spray and I is the intensity with the spray. The dark charge of the camera, I_{DC}, was found to be 1% of full scale. The extinction profiles are shown in Figure 3.16. The four traces show roughly top-hat profiles with 80% to 95% extinction. The extinction values are about 10% higher for the location closer to the nozzle (7 mm vs. 20 mm), and 5% higher for the hot spray. Since PLIF images of the spray at 20 °C show a distinct hollow cone structure, its integrated extinction profile (Fig. 3.16a) was expected to resemble profile B in Fig. 3.12, with a substantial dip in the center. There is some evidence of a dip at the centerline of the profile at 7 mm. The lack of a more detailed structure in the extinction profiles is likely due to the very high levels of extinction.

In fact, these extinction levels are high enough that the use of any optical diagnostic to probe the interior of the spray seems unlikely. For comparison, the results from a Malvern laser-diffraction particle-sizing instrument require corrections for multiple scattering at extinction levels above about 60% [40]. By 95% extinction, it seems unlikely that any of the light that reaches the camera has taken a direct path through the spray. The difficulty for this extinction technique is that the spray cannot be considered optically thin. Therefore, the Abel Transform analysis described above must be used with the consideration that a projection through the spray is disturbed by scattering as well.

3.2.5 Image Interpretation

To aid in interpretation of the PLIF and Mie scattering images in the remainder of this chapter, this section was added to summarize the mechanisms leading to the observed spray images. This topic is revisited in the conclusions (Sec. 3.10).

The fact that confused the initial interpretation of these images was that there were two types of transitions of the images to filled profiles, which occurred in the same range of conditions. First, when PLIF images of acetone are considered, the transition is primarily due to evaporation of the dopant. The acetone vapor is drawn to the core of the spray by the induced gas flows. This can be shown through the intensity profiles described below and the volatility stratification images discussed in Sec. 3.7.4. Second, when the image intensity is related strictly to the droplets, as with Mie scattering or PLIF of low-volatility compounds, the transition observed is due to multiple scattering, based on the same arguments.

The PLIF measurements are affected by scattering in the following manner. The thin (0.5 mm) vertical laser sheet hits the outer layer of the spray. Since the spray is not optically thin (as shown in Figs. 3.7, 10, 16), light is scattered by the small droplets over a narrow angle. The scattered laser light illuminates another portion of the spray that would otherwise not be reached by the laser sheet. Therefore, the effective volume of the spray illuminated by the laser light is increased from the original vertical sheet, albeit at a lower light intensity. This effect can be seen in Figure 3.7. The effective cross-section illuminated can be represented as a Gaussian profile. The projected signal, therefore, reflects not only the amount of fuel within the volume crossed by the spray sheet but also the volume illuminated via secondary scatter, as shown in Figure 3.17. The Mie scattering experiments are affected in a similar manner by multiple scattering.

The degree of scattering depends on the spray density, which can be thought of as the liquid surface area per unit volume. This changes with both the droplet diameter and the size the spray envelope. As the scattering increases, three regimes are considered. Figure 3.18 shows a series of PLIF intensity profiles that are believed to represent these regimes. In the first regime,

profiles A and B, when spray densities are low, there is minimal laser sheet scattering. The lowest spray densities are exhibited by the Zexel injector at cold conditions (profile A). Since scattering is low, the intensity from the central region of the spray is near the background level. The Chrysler injector (profile B) shows a slightly larger effect of scattering due to the smaller droplets produced.

In the second regime (profiles C and D), as the pressure increases the spray width decreases, leading to higher local scattering. As described above, the effective volume illuminated by the spray increases as the spray density increases. The chord through the spray along the line of sight of the camera contains an increasing amount of fluorescing material.

The third regime, represented by profile E, involves the extreme case in which the optical density of the spray is high enough that the light reaching the camera is no longer a projection through the spray. Once the light becomes scattered after only a short distance, the fluorescent light from the interior and the back of the spray is scattered significantly en route to the camera as well. The result is that the light reaching the camera came from droplets at the near edge of the spray. The spray then becomes analogous to a solid, since the imaged light only comes from the surface. All of the sprays above a certain level of optical density (decreasing mean droplet size and spray width) exhibit these very flat, top-hat intensity profiles. This characteristic, therefore, was used as a demarcation for intense optical scattering.

The last two profiles (F and G) represent the case in which acetone vapor is being imaged. As the acetone quickly evaporates, it is drawn to the axis of the spray by the induced flows, forming a vapor core. The projection through the roughly top-hat concentration cross-section of the vapor core results in rounded intensity profiles.

This complex relationship of laser sheet scattering and optical density makes determination of the spray structure from the PLIF images alone very difficult. In general, when a spray produces an intensity profile similar to A-D in Fig. 3.18, with a decrease in the interior of

the spray, the spray cone must be at least partially hollow. If a top-hat profile like E is observed, though, no determination about the internal structure can be made.

3.3 Effect of Superheat

3.3.1 Effect of Superheat on Vapor Distribution

3.3.1.1 Experiments

In order to understand the role of flash boiling in the transitions observed in the vapor images, it is useful to compare the behavior of the spray when dopants of different volatility are added. Flash boiling is dependent on the degree of 'superheat', or the difference between the liquid temperature and the prevalent ambient temperature. Conversely, the degree of superheat can be expressed as the difference between the ambient pressure and the fluid vapor pressure. Both of these values are used in this study, in later sections, the superheat is represented as the normalized excess vapor pressure.

$$\Pi = \frac{P_{VAP} - P}{P} \tag{3.2}$$

This quantity has the advantages of being non-dimensional and being normalized by two limits: zero represents the boiling point of the fluid and negative one represents a non-volatile fluid. For these tests, the superheat temperature values were more easily found in the literature.

In order to vary the superheat temperature, an array of PLIF experiments were developed with a range of potential for boiling using fuels for which the boiling point (or bubble point) could be determined. These tests involved a range of fuel volatilities and cylinder pressures, while keeping a head temperature of 90 °C. Three different fuel volatilities were achieved by adding three different fluorescent dopants to iso-octane (10:1 iso-octane to dopant by volume). Acetone (T_B = 56 °C) was used to represent the high volatility components, and 3-pentanone (T_B = 102 °C) was used to represent low volatility components. An intermediate volatility was

achieved with 2-butanone (T_B = 80 °C). PLIF images were taken of these fuel mixtures at 0.3, 0.6, and 0.9 bar intake pressure, 1 ms after the start of injection. Figure 3.19 shows these images.

These experiments show a similar behavior as the effect of temperature shown in Fig. 3.4. For low or no superheat, the spray cross-section behaves as a hollow-cone spray. For high superheat, the dopant evaporates from the spray and is entrained into the core of the spray, producing a the diffuse solid-cone structure observed. In order to rationalize this behavior, the superheat temperature was estimated for each these cases, as described below.

3.3.1.2 Fuel Temperature Estimation

To the superheat of the fuel, two quantities are needed, the fuel temperature and the bubble point of the mixture. Fuel temperature leaving the injector affects the behavior of the spray as it determines the superheat. The head temperature, near the tip of the injector, was monitored with a thermocouple. The injector was preheated by warming up the engine (early studies with Zexel injector) or using a heat tape (Chrysler injector, later studies).

Heat transfer from the injector to the fuel was assumed to occur at constant wall temperature since the thermal diffusivity of the steel is significantly higher than that of the fuel.

$$\frac{\alpha_{steel}}{\alpha_{iso-octane}} \approx 60 \tag{3.3}$$

Due to the transient nature of the flow in the injector, the heat transfer can be considered in two separate regimes: turbulent convection during the injection event and transient conduction between injections. The relative importance of the two is highly dependent on the residence time of the fuel. The volume of fuel contained in the injector was estimated to be about 50 times as much as is injected each cycle [42]. For this value, the residence time of the fuel is six seconds at 1000 rpm. For such a long residence time, conduction should be dominant. The heat transfer

was therefore modeled as transient conduction into an infinite cylinder. This mode of heat transfer is described by the following equation [43]:

$$\theta = \frac{T - T_W}{T_0 - T_W} = \sum_{\nu=1}^{\nu=\infty} \frac{2}{\beta_\nu J_1(\beta_\nu)} e^{-\beta_\nu^2 Fo} J_0\left(\beta_\nu \frac{r}{R}\right) \tag{3.4}$$

where r is the radius of interest and R is the radius of an injector passage. J_0 and J_1 are the Bessel functions of the zero and first order, respectively, and β_ν is the nth zero of J_0. The Fourier number, Fo, is defined as:

$$Fo = \frac{\alpha t}{R^2} \tag{3.5}$$

where α is the thermal diffusivity and t is time. The mean temperature change for the fuel is calculated by a weighted average of θ from Eq. 3.4 for 50 radial steps. Although Eq. 3.4 was summed over seven terms of ν, only the first was required in this case. These results show that for $r < 0.75$ mm, $\theta_{mean} < 1\%$, suggesting that for passages smaller than 1.5 mm in diameter the heat transfer is over 99% complete considering only conduction. Since most of the passages in the injector are smaller than 1.5 mm and flow-induced mixing will increase heat transfer, the fuel is assumed to exit at the temperature of the injector.

$$T_f \approx T_{inj} \approx T_{TC} \tag{3.6}$$

The fuel temperature is, therefore, taken as the temperature measured by the thermocouples, which is 90 °C for all of the cases in Fig 3.19.

3.3.1.3 Bubble Point Calculation

The minimum temperature at which bubbles can begin to form in a multi-component liquid at a given pressure is given by the equilibrium property called the bubble point [44]. This is the analog to the boiling point for pure compounds, and represents the point at which the volatile component of the mixture starts to vaporize. The method used here to calculate the bubble point temperature is described as follows.

At its bubble point, a liquid is in equilibrium with a vapor composed entirely of species from the liquid. This corresponds to the same definition as in the case of a pure substance in equilibrium with its own vapor. This condition can be described as the sum of the mole fractions of the liquid species in the vapor being unity [44].

$$\sum_i y_i = 1 \tag{3.7}$$

The ratio of components in the liquid and vapor can be described using the equilibrium constant for each component and the ratio of components in the liquid. The equilibrium constant, K_i, is defined as

$$K_i \equiv \frac{y_i}{x_i} \tag{3.8}$$

where x_i is the mole fraction of species i in the liquid phase. Combining equations 3.7 and 3.8 yields the standard definition of the bubble point.

$$\sum_i K_i x_i = 1 \tag{3.9}$$

The equilibrium constant can be estimated by assuming that the gas phase obeys Dalton's Law [45]:

$$P_i = P y_i \tag{3.10}$$

where P_i is the partial pressure of species i, and P is the total pressure. The resulting equation is the Raoult's Law approximation for the equilibrium constant.

$$K_i = P_{VAP,i} / P \tag{3.11}$$

where $P_{VAP,i}$ is the vapor pressure of species i. This approximation holds if the liquid phase is ideal, but for the mixtures of interest here, a correction is needed. Including a measure of the non-ideality of the liquid results in a modified Rauolt's Law equilibrium constant [44].

$$K_i = \gamma_i P_i^{sat} / P \tag{3.12}$$

Here γ_i is the activity coefficient of component *i*. The activity coefficient for each species in a binary mixture can be estimated from experimental data [46] using a correlation. For this calculation, the van Laar activity coefficient correlation for binary mixtures was used [44].

$$ln\gamma_1 = A_{12}\left(\frac{A_{21}x_2}{A_{12}x_1 + A_{21}x_2}\right)^2 \qquad ln\gamma_2 = A_{21}\left(\frac{A_{12}x_1}{A_{12}x_1 + A_{21}x_2}\right)^2 \tag{3.13}$$

This correlation was formulated with vapor pressures calculated from the Antoine correlation [44].

$$log[P^{sat}] = A - \frac{B}{T+C} \tag{3.14}$$

Equations 3.9, 3.12, 3.13, and 3.14 can then be solved simultaneously for the bubble point temperature. This was accomplished using a linear equation solver. Complete sets of the input equations are given in Appendix 6.

The bubble point was calculated for each of the nine test points represented in Fig 3.19. The resulting superheat values are listed in Table 3.1 along with the boiling point of each compound at the same conditions. The last column gives the relative position of the bubble point between the two boiling points. A value of zero in this column would indicate that the mixture boils at the same temperature as the dopant, suggesting that there is no interaction between the two compounds. For the acetone and 2-butanone mixtures, the bubble point is roughly the average of the two boiling points. For the 3-pentanone, on the other hand, the bubble point is slightly suppressed, below either of the component boiling points.

The superheat, ΔT, is then calculated as

$$\Delta T = T_{BP} - T_f \tag{3.15}$$

where T_{BP} is the bubble point temperature of the mixture at the given pressure and T_f is the temperature of the fuel mixture. The superheat temperature for each of the experimental cases is printed in the corner of the corresponding image in Fig. 3.19.

3.3.1.4 Observations

In Figure 3.19, a line is drawn to represent the cases in which a solid-cone transition is seen due to evaporation and those that appear as distinct hollow cones. The transition is defined as the point at which the two distinct lines, representing the hollow cone structure, become blurred and the core of the spray begins to be filled. The transition is seen to the left and above the line. The transition becomes more pronounced towards the upper left as well. This corresponds to more volatile dopants and lower pressures, both of which are consistent with an increased tendency to boil. The superheat follows a similar trend, going from –2 K in the lower right (3-pentanone at 0.9 bar) to 43 K in the upper left (acetone at 0.3 bar). In fact, the line dividing the PLIF images also separates superheats below 20 K on the lower right and superheats above 20 K on the upper left. This suggests that the superheat necessary for flash boiling to be observed is about 20 K.

3.3.2 Effect of Superheat on Liquid Distribution

3.3.2.1 Single Component Fuel Tests

A set of experiments were also performed to determine the effect of fluid superheat on the liquid droplets. To ensure measurement of only the droplets Mie scattering imaging was used. In order to more accurately determine the superheat needed to affect the spray, two parameters need to be better defined: the boiling point of the fluid and the fluid temperature. To remove the errors introduced by the fuel mixing and the bubble point calculation, a single component fuel was chosen. A relatively low boiling-point hydrocarbon, 2-methylbutane (T_B = 30 °C), was chosen to allow significant amounts of superheat without damage to the injector. The fluid temperature was more closely controlled by removing the Chrysler injector from the engine and wrapping it with a heat tape. The heat tape was controlled by a digital temperature controller, which received feedback from the thermocouple mounted to the side of the injector. Before each test, the temperature was allowed to equilibrate for at least five minutes. Each test

consisted of only ten injections, so the fuel injected even in the last injection was in the injector during the equilibration time. The resulting fluid temperature at injection, therefore, should be within ±1 K of the set temperature of the controller.

3.3.2.2 Effects of Pressure and Temperature

Temperature and pressure affect the fuel spray not only through changes in the superheat, but also through changes in the fluid properties, droplet breakup, and entrainment. Changes in the fuel temperature affect its density, viscosity, and surface tension, all of which affect the droplet size. Changes in ambient pressure affect the fuel flow rate and the droplet breakup process. Therefore, it is important to understand these effects when interpreting images for flash boiling behavior.

Changes due to temperature and pressure are summarized in Table 3.2. For demonstrative purposes, the pressure and temperature effects are separated. Temperature effects are listed in terms of an increase from 30 °C to 90 °C. Pressure effects are listed in terms of a decrease from 0.9 bar to 0.3 bar. Mass flow rate and Sauter Mean Diameter (SMD) are estimated from correlations for pressure-swirl atomizers [47]. The mass flow rate can be expressed as follows.

$$\dot{m} = C_D A_o (2\rho_L \Delta P_L)^{0.5} \tag{3.16}$$

Here, A_o is the orifice area, ρ_L is the liquid density, and ΔP_L is the pressure differential across the injector. The discharge coefficient, C_D, is only a weak function of fluid properties. For a temperature change, the mass flow rate is proportional to the square root of the liquid density.

$$\dot{m} \propto \rho_L^{0.5} \tag{3.17}$$

For a pressure change, mass flow rate is proportional to the square root of the pressure differential across the injector.

$$\dot{m} \propto \Delta P_L^{0.5} \tag{3.18}$$

The correlation used for the SMD is a variation of Eq. 6.17 from Lefebvre [47]. The original ambient density dependency is intended for a high-pressure range (> 4 bar). For a lower pressure range, a significantly different ambient pressure correlation is suggested.

$$SMD \propto P_A^{0.27} \tag{3.19}$$

Assuming density is proportional to pressure (ideal gas), this can be included in the overall SMD correlation.

$$SMD = A\sigma^{0.25}\mu_L^{0.25}\rho_L^{0.125}d_o^{0.5}\rho_A^{0.27}\Delta P_L^{-0.375} \tag{3.20}$$

For a variation in temperature, this can be simplified to the following.

$$SMD \propto \sigma^{0.25}\mu_L^{0.25}\rho_L^{0.125}T_A^{-0.27} \tag{3.21}$$

For a variation in ambient pressure, the following is the SMD proportionality.

$$SMD \propto P_A^{0.27}\Delta P_L^{-0.375} \tag{3.22}$$

The resulting 4% decrease in predicted mass flow rate for the temperature increase and 1% increase for the pressure reduction, should have no noticeable effect on the results. The change in SMD, however, is significant: a 23% decrease for the temperature increase and a 26% decrease for the pressure reduction. Therefore, changes in the spray, due to the decrease in droplet size, are expected while approaching flash boiling conditions (high temperature, low pressure) independent of fuel vaporization. The PDPA measurements (Sec. 4.6.5), however, show that additional reductions in droplet size are related to the flash boiling mechanism.

3.3.2.3 Observations

Samples of the results are shown in Figure 3.20 along with their superheat temperatures. These images were taken 1 ms after the start of the 1.5 ms injection and the ambient pressure was atmospheric. Four different effects are shown with increasing temperature in this image series.

1) Decrease in width: Between the 0 K and 50 K superheat images, the spray width decreases due to the decreased droplet size for a fixed pressure. As described above, the droplet size decreases due to changes in the fluid properties and eventually flash boiling. The smaller droplets then interact more strongly with the induced gas flows, which draw the droplets toward the axis of the spray.

2) Scattering transition: Between the 20 K and 30 K superheat images, the multiple-scattering transition is observed. Further experiments showed that the transition occurs between 22 and 23 K superheat.

3) Initial cone angle: Between the 30 K and 70 K superheat images, the angle of the spray cone as it leaves the injector tip increases dramatically. Comparison of initial cone angle increase and volatility-induced droplet size reduction results (Sec. 4.6.6), suggests that both of these effects are related to flash boiling. These tests together suggest that flash boiling begins affecting the 2-methylbutane spray around 35 K superheat.

4) Turbulence: In the 60 and 70 K superheat, the image distribution becomes much more non-uniform. The structure appears to be consistent with formation of turbulent eddies. At these very high superheats, the droplets are likely to be very small (< 10 μm) and a large volume of vapor is generated. The spray at this point may be analogous to a vapor jet with flow-following seeding particles. A vapor jet produced from this spray would have a Reynolds number on the order of 100000, which is significantly larger than the value of about 100 needed for a gaseous jet to be turbulent. This effect was only observed in these experiments, apparently due to the very high superheat.

3.3.3 Flash Boiling Interpretation

If a liquid at its bubble point is further heated, it will continue to warm up until the nucleation and growth rates of bubbles is high enough to dissipate the added heat. In practical systems, the necessary superheat is typically limited by the surface roughness of the container.

With sufficient roughness to facilitate nucleation, the superheat is typically very low. If no external nucleation sites are provided the liquid will superheat until bubbles can form in the bulk liquid. This thermodynamic limit, at which liquid can no longer exist, is termed the limit of superheat. At atmospheric pressure, the limit of superheat is typically about 0.9 of the critical temperature [48]. It approaches the critical temperature as the pressure approaches the critical pressure. Table 3.3 shows saturation and limit of superheat temperatures for some of the compounds of interest here. These limits of superheat are over 100 K above the saturation temperature and well above the temperatures experienced in this testing. This shows that any flash boiling observed is limited by the bubble nucleation rate. Therefore, cavitation, surface roughness, and turbulence in the injection process will have a significant effect on the onset of flash boiling.

A sampling of the literature on flash boiling shows that the superheat required to observe flash boiling varies greatly between injection systems. Using a water jet from a 2 mm diameter sharp-edged orifice, Brown and York [23] showed a 75% reduction in SDM with a superheat of 24 K. Although reductions here are not nearly so large, the fact that the initial SMD in that study was so large (336 μm) may influence the relative reduction. Oza and Sinnamon [27] show a significant change in the appearance of a methanol jet with ~15 K superheat. Small negative superheats were sufficient for Senda, *et al.* [29] to observe a decrease in spray angle and an increase in SMD for both n-pentane and n-hexane. At higher superheats, this trend reversed giving increased spray angle and decreased SMD. This two-part trend was also observed in a study of flash boiling with port fuel injection by Aquino, *et al.* [31].

The results presented in the previous sections suggest that with these pressure-swirl injectors, flash boiling begins to evolve vapor rapidly around 20 K superheat and begins to affect the spray structure around 35 K superheat. Considering the wide range of results for different injection systems, the present results seem reasonable.

3.4 Spray Development

The initial purpose of considering spray development experiments was to determine if flash boiling occurred throughout injection. Spray development tests also allowed the measurement of spray penetration rates, demonstrated pre-spray atomization, and helped to explain the flash boiling mechanism.

Figure 3.21 shows three spray development series for the Zexel injector. These tests were performed with an acetone/iso-octane fuel mixture and a 0.3 bar intake pressure. The first series uses PLIF at cold head temperatures. The second series also uses PLIF but at high temperature. The third is again at high temperature but using planar Mie scattering. The four-phase spray development description advanced by Shelby can be applied in a straightforward manner to the cold spray [16, 32]. Once the injection signal is applied to the injector driver, about 360 μs pass before fuel is observed exiting the injector. This time is required to charge the injector coil, lift the needle, and accelerate the fluid. The initial fluid exiting the injector resided downstream of the swirl ports, and so has little angular velocity. This liquid forms the second development phase: the pre-spray. This poorly atomized slug of fuel forms a jet, which penetrates quickly. The pre-spray formation can be seen in the images taken 400 and 500 μs after the start of injection (ASOI), and its penetration is observable at the leading edge of the spray at 600 and 700 μs ASOI. The third development phase begins between 500 and 600 μs ASOI, when the angular momentum of the fluid exiting the orifice begins to increase. The cone angle quickly increases to approximately its steady-state value. This phase can be seen from 500 to 700 μs ASOI. The fourth phase is difficult to observe with the Zexel injector. With the Chrysler injector, the cone angle decreases slightly to its steady-state value as the induced gas flows are set up in the spray.

Under hot conditions, flash boiling appears to influence the spray from the very beginning. The phases of development, however, appear to occur in the same manner. The

delay time is about the same as for the cold spray. The pre-spray is wider and more diffuse, and in the case of the Mie scattering, initially penetrates more quickly. The Mie scattering images of the hot spray generally show a larger profile than the PLIF images, possibly for a few reasons. First, until the induced flows are developed, the vapor acetone may remain more concentrated near the injector. Second, the fluorescence yield of the acetone vapor drops somewhat as it is mixed with air. Third, the higher intensity of the Mie scattering signal causes the periphery of the spray to be more visible. The slower penetration and diffuse nature of the pre-spray from 400 to 700 μs suggests it is better atomized than in the cold case. The transition from the pre-spray to the main spray is not as obvious in the hot case. Between 500 and 700 μs the width of the base of the spray increases, though, suggesting that the transition occurs similarly. The fact that the development phases occur similarly in the hot spray as in the cold spray suggests that the flash boiling is not affecting the basic operation of the pressure-swirl nozzle.

Similar sets of spray development pseudo-movies can be seen for the Chrysler injector in Appendix 7. These six cases represent the conditions used for the PDPA measurements. They are PLIF images, using indolene with an injection timing of 180 °ATDCI. With the Chrysler injector, the delay time is shorter (about 180 μs). Also, between 650 and 800 ms, the fourth phase of development can be observed in which the cone angle decreases to its equilibrium value. The slower penetration of the pre-spray at hot conditions is more obvious for the Chrysler injector as well. In fact, even the high-pressure high-temperature case (P = 0.9 bar, T = 90 °C) shows significant improvement of the atomization of the pre-spray over the cold cases.

Figure 3.22 shows the closing transient for the conditions corresponding to Fig. 3.21. These images show one needle bounce about 700 μs after the end of the injection signal. The improved atomization is shown quite clearly in the coarseness of the spray in the cold case compared to the hot case.

3.5 INDOLENE RESULTS

Most of the imaging experiments described above involve fuel mixtures of iso-octane and a ketone dopant. Effects due to flash boiling are evident with this fluid, but the question remains if these effects are prominent with realistic fuels. Figure 3.23 shows indolene sprays at the same conditions used for the acetone/iso-octane sprays in Figure 3.5, and the results are similar. The indolene spray exhibits the image transition in both the PLIF and Mie scattering images. The difference between the indolene and doped-iso-octane sprays is primarily related to the volatiliy of the fluorescing compound. Since the fluorescent compounds in the indolene are heavy aromatic compounds with relatively high boiling points (roughly $T_B > 150$ °C) the fluorescent signal tracks liquid not vapor. Therefore, the transitions in both the PLIF and Mie scattering images are due to scattering of the laser sheet. Confirmation that the effect seen here is not merely due to changes in the fluid properties is provided by the PDPA results (Sec. 4.6.5).

The fact that the indolene sprays should exhibit flash boiling tendencies, as well as the acetone/iso-octane mixtures, is supported by a comparison of their volatilities. Since flash boiling involves evaporation of some fraction of the light ends of the fuel, comparing the volatily of the light ends is appropriate. For the indolene, the temperature at which 10% will evaporate (the T_{10} point) is quoted in the fuel specifications as 49-57 °C. A T_{10} point was calculated for the acetone/iso-octane mixture using an isothermal flash calculation using the bubble-point calculation described in Sec. 3.3.1.3. The input data involved in this calculation is given in Appendix 6. This calculation resulted in a T_{10} value of 87 °C, substantially higher than for the indolene.

Two sets of experiments were designed to locate the onset of the multiple-scattering transition for the Chrysler injector with indolene. The first set, shown in Figure 3.24, involved changing the intake pressure at constant temperature (80 °C). These PLIF images were taken using the full field-of-view available from the engine's third window. Two errors from deposits

on the windows occur in these images. First, the decrease in intensity about 20 mm below the injector is caused by deposits on the upstream window reducing the laser sheet intensity. The jagged marks about 40 mm down are caused by deposits on the imaging window. The intensity profile below the images was taken at the dashed line, 10 mm below the injector. The limiting case of the transition appears at 0.7 bar. Here the intensity in the core of the spray is only slightly lower than at the edges. The second set of images demarking the onset of the multiple-scattering transition in indolene is shown in Figure 3.25. These experiments were performed in an identical manner to the single-component tests described in Sec. 3.3.2.3. These sprays were made using the Chrysler injector with atmospheric ambient pressure. These tests show the onset of the transition at 100 °C. Both of these tests show the transition to begin at similar values of the normalized excess vapor pressure ($\Pi = (P_{VAP}-P)/P \approx 3$) and predicted Sauter mean diameter (SMD $\approx$ 20 μm).

Fuel temperatures of 90 to 100 °C and atmospheric ambient pressure are certainly within reason for a DISI engine operated under early injection or even throttled late injection. Discussions of additional data regarding indolene sprays is contained in the sections below.

3.6 Injection Timing

The images in Figures 3.26 a&b were taken three different injection timings to show any effect of the bulk upward or downward flow on the spray. They also give a concise view of many of the conditions an indolene fuel spray might face in a DISI engine. Five different effects have been observed between the injection timings.

1) Spray narrowing: As the ambient pressure increases, the spray narrows significantly, especially for injection at 270 degrees after top-dead-center in the intake stroke (°ATDCI) with the higher intake pressure. This is an often-observed phenomenon related to the stronger induced flow associated with the higher gas density.

2) Spray distortion: For injection at 90 °ATDCI, there is significantly more distortion to the spray. The distortions observed in the sprays during the intake stroke proved to be from the intake flow. The square piston optical engine has no structured swirl or tumble cylinder flows. The symmetrical location of the intake valve does not allow for swirl. Some amount of tumble is likely, but since the intake flow will not flow smoothly across the far wall, it is likely to be weak. This is evident in the images taken at 180 and 270 °ATDCI in Fig. 3.26a. They show little distortion from cylinder flows. On the other hand, there is a substantial distortion apparent in the images taken at 90 °ATDCI. The main difference between injection during the intake stroke and at BDC is the presence of flow from the intake valve. Figure 3.27 shows a schematic of the orientation of the intake flow to the spray. Relative to the images, the intake valve is to the left and behind the injector. Assuming that the intake flow roughly follows the 45° angle of the intake valve seat, the flow crosses the axis of the spray about 30 mm below the injector. This geometry is consistent with the distortion observed in the images. The images taken during the intake stroke show a well-formed, symmetric spray until about 30 mm below the injector. In addition, in all but the low-pressure hot spray, the distortion is to the right, away from the intake valve. The distortion is more pronounced in the high-pressure cases due to the higher gas density. In fact, the images taken at 180 °ATDCI with 0.9 bar intake pressure show still show a distortion even though the intake stroke is over. Because of these distortions, experiments performed after this used an injection timing of 180 °ATDCI rather than 90 °ATDCI.

3) Pre-spray atomization: The penetration distance of the pre-spray decreased with increased temperature and ambient pressure. Under cold conditions, as the ambient pressure is increased, the pre-spray remains well defined, but it penetrates more slowly due to the increased ambient density. At all pressures, the pre-spray appears much better atomized at high temperature. The smaller droplets are more affected by drag, and so penetrate more slowly.

4) Multiple scattering: An effect related to the multiple scattering in the sprays, which is not obvious elsewhere, can be seen here. In the cold cases, as the ambient pressure increases

from BDC to late injection with 0.3 bar intake pressure to BDC to late injection with 0.9 bar intake pressure (0.3, ~0.6, 0.9, ~1.8 bar), the image becomes more filled despite increasing droplet diameter. This reiterates the fact that the scattering is dependent on the spray density, not only the mean diameter.

5) Ambient conditions: Volatility effects appear stronger with injection during the intake stroke (90 °ATDCI) than at BDC (180 °ATDCI). This can be seen in the more filled images for early injection at high pressure and the wider initial cone angle at low pressure. The temperature will be somewhat higher during the intake stroke due to higher fraction of residual gas. In addition, the ambient pressure will be lower due to flow restriction across the valve and in the intake system.

3.7 VOLATILITY STRATIFICATION

3.7.1 Fuel Mixtures

One way to gauge the influence of evaporation on the spray structure is to measure any spatial separation of high-volatility components ('light' components) from low-volatility components ('heavy' components). This method substitutes for our inability to measure the vapor distribution. When a variation in distribution between light and heavy components is observed, the difference can be assumed to be due to the vapor phase of the lighter compound. As long as both compounds remain in the liquid state, there is no opportunity for segregation of the components.

In order to measure any separation of light and heavy fuel components in the DI spray, fuel mixtures doped with ketones of varied boiling point were produced. Three ketone dopants were chosen with boiling points near the T_{10}, T_{50}, and T_{90} points of gasoline (acetone, 3-pentanone, and cyclohexanone, respectively). The remaining compounds in the fuel were chosen to provide a distillation curve similar to gasoline, while keeping cost low, maintaining a high

octane rating, and avoiding absorption of the laser light. Properties of the fuel components are shown in Table 3.4 [49]. Three base fuel components were initially chosen to match the boiling points of the dopants, so that doped fuels could simply be made by replacing one of the compounds with the dopant without affecting the distillation curve. However, since the ketones do not interact with the other hydrocarbon compounds to the same degree that the hydrocarbons interact with each other, adjustments to the fractions of compounds were required to keep the distillation curve from changing. Also, one lighter and one heavier compound were needed to match the extremes of the distillation curve.

The distillation method used for the test fuels is similar to that described in the ASTM Test Method D86 for natural gasoline [50]. The most significant departure is the use of a heating plate rather than an oil bath. The error due to this substitution is only evident at high temperatures where the upper vessel walls were cooler than the liquid. This made measurement of the final boiling point difficult, since the recorded value was highly dependent on the rate of heating. Although once a consistent rate of heating was used, the final boiling point values were fairly repeatable. A filter flask (125 ml) was used in place of the specified distillation flask, a shielded K-type thermocouple was used instead of a thermometer, and a Tygon tube was used to connect the filter flask to the condenser. The Tygon tube needed to be supported at higher temperatures. Recovered fractions ranged from 95.5% to 97.0% for most cases. These numbers are lower than specifications, at least partially due to the condensation on the cool walls of the evaporation flask. Tests with cyclohexanone dopant showed only 93% recovery due to an interaction with the Tygon tube at high temperatures. Due to this low recovered fraction, no temperature is recorded for the 90% recovered point. Residue remaining in the evaporation flask ranged from 0.7 to 1.0 ml of the 100 ml sample. Temperature readings were not corrected for barometric pressure since the correction would typically be less than 1 °C, which was the precision of the thermocouple reader.

Figure 3.28 shows three measurements of the distillation curve of Amoco Indolene High Octane Motor Fuel III (brand code 15211). Between these tests, the heating rate of the sample was refined to produce a condensation rate within the specifications of the ASTM method. Repeatability was good, despite the changes in heating rate, except for the final boiling point (FBP). The largest changes made in the heating rate were in the 90%-to-FBP range, and the FBP temperature appears to be sensitive the heating rate with this apparatus. The heating rate of the third test (the one reaching 212 °C) most closely resemble the specifications. This test was then used to compare to the test fuel mixtures.

First, an undoped fuel mixture was developed to provide a basis for the doped mixtures. The doped fuel mixtures were then slight modifications of this base fuel. Figure 3.29 compares the distillation curves of the fuel mixtures with that measured for indolene. Agreement was very good with the largest errors occurring at the initial boiling point (IBP) and final boiling point (FBP). Reduction of the IBP, without reducing the T_{10} point, would require a hydrocarbon with a boiling point lower than 30 °C, which is not readily available in liquid form. The FBPs for the test fuel mixtures are reasonable, and for the intended purpose of these fuels, the FBP is not critical. Table 3.5 gives the composition of the fuel mixtures and their distillation characteristics.

The mixtures doped with acetone and cyclohexanone were used in an array of tests covering two temperatures (30 and 90 °C), two intake pressures (0.3 and 0.9 bar), and three injection timings (90, 180, and 270 °ATDCI).

3.7.2 PLIF Calibration

3.7.2.1 Calibration Method

In order to compare images from tests using the acetone-doped and cyclohexanone-doped fuel mixtures, a calibration method was employed. Since these tests were intended to compare distributions of light and heavy ends of the fuel in the spray, direct comparison of image intensity became important. This is complicated by the fact that the two dopants vary in

fluorescence yield by nearly a factor of two. While a relatively simple calibration involving only the fluorescence yield may suffice, quantitative concentration results are preferable. To determine the dopant concentration, the images were compared to a homogeneous mixture of acetone vapor. Corrections were performed for background intensity, laser sheet intensity variations, laser energy shot-to-shot fluctuations, and fluorescence yield. A schematic of the calibration method is shown in Figure 3.30.

To monitor the laser energy, a portion of the laser energy was directed onto a diffuser, which was imaged by the camera simultaneously with the spray. This modification to the optical system is shown schematically in Figure 3.31. A beam splitter is used to redirect 10% of the beam to the diffuser. Since the intensity of the diffuser fluorescence was too high compared to the spray, a lens was used to diverge the laser before reaching the diffuser. The remaining 90% of the laser beam proceeded through the standard PLIF optics described in Section 2.3.3.3. The diffuser was imaged with the camera by placing a mirror in a portion of the field of view of the camera. This did not interfere with the spray image since the aspect ratio of the camera allowed for the excess width.

Four sets of images were required to perform the calibration, all of which contain the laser energy reference. First, are the images to be calibrated. Second, is a background image without the laser firing. This image contains the dark charge of the camera and any ambient light captured. Since the ambient light was minimal and the same array temperature was used in all cases (resulting in a similar dark charge), a single background was used for spray and reference images. The background image used was the average of ten frames. The third image was the acetone vapor reference. To produce a homogeneous vapor mixture in the cylinder, nitrogen was bubbled through liquid acetone. The bubbler and approximately five feet of the nitrogen tube before it were immersed in an ice bath to keep a constant temperature. The vapor concentration was assumed to be the vapor pressure of acetone at 0 °C. The vapor mixture was fed continuously into the combustion chamber through the pressure transducer mounting location

while the valves were closed. Images of the vapor were recorded when the distribution no longer changed (after about 5 minutes), and ten of them were averaged. These images contain not only the reference intensity against which the spray images are calibrated, but also information of the variation in laser intensity across the combustion chamber. A variation in the intensity of the vapor-reference images, though, was caused by absorption of the laser as well. The fourth set of images was added to correct for this. Since a large portion of the variation in laser intensity across the combustion chamber is due to the expansion of the laser into the wide sheet, images were taken without the beam expansion. The decrease in intensity across these images in the direction of the laser was assumed to be entirely due to absorption. An exponential decay was fit to the averaged profile from ten images. This fit, in turn, was used to correct the vapor reference image. Figure 3.32 shows the intensity profile across the combustion chamber portion of one of these images. Because of the falloff seen to the right, a pixel range from about 50 to 300 was used for the fit.

As Fig. 3.30 shows, the calibration begins by subtracting the background image from both the spray and vapor-reference images. The vapor reference image is then corrected for laser absorption by the fit determined from the vapor reference without beam expansion. An image of this case is shown in Figure 3.33. The smaller region to the right is the laser intensity reference. The ratio of the spray image to the vapor reference is then taken. This step normalizes the intensity of the spray image and removes the effect of the variations in beam intensity. Next, the image intensity is scaled so that the average intensity of the laser reference is unity. This corrects for shot-to-shot variations of the laser and changes in the camera sensitivity (f-stop, intensifier gain). An attempt is then made to correct for the change in fluorescence yield caused by the difference in temperature between the vapor-reference and in the spray. Since the dopant temperature in the spray is only approximately known, this is a rough correction. Fortunately, it is also a relatively small correction. The correction for the difference in fluorescence yield between the dopant in the spray and the acetone vapor reference is then made. Finally, the image

is multiplied by the concentration of the acetone vapor reference. Figure 3.34 shows a spray image before and after calibration. The large amount of noise outside the engine window region results from the small values in both the numerator and denominator when the ratio of the spray image to the vapor reference is taken. The saturation level of the intensity scale used in the resulting images was set to match the lower saturation level of the two images. Unfortunately, this often limited the dynamic range of one of the two images. This can be seen from the relatively large saturated region in the calibrated image in Fig. 3.34.

In the following sections, the dopant concentration is represented as the equivalence ratio that this concentration of dopant would represent at atmospheric pressure, assuming that the rest of the fuel follows the dopant.

3.7.2.2 Fluorescence Yield Measurements

To determine the fluorescence yield ratio for the calibration, a series of tests was performed with the dopants in both liquid and vapor states. One set of liquid tests and two sets of vapor tests were performed with the PLIF system. The liquid tests were performed with a covered quartz cuvette. The cuvette has a square cross-section and a volume of 4 ml. The liquid samples (3.5 ml) contained a 1000:1 volume ratio of iso-octane to dopant. This gave roughly the same concentration as the acetone vapor reference described in Sec. 3.7.2.1. The volumes were measured with a 5 ml pipette for the iso-octane and a 10 µl syringe for the dopant. Once the ingredients were added, it was stirred, and the cuvette was covered. The cuvette was then placed on the piston inside the combustion chamber and excited with the same laser sheet used for the PLIF spray tests. An intensity value was calculated by averaging over the uniform portion of the fluorescence from ten images. A similar test was performed with undoped iso-octane. The intensity value for the iso-octane was then subtracted from the doped results. The results for the three dopants of interest (and indolene for reference) are shown in Table 3.6, normalized against the intensity of acetone. The precision of these tests is limited by the difficulty of measuring the

small volumes of liquid, use of the intensified camera for intensity, and possible contamination of any of the fluids. For example, while the quantum yields of acetone and 3-pentanone are shown as very similar, Fujikawa *et al.* [34] show a 30% higher fluorescence yield for 3-pentanone (at 248 and 266 nm excitation). Even though the fluorescent compounds in indolene are diluted by all of the lighter ends, its overall fluorescent yield is higher than that of the ketones.

The first set of vapor tests was based on the acetone vapor reference. The first of the two cases in this set was the acetone vapor reference described in Sec. 3.7.2.1. To test the effect of oxygen quenching, the second used air as the carrier gas instead of nitrogen. These results show that the intensity of acetone in air was only 80% of that in nitrogen. A 20% reduction in fluorescence yield due to oxygen quenching is reasonable considering the low pressure dependence of acetone fluorescence [35].

The second set of vapor tests was performed with the quartz cuvette described above. A small amount of the dopant was added to the bottom of the cuvette. It was then covered and allowed to equilibrate. The vapor is therefore in air, which allows oxygen quenching. Since the liquid tended to climb the walls, only about twice the amount needed to fill the cuvette with vapor was added (typically 5-10 μl). The intensity from an empty cuvette was subtracted to obtain the vapor value. Once corrected for the differences in density, the vapor intensity values were compared to the liquid values, as shown in Table 3.7.

Combining these different results, values of the fluorescence yield ratio, between the acetone vapor reference (in nitrogen) to the dopants in various states. These results are shown in Table 3.8. While either liquid or vapor states of acetone are likely in the spray, liquid states of 3-pentanone and cyclohexanone are more likely.

3.7.2.3 Calibration Uncertainty

While the calibration method described above is capable of determining the dopant concentration from an image, the application of the calibration is limited by a substantial stack-up of potential errors. Estimated calibration errors are presented on the schematic of the calibration procedure (Fig. 3.30). The initial 6% error in the spray image is due to camera noise and residue on the windows, which may not be present in the calibrations. The error in the vapor reference is likely much lower since ten frames are averaged. Correcting for the laser reference is straightforward and so should incur little error. The temperature of the dopant in the spray, while difficult to determine at each point, falls within a definable range. Since the temperature dependence of the dopants is relatively small, the intensity change over this range should not be large. Despite the fluorescence yield measurements described above (Sec. 3.7.2.2), the error in the fluorescence yield ratio may be substantial. Particularly, the ratio of liquid to vapor acetone in the spray could cause up to a 75% error, according to the fluorescence yield measurements. Also, uncertainties exist in the concentration of the acetone vapor reference. The bubbler may not have been completely efficient, leaving the vapor unsaturated. The temperature inside the bubbler may not have equilibrated with the ice bath, leading to errors in the vapor pressure of the acetone. Overall, the error was estimated at ±30%.

Additional errors may be present, which were difficult to account for. First, multiple scattering of the laser would cause fluorescence from material outside of the laser sheet. This unintentional fluorescence will increase the signal in some part of the image. This is believed to occur for cases with smaller mean droplet diameters (see Sec. 3.2.3). Second, absorption of the laser light in the spray images is not accounted for. This would decrease the signal further away from the laser (to the left).

Due to the calibration errors, no comments are made about the absolute concentrations in the results. The functionality of the calibration is in comparing the results with the different dopants described below.

3.7.3 Case I: Slow Evaporation

The fuel mixtures and PLIF calibration method described above were used with a set of experiments involving two injector temperatures (30 and 90 °C), two intake manifold pressures (0.3 and 0.9 bar), and three injection timings (90, 180, and 270 °ATDCI). These tests used the injector supplied by Chrysler. The series of 10 images taken span 400 to 3200 μs after the start of injection. Differences due to injection timing are much as they are described in Section 3.6. Changes due to the evaporation characteristics, through the temperature and pressure, are described in these next three sections (3.7.3-5).

At low temperature (30 °C), comparisons of the acetone and cyclohexanone images suggest a minimal amount of evaporation. Figure 3.35 shows a series of images at 30 °C and 0.3 bar. The first four images show the development of the spray in 200 μs increments. The last image is the fully developed spray, just before the end of injection. The two sets of images are very similar—in the cone angle, the apparent sheet thickness, and the pre-spray penetration. The differences can be noticed in the higher concentration of the acetone along the centerline. While there is some evidence in the development images, this is most clearly shown in the fully developed image. This can be explained as vapor acetone being drawn to the axis of the spray by the induced flows. Judging from the images, the acetone vapor is drawn to the axis and penetrates faster than the droplets (represented by the cyclohexanone). In addition, little of the acetone is apparent in the vortex outside the spray, suggesting that it may have evaporated out of the droplets before they were entrained into the vortex. Vapor acetone may be drawn into the vortex, but since the fluorescence yield of the vapor acetone is significantly lower than for the liquid, such small amounts of vapor may not be detectable. The cold tests at 0.9 bar (not shown) exhibit a similar effect.

3.7.4 Case II: Non-disruptive Evaporation

Under the hot conditions (90 °C), significant differences can be observed between the acetone and cyclohexanone distributions. While this was expected for the low-pressure cases where flash boiling has been observed, the lower extent of evaporation in the high-pressure cases represents an intermediate regime. While the changes to the spray structure are likely to be progressive as the conditions increase in their potential for evaporation, the results are being considered here with respect to three different regimes. The different observations noted in each regime might represent additional aspects of the physics that become prominent as the potential for evaporation increases.

In the intermediate regime described in this section, the light ends of the fuel, represented by the acetone, appear to evaporate very quickly while the heavy ends, represented by the cyclohexanone, have a structure that is changed very little from cold conditions. Figure 3.36 shows one such comparison. These tests were performed with a low intake pressure but with injection during the compression stroke. The cylinder pressure at the time of injection is believed to be around 0.6 bar. The cyclohexanone image has a lower intensity along the axis, showing a hollow-cone structure. It also has the same initial cone angle as the cold cases. The spreading at the bottom of the spray is caused by interaction with the rising piston. From this image, significant evaporation is not clear. The acetone image, on the other hand, follows the profile of the cyclohexanone image for only about the first 10 mm. After that, the acetone distribution ceases to spread out and actually contracts towards the spray axis. Since very little acetone is observed out at the radial positions where the cyclohexanone intensity peaks, the acetone is assumed to have evaporated out of the droplets. This represents evaporation of probably 10-20% of the volume in roughly 150 μs. While this rate of vapor generation is high, it is apparently not violent enough to cause an increased initial cone angle. For this reason, this intermediate regime has been termed non-disruptive evaporation. Another example of this regime is shown in Figure 3.37. These tests were performed with 0.9 bar intake pressure and

BDC injection timing. The cylinder pressure at the time of injection of about 0.9 bar, is higher than in the previous example. Interpretation of these images is somewhat complicated by the relatively strong effects of the in-cylinder flows. For the first four images of the spray development, the two distributions are very similar. The main difference is that the acetone distribution appears more filled. Once the spray has penetrated further (2800 μs), the evaporation of the acetone is again obvious.

3.7.5 Case III: Flash Boiling

The third regime observed in the tests comparing the acetone and cyclohexanone distributions is that previously associated with flash boiling. Figure 3.38 shows images from the test with 0.3 bar intake pressure and 90 °C temperature. The cyclohexanone images show a high degree of scattering, due to substantially reduced droplet size, and an increased initial cone angle. The decreased droplet size is partially due to temperature and pressure changes (Sec. 3.3.2.2) and partially related to flash boiling, as described in connection with the PDPA data (Sec. 4.6.5 and 4.6.6). The increased initial cone angle, from 60 to 95 degrees, suggests a disruption of the spray formation near the injector associated with flash boiling. Because of this change in spray structure, this regime was termed disruptive evaporation.

While the cyclohexanone images were expected from the indolene images, the acetone images were somewhat surprising. Noticeable in all but the first frame, the acetone deviates from the profile of the cyclohexanone less than 10 mm downstream from the injector. The acetone appears to evaporate from the droplets and is then drawn into a column down the axis of the spray. The motion of the vapor towards the centerline is expected from the flows induced by the spray. This jet of acetone vapor is only about half the width of the spray, as represented by the cyclohexanone image. The acetone vapor also penetrates into the combustion chamber faster than the bulk of the spray. All of the differences observed between this set of images and those

in the previous section (Sec. 3.7.4) suggest an increased rate of evaporation, which is expected from the lower ambient pressure.

These last three sections describe comparisons of the behavior of the light and heavy ends of the fuel through observations of acetone and cyclohexanone dopants in fuel mixtures with similar distillation curves. The results suggest that as the potential for evaporation increases, the spray response can be described in three regimes. I) Slow Evaporation: When evaporation is small the distributions of the light and heavy ends are very similar, except for a small amount of vapor from the light ends being drawn to the axis of the spray. II) Non-Disruptive Evaporation: With an intermediate amount of evaporation, the light ends are evaporated out of the droplets quickly, but the overall structure of the spray remains largely unchanged. III) Flash Boiling: When evaporation is substantial, the light ends evaporate very quickly, the initial cone angle is increased, and the mean droplet size has typically been reduced to the point where images show a top-hat profile.

3.8 Spray Slit Tests

When the initial imaging and PDPA tests disagreed on the internal structure of the hot sprays, a set of experiments was performed using a slit in the path of the spray. The scattering limitations of both diagnostics arise from the presence of droplets in the spray that are not being measured. In the case of the imaging experiments, droplets out of the laser sheet path are being illuminated by scattered light. To prevent this, a slit was added to remove the unwanted droplets. A schematic of the slit setup is shown in Figure 3.39, drawn approximately to scale. Each of the two halves is 20 mm wide by 60 mm long and made from 0.2 mm thick sheet metal. Experiments were performed at atmospheric pressure since the engine could not be operated with the slit in place. To allow adequate superheat at atmospheric pressure, 2-methylbutane was used as the fluid. This necessitated the use of Mie scattering for imaging. Averaged images from cold and hot experiments (20 and 80 °C) are shown in Figure 3.40. These images were taken

with a wide laser sheet (5 mm) to illuminate the majority of the droplets passing through the slit. The slit was positioned at four distances from the injector (10, 15, 20, and 25 mm). The smaller images to the left are the corresponding images from Fig. 3.20, presented at the same scale. The original (non-slit) cold image shows a hollow-cone structure. In the slit images, the light band is the slit. Above the slit, the image is saturated, since these images were taken with a larger camera aperture than the non-slit images. Below the slit is the image of the liquid passing thought the slit. These images show two lines of high intensity at the periphery of the spray, again suggesting the hollow-cone structure. There is some disturbance due to the slit. The images were averaged because the frame-to-frame variation was large. The images also spread radially faster after passing through the slit. Neither of these observations seems to be significant enough to change the interpretation of the results. The original image of the hot spray showed significant multiple scattering. Despite the filled appearance observed without the slit, the slit images once again show a hollow structure.

These results were useful for not only determining the hot spray structure, but also motivating the formulation of the multiple-scattering interpretation of the image transitions, as described in Sec. 3.2. Since they show quite clearly that the core of the spray is not filled with droplets, the initial interpretation had to be revised.

3.9 Spray Structure

3.9.1 Spray Penetration

Measurements of the spray penetration can give information on the atomization of the spray as well as overall changes in the spray structure. While the initial velocity of the droplets varies little with operating conditions, changes in the relative drag force on the droplets can vary greatly. Since the drag is relatively larger for smaller droplets, better-atomized sprays tend to penetrate more slowly. In particular, the relative droplet size of the pre-spray is indicated by the

spray penetration, since the liquid from the pre-spray stays at the leading edge of the spray in all cases. Early spray penetration measurements, of the type done by Shelby [16], involved visual determination of the leading edge of the spray from a series of PLIF images. With these early tests, the field of view axially was limited to 30 mm. In these measurements, Shelby determined a penetration velocity of 78 m/s for the Zexel injector and 86 m/s for the Chrysler injector at 5 MPa fuel pressure and approximately 0.5 bar ambient pressure using a 3-pentanone/iso-octane fuel mixture. Similar measurements were performed with the first four frames in Fig. 3.21. The tests represented in this figure were performed with the Zexel injector at 0.3 bar intake pressure. Measurement of the cold case (~35 °C) shows a penetration velocity of 101 m/s. The fact that this is about 20% higher than that measured by Shelby can be explained by the lower ambient pressure. These values can be compared to penetration velocities for the same spray at high temperature (~95 °C). The penetration velocity in this case is measured to be 66 m/s, which is 35% lower than the cold case, which obviously represents a drastic change in the spray.

Additional measurements were performed with the fuel-mixture tests described in Sec. 3.7, as shown in Figure 3.35-38. Since these measurements were intended to show the differences in spray penetration caused by the various operating conditions, the results for each operating condition were averaged over the other operating conditions. For example, the data for the cold trace in the temperature plot (Fig. 3.41a) are the average of the measurements of cold tests with all three injection timings, both intake pressures, and both dopants. Although the experiments were carried out past 1 ms, the plots end there since droplets from the pre-spray were often difficult to identify after this time. The most substantial change is due to the increase in pressure. This shows a decrease in penetration velocity of about 30%, similar to that measured above for the Zexel injector. The higher ambient pressure case has a slower penetration rate due to the increased drag caused by the higher air density. The slower penetration for the late injection case is primarily caused by the increase ambient pressure during the compression stroke. The difference in penetration rates for the two earlier injection timings

could be caused by a decrease in ambient pressure caused by intake flow restriction or the bulk downward airflow during the intake stroke. The bulk flow in the cylinder should be roughly equal to the piston speed. At 90 °ATDCI the piston speed is about 6 m/s while it is zero at 180 °ATDCI. This change of 6 m/s is strikingly similar to the 5.5 m/s difference between the penetration rates for the two early injection timings. On the other hand, study of the indolene flow-dependence images in Fig. 3.26 suggests that the cylinder pressure is lower during 90 °ATDCI injection. In both the low and high-pressure cases, the multiple-scattering transition appears more significant for the early injection timing. Since the change in penetration rate observed here is a significant fraction of the change from 0.3 to 0.9 bar, this pressure change is unlikely to be sufficient to cause the observed difference. The 10% difference in penetration between the two dopants should be due to vapor production. Especially in the highly-evaporating cases, the acetone vapor is drawn to the axis of the spray where it tends to penetrate more quickly than the droplets, in which the cyclohexanone is contained.

To remove the subjectivity involved with the measurements involved above, and to allow measurements at later times, a different measurement technique was developed. It considers the axial distance at which 95% of the fluorescence intensity has been accounted for. An algorithm was written for this measurement technique (shown in Appendix 8) to allow quick processing. The algorithm initially sets all pixels below a threshold (5000/65536) to zero to remove background noise. The intensity is then integrated over the image. Then, beginning at the injector, the intensity is integrated row by row until 95% of the total integrated intensity is reached. The axial location of that row is then considered the penetration depth of the spray. This technique was applied to the PLIF images from Sec. 3.7, as above. The results were then averaged and plotted in the same way as in Fig. 3.41, which is shown in Figure 3.42. For up to one millisecond, these results exhibit the same trends as described above. An artifact of the measurement technique becomes apparent in many of the profiles after one millisecond. As the spray develops, the measurement technique initially tracks the pre-spray. But at some point,

usually around one millisecond, the pre-spray becomes insignificant compared to the rest of the spray. At this point the measurement technique shifts back to the main spray. This artifact is prominent in cold sprays in which the pre-spray separates significantly from the main spray. In hot sprays, though, this effect is not noticeable. As the temperature plot (Fig. 3.42a) shows, while the pre-spray of the cold sprays penetrates more quickly than the hot sprays, the main spray actually penetrates more slowly. The cold pre-spray penetrates more rapidly because it contains larger droplets. The hot main spray penetrates more quickly because its momentum is directed downward by the induced flows, rather than spreading radially. The other three plots show the same trends as described above, but with a penetration velocity that decreases with time.

In summary, the penetration of the main portion of the spray is faster for higher temperatures, lower ambient pressure, early injection timings, and higher volatility components of the fuel.

3.9.2 Spray Width

The spray width was also measured using the automated measurement technique described above for the spray penetration. In the same algorithm (App. 8), the spray width is measured using 95% of the integrated intensity. Once the threshold has l een applied, and the overall integrated intensity calculated, the width is measured. Beginning at the centerline of the spray, symmetric columns of pixels are integrated until 95% of the total value is obtained. The radial location at which this is true is chosen as the spray half-width. The spray width is plotted in Figure 3.43 in the same manner as the spray penetration. An artifact from the measurement technique exists in this data as well. In some of the late-injection cases, the spray deflects off the face of the piston in the later images. This manifests itself in the late injection cases (270 ° ATDCI) as an increase in width at the later times.

The strongest effect apparent in this data is with the change in temperature. Going from the cold to hot conditions, the spray width decreases by nearly 40%. This is caused by the smaller droplets and the vapor in the hot conditions being drawn toward the axis of the spray by the induced flows. The higher ambient density (with high pressure) causes stronger induced flows, again reducing the spray width. This effect is active in decreasing the width of the late-injection-timing case as well. While the reason why the BDC timing exhibits the widest spray of the three injection timings is not apparent, the lower width for the 90 °ATDCI injection-timing case may be the result of the stronger in-cylinder flows. The average width of acetone sprays is also decreased due to vapor acetone being drawn to the spray axis.

In summary, the spray width is maximized for lower temperatures, low ambient pressures, BDC injection timing, and low volatility fuel components. In general, higher ambient densities create more compact sprays, both in penetration and width. Sprays with smaller droplets and vapor tend to be narrow but penetrate quickly. Finally, the bulk cylinder flow may decrease the spray width while increasing its penetration.

3.9.3 Initial Cone Angle

One of primary changes to the spray structure attributed to flash boiling is the increase in initial cone angle. This effect, illustrated in Figure 3.44, occurs in all of the heavily flash boiling sprays. Initial cone angle increase with the Zexel injector can be seen in the early acetone/iso-octane mixtures at 0.3 bar in Fig. 3.4 and in the spray development images in Fig. 3.21. Examples abound for the Chrysler injector, most notably in the 2-methylbutane images in Fig. 3.20, but also for the fuel mixtures described in Sec. 3.7 and indolene in Figs. 3.26 and 3.38. Measurements of the initial cone angle were made by measuring the spray width at a fixed distance from the injector. The axial distance of the measurement point began at 4.5 mm for the smaller initial cone angles, but was progressively decreased for the wider initial cone angles due to the greater curvature. Two sets of results from the temperature-controlled 2-methylbutane and

indolene experiments (Figs. 3.20 and 3.25) are shown in Figure 3.45. Both sets of experiments were performed with an atmospheric ambient pressure. While the 2-methylbutane data shows a slight increase in cone angle around a normalized excess vapor pressure ($\Pi = (P_{VAP}-P)/P$) of 1.2, the significant increase in the initial cone angle does not begin until about $\Pi = 2.0$ to 2.5. Above this point, the cone angle rises roughly linearly with Π. The reduction in SMD predicted by this trend agrees with the volatility-induced droplet-size reduction, as described in Sec. 4.6.6, suggesting that the droplet size reduction is primarily due to the increase in cone angle of the liquid sheet before breakup.

The indolene data, while somewhat sparse in the critical transition region, shows a similar trend. The differences between the indolene and 2-methylbutane results may be due to the multi-component nature of indolene. If a relatively large fraction of the liquid vaporizes to increase the initial cone angle, the multi-component nature of the indolene may become important. The vapor pressure for indolene is based upon the lightest ends. As these light ends evaporate, the temperature needs to increase to maintain the same vapor pressure. This effect may account for the higher superheat required for the initial cone angle increase with indolene.

While related to flash boiling, the mechanism behind the increase in initial cone angle is not clear. One theory is that the vapor generation in the spray created higher pressure in the core of the spray pushing the spray sheet outward. The modeling effort described in Chapter 5, though, failed to recreate this effect with the addition of vapor generation. Also, while the breakup of droplets by flash boiling will impart some of them with higher a radial velocity, this effect is unlikely to be potent enough to push so much of the liquid out so quickly. The most likely mechanism seems to be related to a change in the liquid sheet. It is possible that the superheat has become substantial enough for evaporation to occur inside the injector. This would certainly affect the thickness and stability of the liquid sheet as it leaves the orifice.

3.10 CONCLUSIONS

This work began with the knowledge that at high temperatures PLIF images showed a transition to a hollow-cone structure when acetone was used as the dopant. The initial goal of the imaging experiments was to determine the nature of this transition and the conditions that lead up to it. The following are the observed changes in characteristics of the spray divided into three regimes with increasing superheat as illustrated in Figure 3.46.

Below the boiling point of the fluid, evaporation is slow and images show the expected hollow cone structure. Distributions of light and heavy ends of the fuel are similar (Sec. 3.7.3), showing little separation due to evaporation. The mean droplet size is relatively large, resulting in low light scattering and a relatively weak interaction with the gas flows. Especially at low pressure, the weaker interaction with the gas flows results in low contraction of the spray, leading to wide-spreading spray structures, and a pre-spray that penetrates quickly, separating from the body of the spray. Changes in the droplet diameter with fuel temperature and ambient pressure (Sec. 3.3.2.2) in this range have little observable effect on the spray, but become significant above the boiling point.

As the spray is superheated past its boiling point, evaporation becomes rapid and the droplet diameter decreases significantly. Light ends of the fuel were shown to evaporate within roughly 15 mm below the injector, while the heavy ends keep a distribution similar to that of the cold spray (Sec. 3.7.4). As the droplet size falls due to increased fuel temperature and decreased ambient pressure, the scattering of the laser sheet by the spray increases, raising the intensity observed in the interior of the spray. At some point (about 20 μm for sprays at 1 atm. ambient pressure), the optical density of the spray is high enough that images of the spray droplets (Mie scattering or PLIF of heavy components) exhibited a top-hat intensity profile. As the droplet size decreases, the interaction of the droplets with the gas flows increases as well. This reduced droplet size leads to slower penetration of the pre-spray, such that it separates little from the

body of the spray. In addition, the greater interaction with the gas flows induced by the spray draws it down towards the injector axis, narrowing the spray.

As the spray is superheated further (past $\Pi \approx 2$ for 2-methylbutane or $\Pi \approx 3.5$ for indolene), evaporation becomes violent enough to affect the spray structure. The light ends of the fuel were shown to evaporate within about 10 mm of the injector (Sec. 3.7.5). This evaporation is rapid enough to cause an increase in the initial cone angle of the spray (Sec. 3.9.3), possible through an increase in pressure in the interior of the spray cone. Despite the wide initial cone angle, the flash-boiling sprays are narrow, due to the large interaction with the induced flows caused by the very small droplets. Despite the small droplets, the body of these sprays penetrates quickly, likely due to the vapor production (see Sec. 5.2.3). In addition, the small droplets and vapor production affect the structure throughout development and dissipation of the spray. However, the flash-boiling spray exhibits the same stages of development observed for the cold sprays.

An additional parameter of the operating conditions, not directly related to evaporation, was the injection timing. While the overall effect of cylinder flows on the spray is minor during injection, with early injection timing (90 °ATDCI), the intake flows significantly disturb the spray after about 25 mm, especially with high intake pressures. With late injection timing (270 °ATDCI), the increased ambient pressure results in decreased radial and axial penetration of the spray.

The following chapter discusses the results of the PDPA measurements of droplet size distributions and velocities and compares these results with the structure shown by the imaging experiments.

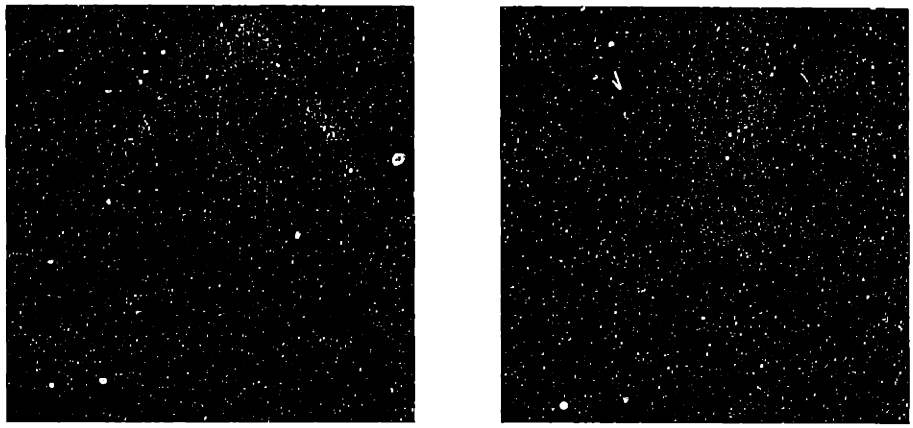

Figure 3.1: Images of spray transition during engine warm-up. Acetone/iso-octane fuel mixture (10:1 by vol.), SOI = 60 °ATDCI, image taken 1 ms ASOI, intake pressure below 0.5 bar.

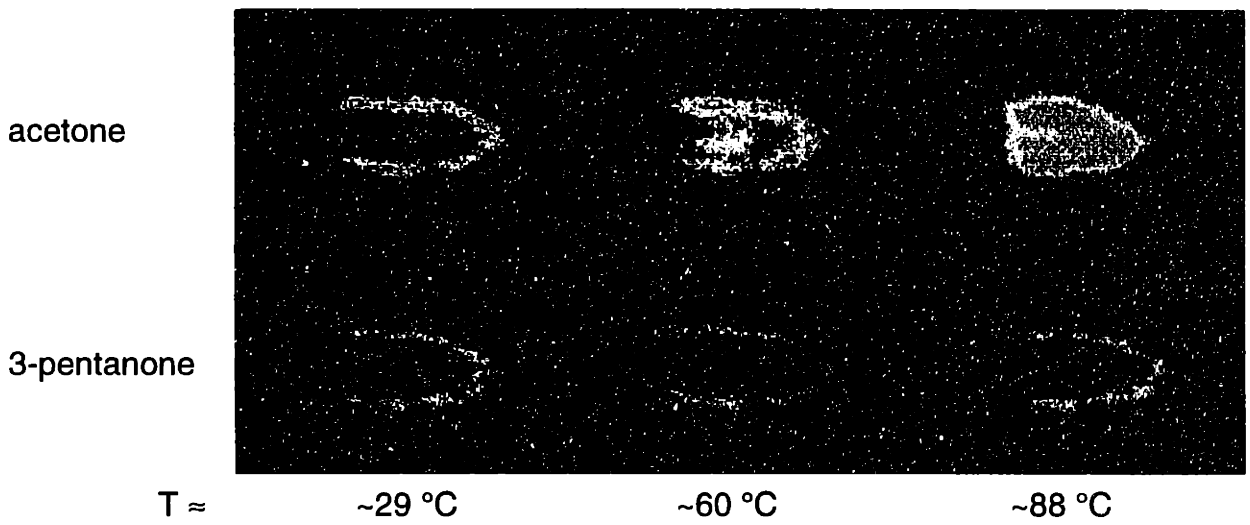

Figure 3.2: Horizontal images of acetone and 3-pentanone-doped sprays throughout an engine warm-up. Iso-octane fuel, SOI = 62 °ATDCI, image taken 1 ms ASOI, intake pressure below 0.5 bar.

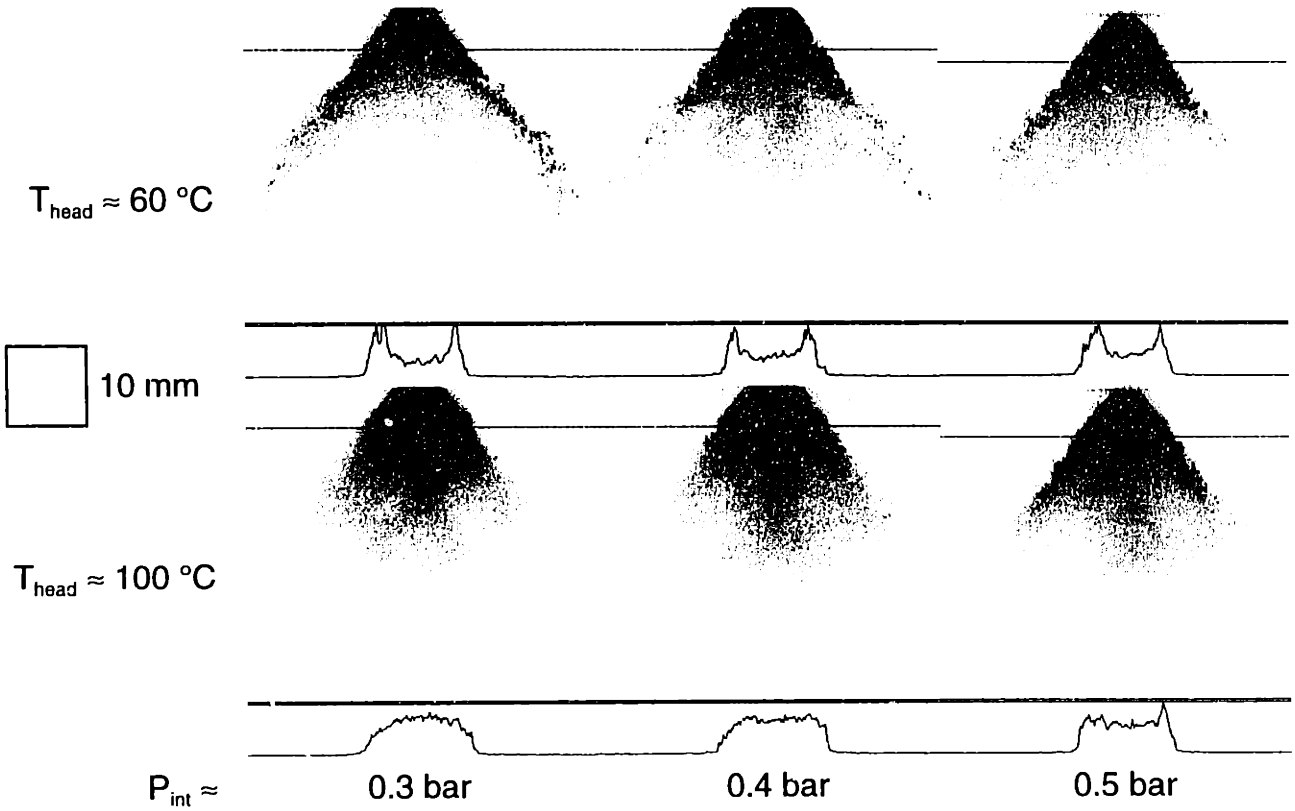

Figure 3.3: Effect of intake pressure on image transition with temperature. Zexel injector, PLIF, iso-octane doped with acetone, SOI = 60 °ATDCI, image taken 1 ms ASOI.

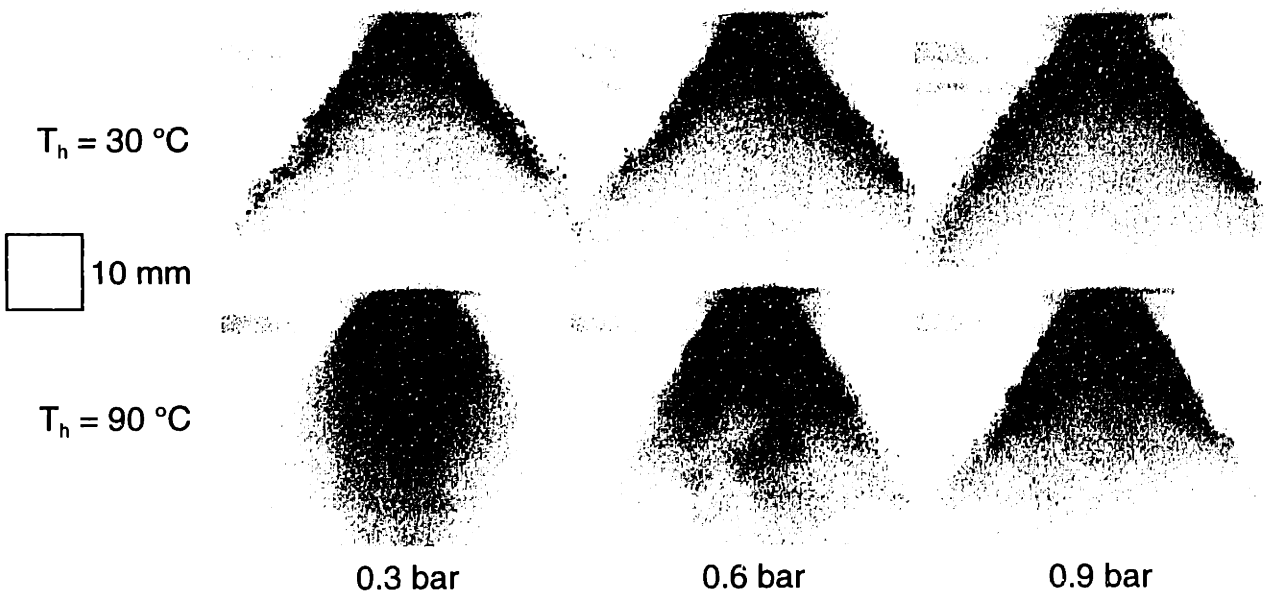

Figure 3.4: Effect of pressure and temperature on acetone/iso-octane spray. Zexel injector, PLIF, SOI = 90 °ATDCI, image taken 1 ms ASOI.

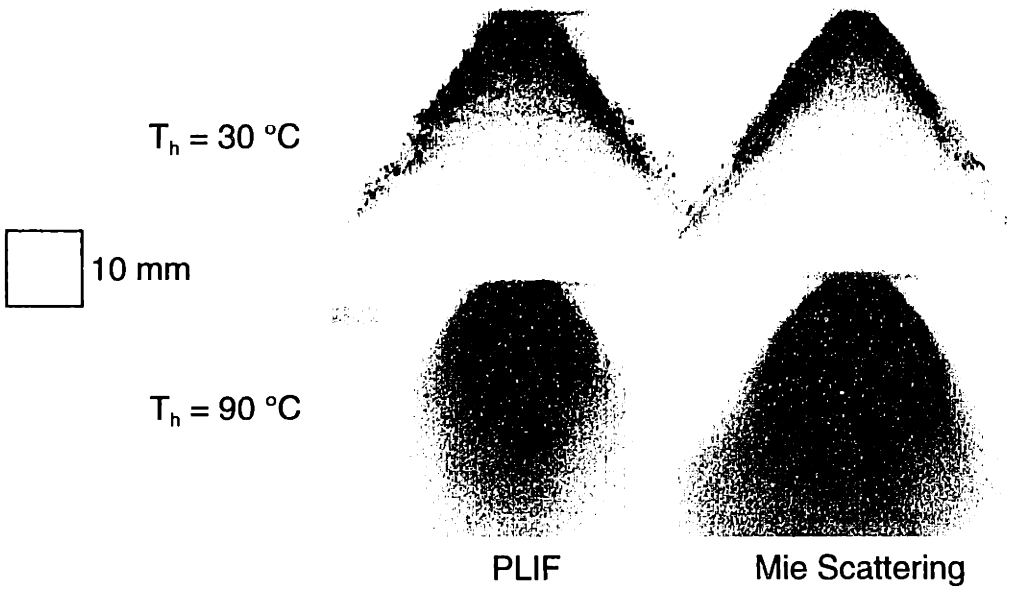

Figure 3.5: Comparison of image transitions with PLIF and Mie scattering. Zexel injector, acetone/iso-octane fuel mixture, 0.3 bar intake pressure, SOI = 90 °ATDCI, image taken 1 ms ASOI.

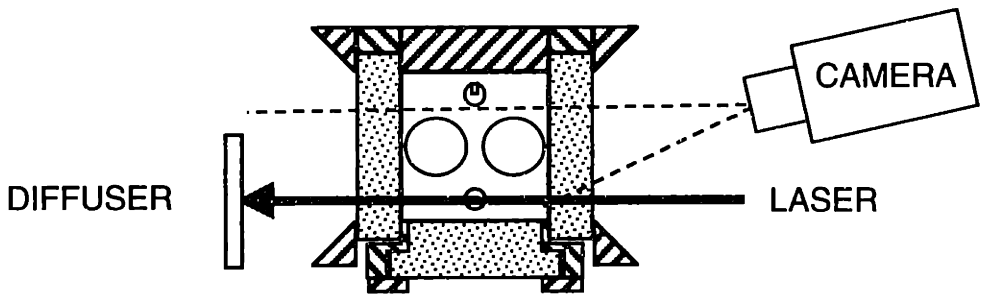

Figure 3.6: Schematic of optical setup for off-axis PLIF images.

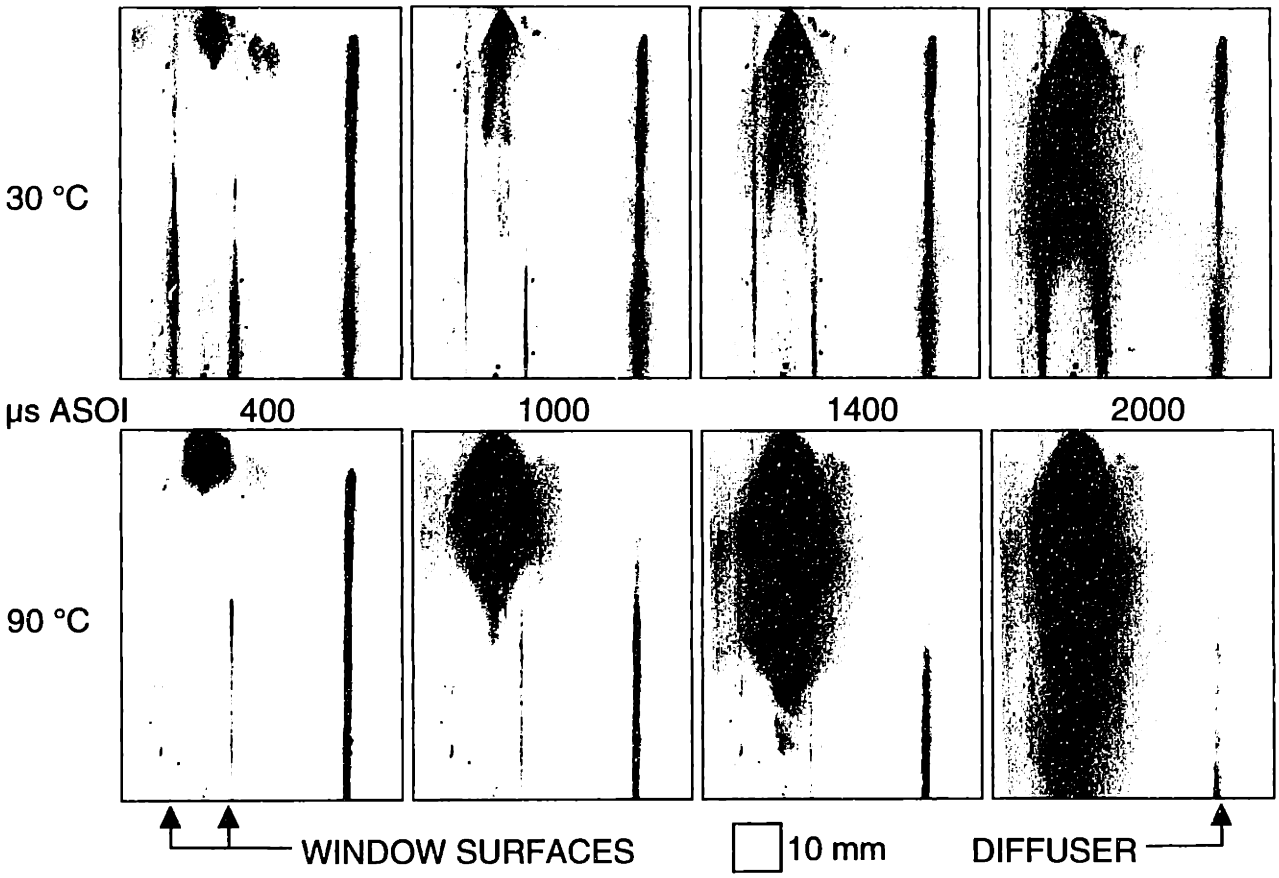

Figure 3.7: Off-axis PLIF images. Chrysler injector, indolene, 0.3 bar intake pressure, SOI = 183 °ATDCI, 2.7 ms injection.

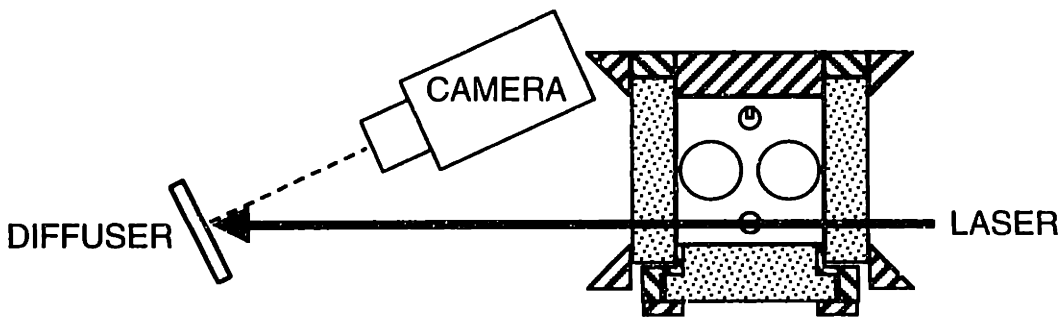

Figure 3.8: Schematic of optical setup for PLIF laser-sheet extinction tests.

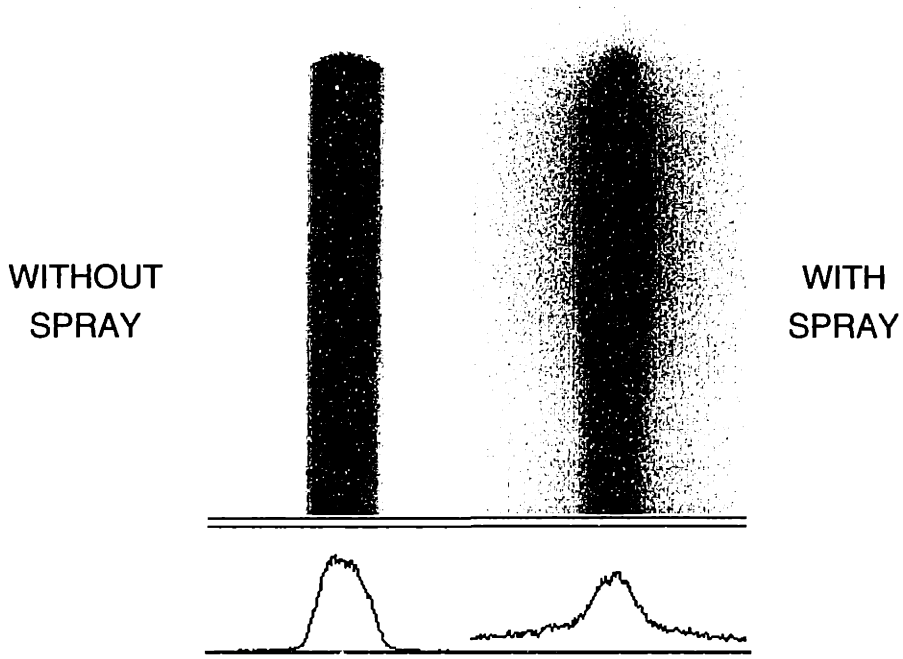

Figure 3.9: Images of extinction and small-angle scattering of PLIF laser sheet. Chrysler injector, 20 °C, atmospheric ambient pressure. Same gain.

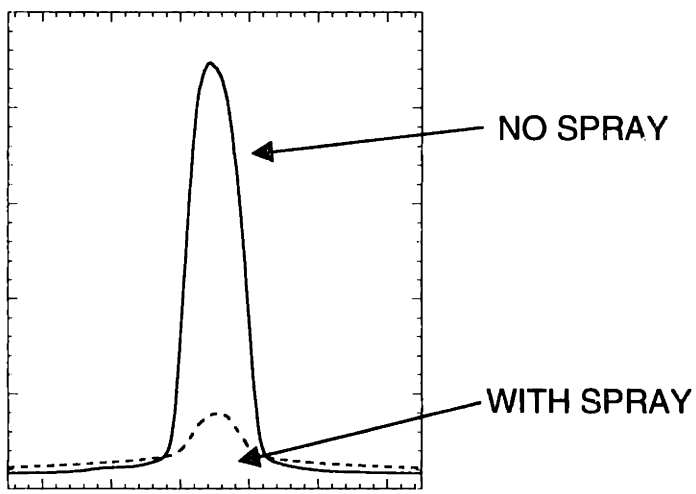

Figure 3.10: Averaged intensity profiles of PLIF laser sheet with and without spray. Chrysler injector, 20 °C, atmospheric ambient pressure.

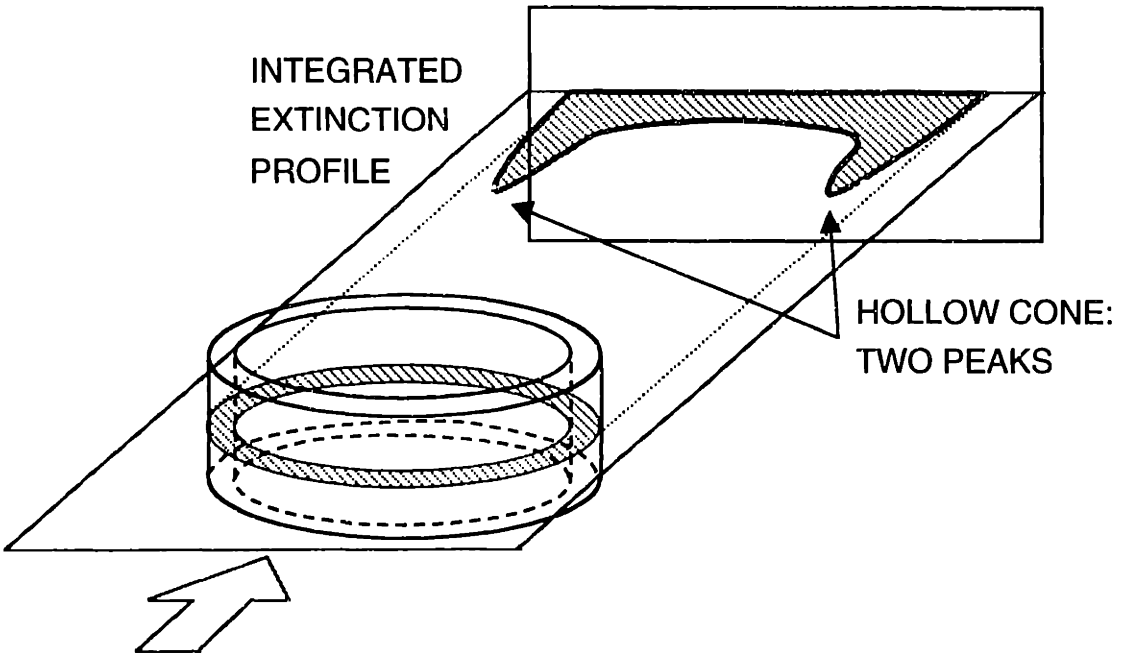

Figure 3.11: Illustration of the projection through a hollow, axisymmetric optically-thin body. Drawn to represent extinction profile–equivalent to PLIF image formation of fully-illuminated spray.

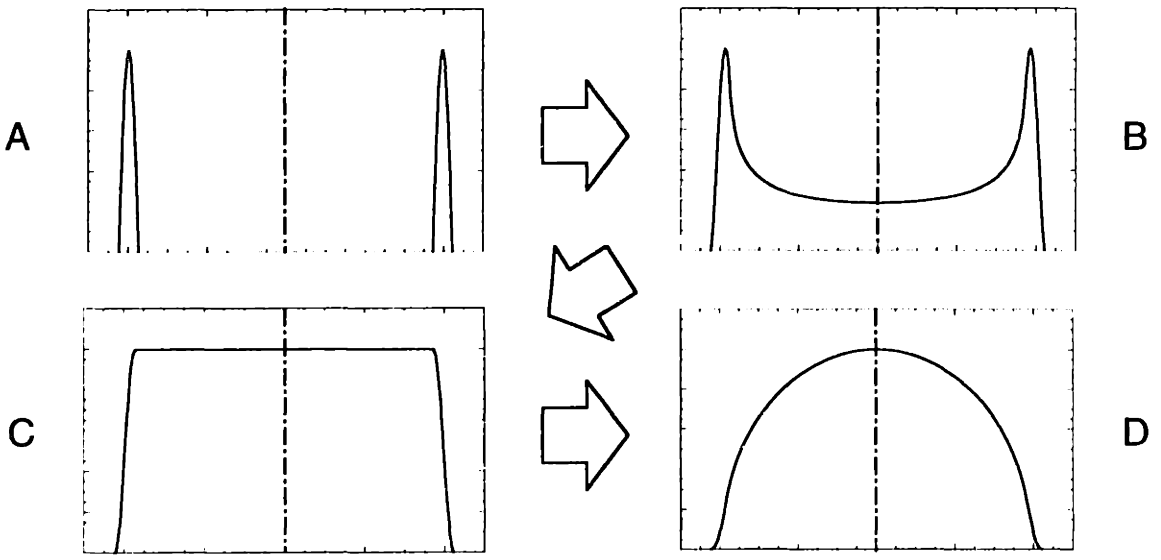

Figure 3.12: Abel Transform profile series. The projection through an axisymmetric object with the cross-section A is profile B, etc.

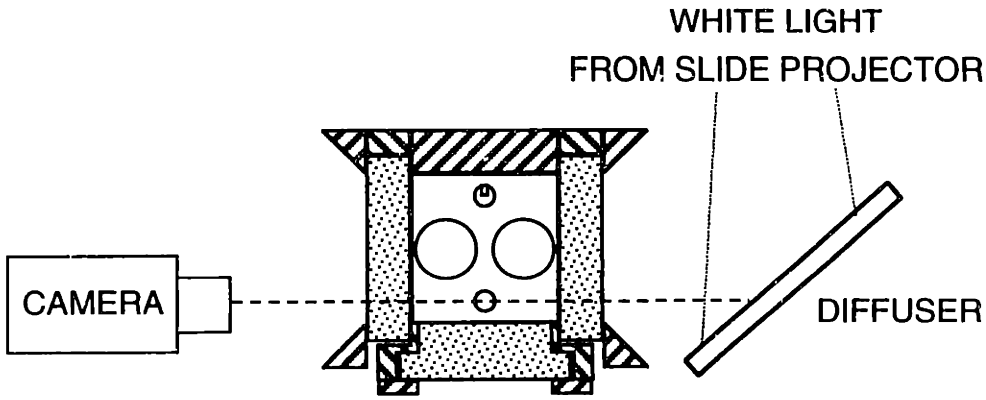

Figure 3.13: Schematic of optical setup for back-lit experiments.

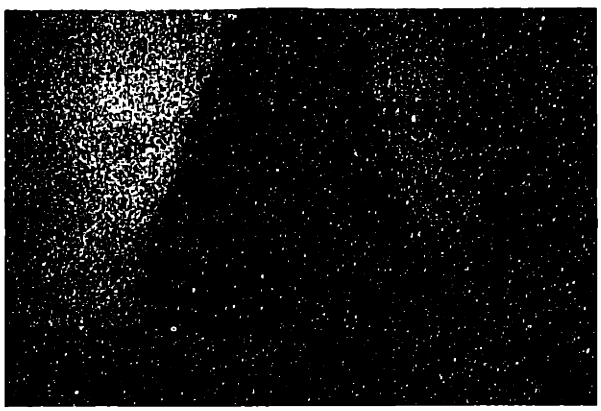

Figure 3.14: Sample back-lit spray image. Chrysler injector, atmospheric ambient pressure, 30 °C, image taken 8 ms ASOI.

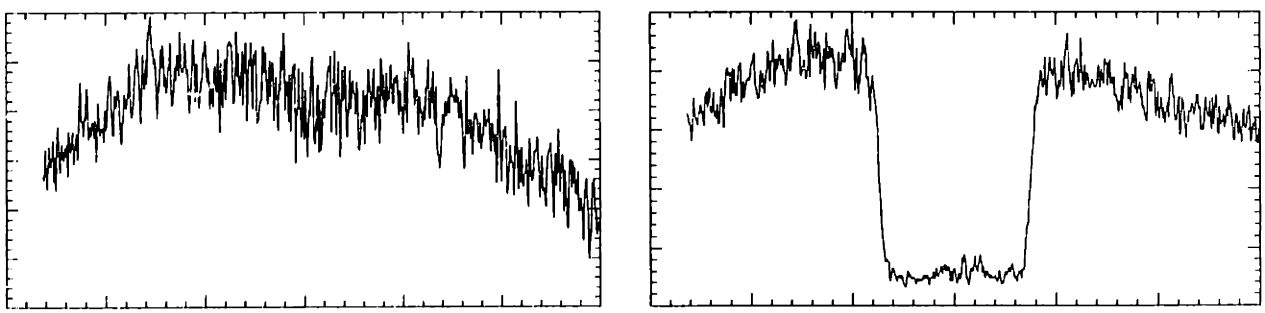

Figure 3.15: Sample intensity profiles of back-lit images. Without spray (a) and with spray (b).

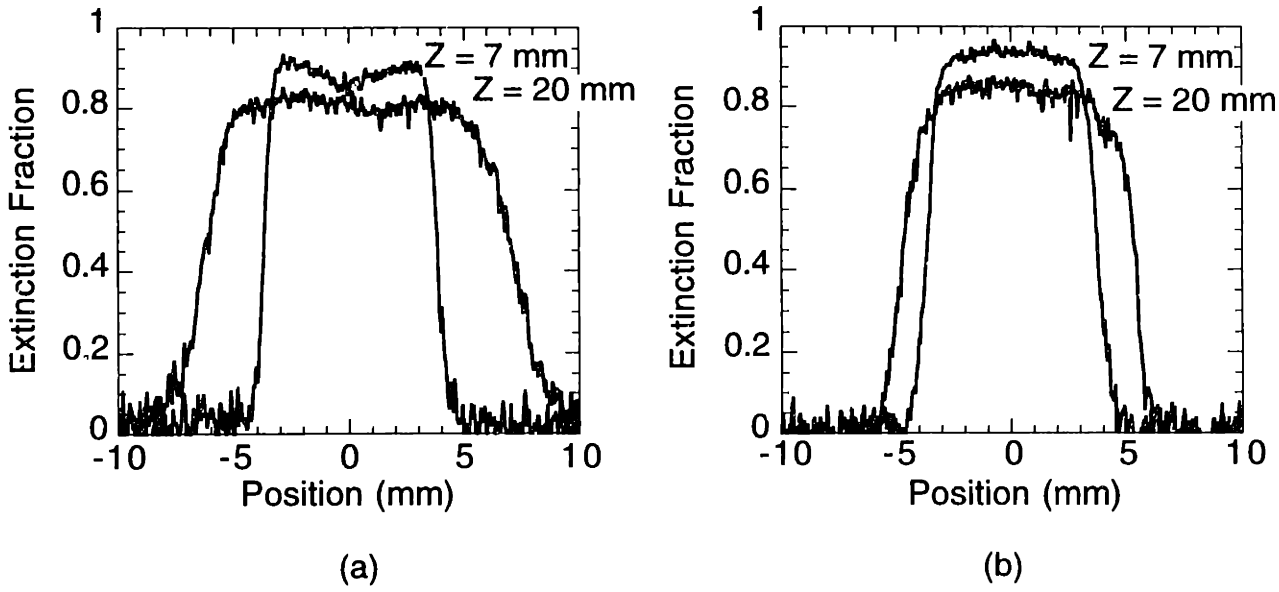

Figure 3.16: Extinction profiles for back-lit sprays. Two temperatures,20 °C (a) and 60 °C (b), and two distances from the injector (7 and 20 mm). Chrysler injector, atmospheric ambient pressure, image taken 8 ms ASOI.

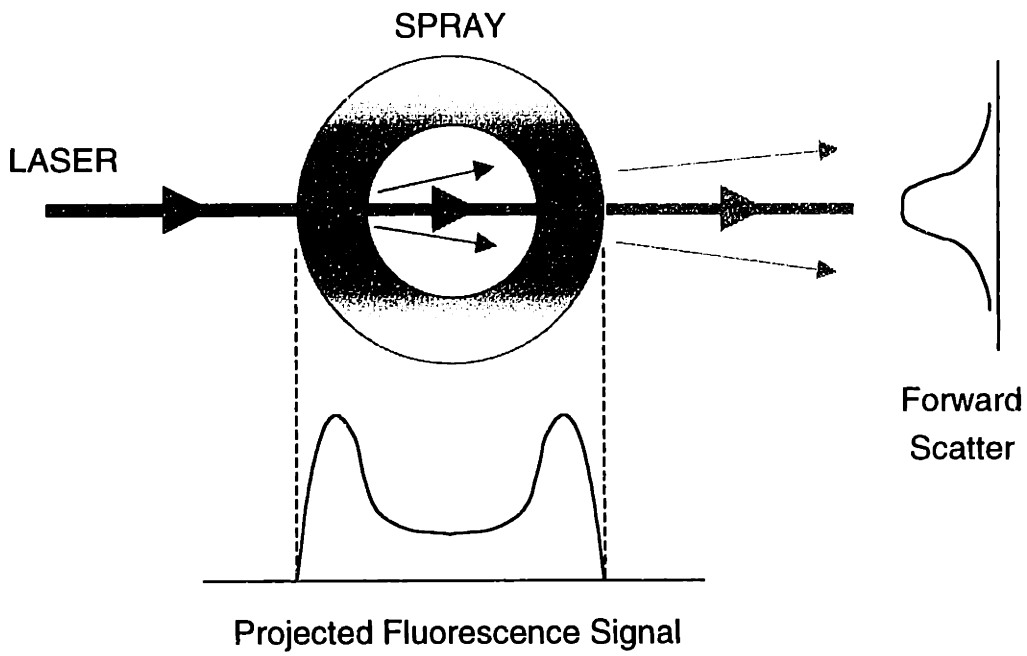

Figure 3.17: Schematic of effects of laser sheet scattering in imaging experiments.

	PLIF Intensity Profile	Pressure *(bar)*	Temperature *(°C)*	Injector	Fuel
A	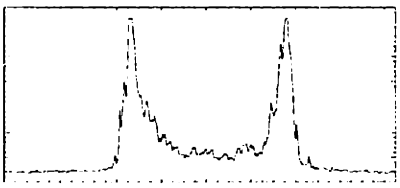	0.3	30	Zexel	acetone / iso-octane
B	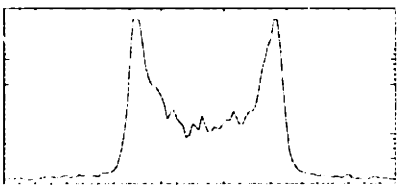	0.3	30	Chrysler	indolene
C	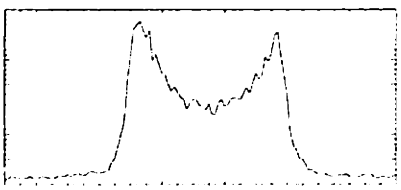	0.9	30	Chrysler	indolene
D	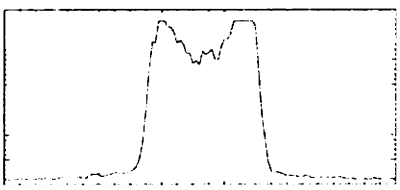	~1.8	30	Chrysler	indolene
E		0.3	90	Chrysler	indolene
F	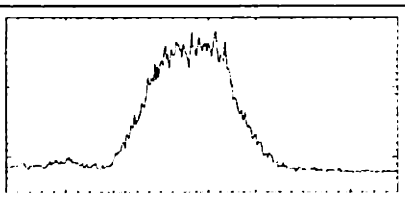	0.3	90	Zexel	acetone / iso-octane
G	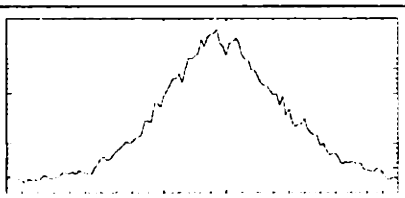	0.3	90	Chrysler	mixed w/ acetone

Figure 3.18: Comparison of PLIF intensity profiles with respect to scattering. Profiles have the same length scale (x-axis). Intensity scale varies. Profiles A-F taken at Z = 15 mm, profile G taken at Z = 50 mm.

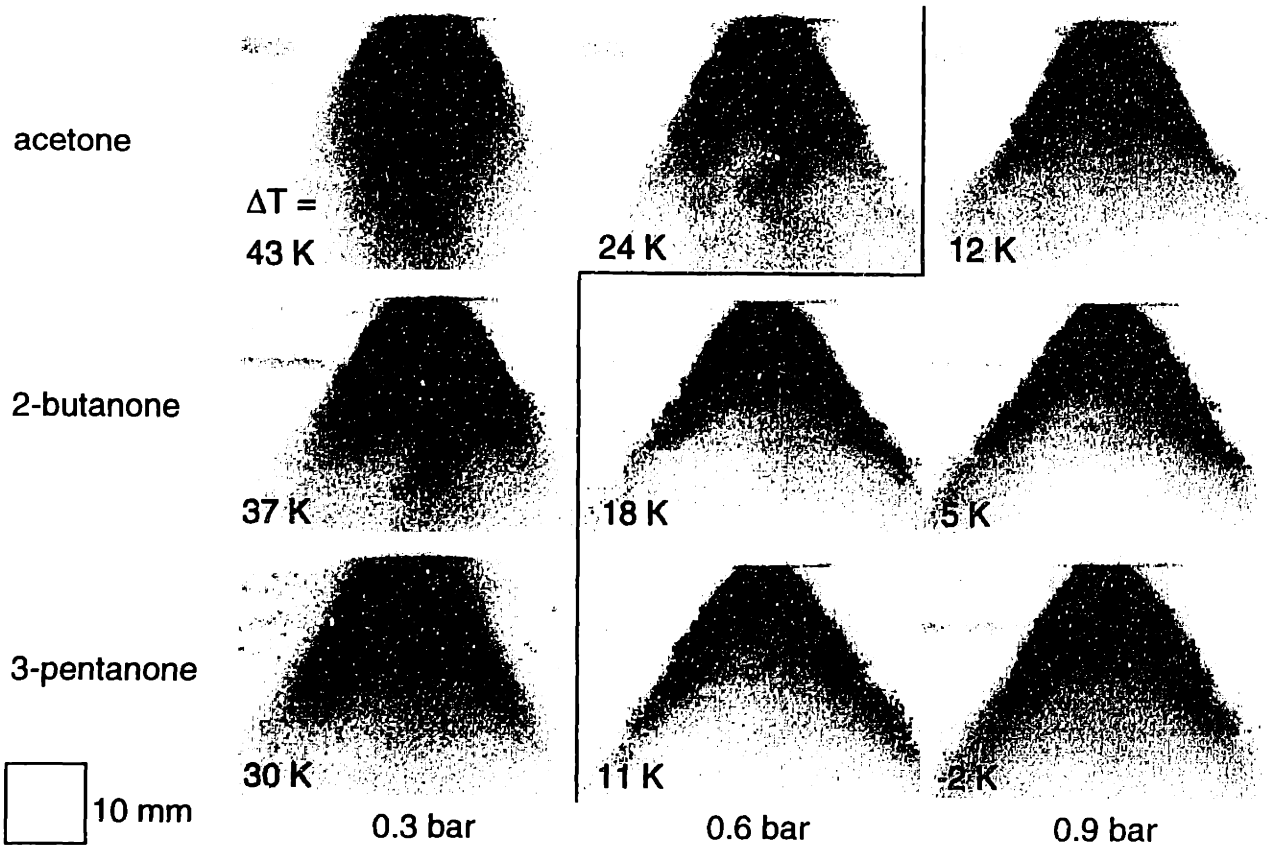

Figure 3.19: Effect of superheat on vapor profiles. Images to the left and above the line show significant vapor production. PLIF images of iso-octane sprays with 3 dopants at 3 pressures. Fuel temperature 90 °C. Superheat temperatures for each case included for comparison.

Table 3.1: Bubble point calculation summary.

Dopant	Pressure (bar)	Dopant $T_{B\text{-}d}$ (°C)	Mixture T_{BP} (°C)	Base Fuel $T_{B\text{-}f}$ (°C)	$\frac{(T_{BP} - T_{B\text{-}d})}{(T_{B\text{-}f} - T_{B\text{-}d})}$
acetone	0.3	24.7	46.5	61.7	59%
	0.6	41.9	65.8	82.1	59%
	0.9	53	78.3	95.6	59%
2-butanone	0.3	46.1	52.9	61.7	44%
	0.6	64.4	72.2	82.1	44%
	0.9	76.3	84.7	95.6	44%
3-pentanone	0.3	66.5	59.6	61.7	144%
	0.6	85.9	79.5	82.1	168%
	0.9	98.5	92.5	95.6	207%

The bubble point is calculated for a 10:1 mixture of base fuel (iso-octane) to dopant.
$T_{B\text{-}d}$ boiling point of dopant; T_{BP} bubble point temperature; $T_{B\text{-}f}$ boiling point of base fuel

Table 3.2: Temperature dependence of spray properties.

Parameter Ratio		X(90 °C) / X(30 °C)	X(0.3 bar) / X(0.9 bar)
surface tension	σ/σ_0	0.71	
viscosity	μ/μ_0	0.55	
liquid density	ρ_L/ρ_{L0}	0.92	
gas temperature	T_A/T_{A0}	~1.05	
pressure differential	$\Delta P/\Delta P_0$		1.01
mass flow rate	$\dot{m}/\dot{m}_0$	0.96	1.00
mean diameter	SMD/SMD_0	0.77	0.74

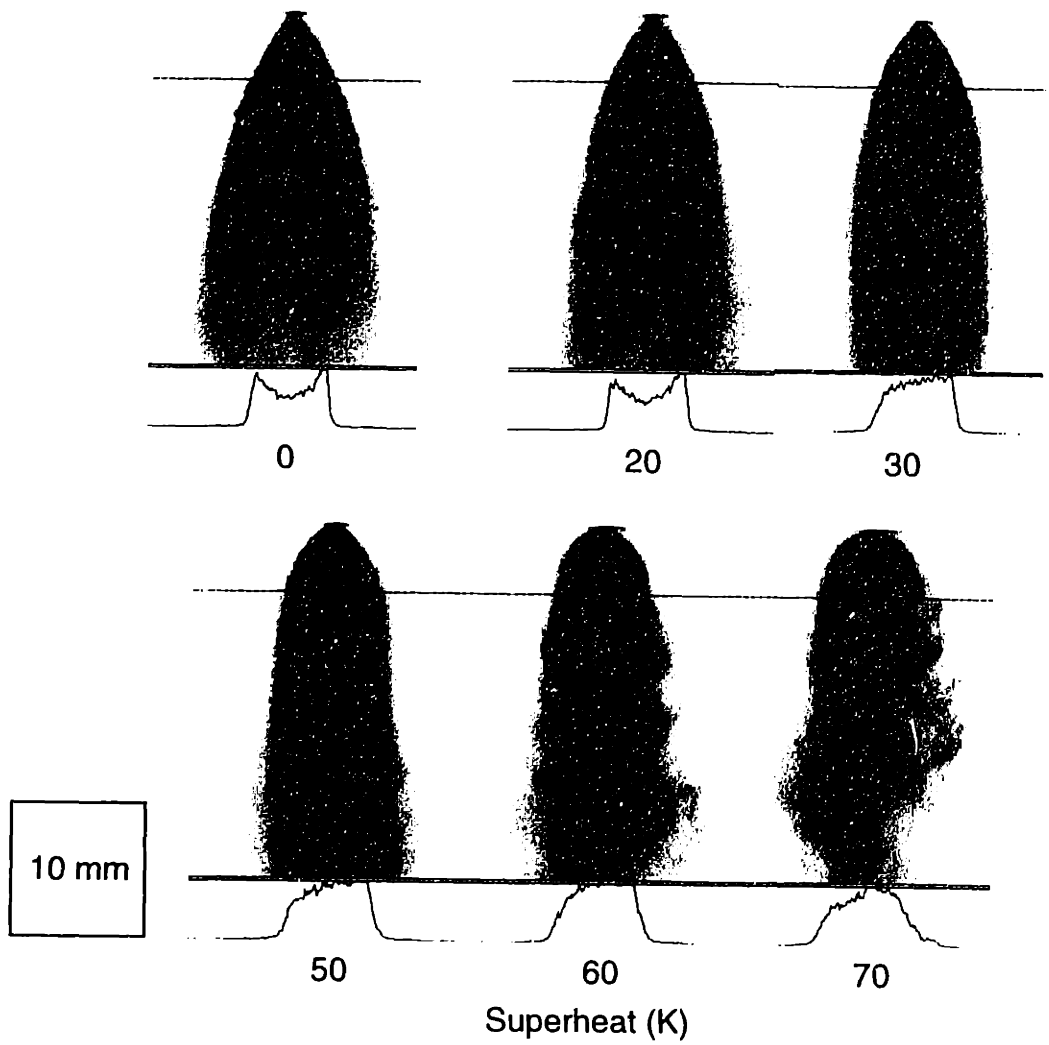

Figure 3.20: Mie scattering images of temperature-controlled 2-methylbutane sprays. Chrysler injector, atmospheric ambient pressure, image taken 1.5 ms ASOI.

Table 3.3: Limit of superheat.

Substance	Saturation (°C)	Limit of Superheat* (°C)
2-methylbutane	30	139
cyclopentane	50	184
acetone	56	174
2,2,4-trimethylpentane	99	215

* at 1 atm. From [van Stralen].

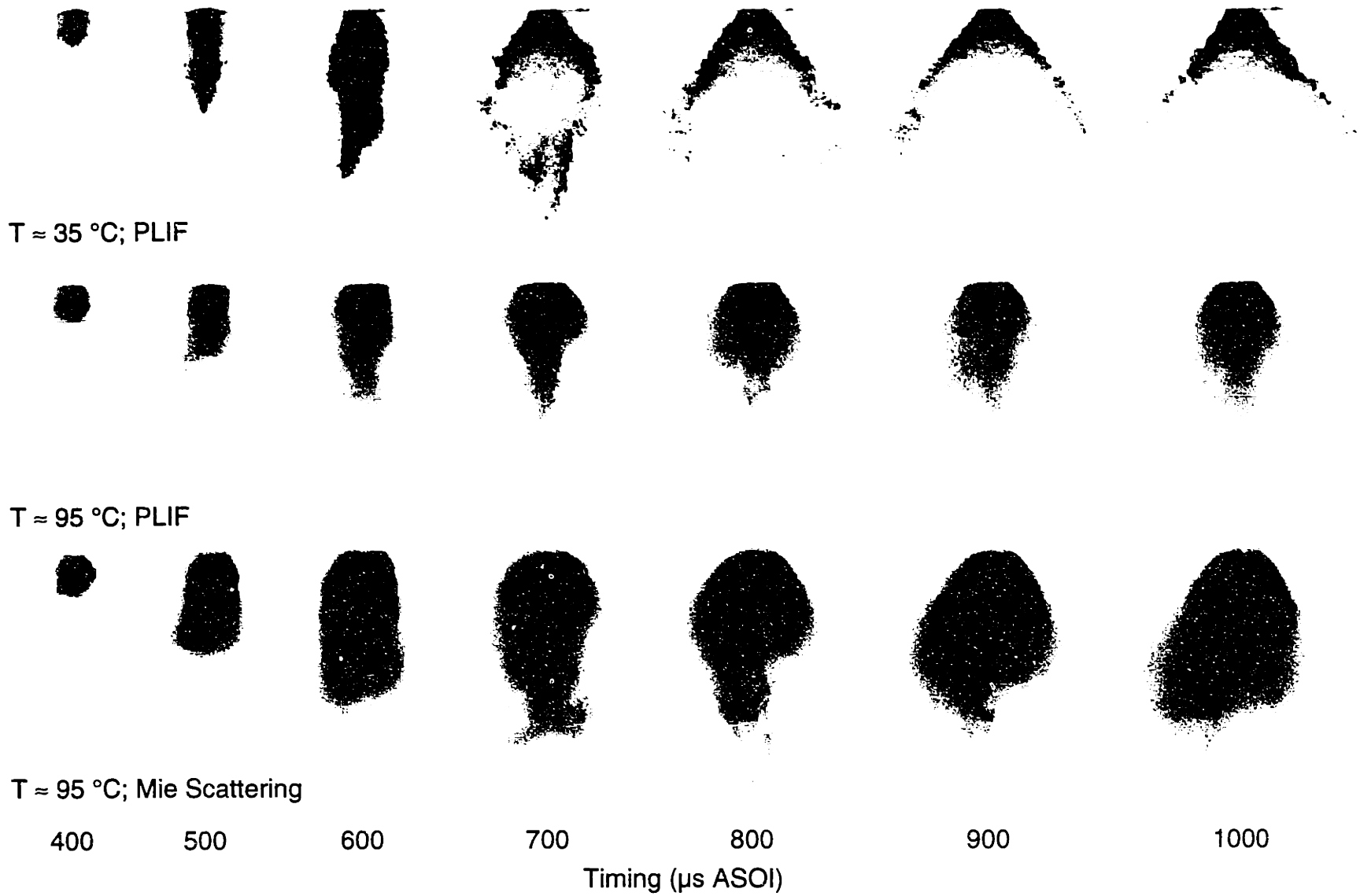

Figure 3.21: Comparison of spray development under cold and hot conditions. Zexel injector, acetone/iso-octane fuel, 0.3 bar intake pressure, SOI = 90 °ATDCI.

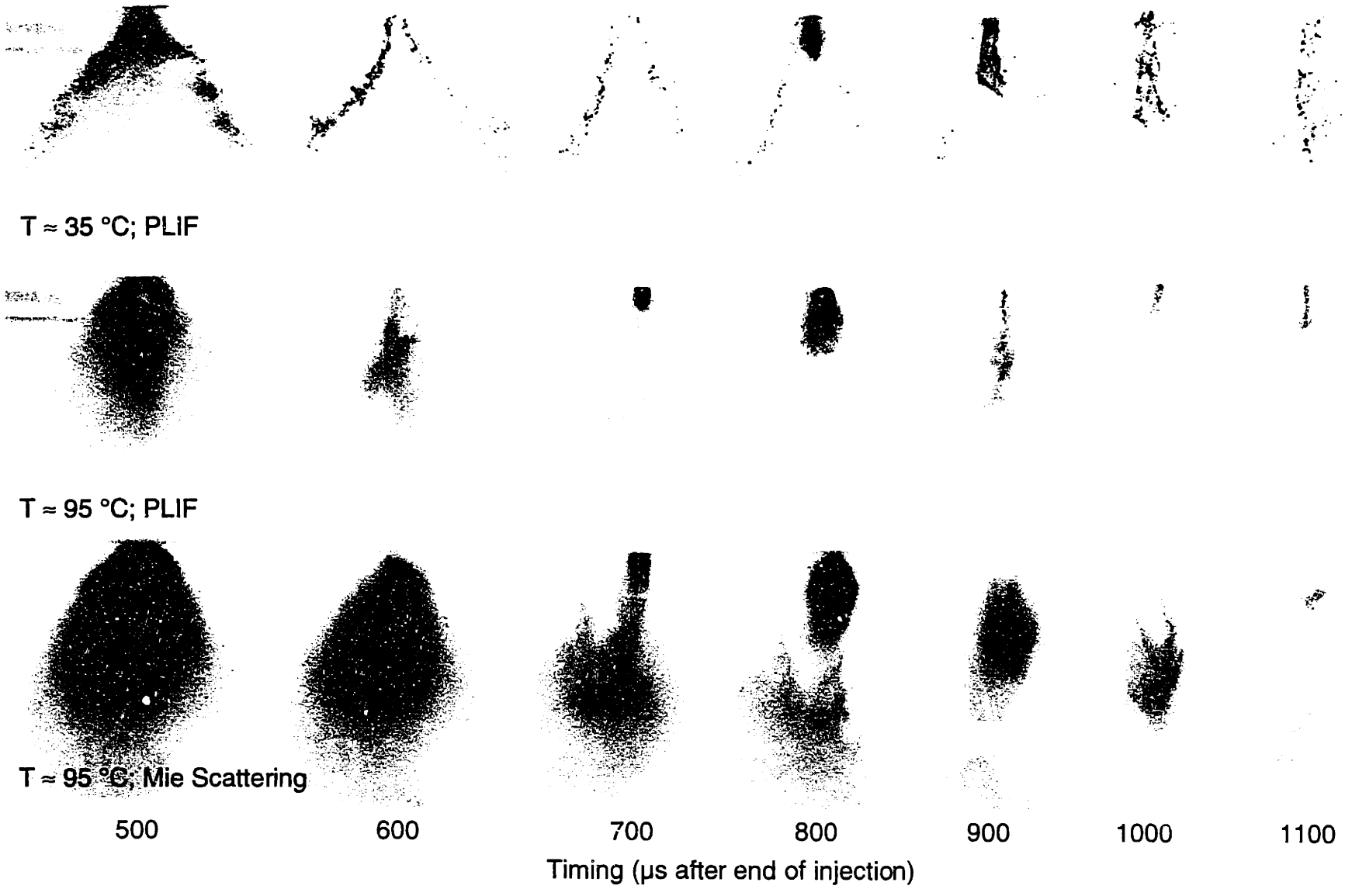

Figure 3.22: Comparison of spray degeneration under cold and hot conditions. Zexel injector, acetone/iso-octane fuel, 0.3 bar intake pressure, SOI = 90 °ATDCI.

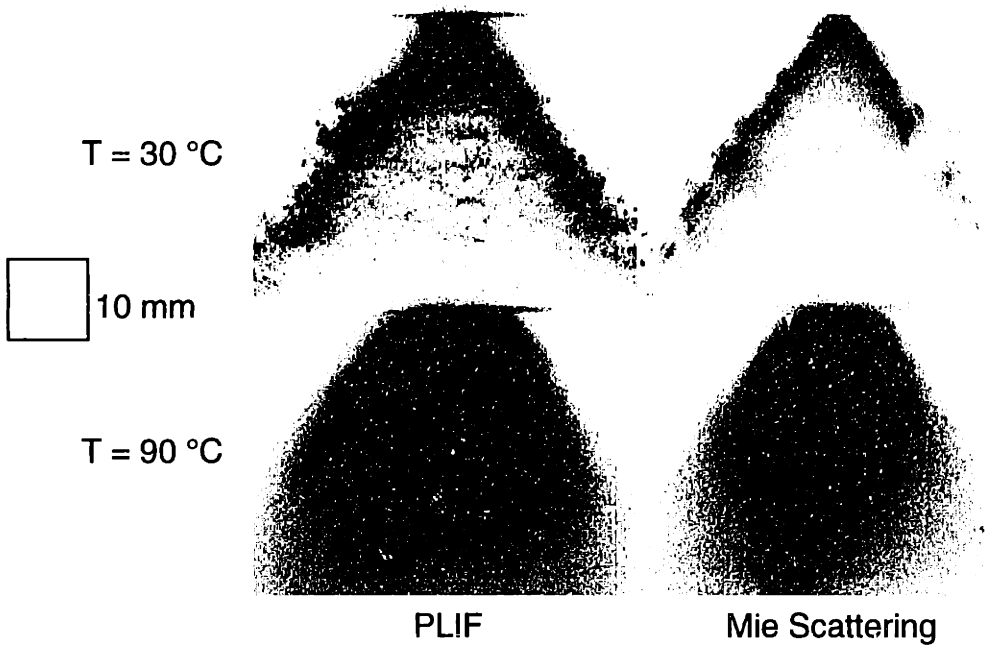

Figure 3.23: Image transition observations in indolene with PLIF and Mie scattering. Zexel injector, 0.3 bar intake pressure, SOI = 90 °ATDCI, image taken 1 ms ASOI.

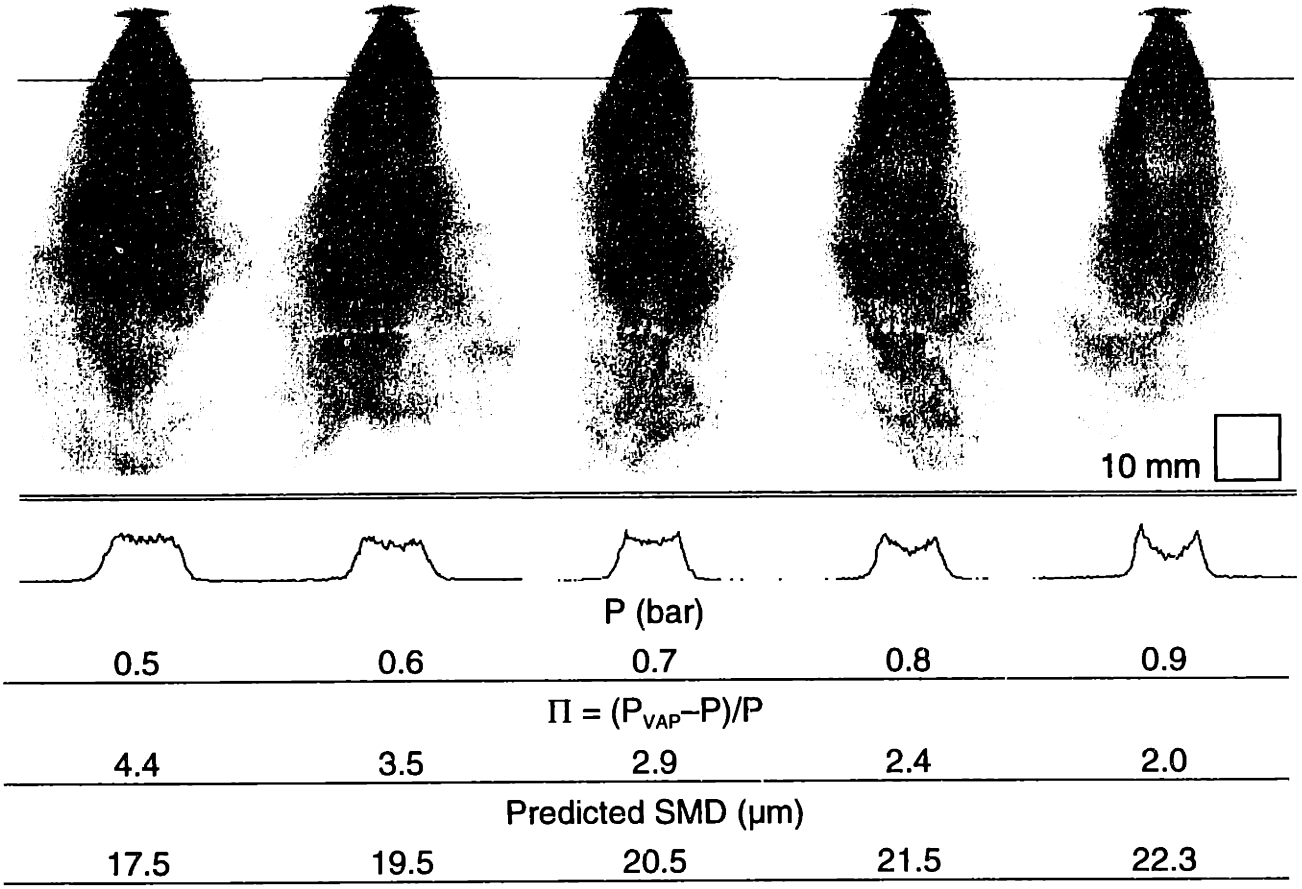

Figure 3.24: Pressure dependence of indolene image transition. Intensity profile is from 10 mm below injector (dotted line). PLIF; Chrysler injector; 80 °C; SOI = 90 °ATDCI; image taken 2 ms ASOI. SMD predicted from Sec. 4.6.6.

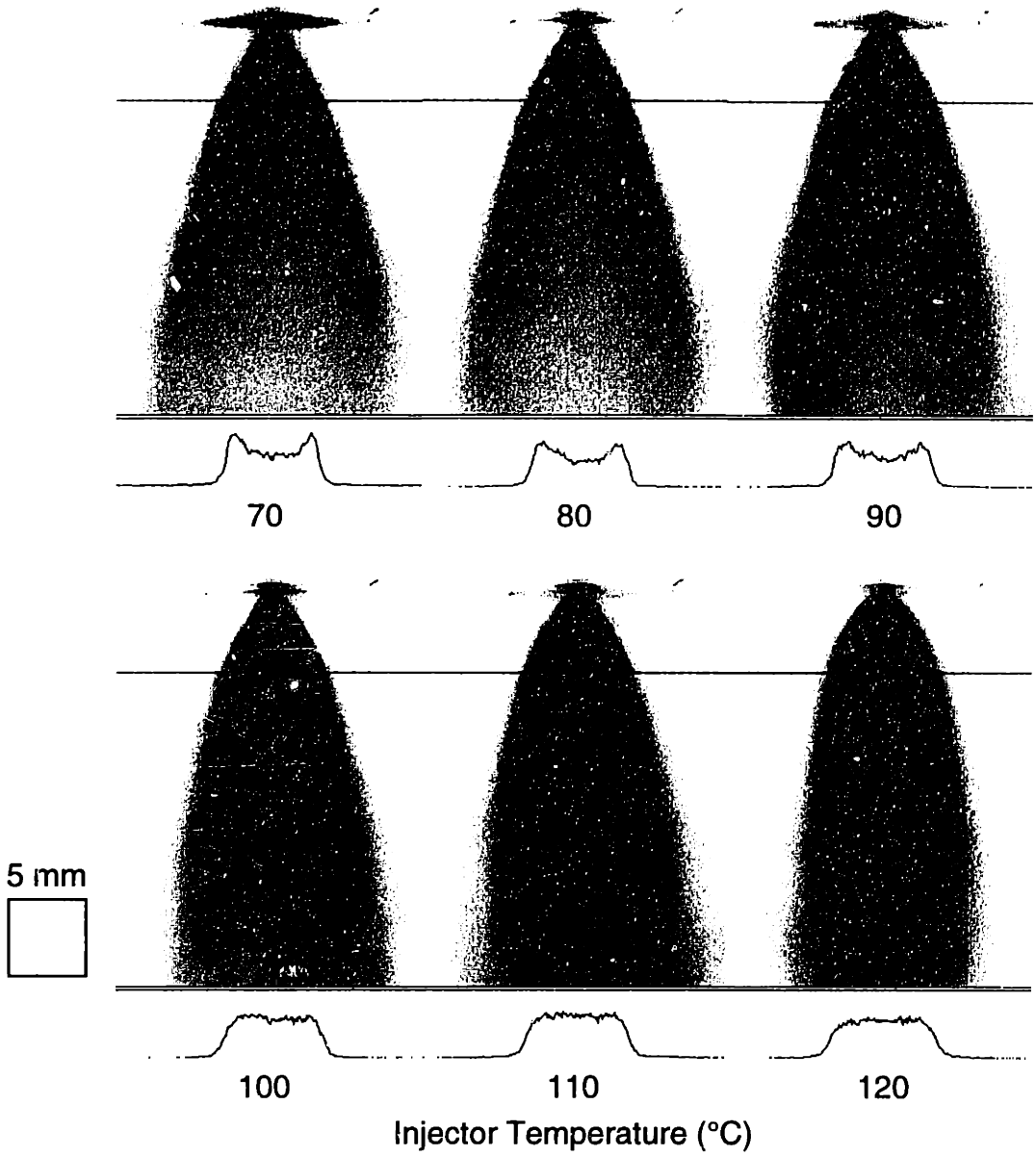

Figure 3.25: PLIF images of temperature-controlled indolene sprays. Chrysler injector, atmospheric ambient pressure, 1.5 ms injection duration

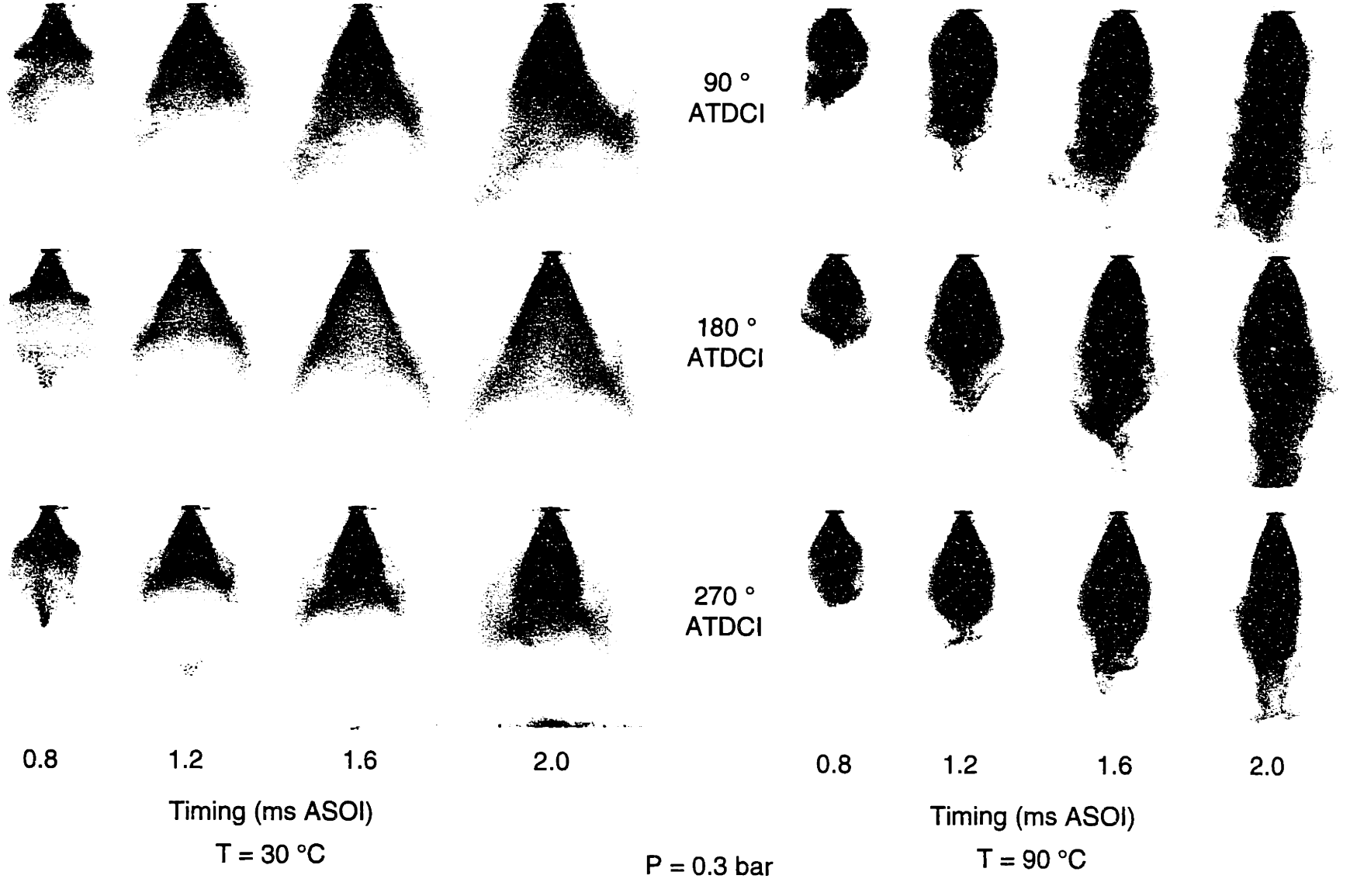

Figure 3.26a: Effect of injection timing on spray structure under varied operating conditions: low pressure (0.3 bar).

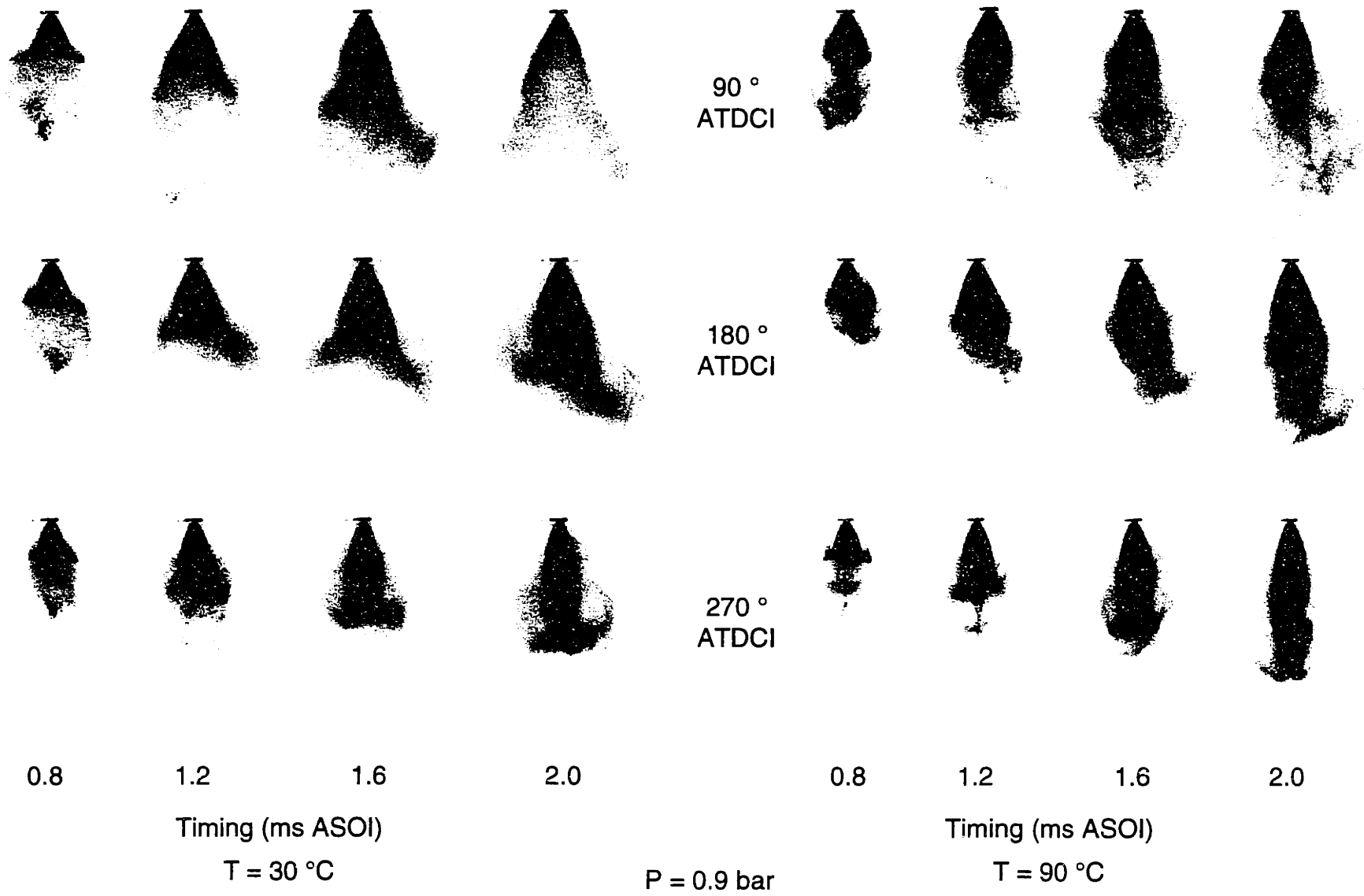

Figure 3.26a: Effect of injection timing on spray structure under varied operating conditions: high pressure (0.9 bar).

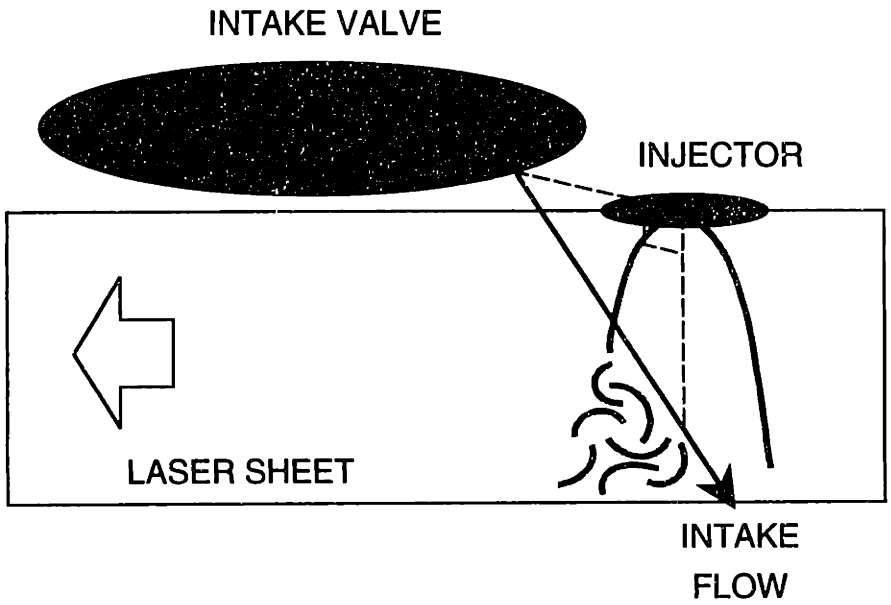

Figure 3.27: Schematic of path of intake flow across the fuel spray.

Table 3.4: Fuel mixture component properties.

Fuel Species	Boiling Point (°C)	Blending RON[a]
2-methylbutane	30	99
cyclopentane	50	141
2,2,4-trimethylpentane	99	100
isopropylbenzene	154	132
1,3-diisopropylbenzene	203	165[b]
acetone	56	*112*[c]
3-pentanone	102	*62*[c]
cyclohexanone	155	*110*[c]

(a) blending research-octane-numbers (RON) from [Owen].

(b) estimated from differences between benzene, ethylbenzene, and diethylbenzene, and isopropylbenzene.

(c) for ketones, RON of corresponding hydrocarbon is given.

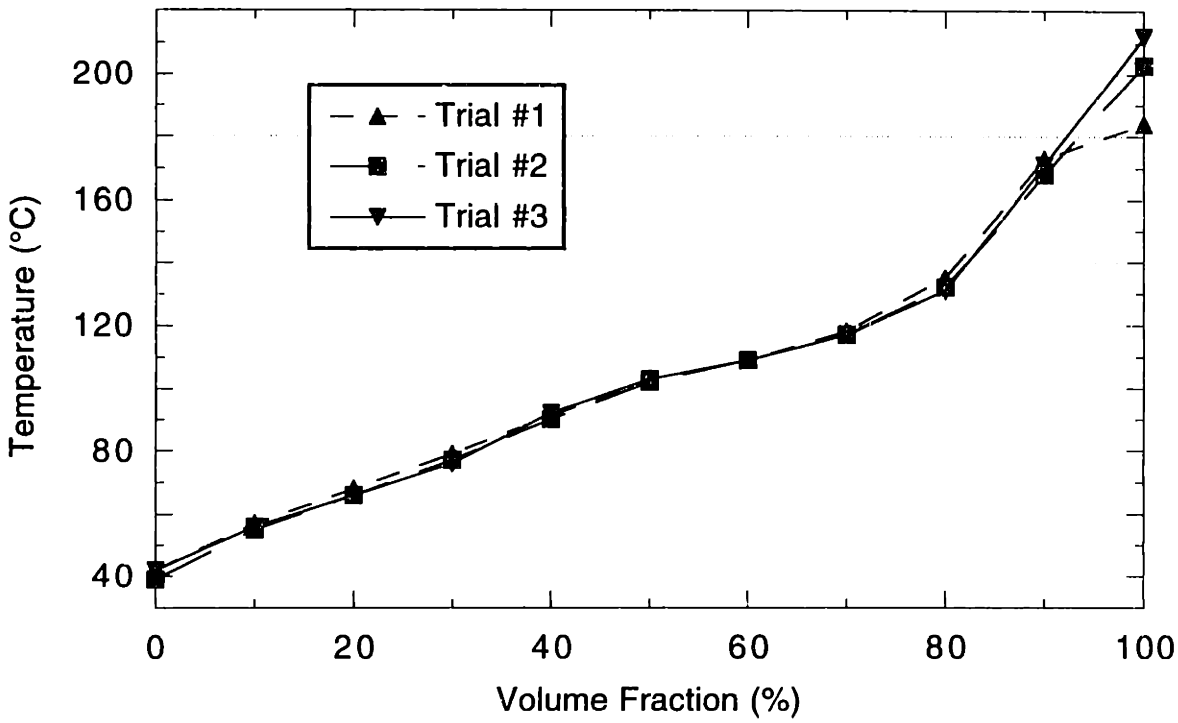

Figure 3.28: Comparison of three distillation tests with indolene.

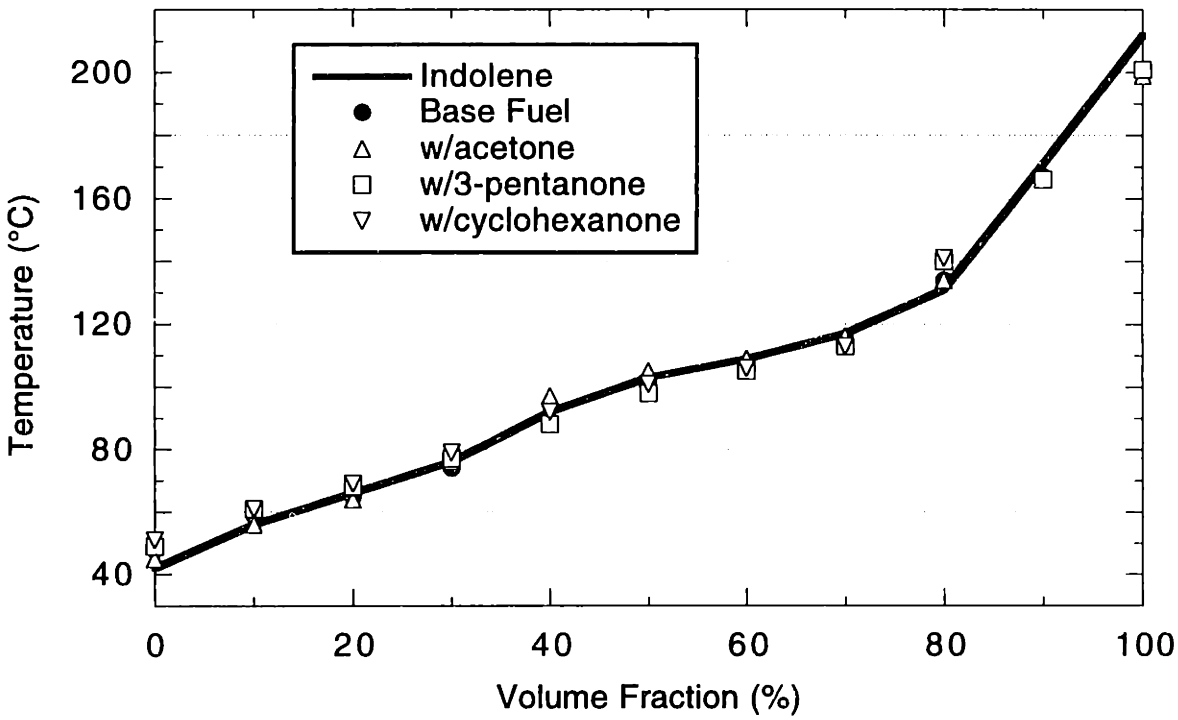

Figure 3.29: Comparison of distillation curves of fuel mixtures to indolene.

Table 3.5: Test fuel mixture compositions and properties.

	Indolene	Base fuel	w/ acetone	w/ 3-penta-none	w/ cyclo-hexanone
Species Fraction					
2-methylbutane		0.15	0.10	0.15	0.15
cyclopentane		0.15	0.05	0.13	0.13
2,2,4-trimethylpentane		0.45	0.50	0.37	0.47
isopropylbenzene		0.18	0.18	0.18	0.08
1,3-diisopropylbenzene		0.07	0.07	0.07	0.07
DOPANT		---	0.10	0.10	0.10
Distillation (°C)					
IBP	42	48	45	49	51
10%	56	59	56	61	61
20%	66	65	64	68	69
30%	76	74	76	77	79
40%	92	89	97	88	92
50%	103	101	105	98	101
60%	109	107	109	105	106
70%	117	115	116	113	113
80%	131	134	134	140	141
90%	171	167	166	166	
FBP	212	200	199	201	200
Octane rating (RON)*	97	116	113	112	116
Aromatic vol. fraction	0.29	0.25	0.25	0.25	0.17
Hydrogen / carbon ratio	1.86	2.02	2.01	2.00	2.03
Heat of Comb. (MJ/kg)	43.0	43.4	41.8	42.3	42.4

* RON values for fuel mixtures determined from blending values in Table 3.4.

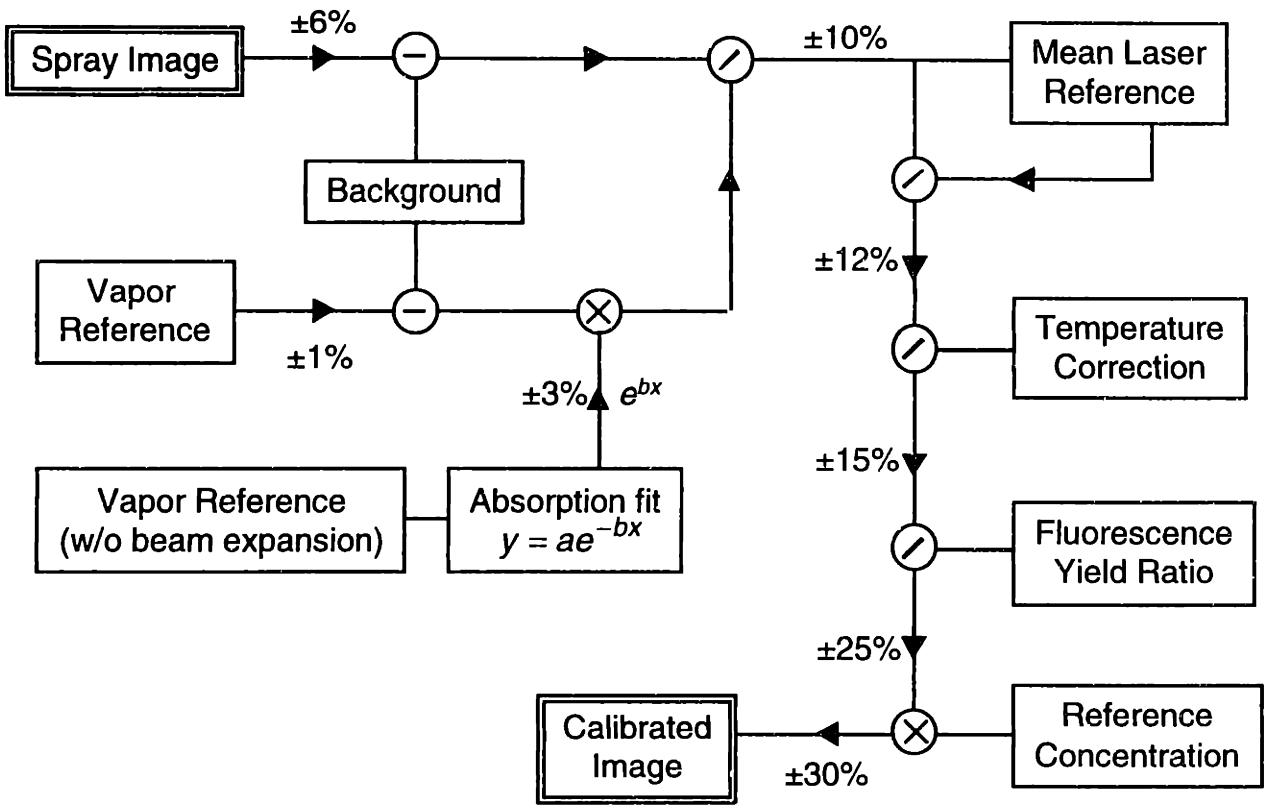

Figure 3.30: Schematic of image calibration process.

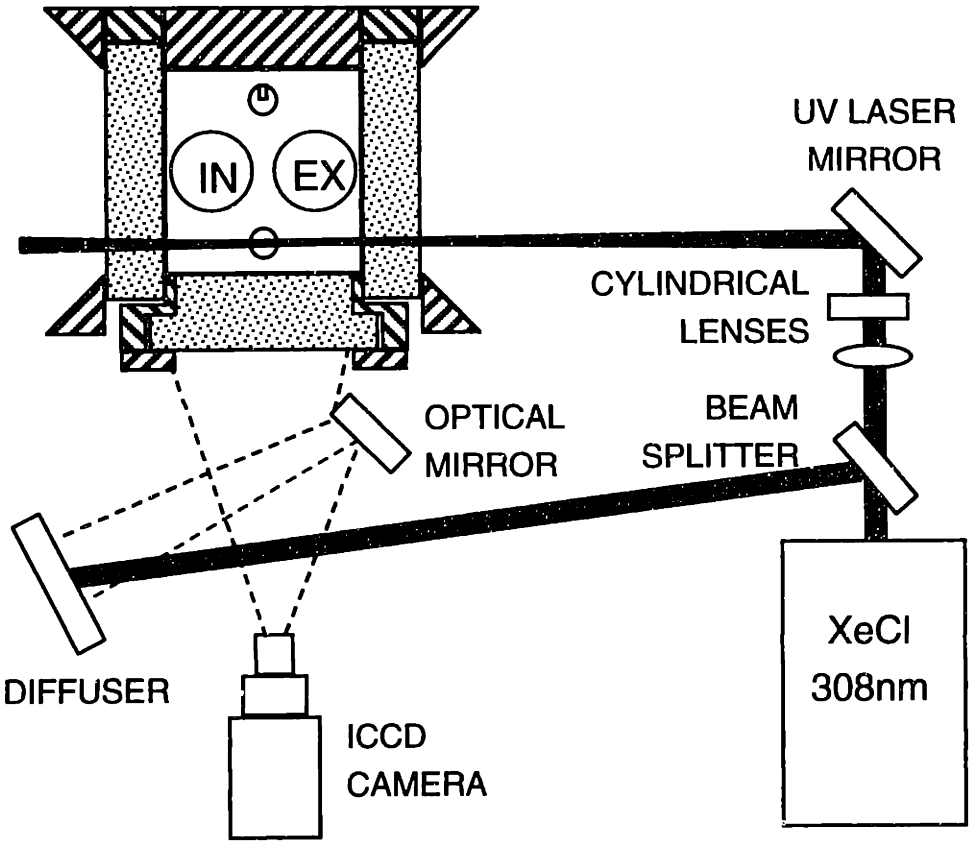

Figure 3.31: PLIF optical setup, including laser beam reference

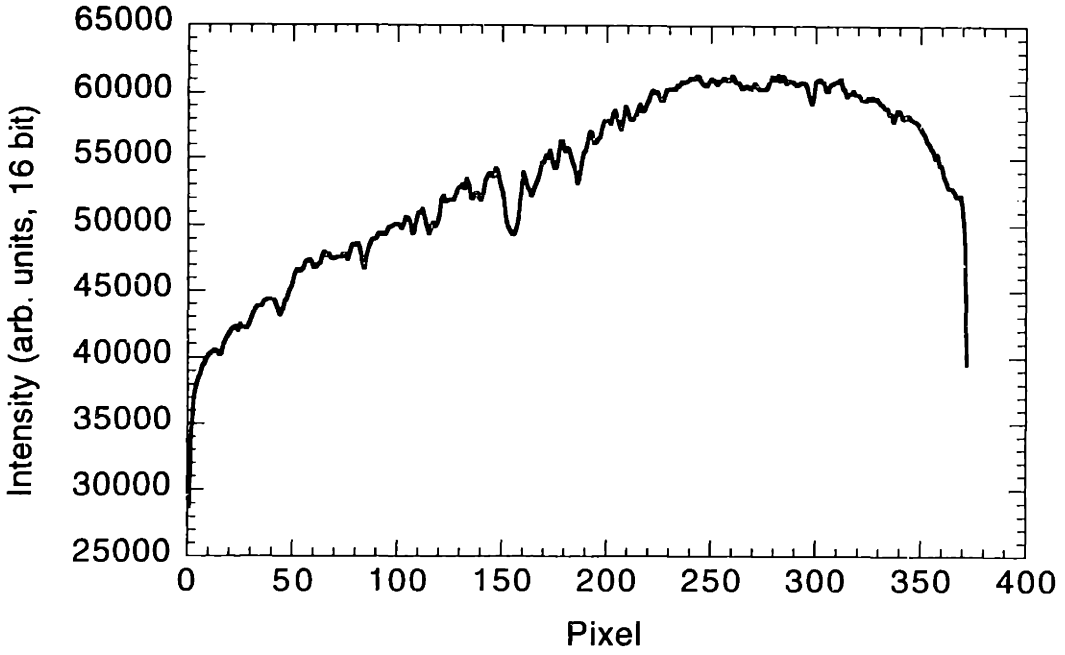

Figure 3.32: Intensity across acetone vapor reference without laser expansion. Averaged over 10 frames and 100 lines. Noise remaining is largely due to scratches in the engine window.

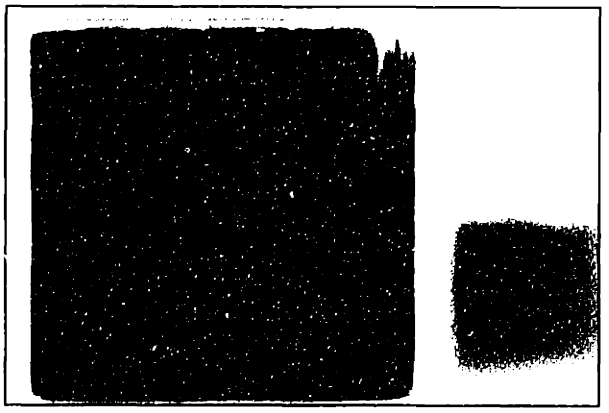

Figure 3.33: Image of acetone vapor reference after absorption correction.

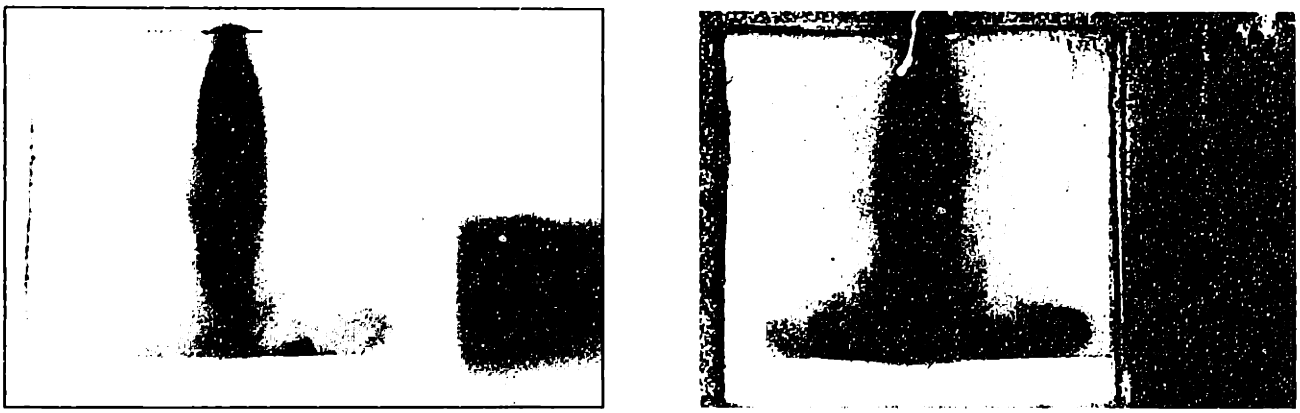

Figure 3.34: Comparison of original and calibrated images. Acetone dopant, T = 90 °C, SOI = 270 °ATDCI, image taken 2.8 ms ASOI.

Table 3.6: Comparison of dopant fluorescent yields in the liquid state.

Compound	Relative fluorescence yield
acetone	1
3-pentanone	1.00
cyclohexanone	1.71
indolene	4.80

Table 3.7: Comparison of liquid and vapor phase fluorescent yields. Vapor phase in air.

Phase	acetone	3-pentanone
vapor	1	1
liquid	1.79	1.39

Table 3.8: Fluorescence yield ratio of dopants to acetone vapor reference.

Dopant	Phase	Environment	Relative fluorescence yield
acetone	*vapor*	*nitrogen*	*1*
acetone	vapor	air	0.8
acetone	liquid	air	1.4
3-pentanone	liquid	air	1.4
cyclohexanone	liquid	air	2.4

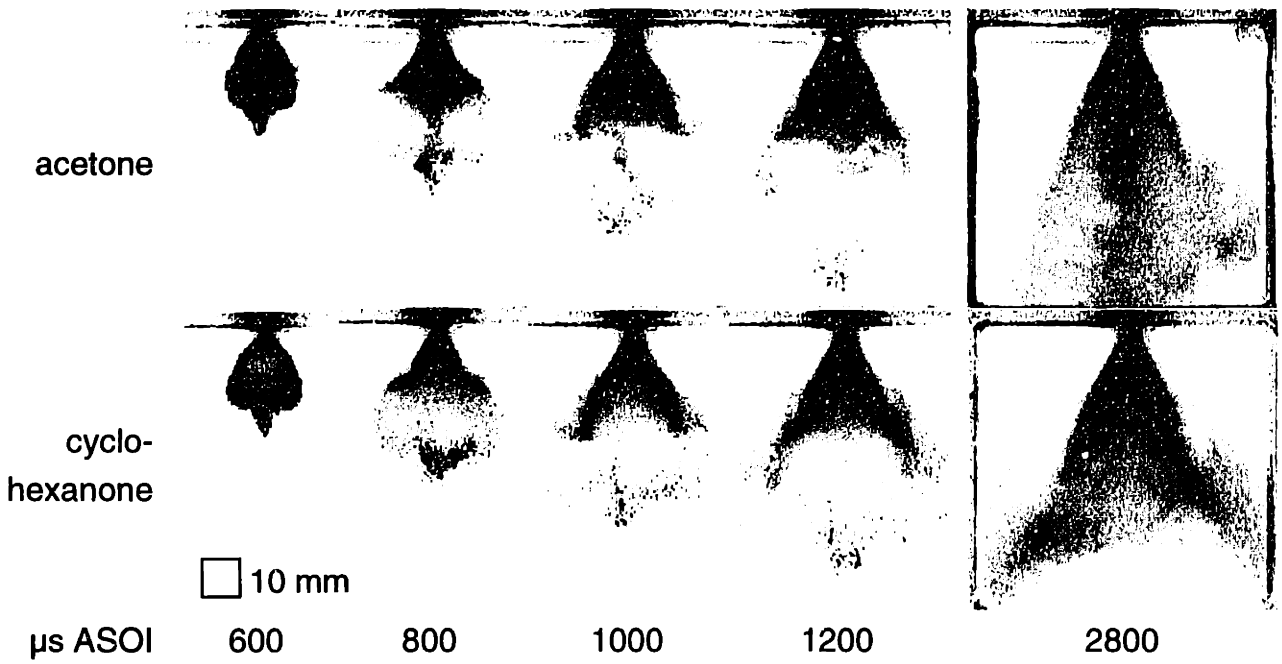

Figure 3.35: Comparison of acetone and cyclohexanone distributions in spray under conditions for minimal evaporation. PLIF, Chrysler injector, P = 0.3 bar, T = 30 °C, SOI = 180 °ATDCI.

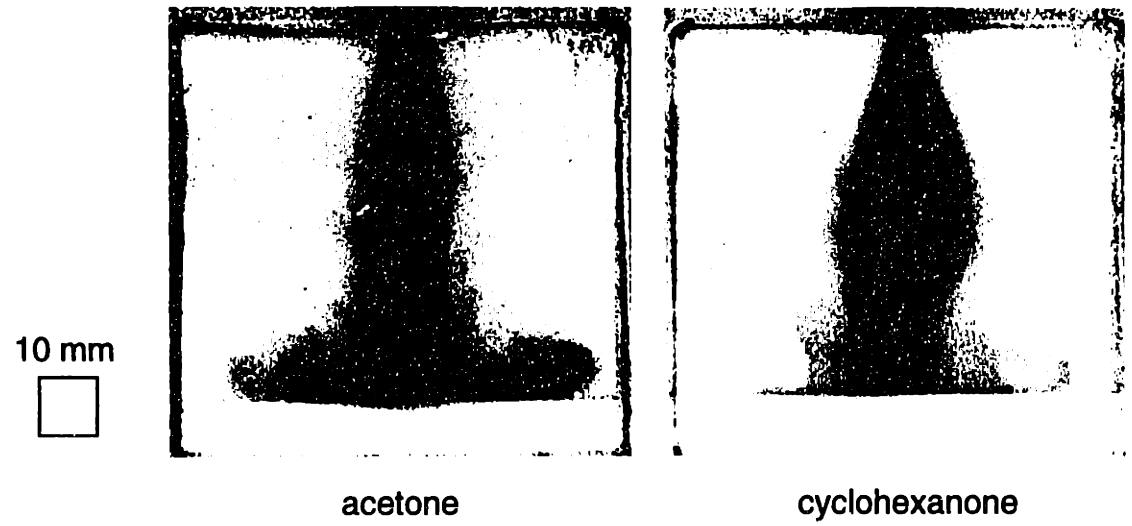

Figure 3.36: Demonstration of volatility stratification. Acetone and cyclohexanone distributions under conditions for moderate evaporation. Chrysler injector, 0.3 bar intake pressure, T = 90 °C, SOI = 270 °ATDCI, image taken 2.8 ms ASOI, cylinder pressure at time of injection: ~0.6 bar.

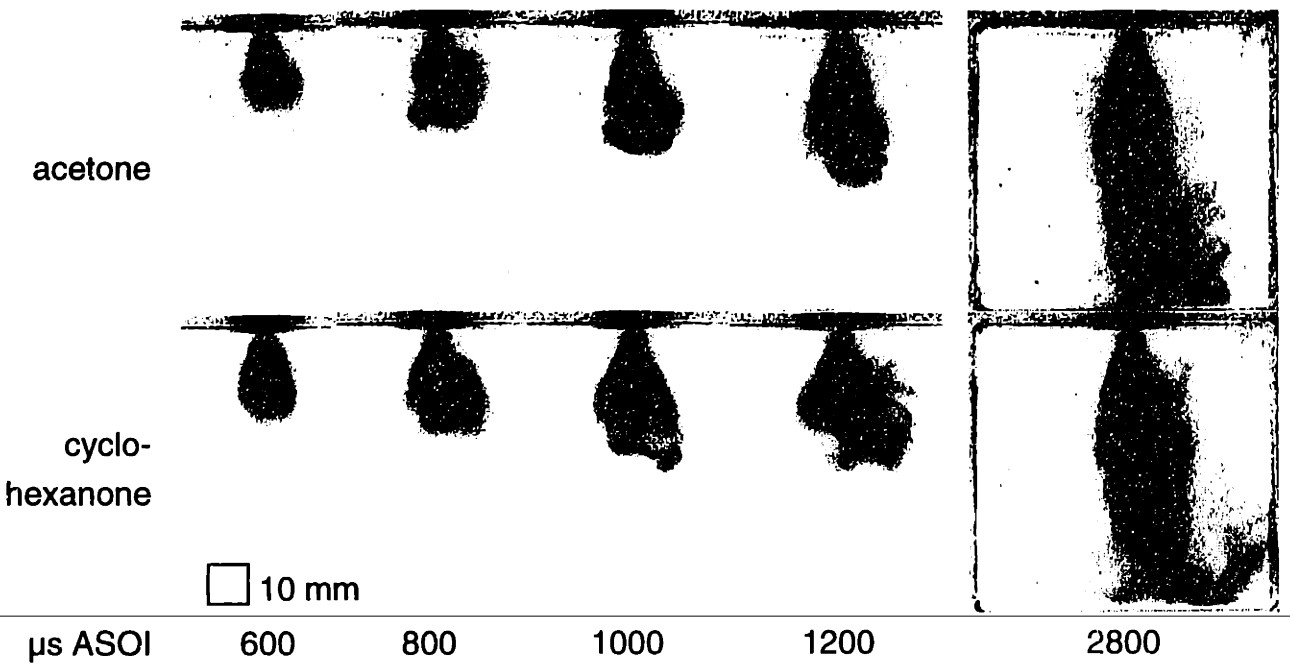

Figure 3.37: Comparison of acetone and cyclohexanone distributions in spray under conditions for moderate evaporation. Chrysler injector, P = 0.9 bar, T = 90 °C, SOI = 180 °ATDCI.

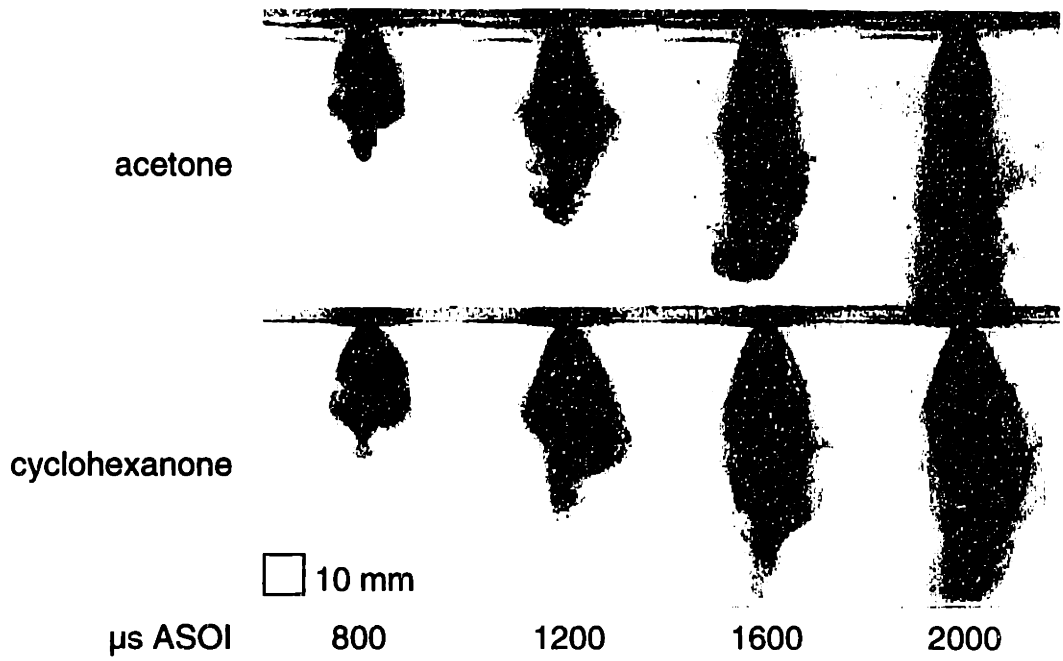

Figure 3.38: Comparison of acetone and cyclohexanone distributions in spray under conditions for heavy evaporation. Chrysler injector, P = 0.3 bar, T = 90 °C, SOI = 180 °ATDCI.

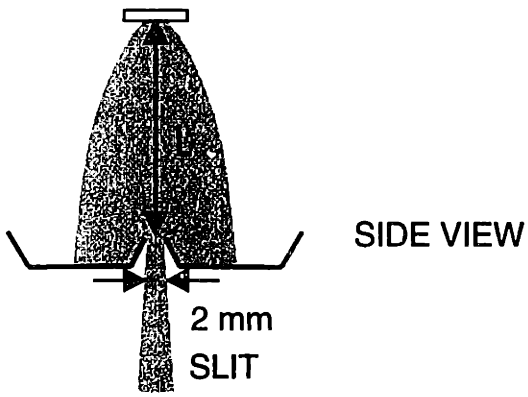

Figure 3.39: Schematic of spray slit structure. Side view. Slit is 2 mm with located at various positions L below the injector. Slit halves are 20 mm wide by 60 mm long and made of 0.2 mm thick sheet metal. Approximately to scale.

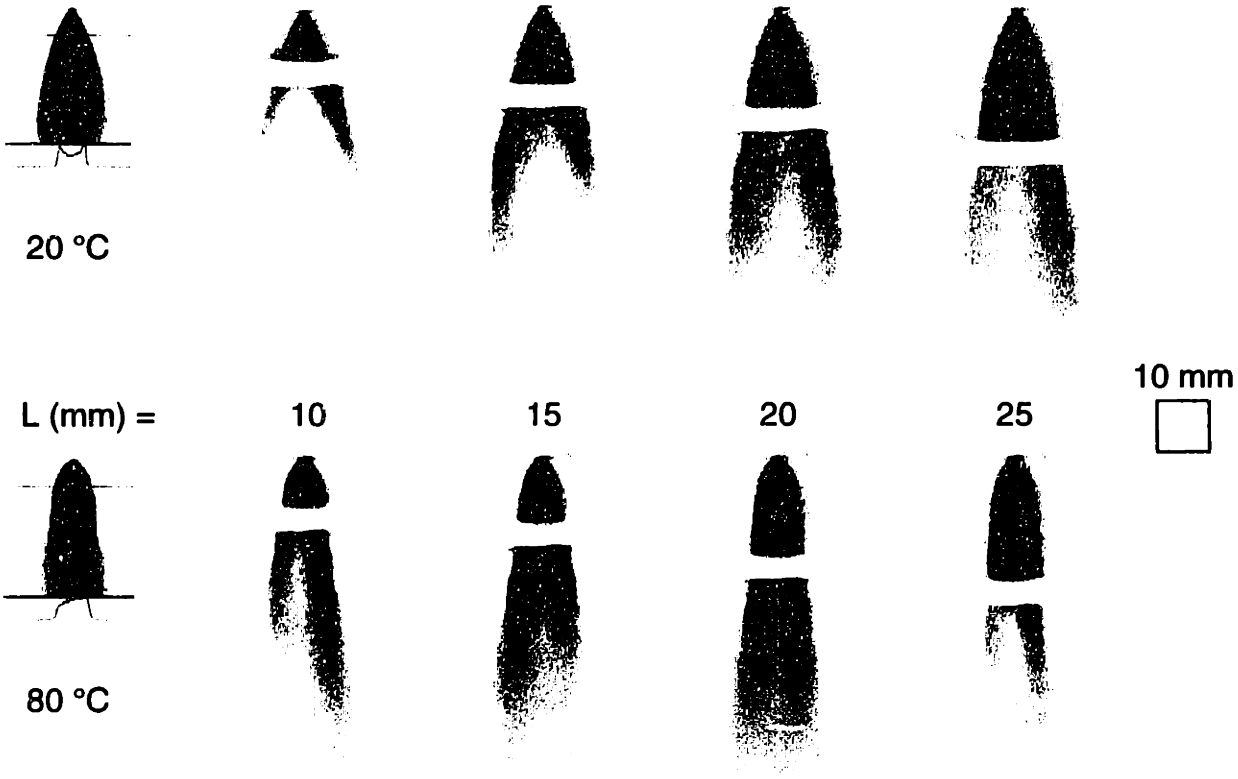

Figure 3.40: Spray slit images. Mie scattering, atmospheric ambient pressure, 2-methylbutane fluid, images taken 8 ms ASOI, 10 images averaged, 5 mm wide laser sheet. Frame to left is corresponding image from Fig. 3.20 at same scale.

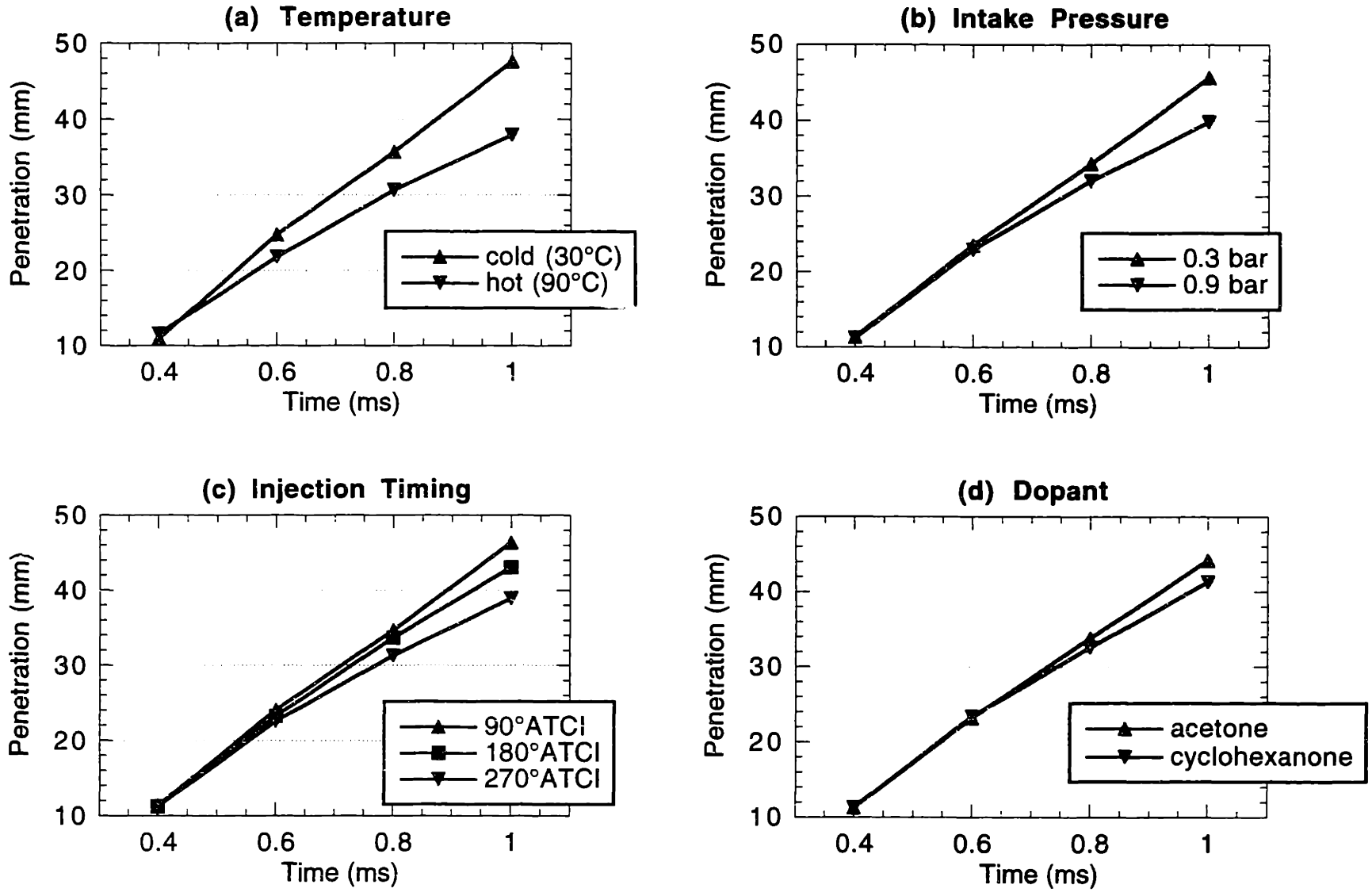

Figure 3.41: Spray penetration dependencies using visual method. From experiments described in Sec. 3.7. Each case is averaged over other parameters. Chrysler injector.

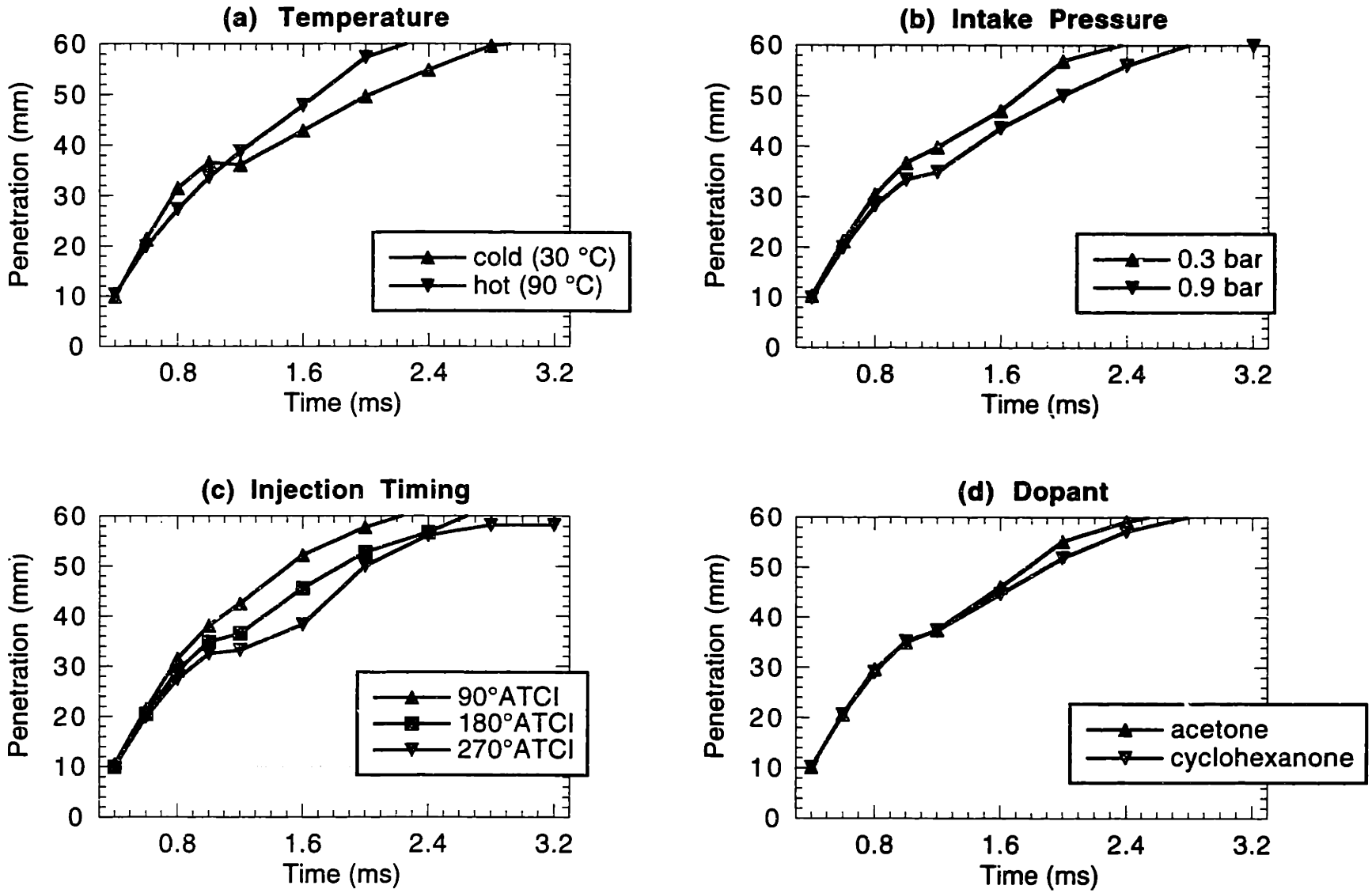

Figure 3.42: Spray penetration dependencies using 95%-intensity method. From experiments described in Sec. 3.7. Each case is averaged over other parameters. Chrysler injector.

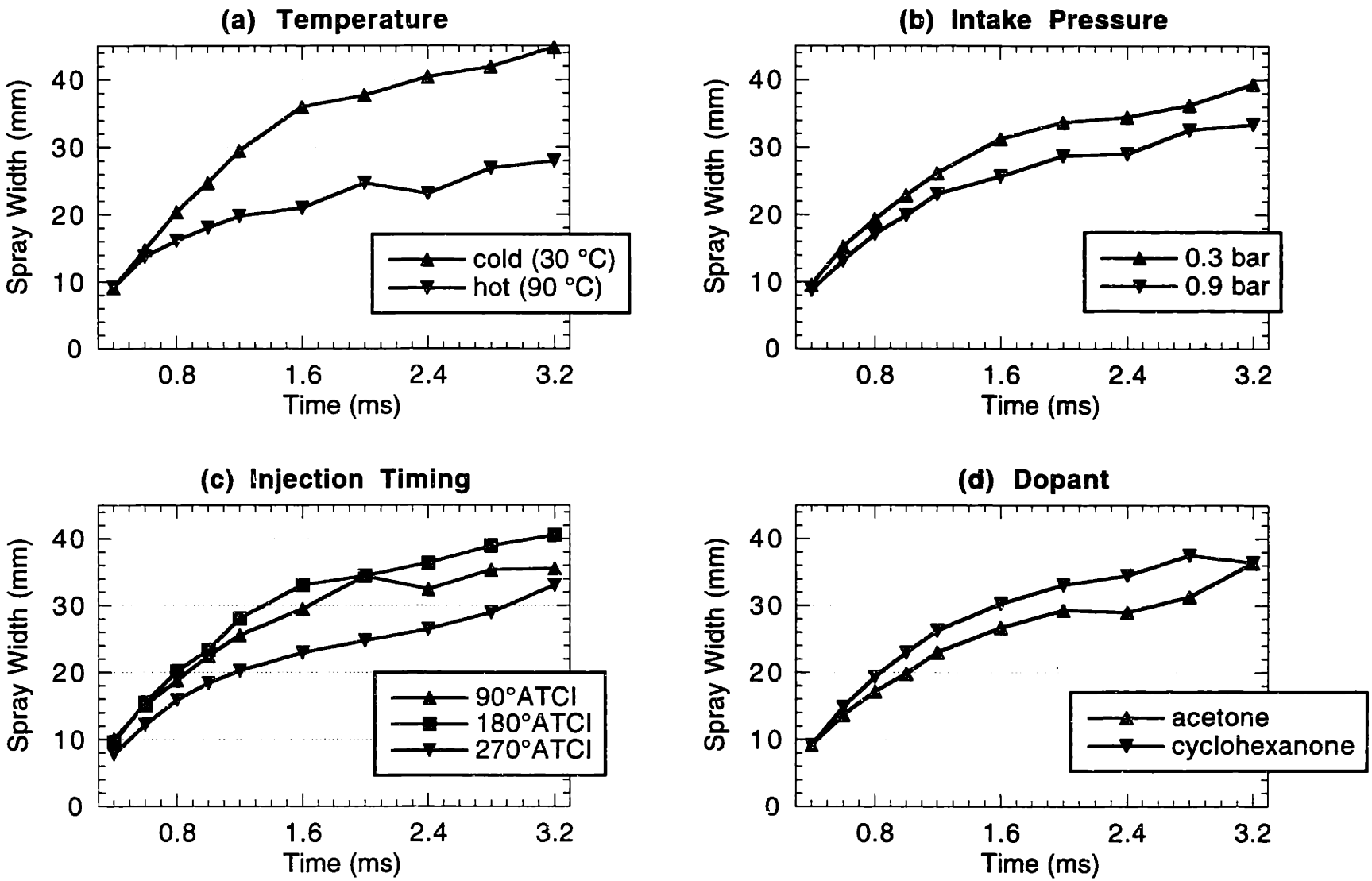

Figure 3.43: Spray width dependencies. From experiments described in Sec. 3.7. Each case is averaged over other parameters. Chrysler injector.

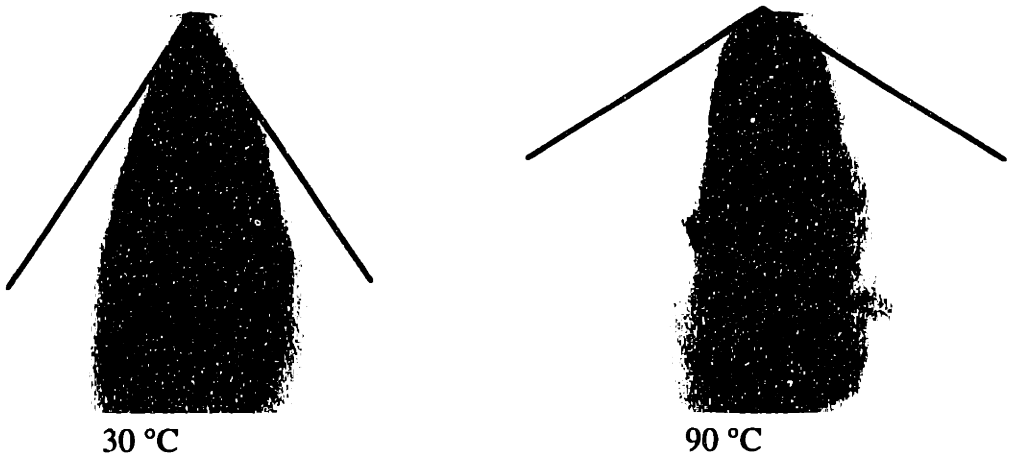

Figure 3.44: Illustration of increase in initial cone angle. Chrysler injector, 2-methylbutane, ambient pressure.

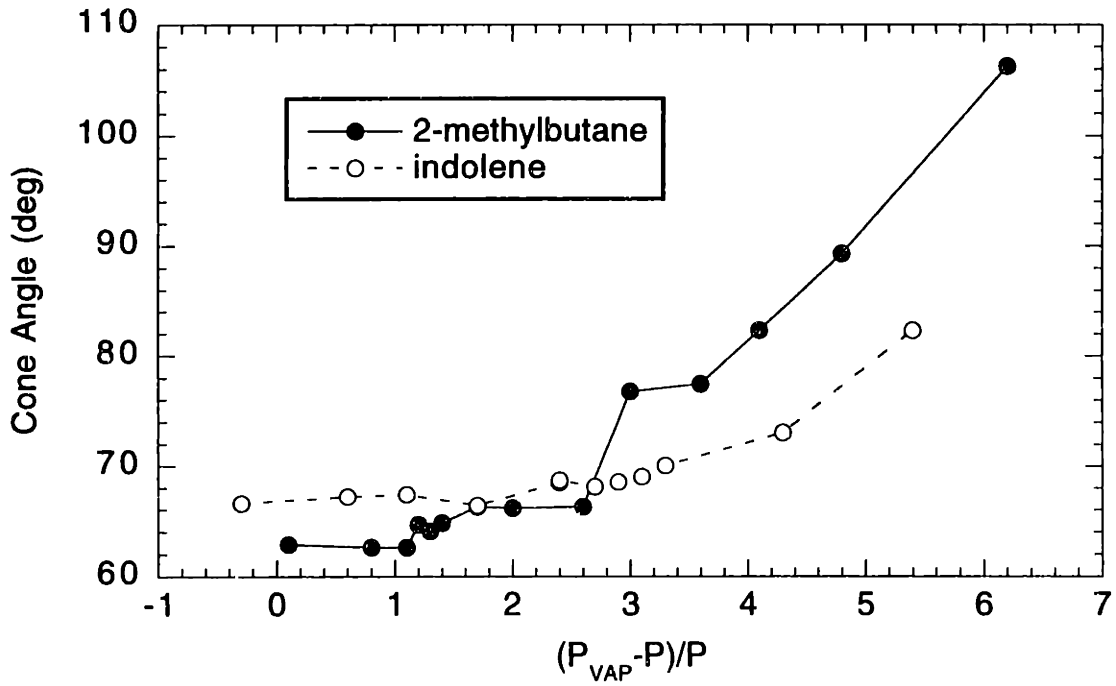

Figure 3.45: Spray initial cone angle as a function of excess vapor pressure. From images in Figs. 3.20 and 3.25. Chrysler injector, ambient pressure.

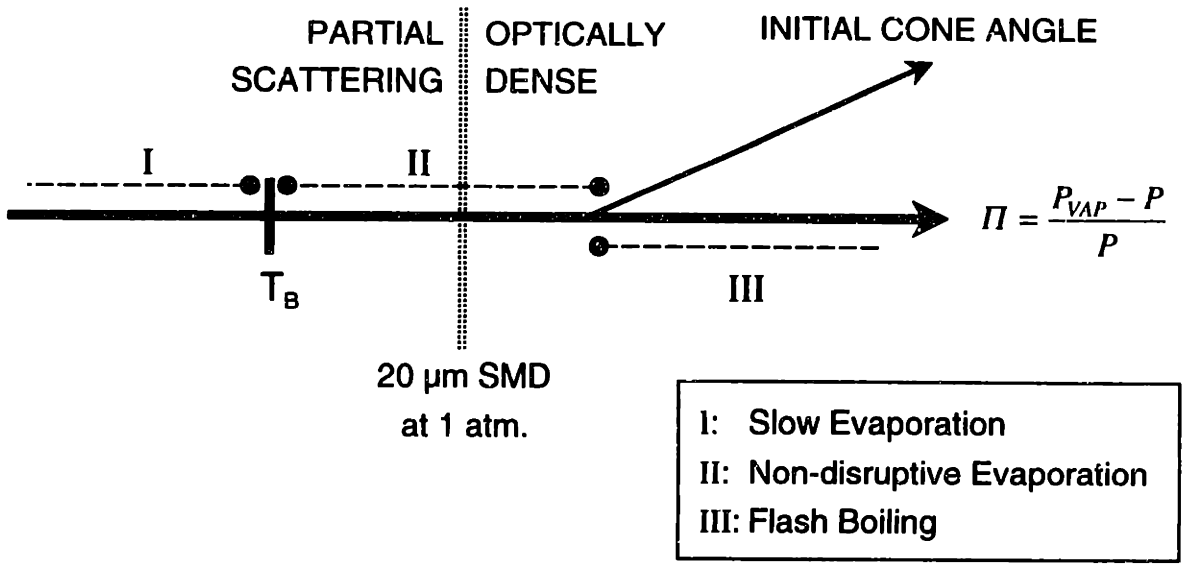

Figure 3.46: Schematic of spray regimes as a function of normalized excess vapor pressure as understood from imaging experiments.

CHAPTER 4

PDPA RESULTS

4.1 INTRODUCTION

Phase Doppler Particle Analysis (PDPA) experiments were included in this study to add information on the droplet diameter distributions of the sprays and to provide information regarding the spray structure through the velocity and droplet frequency. Significant changes in the droplet diameter with operating conditions were indicated by the imaging experiments. PDPA measurements can quantify these changes as a function of the operating conditions.

The main set of experiments described here were designed to characterize sprays realistic to engines from a wide range of early-injection operating conditions, over a reduced number of tests. Indolene was chosen as the fuel to keep volatility properties realistic. The only disadvantage to using indolene is that the engine windows became dirty more quickly with indolene than single-component fuels (i.e. iso-octane). Injection timing was limited to 180 °ATDCI (BDC), where the cylinder gas temperature and pressure are best defined and the effect of cylinder flows is minimized. This is important since the sprays are only measured at one tangential position, so distortions in the spray would result in measurement errors. The Chrysler injector is used because the Zexel injector used is has been replaced by updated designs. The temperatures and intake pressures of the six operating conditions tested are shown in Table 4.1. A low vaporization case (P = 0.9 bar, T = 30 °C) was chosen as reference. Two series leading to the high volatility case (P = 0.3 bar, T = 90 °C) one of increasing temperature and one of decreasing pressure were taken. Sprays at each of these operating conditions were measured with the PDPA at up to ten measurement locations. These locations are shown schematically in Figure 4.1. At 25 mm axially down from the injector, measurements were taken from 0 to 15 mm radially in 5 mm increments. Measurements at an axial position of 50 mm were taken at

redial positions from the centerline to either 20 or 25 mm, depending on the width of the spray. Only the two cold sprays were wide enough to justify measurements out to 25 mm. Each test point was repeated until proper settings were found and results were repeated. Most tests were limited to either 5000 validated samples or 60 seconds to limit the temperature rise of the engine throughout the test.

Diameter and velocity histograms for both 25 and 50 mm axial positions at 10 mm radial position are shown in Appendix 9. The droplet count is divided by the elapsed time over the test to yield a droplet rate. The upper limit of the diameter ranges easily includes the largest measured droplets. On the other hand, there often appears to be a significant number of droplets smaller than the lower limit of the diameter range. These very small droplets are not very significant, since they contain a small fraction of the total liquid volume. At both axial positions, the mean droplet velocity reaches its peak at a radius of about 10 mm. The upper velocity range of the two used (-2.0 to 47.9 m/s) encompasses the droplets observed very well. At larger radii, when the mean velocity decreases, enough droplets have negative velocities that the lower range is more effective (typically –4.8 to 28.3 m/s). In general, the diameter histograms are better behaved at the larger diameters. There is often a dip at 10 μm and a noisy signal below that value. The cause of the dip at 10 μm could not be determined. Re-alignment of the optics could sometimes reduce it, but no systematic cure could be found.

As shown in the following sections, the spatial and temporal distributions of the data were analyzed, along with correlations of the diameter.

4.2 Scattering Error

Initial analysis of the PDPA data conflicted with the images on the internal structure of the hot sprays (see Sec. 4.3.3). In order to determine the cause of this discrepancy, the tests shown in this section were performed to show that the PDPA data are affected by unintended

light scattering. This limitation of the diagnostic is discussed here so that the results can be properly analyzed.

A schematic of the three measurement locations compared in this test are shown in Figure 4.2. The circle represents a horizontal cross-section of the spray. The near cylinder wall is shown for orientation. The solid lines represent the laser beams approaching the measurement point. The dashed lines represent the scattered light leaving the measurement point. All three test points were at a radial location of 10 mm, but different tangential locations. Case A represents the strategy generally used. This measurement point is at the farthest location inside the combustion chamber, where the lasers and scattered light travel the minimum distance through the spray. In Case B, the laser beams pass through the spray before reaching the measurement point. In Case C, the scattered light passes through the spray on the way to the detector. A spray at low pressure (0.3 bar) and intermediate temperature (60 °C) was measured at these three locations. Droplet frequency as a function of time after start of injection is plotted for these cases in Figure 4.3. Case A appears much like all tests at this location and much as expected. The droplet measurement frequency is high and relatively uniform throughout the injection. Both of the other cases, on the other hand, exhibit very low droplet counts during the injection. The initial rise and the decay after injection are similar, but during the spray, the frequency is cut by around 95%. Apparently, the spray interferes with both the laser beams and the scattered light, making coherent measurements nearly impossible. The first few droplets passing the measurement point are recorded until the spray develops sufficiently. Successful measurement is restored after the injector closes and the spray dissipates. Failure of the PDPA system should not be surprising considering the high light extinction through these sprays shown in Sec. 3.2.

This error due to scattering is important for measurements of the interior of the spray. For measurements on the axis of the injector, both the laser beams and the scattered light must pass through the spray. In fact, the droplet frequency profiles for interior points (see Sec. 4.3.3)

look much like the plots of Cases B and C in Fig. 4.3. This means that there may be droplets in the interior of the sprays, which are not being detected. If the scattering is causing droplets to be missed during injection, the averaged properties will be affected. The implication for each property is discussed in the corresponding sub-section of the temporal distributions.

4.3 Temporal Distributions

4.3.1 Diameter

The external input to the PDPA was used to measure the time since the start of injection in order to study the temporal distributions of the spray properties. The time information is used for separating pre-spray and post-spray effects from the fully developed spray. This is also important for interpreting the possible effects of a bias introduced by the scattering error described in Sec. 4.2. The data is separated by averaging over short time bins (375 μs).

A pair of sample temporal distributions of mean droplet diameter is plotted in Figure 4.4. These samples are 25 and 50 mm axially and 10 mm radially from a spray at high pressure (0.9 bar) and high temperature (90 °C). These profiles are representative of the typical test. The Sauter mean diameter (SMD) is calculated over 375 μs bins. The injection time of 7.5 ms is shown on the plot. Overall, the SMD shows little variation with time. When the droplet rate is high, the SMD is very consistent. In this case, the high droplet rate is during the injection, where the SMD is nearly constant. In the pre-spray and post-spray, when the droplet rate is low, the SMD profile exhibits significant scatter. The pre-spray generally shows a slightly lower SMD (its poorer atomization arises from a wider diameter distribution including much larger droplets).

A bias in mean diameters averaged over the entire spray resulting from scattering errors would be minor due to the consistency of the SMD with time. A significant scattering error would bias the average toward the value immediately after injection. Since the value after injection is very similar to the value during injection, however, the error would be minor.

4.3.2 Velocity

In a manner very similar to that described in the previous section for mean droplet size, the average droplet velocity as a function of time was calculated. As mentioned before, the velocities mentioned here are the axial component of the droplet velocity. Although some of the droplets may have significant radial or tangential velocities, the spray primarily travels axially. Temporal distributions of velocity are plotted in Figure 4.5 for the same tests used in Fig. 4.4 for the mean diameter. These profiles show a relatively constant velocity throughout injection with a sharp decrease after the end of injection. The constant average velocity during injection is similar in all tests. The magnitude of the decrease after injection varies significantly between tests and measurement locations. The occurrence of this velocity decrease is expected as the spray momentum dissipates. The velocity should decay towards zero. This observation is consistent with the velocity plots, but the averages generally become very noisy before coming close to zero. This is reasonable since if the velocity were zero no droplets would pass through the measurement point. Also, there may be some upward biasing when the average is low since more of the measurements will be falling below the velocity range. Of the measurements that show the decrease, the measurement locations with the highest velocity during injection show the greatest decrease, which is not surprising considering that they have the farthest to fall.

Errors due to scattering will likely cause a decrease in average velocity, since scattering error would bias the average to the velocity shortly after injection. Unlike with the SMD, the velocity shows a different value after injection than during injection. The decrease in velocity after injection would then bias the average velocity downward.

4.3.3 Droplet Frequency

The droplet frequency as a function of time was calculated to show the spray structure. The droplet frequency is simply the number of droplets recorded in a certain time bin divided by the number of injections and the size of the bin. Ideally, measurements in the core of the spray,

during injection, would show whether the spray was hollow or not. Calculations of the droplet frequency are shown in Figure 4.6 for the low-volatility case (0.9 bar, 30 °C). For comparison, the high-volatility case (0.3 bar, 90 °C) is shown in Figure 4.7. The data are plotted as profiles of droplet frequency, expressed in counts per millisecond, as a function of time since the start of injection for each of the measurement locations. The upper plots show measurements from 25 mm below the injector. In both cases, the majority of the droplets are measured at 10 mm radially, near where the images suggest the spray sheet is located. These profiles show a relatively high rate of droplet measurements throughout the injection (2.7 or 7.5 ms), with a quick decay to zero after injection ends. The outermost profiles (R = 15 mm) show a small peak in droplet frequency initially with a lower value through the remainder of injection. The initial peak is more pronounced under cold conditions. This initial peak may be explained by the opening transient of the injector, in which the cone angle initially overshoots the equilibrium value. During this cone angle overshoot, more droplets are thrown out to the R = 15 mm location.

The R = 5 mm profile, for both conditions, shows a small peak in droplet frequency at the beginning of injection, a low count during injection, and a large peak after injection. The centerline profile is typically a more radical version of the R = 5 mm profile. Initial analysis of these profiles suggested that they were consistent with the hollow-cone spray structure. For the cold case (Fig. 4.6) this observation is consistent with the imaging results. The low droplet count in the core of the spray is consistent with the hollow-cone structure. On the other hand, these profiles conflict with the imaging data for the hot case (Fig. 4.7). This discrepancy prompted the scattering studies in Secs. 3.2 and 4.2. These tests suggest that the PDPA cannot detect droplets in the core of the spray. In addition, aspects of the cold profiles suggest that the profiles are shaped more by the scattering error than the actual spray structure. First, there is often a dip in the 10-mm profile at the time corresponding to the peak in the 15-mm profile. This suggests that

the presence of droplets at 15 mm prevents measurements at 10 mm. Second, the high rate of increase in droplet frequency in the centerline and 5 mm profiles seems physically unrealistic.

The lower plot in each figure shows the droplet frequency profiles at 50 mm below the injector. These plots show similar behavior to the 25-mm plots. In the cold case (Fig. 4.6), the spray has widened significantly. The high profiles, associated with the spray sheet, are seen at 15 mm as well as 10 mm. The outside profiles, with an initial peak and lower value through the rest of the injection, are seen at 20 and 25 mm. Again, the centerline and 5 mm profiles show a small initial and large final peak in droplet frequency with a low value during injection. The hot case (Fig. 4.7), on the other hand, does not widen significantly, which agrees with the behavior seen in the images. Except for the lower values, the profiles appear much as in the upstream case (25 mm). Two explanations for the lower droplet frequencies seem possible. First, the majority of the droplets may have spread out slightly and are falling between the 10 and 15-mm measurement points. Second, under these conditions, a significant fraction of the droplets may have evaporated.

The extent to which the scattering error affects the results in each location is unclear. The main effect would be to decrease the average droplet frequency in the interior points.

4.4 Spatial Distributions

4.4.1 Diameter Profiles

Mean diameters were calculated for each measurement point in two ways. First, the PDPA software calculates mean diameters for all of the droplets measured. The values used were averaged over two repeated tests. Second, because of the potential for biasing of these results by the scattering error (see Secs. 4.2 and 4.3.1), mean diameters were calculated using only the data collected from the fully developed spray. Neglecting any scattering error, the first measurement is useful to the engine designer since it includes all of the droplets produced by the

injector. The second measurement is more useful for describing the structure of the spray. By concentrating on the steady-state spray, this measurement is sensitive to spatial variations without temporal variations confusing the interpretation. Although the droplets measured during the steady-state spray may only be a small fraction of those present at some locations, the properties of those that are measured should be valid. The steady-state average is noisy in some cases since few droplets were measured during the steady-state portion of the spray.

Sauter mean diameters (SMD) averaging over both ranges are shown in Figure 4.8 for a range of temperature at 0.3 bar intake pressure and in Figure 4.9 for a range of intake pressures for 90 °C. The upper plots are at 25 mm below the injector, and the lower plots 50 mm below. The solid symbols are averaged over all the data, and the open symbols are averaged over the steady-state spray. In general, the profiles show a slight increase in SMD with increasing radius. There seems to be a repeatable structure in the low-pressure sprays (Fig. 4.8) at Z = 25 mm, in which the SMD initially decreases from the centerline to 5 mm before increasing gradually. This does not appear to be due to the pre-spray, since the SMD from the fully developed spray shows the same effect. The decrease in SMD with increasing temperature or decreasing pressure is discussed in detail in Sec. 4.6. The plots here, though, show that these decreases are consistent throughout the spray. In addition, comparing the upper and lower plots, the downstream SMD is significantly larger. This effect is studied in Sec. 4.6.2.

The fact that there is no systematic difference between the two methods of calculating the average suggests that any scattering error has little effect on the SMD. Since the SMD is relatively consistent throughout space and time (see Sec. 4.3.1), any biasing by the scattering can have little effect.

4.4.2 Velocity Profiles

Spatial profiles of mean axial velocity were calculated in the manner described above for the SMD. These results are plotted in Figures 4.10 for increasing temperature at 0.3 bar and in

4.11 for decreasing pressure for 90 °C. The upper plots are at 25 mm below the injector, and the lower plots are at 50 mm below. The solid symbols are averaged over all the data, and the open symbols are averaged over the steady-state spray. Unlike with the SMD, these plots show no organized change with operating conditions. The solid symbols in the lower plots (50 mm below injector) are especially consistent. This consistency in velocity was somewhat surprising considering the changes in spray structure and penetration rates observed with the imaging experiments. At 25 mm below the injector, the peak velocity is at 10 mm radius, which roughly coincides with the location of the spray sheet. Inside this point, the velocity drops slowly, while outside this point it falls off quickly. Both the open and closed symbols show this behavior. At 50 mm below the injector, however, the open and closed symbols show very different behavior inside 10 mm radius. The solid symbols, averaging over all droplets, show a very flat velocity profile near the centerline with a slight peak at 10 mm and a nearly linear decrease outside that distance. The open symbols, averaging over droplets only during the steady-state portion of the spray, at 10 mm radius and beyond. Inside 10 mm, though, these profiles continue to increase towards the centerline. There is substantial noise in these average velocities, due to the small number of droplets measured at these points from the fully developed spray. The open symbols are expected to be higher since most of the droplets excluded from this average are from the post-spray in which the velocities are decreasing rapidly (see Sec. 4.3.2). This effect is exaggerated near the centerline where the majority of the droplets are measured during the post-spray.

4.4.3 Volume Flux Profiles

Spatial profiles of liquid volume flux have been calculated as well. The volume flux is calculated by the PDPA software by summing the volume of all the droplets measured and then dividing by the elapsed time and the area of the probe volume normal to the direction of measurement. The accuracy of the volume flux calculation is limited by its dependence on the

validation fraction. Since the validation fraction varied with operating conditions and with each re-alignment, there is significant uncertainty in these results. However, these results are useful for checking consistency. Figure 4.12 shows the spatial profiles of volume flux as function of temperature at 0.3 bar intake pressure, and Figure 4.13 shows them as a function of pressure at 90 °C. The upper plots are at 25 mm below the injector, and the lower plots are at 50 mm below. Averages of only the droplets measured during the steady-state injection were not made since the temporal profiles in Sec. 4.3.3 better show this dependence. The upper plot in Fig 4.12 shows very consistent profiles with a strong peak at a radius of 10 mm. This agrees with the spray images, which show the spray sheet near 10 mm. The lower plot, at 50 mm below the injector, is not nearly as consistent. The profile at 90 °C is consistently lower than the others possibly due to evaporation. The profile at 30 °C, on the other hand, shows much higher values at higher radii. The shift to higher radii agrees with the wide images of the cold spray. The higher overall flow is not realistic, and could be explained by higher droplet validation with the larger droplets. In the upper plot of Fig. 13, shape of profiles is similar, with significant peaks at 10 mm. The height of the peak roughly agrees with the amount of fuel injected as well. As the load increases, a larger pulse width is used to deliver more fuel. The high-pressure profile is too high, though, relatively. This, again, may be due to the higher validation rate with larger droplets. The lower plot, at 50 mm below the injector, shows a similar effect at all radii.

In general, these plots show that the spray is tightly distributed around the spray sheet at 25 mm, while by 50 mm the distributions are much more spread out and much less certain.

4.5 Diameter-Velocity Correlation

One of the typical cross-correlations studied for PDPA spray data is the diameter-velocity correlation. Since the droplets start with nearly the same velocity, their velocity at the measurement point depends on drag. Larger droplets have a larger mass per amount of drag they experience, so the large droplets are observed travelling faster. A positive correlation, however,

is not always observed for the hollow-cone spray. Figure 4.14 shows diameter-velocity correlations for the cold high-pressure spray (30 °C, 0.9 bar). The upper plot shows data from 25 mm below the injector and the lower plot from 50 mm below. These profiles were calculated as the average velocity for the droplets in each 1 μm size bin. Due to the scatter in the profiles, a linear fit for each is plotted as well. The height of each profile is related to its overall average velocity (see Sec. 4.4.2), but the slope of the profiles is of interest here. Starting at the periphery of the spray (r = 15 mm) at 25 mm, a positive correlation is shown. This is true at 10 mm as well, but at 5 mm the correlation is very flat. At the centerline, the correlation is actually negative. In the lower plot, at 50 mm below the injector, a similar trend is seen with 15, 20, and 25-mm profiles showing a positive trend, and 0, 5, and 10-mm showing flat profiles. At both axial distances, the correlation changes character near the spray sheet. On or outside the spray sheet, a positive diameter-velocity correlation is observed. This is the typical situation in which drag by the originally stagnant surrounding air slows the smaller droplets more. Inside the spray sheet, the flat profile is observed. The droplets observed inside the spray sheet were mostly entrained there by the flows induced by the spray. Most of the droplet observations inside the spray sheet, though, occur after the end of injeciton. After injection has stopped, the gas flows that have been established draw the droplets to the core of the spray cone. This mixing process may tend to equalize the velocities of the larger and smaller droplets.

4.6 Droplet Diameter

4.6.1 Imaging Diameter Estimation

In this and the following sections, variations in the PDPA droplet diameter measurements with operating conditions are considered. This section focuses on comparing the changes in droplet diameter measurements made by the PDPA with estimates of SMD via Mie scattering and PLIF images (also see Sec. 3.1.3). The use of the image comparison to estimate changes in

the droplet diameter depends on the fact that the scattering intensity is inversely proportional to the droplet diameter for a fixed fluid volume. The PLIF intensity, on the other hand, is proportional to the dopant mass. The droplet diameter is proportional to the ratio of the liquid volume (V) to its surface area (A). The mean diameter that represents this is the Sauter mean diameter.

$$SMD \propto \frac{V}{A} \tag{4.1}$$

Assuming that the fluorescing compound follows the droplets, the PLIF image is a measure of the fuel volume in the laser sheet, correcting for changes in the fluorescence yield.

$$V \propto \frac{I_L}{\phi} \tag{4.2}$$

where I_L is the intensity of the laser sheet and ϕ is the fluorescence yield. The assumption that the fluorescent compound follows the droplets should be very good since indolene was used for tests. The correction for fluorescence yield of indolene, though, may be somewhat inaccurate since the values were measured for gaseous samples [51]. The Mie scattering intensity is then proportional to the total droplet surface area, as described in Appendix 5. Combining Eqs. 4.1 and 4.2 and substituting for the droplet surface area results in a single equation to estimate changes in the SMD.

$$\frac{SMD_a}{SMD_b} = \frac{I_{MIE,b}}{I_{MIE,a}}\left(\frac{I_{LIF,a}}{I_{LIF,b}}\frac{\phi_b}{\phi_a}\right) \tag{4.3}$$

To make this comparison, time-series of PLIF and Mie scattering images were taken at the three low-pressure conditions used for the PDPA measurements (0.3 bar, 30, 60, and 90 °C). Assuming that the flow rate is constant, the integrated intensity of the images in the time series should increase linearly. To use this fact to combine the information on the images, linear fits were made to the image intensities. The ratios of the slopes of these fits were used as the ratios of intensity in Eq. 4.3. Figure 4.15 compares the normalized mean diameters from these results

with those from the PDPA results. Error bars on the PDPA data represent the scatter of the different measurement locations. Agreement between 30 and 60 °C is good, however more experiments are needed to determine if the agreement is consistently this good. On the other hand, the imaging estimation appears to over-predict the diameter reduction at 90 °C. By 90 °C, multiple scattering becomes an issue (see Sec. 3.2). Since both the Mie scattering and PLIF will experience laser sheet scattering, the effect should cancel out in the calculation. However, since the Mie scattering has a directional dependence, unlike the fluorescence, any multiple scattering should have a greater effect on the scattering image. This is consistent with the over-prediction of the diameter reduction. In addition, the PDPA is more likely to miss small droplets, thereby biasing the SMD it measures upward as it falls.

From the results presented here, the imaging diameter estimation appears to work well as long as the measurement is made under conditions in which optical density is not too high.

4.6.2 Downstream Diameter Increase

A cursory study of Figs. 4.8 and 4.9 shows that the SMD at the downstream location (50 mm) is consistently higher that at the upstream location (25 mm). This increase in mean diameter with axial distance is obvious at most every measurement point. Two hypotheses were given for this behavior. First, the smaller droplets may be evaporating completely (or below the range of the PDPA), resulting in a larger mean diameter. Second, droplets may be coalescing. Two droplets combining into a larger droplet will increase the mean diameter as well. If evaporation is the mechanism, a reduction in the number of small droplets measured should decrease downstream. The plots in Appendix 9 show the measurement rate over the droplet diameter range for each operating condition at both the upstream and downstream locations. These profiles were taken at a radius of 10 mm, on the spray sheet. In most cases, a higher rate of large droplets and a lower rate of small droplets are observed at the downstream position. However, since the fraction of the overall spray that these represent is not known, whether the

number of smaller droplets decreased or the number of larger droplets increased cannot be determined. Knowing only that the ratio changes provides no information beyond the original observation that the mean diameter increases. One case that provides some insight is the high-volatility case (0.3 bar, 90 °C). This case shows a drastic decrease in the overall droplet measurement rate. In the cold cases this could be explained by spray spreading beyond the 10 mm radius, but this is the narrowest spray of the set. If the measurement rate decrease is assumed to be due to evaporation, the fact that the rate above 15 μm increases, becomes telling. If the total number of droplets is decreasing but the number of larger drops is increasing, that can only be explained by coalescence.

To help determine the cause of this mean diameter increase, a correlation between the diameter increase and volatility was sought. If the diameter increase is due to evaporation, the extent to which it is observed should depend on the superheat. To check this, the ratio of downstream to upstream SMDs was plotted against the normalized excess vapor pressure in Figure 4.16. The six indolene cases were plotted according to their pressure to identify any separate temperature or pressure dependencies. These points, though, show no obvious correlation. The round point is from an additional experiment using Stoddard solvent. Even though the Stoddard solvent has a small vapor pressure, it exhibits a substantial increase in SMD. This data suggests that evaporation is not the main factor in the diameter increase.

This observation is supported by the modeling described in Chapter 5. The model has the coalescence sub-model deactivated. Any change in the mean diameter, therefore, is due to evaporation. The model does not show a diameter increase, but rather a substantial decrease. This departure from conventional understanding results from the entrainment of the smaller droplets to the core of the spray where the lower temperatures and higher vapor fractions slows their evaporation.

These observations suggest that coalescence, not evaporation, is the dominant mechanism by which the mean droplet diameter increases downstream in these sprays.

4.6.3 Temperature Correlation

The primary check of the droplet diameter data was to compare it with published correlations for against temperature and pressure for pressure-swirl injectors. The correlation used as the basis for this comparison is Eq. 6.17 from Lefebvre [47].

$$SMD = A\sigma^{0.25}\mu_L^{0.25}\rho_L^{0.125}d_o^{0.5}\rho_A^{-0.25}\Delta P_L^{-0.375} \tag{4.4}$$

The ambient density dependency in this correlation is intended for a high-pressure range (> 4 bar). For a low pressure range, a significantly different ambient pressure dependence is suggested.

$$SMD \propto P_A^{0.27} \tag{4.5}$$

Since the ambient pressure affects the spray through the ambient density, this dependence was assigned to the density. Using the ideal gas law, the ambient density was divided into the ambient pressure and temperature If the ambient gas composition changes substantially, a correction for the gas constant must be added. However, since the change in the gas constant of the charge changes little with residual [52], this was neglected here.

$$SMD = A\sigma^{0.25}\mu_L^{0.25}\rho_L^{0.125}d_o^{0.5}\left(\frac{P_A}{T_A}\right)^{0.27}\Delta P_L^{-0.375} \tag{4.6}$$

For a variation in temperature, this can be simplified to the following.

$$SMD \propto \sigma^{0.25}\mu_L^{0.25}\rho_L^{0.125}T_A^{-0.27} \tag{4.7}$$

The changes in fuel properties with temperature are calculated from correlations [53]. The ambient temperature in the firing engine is not well known. As intake pressure decreases, the charge temperature increases due to higher levels of residual gas. This change was estimated using a cycle simulation model. The charge temperature will also change with the combustion chamber wall temperature, which is assumed to be equal to the measured head temperature. The charge temperature was estimated using the following relationship.

$$T_A = 330 - \frac{P}{1000} + \frac{T}{3} \tag{4.8}$$

Here, intake pressure, P, is in Pa, the temperatures are in Kelvin. The resulting charge temperatures range from 340 K (0.9 bar, 30 °C) to 420 K (0.3 bar, 90 °C).

The heavy line in Figure 4.17 shows this correlation normalized at 30 °C. It shows a roughly 20% reduction in SMD over the range of temperatures used here. The large point represents the size reduction shown by the PDPA at 0.9 bar intake pressure. The error bars show the scatter between the different measurement locations. At these low volatility conditions, the data and correlation agree well. The small circles represent the PDPA data at 0.3 bar intake pressure. The value for each measurement point is shown by a separate trace. At 60 °C, the data and correlation agree. As the temperature increases to 90 °C, the PDPA diameter measurements fall significantly below the values expected from the correlation.

The four cases with dashed lines represent measurement points that showed a different behavior than the rest in both Fig. 4.17 and Fig. 4.18 from the next section. The long-dashed lines are from the widest points at both axial distances. Their unusual behavior is likely due to the fact that droplets measured here were not entrained inward with the bulk of the spray. Similarly, the short dashed lines represent measurement points inside the spray cone at 25 mm below the injector. Droplets reach these points only by having been entrained well within the spray cone.

4.6.4 Pressure Correlation

This section compares the PDPA measured droplet diameters to a pressure correlation, in a manner similar to the previous section. The correlation used is Eq. 4.3 simplified to contain only the pressure dependent terms.

$$SMD \propto \left(\frac{P_A}{T_A}\right)^{0.27} \Delta P_L^{-0.375} \tag{4.9}$$

Here, the ambient pressure, P_A, is assumed to be the intake pressure, the ambient temperature, T_A, is estimated using Eq. 4. , and the pressure across the injector, ΔP_L, is the difference between the fuel pressure (5 MPa), and the ambient pressure.

Figure 4.18 compares this correlation with the mean droplet size measured with the PDPA using indolene. The large point represents the size reduction shown by the PDPA at 30 °C. At these low volatility conditions, the data and correlation agree well. The small points represent the PDPA data at 90 °C. The value for each measurement point is shown by a separate trace. As described in the previous section, the dashed lines represent cases in which the behavior differs from the rest, likely due to influences of entrainment. At decreased ambient pressure, both 0.6 and 0.3 bar, the PDPA measurements fall significantly below the correlation. The depression in SMD is observed at high-volatility conditions with both the temperature and pressure correlations suggesting an additional breakup mechanism.

4.6.5 Volatility-Induced Breakup

The droplet size discrepancy shown in the two previous sections at high temperature and low pressure suggests that an additional breakup mechanism exists. The correlations agree with the data at low-volatility conditions. The discrepancies, however, appear at high-volatility conditions. This supports the initial theory of a flash-boiling breakup mechanism. To determine if this is the case, the behavior of the difference between PDPA results and the correlation was studied. This difference was defined as the ratio between the SMD reduction shown by the PDPA and the reduction predicted by the correlation.

$$\Psi = \frac{\left(\left. \frac{SMD}{SMD_0} \right|_{PDPA} \right)}{\left(\left. \frac{SMD}{SMD_0} \right|_{Corr} \right)} \tag{4.10}$$

Assuming the correlation correctly predicts changes in SMD due to fluid property and ambient density changes, this value shows the change in SMD due to any additional effects, presumably flash boiling. This property will have a value of unity when the PDPA data and correlation agree and will decrease below that if an addition breakup mechanism is present. The correlation used was Eq. 4.6. To examine any volatility dependence, Ψ was then plotted against the normalized excess vapor pressure, Π, in Figure 4.19.

$$\Pi = \frac{P_{VAP} - P}{P} \tag{4.11}$$

Here, P_{VAP} is the vapor pressure of the fuel, and P is the ambient pressure. The indolene data is the same from the previous sections, plus six extra data points in the $\Pi = 4$ to14 range. The 2-methylbutane and iso-octane data were taken specifically to verify this relationship. All the data shown was taken 50 mm below the injector. The normalizing point in this plot (SMD_0 in Eq. 4.10) is indolene at 0.9 bar and 30 °C. The 2-methylbutane data shows the structure most clearly. Up to about $\Pi = 2.5$, the data and correlation agree within about 3%. Above that point, Ψ falls off sharply. This plot, with its breakpoint around $\Pi = 2.5$, bears a striking resemblance to the behavior of the initial cone angle (Sec. 3.9.3), suggesting that these two effects are due to the same mechanism. Similarly, the indolene results show agreement up to about $\Pi = 3.5$, followed by a drop-off. The indolene initial cone angle results also show the corresponding behavior. The shallower slope for the indolene is likely due to its multi-component makeup. The vapor pressure of indolene will decrease as the lighter ends evaporate.

The behavior of the difference in SMD between the PDPA results and the correlations, supports the theory that a flash-boiling droplet breakup mechanism exists. Beyond a certain level of superheat, which is dependent on the fuel, flash boiling causes additional breakup of the droplets that is roughly proportional to the increase in superheat, as expressed by Π.

4.6.6 Initial Cone Angle Cross-Correlation

The behavior of the volatility-induced droplet diameter reduction mechanism described in the previous section was found to be very similar to the behavior of the increase in initial cone angle described in Sec. 3.9.3. Both characteristics were constant below about $\Pi = 2$ and above that were roughly proportional to Π. Since this suggested that the characteristics are related, a correlation was sought.

The SMD of the spray is known to be smaller for larger cone angle injectors. This behavior is shown in the following correlation for pressure-swirl injectors by Lefebvre [47].

$$SMD = 4.52\left(\frac{\sigma\mu_L^2}{\rho_A \Delta P_L^2}\right)^{0.25}(t\cos\theta)^{0.25} + 0.39\left(\frac{\sigma\rho_L}{\rho_A \Delta P_L}\right)^{0.25}(t\cos\theta)^{0.75} \tag{4.12}$$

where t is the liquid film thickness in the orifice and θ is the half cone angle, which were included as a simple geometric relationship for the liquid sheet thickness leaving the injector (t_s).

$$t_s = t\cos\theta \tag{4.13}$$

To determine which term in Eq. 4.12 is dominant, they were evaluated using t = 0.2 mm and values for indolene at P = 0.3 bar and T = 90 °C. Due to the low viscosity and high pressure differential under these conditions, the second term, which is a Weber number relationship, was a factor of 20 larger than the first term. Therefore, the following relationship was used to predict the decrease in droplet size due to the increase in initial cone angle.

$$\Psi_{CA} = \left(\frac{\cos\theta}{\cos\theta_0}\right)^{0.75} \tag{4.14}$$

This value was plotted along with the volatility induced size reduction (see Fig. 4.19) against the normalized excess vapor pressure (Π) in Figure 4.20. The agreement between these two values for both indolene and 2-methylbutane, suggests that the increase in initial cone angle is sufficient to explain the observed volatility-induced size reduction.

These results suggest the following line of reasoning. (1) The role of volatility in these sprays is to increase cone angle of the liquid sheet before breakup, likely through rapid vapor generation increasing the pressure in the core of the spray. (2) The increased cone angle causes the observed droplet size reduction, rather than by breakup of the droplets by internal boiling.

4.6.7 SMD Prediction

Along with the SMD correlation, the flash-boiling breakup mechanism described in the previous section can be used to predict the SMD. The correlation appears as follows.

$$SMD = A\sigma^{0.25}\mu_L^{0.25}\rho_L^{0.125}d_o^{0.5}\left(\frac{P_A}{T_A}\right)^{0.27}\Delta P_L^{-0.375} \tag{4.6}$$

Since the mechanism behind the volatility-induced droplet diameter reduction, as shown in Fig. 4.19, appears to be due to a complex relationship of vapor production, redirection of the liquid sheet, and the Weber number, a simple two part linear fit was chosen to avoid the added complexity.

$$\Psi = \begin{cases} 1 & \Pi \le 1.75 \\ 1 - a(\Pi - 1.75) & \Pi > 1.75 \end{cases} \tag{4.15}$$

Here, a is 0.018 for indolene and 0.052 for 2-methylbutane. The estimation used for the ambient temperature in the firing engine at BDC is as follows (using Pa, K; Sec. 4.6.3).

$$T_A = 330 - \frac{P}{1000} + \frac{T}{3} \tag{4.8}$$

Comparing this with the PDPA diameter measurements, a value for A in Eq. 4.6 can be calculated. Using an orifice diameter, d_o, of 0.46 mm, a value of 0.76 was found for A for SMD in μm and other values in MKS units. The overall result is the following.

$$SMD = 0.76\sigma^{0.25}\mu_L^{0.25}\rho_L^{0.125}d_o^{0.5}\Delta P_L^{-0.375}\left(\frac{P_A}{T_A}\right)^{0.27}\Psi \tag{4.16}$$

This relationship is plotted with the data in Fig. 4.19. They agree with an RMS error of 3.2%. The correlation was calibrated for the Chrysler injector 50 mm below the injector tip with 5 MPa fuel pressure.

4.7 CONCLUSIONS

The Phase Doppler particle analysis experiments described in this chapter show the behavior of the droplet diameter distribution with operating conditions and fuel volatility. They also provide insight into the spray structure through the spatial and temporal distributions of diameter, velocity, and droplet frequency.

In close agreement to published correlations under low-vaporization conditions, the mean diameter decreases with increasing fuel temperature and decreasing ambient density. An additional breakup mechanism is observed under flash boiling conditions. Beyond a certain level of superheat, the SMD reduction due to this mechanism decreases roughly linearly with the normalized excess vapor pressure. The increase in initial cone angle, observed from the imaging experiments (Sec. 3.9.3), is sufficient to explain this volatility-induced size reduction. This suggests that the vapor production increases the cone angle of the liquid sheet before breakup, thereby reducing the mean droplet size. Therefore, no breakup mechanism related to boiling inside the droplets is apparent in these results. A fit to the volatility-induced SMD reduction was then used with published correlations to predict the SMD.

Figure 4.21 shows an extension of the schematic (from Sec. 3.10) of the spray regimes as a function of normalized excess vapor pressure. The flash-boiling breakup mechanism has been added in parallel to the increase in initial cone angle, characterizing the flash-boiling regime. The point at which these effects become noticeable is about $\Pi = 2$.

In general, the spatial and temporal distributions appear much as expected, although some unexpected trends were observed. The droplet diameter showed consistent distributions with space and time. A smaller distribution was expected, though, in the core of the fully-developed

spray. The mean velocity shows a decrease after the end of injection and to the outside of the spray sheet, as expected. The velocity peak is at the spray sheet initially, but farther downstream the peak is closer to the injector axis. In addition, the velocity downstream is more evenly distributed, showing significant momentum transfer. However, the consistency of the mean velocity between the operating conditions was not expected, because of the changes in spray structure and penetration with operating conditions observed with the imaging experiments. The measurements of volume flux show the expected distributions. They peak at the spray sheet and increase with increasing load, and little change is seen with temperature. Additionally, the behavior of the diameter-velocity correlations and the explanation of the increase in mean diameter downstream reinforce the observation that the behavior of these sprays is different like single-orifice-type sprays.

Section 4.2 showed that light scattering caused a 95% reduction in the rate of droplet measurements when either the lasers or the scattered light pass through the bulk of the spray. This condition was necessary for measuring points in the interior the spray cone. This resulted in temporal droplet frequency plots for the interior locations, which have a low rate during the spray with a small peak before and a large peak after (see Sec. 4.3.3). This reduction of droplet measurements during the spray caused a bias in the average diameter and velocity measurement towards their values shortly after injection. Since the diameter temporal distribution was relatively constant, this causes little biasing. The mean velocity, on the other hand, was biased downward due to the decrease in velocity after injection (see Sec. 4.4.2). This error caused a decrease in the spatial volume flux profiles (Sec. 4.4.3) at the inner radii, but the extent of this error is not known.

The droplet diameter reductions measured by the PDPA, along with suggested vapor production, explain many of the structural changes observed in the images of Chapter 3. The modeling work in Chapter 5 uses these same effects to reproduce some of these structural changes.

Table 4.1: Operating conditions for PDPA tests.

		Temperature (°C)		
		30	60	90
Intake Pressure (bar)	0.3	X	X	X
	0.6			X
	0.9	X		X

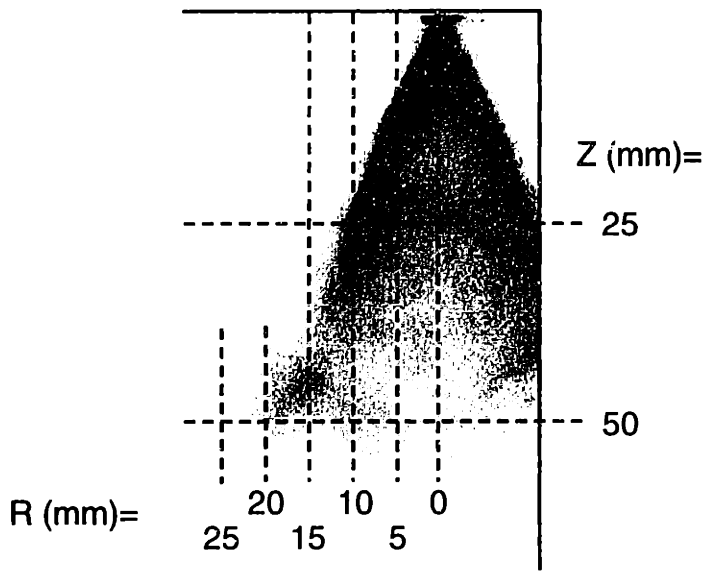

Figure 4.1: Measurement locations for PDPA measurements. Solid line to the right of the spray represents the near wall of the combustion chamber.

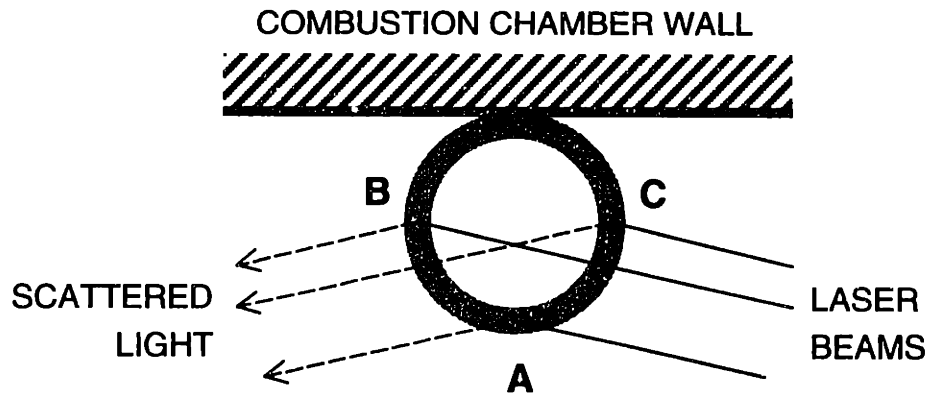

Figure 4.2: Schematic of symmetrically similar measurement locations.

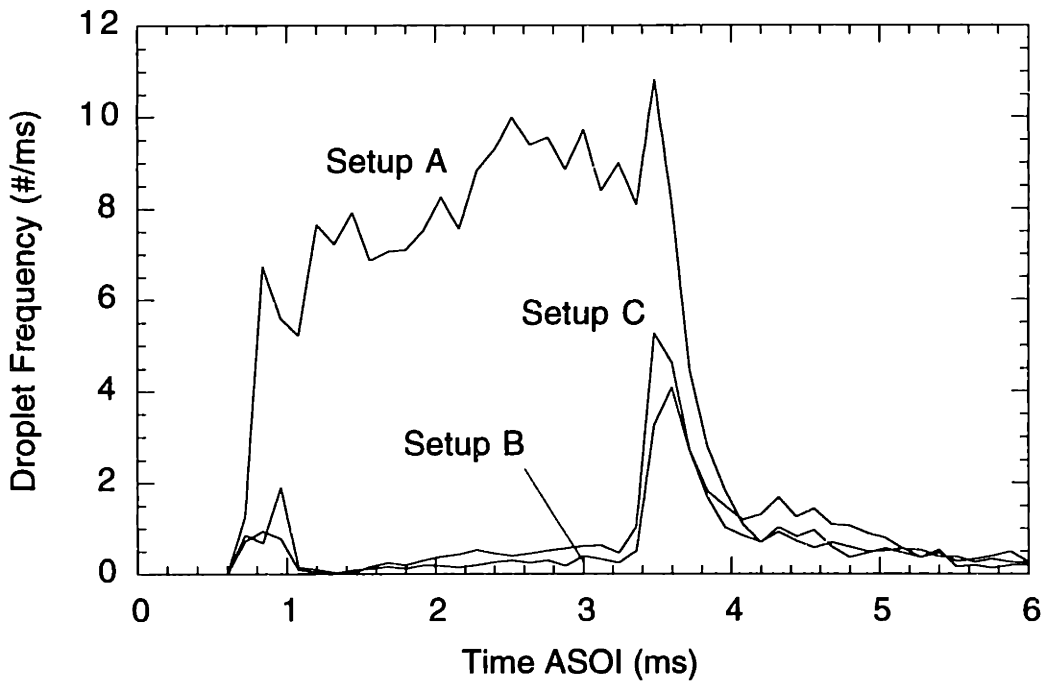

Figure 4.3: Droplet frequency plots of symmetrically similar measurement points showing scattering error. Z = 25 mm, R = 10 mm, 0.3 bar intake pressure, T = 60 °C, 2.7 ms injection.

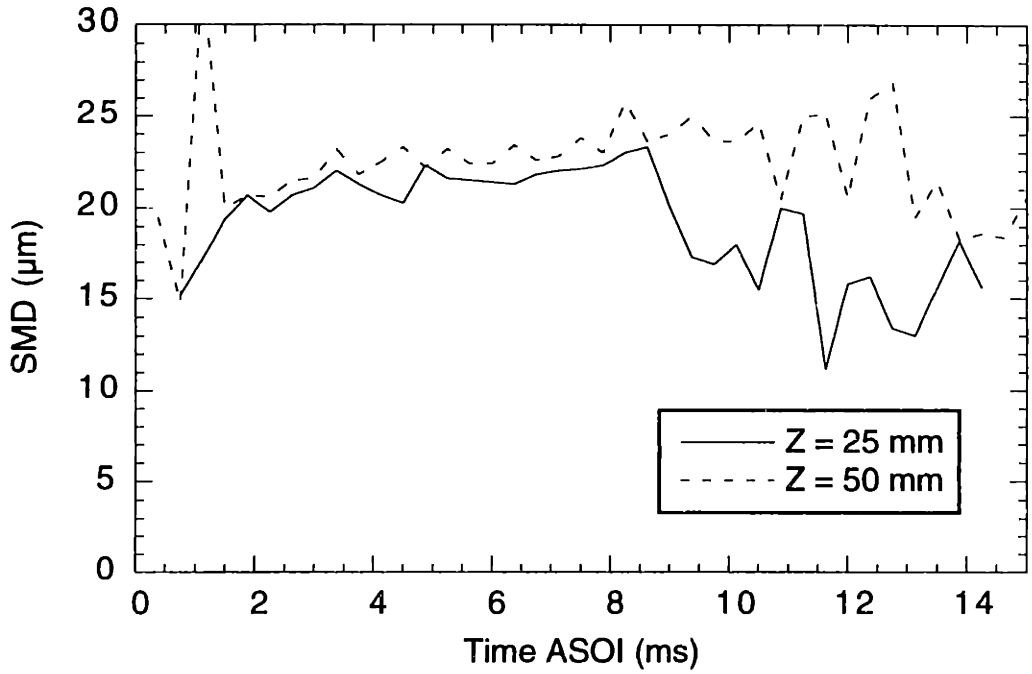

Figure 4.4: Sample temporal distribution of SMD. R = 10 mm, P = 0.9 bar, T = 90 °C, 7.5 ms injection duration, 375 µs bin size.

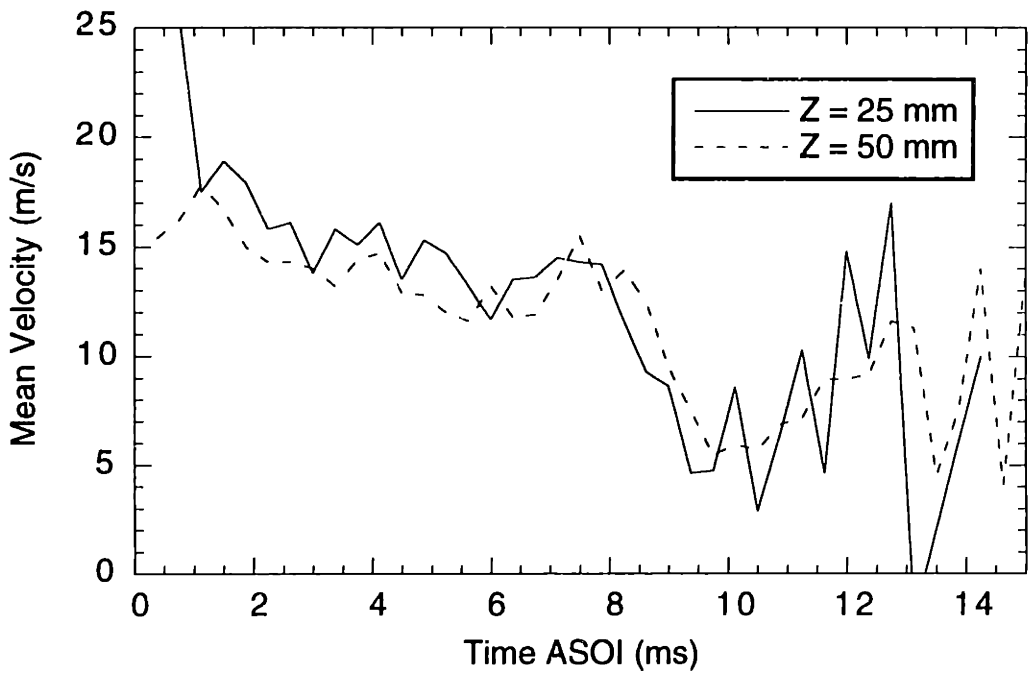

Figure 4.5: Sample temporal distribution of axial velocity. . R = 10 mm, P = 0.9 bar, T = 90 °C, 7.5 ms injection duration, 375 µs bin size.

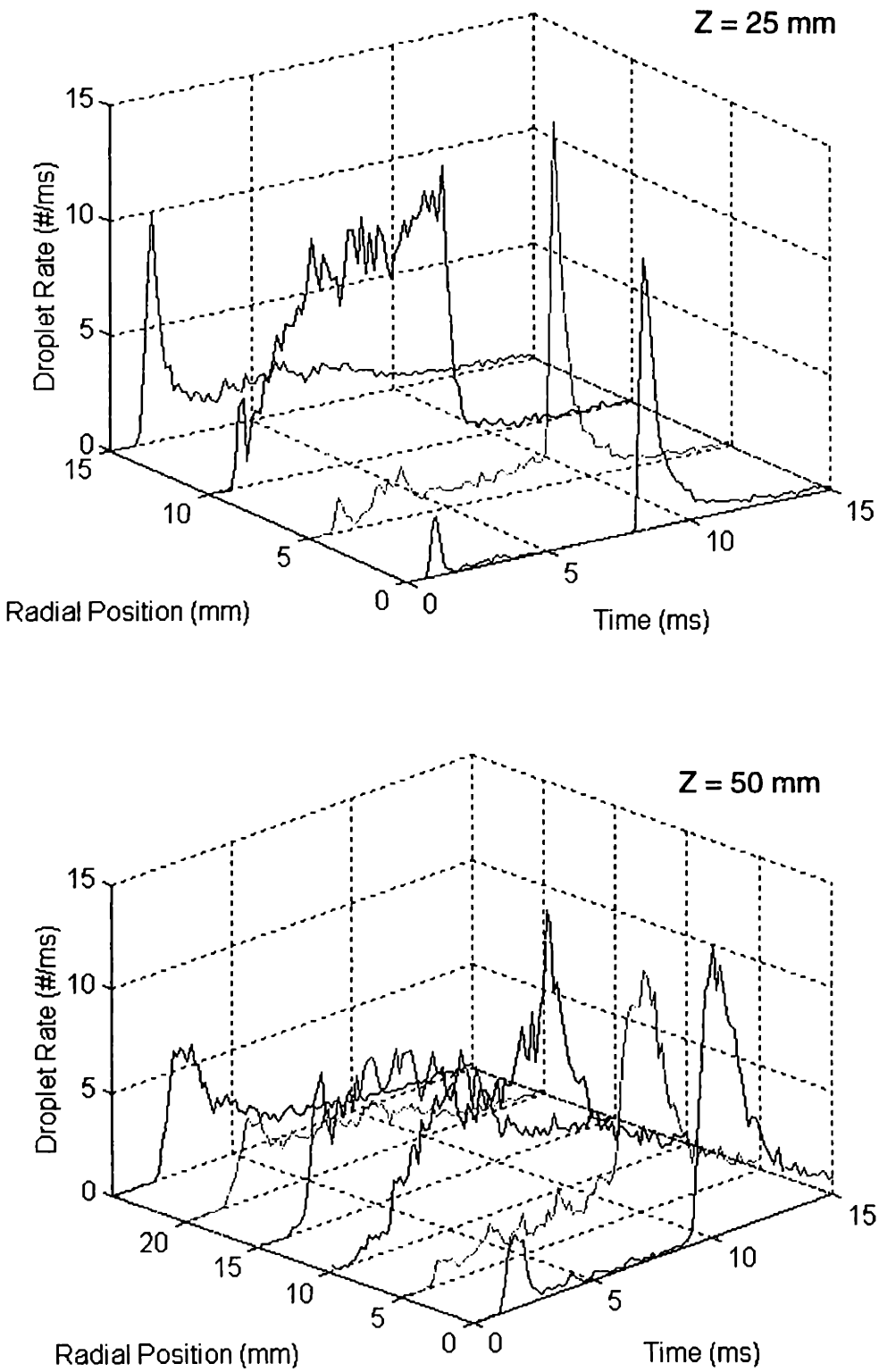

Figure 4.6: Temporal distributions of droplets frequencies at all measurement locations for low-volatility spray. PDPA data, P = 0.9 bar, T = 30 °C.

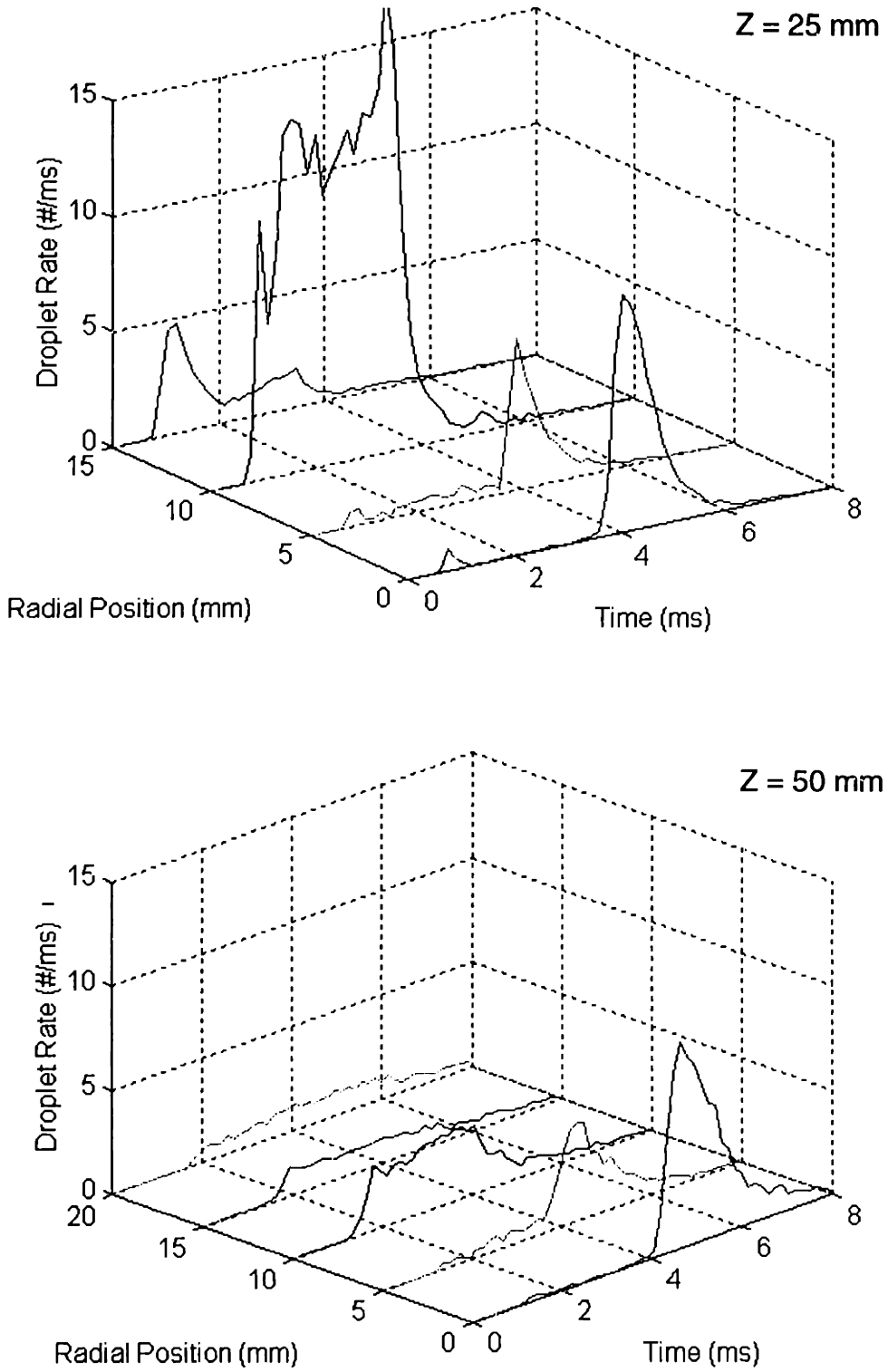

Figure 4.7: Temporal distributions of droplets frequencies at all measurement locations for high-volatility spray. PDPA data, P = 0.3 bar, T = 90 °C.

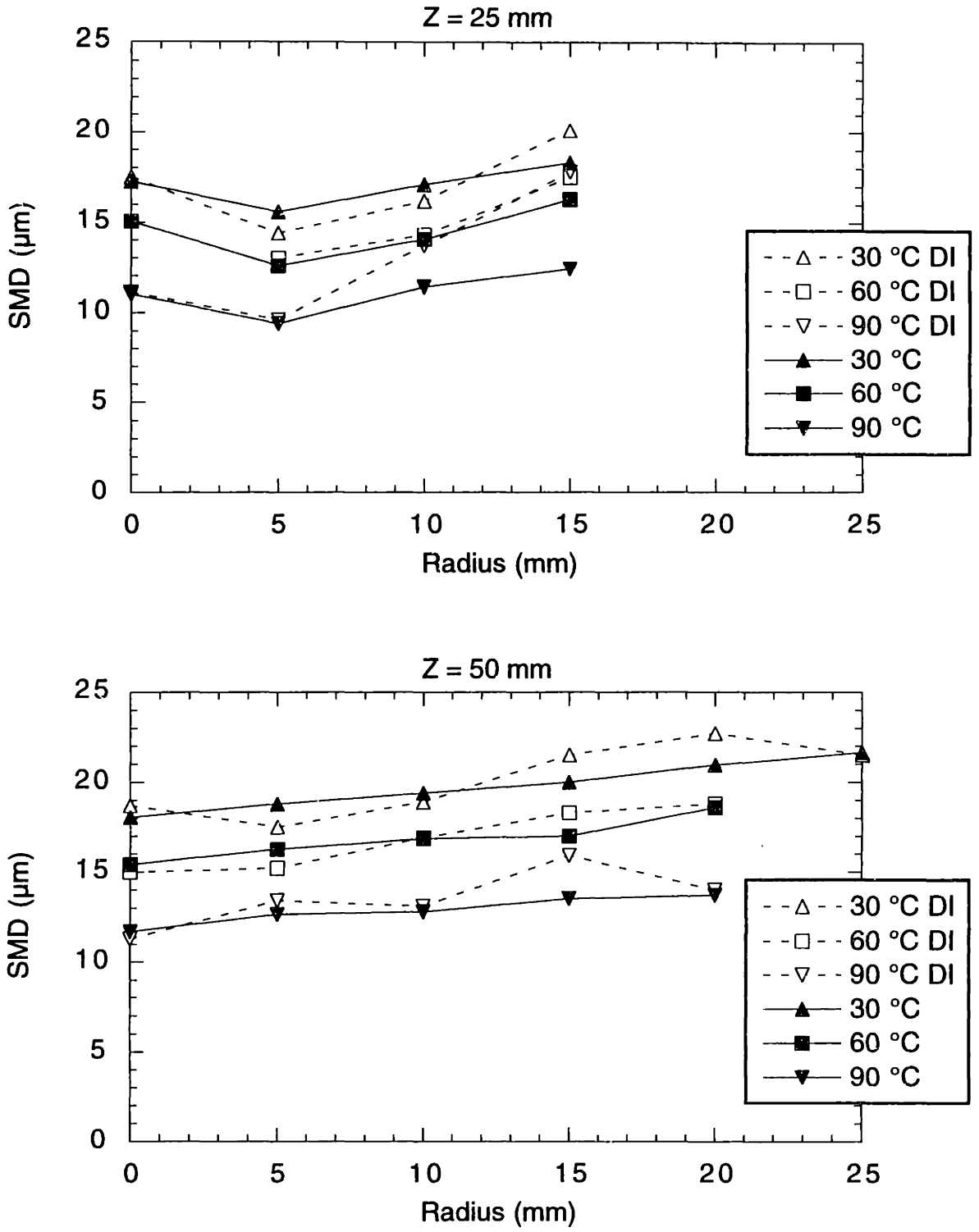

Figure 4.8: Spatial distributions of SMD at 0.3 bar intake pressure. Open symbols are during fully developed injection only (DI), closed symbols are averaged over entire injection.

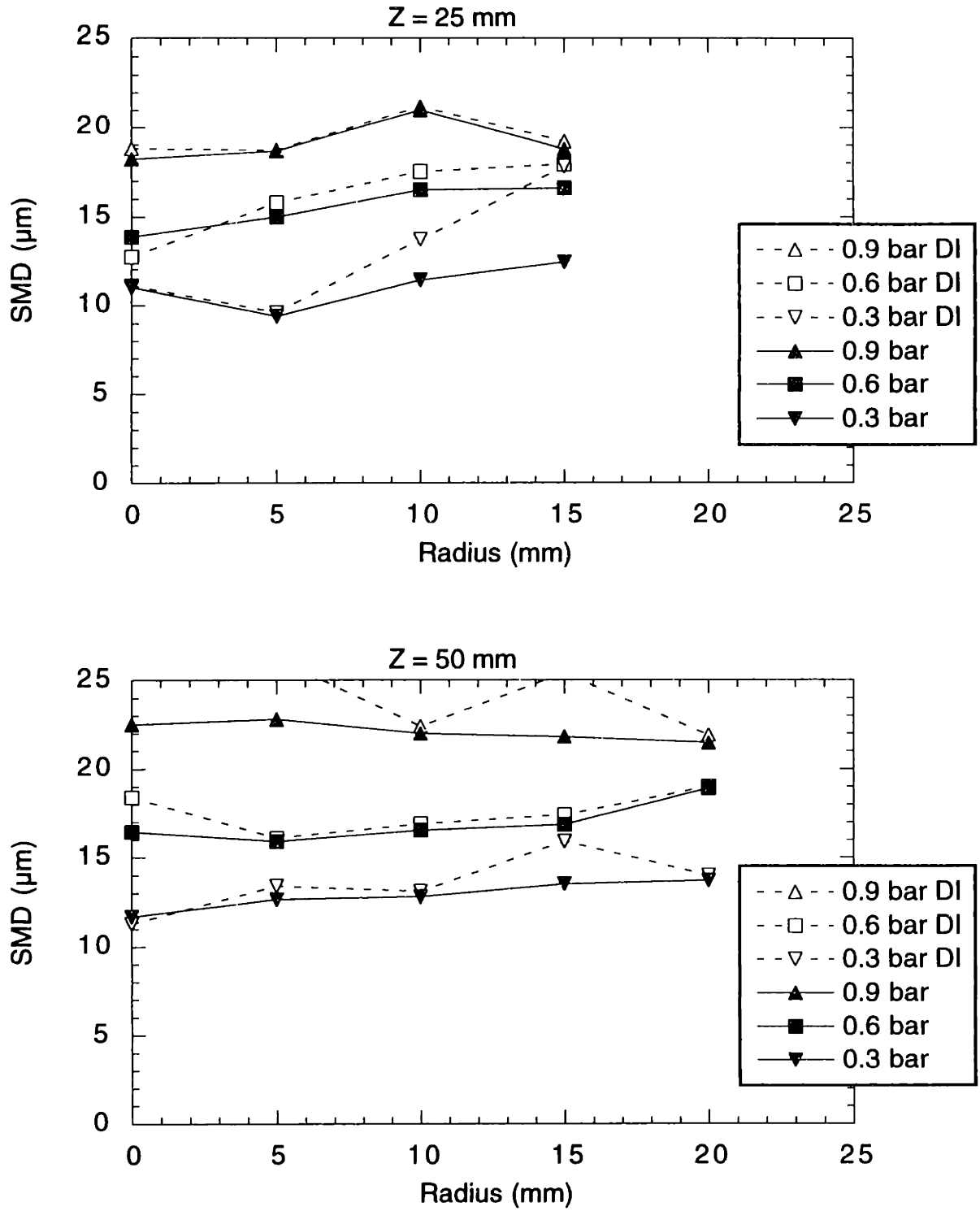

Figure 4.9: Spatial distributions of SMD at 90 °C. Open symbols are during fully developed injection only (DI), closed symbols are averaged over entire injection.

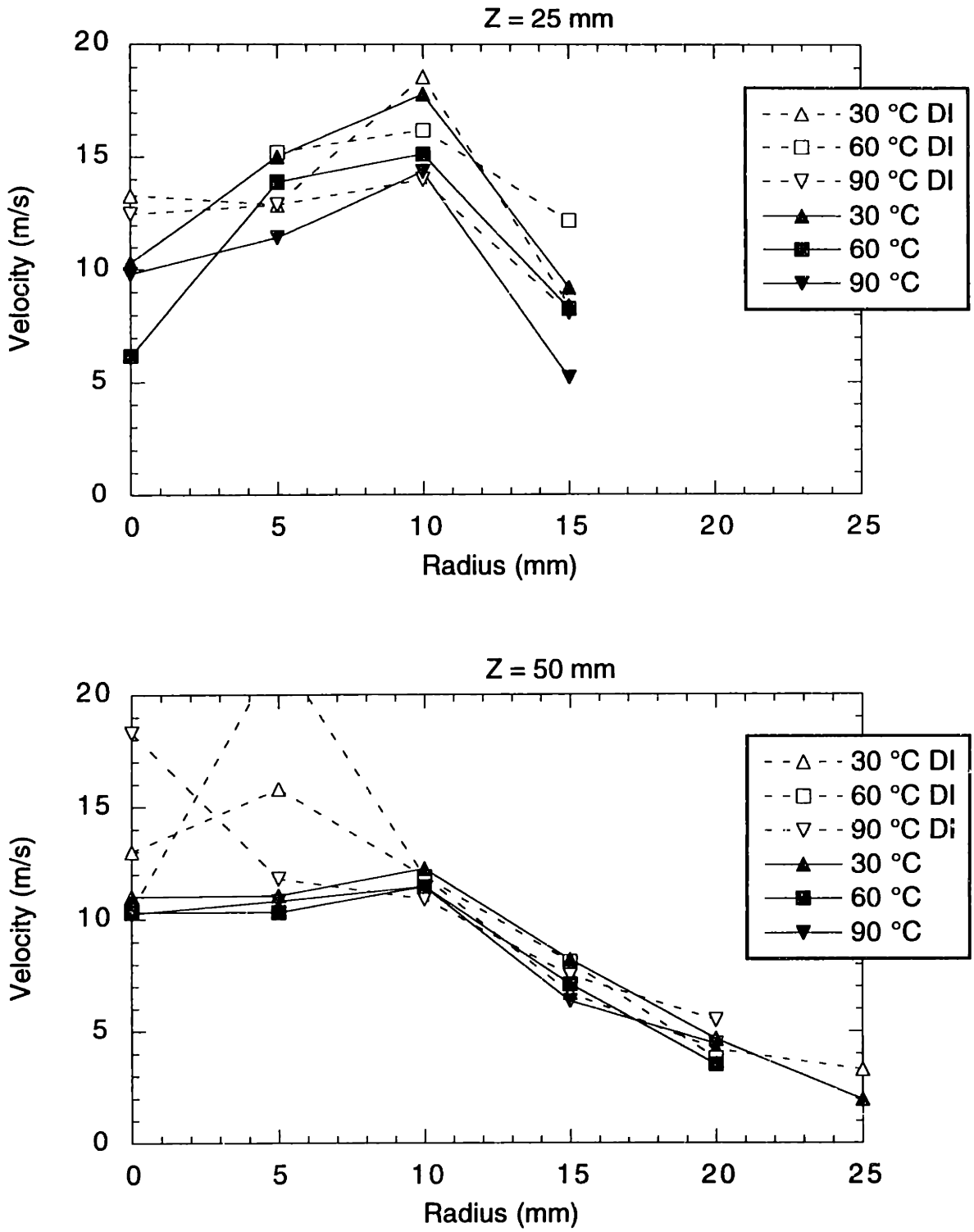

Figure 4.10: Spatial distributions of axial velocity at 0.3 bar intake pressure. Open symbols are during fully developed injection only (DI), closed symbols are averaged over entire injection.

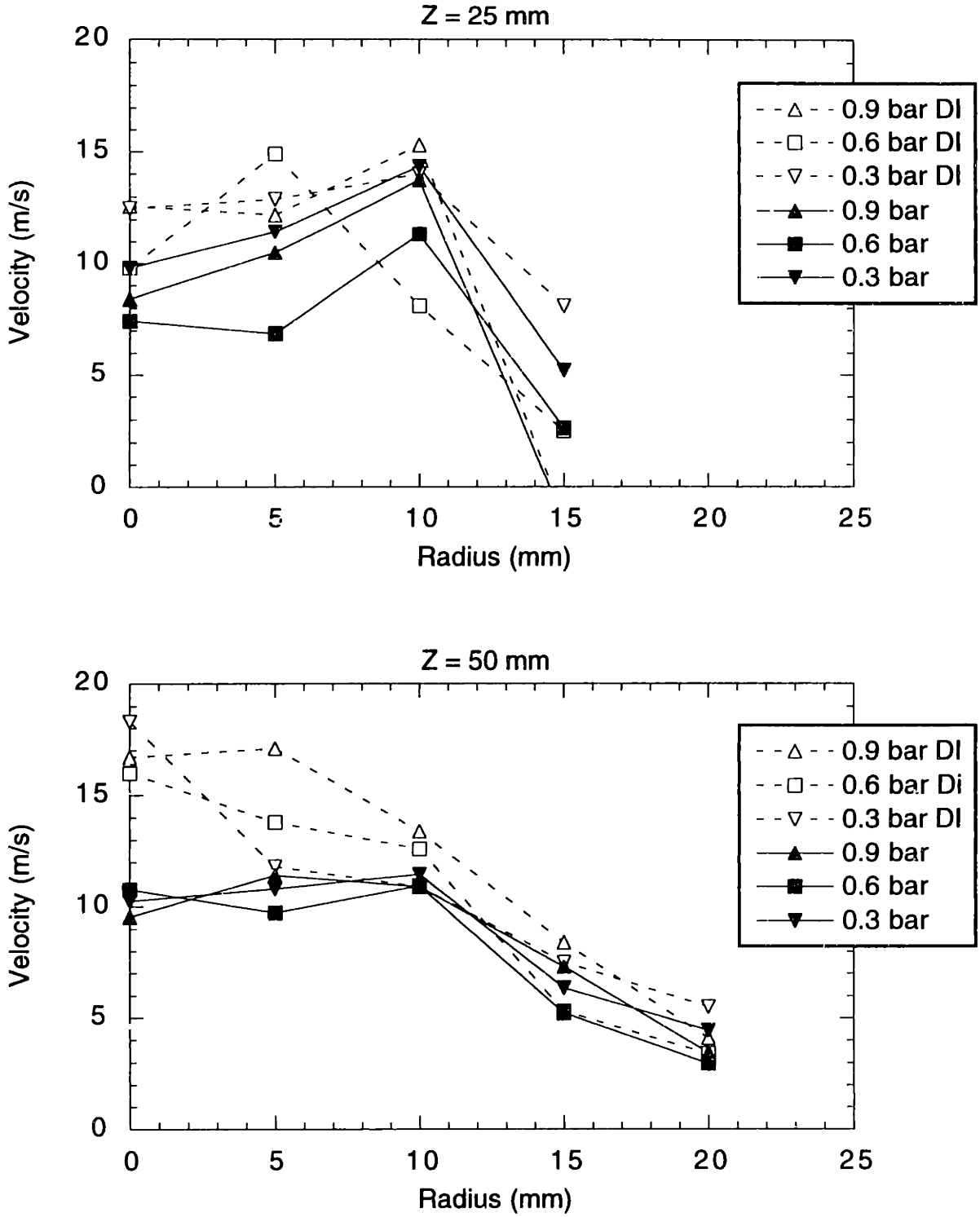

Figure 4.11: Spatial distributions of axial velocity at 90 °C. Open symbols are during fully developed injection only (DI), closed symbols are averaged over entire injection.

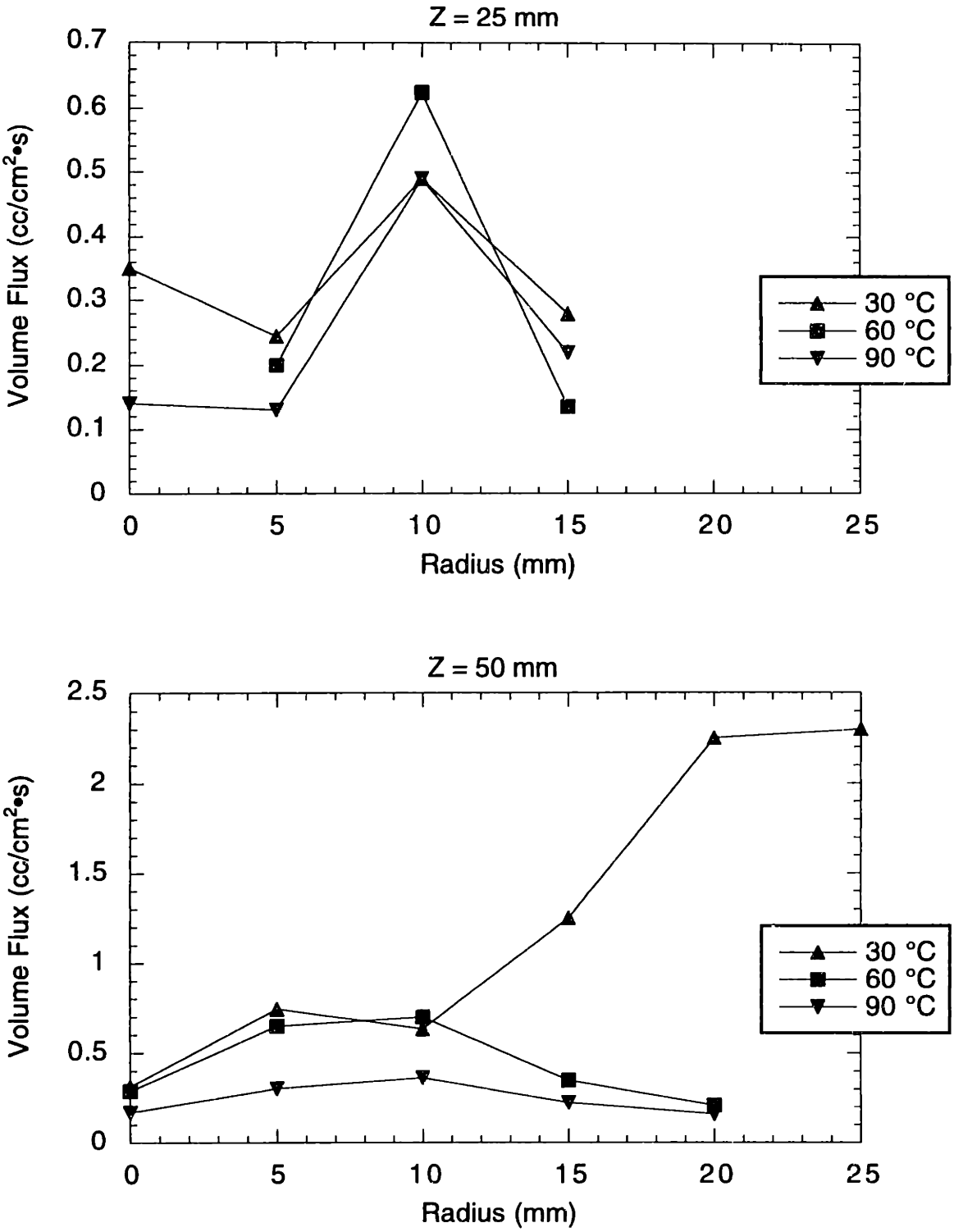

Figure 4.12: Spatial distributions of liquid volume flux at 0.3 bar intake pressure. Open symbols are during fully developed injection only (DI), closed symbols are averaged over entire injection.

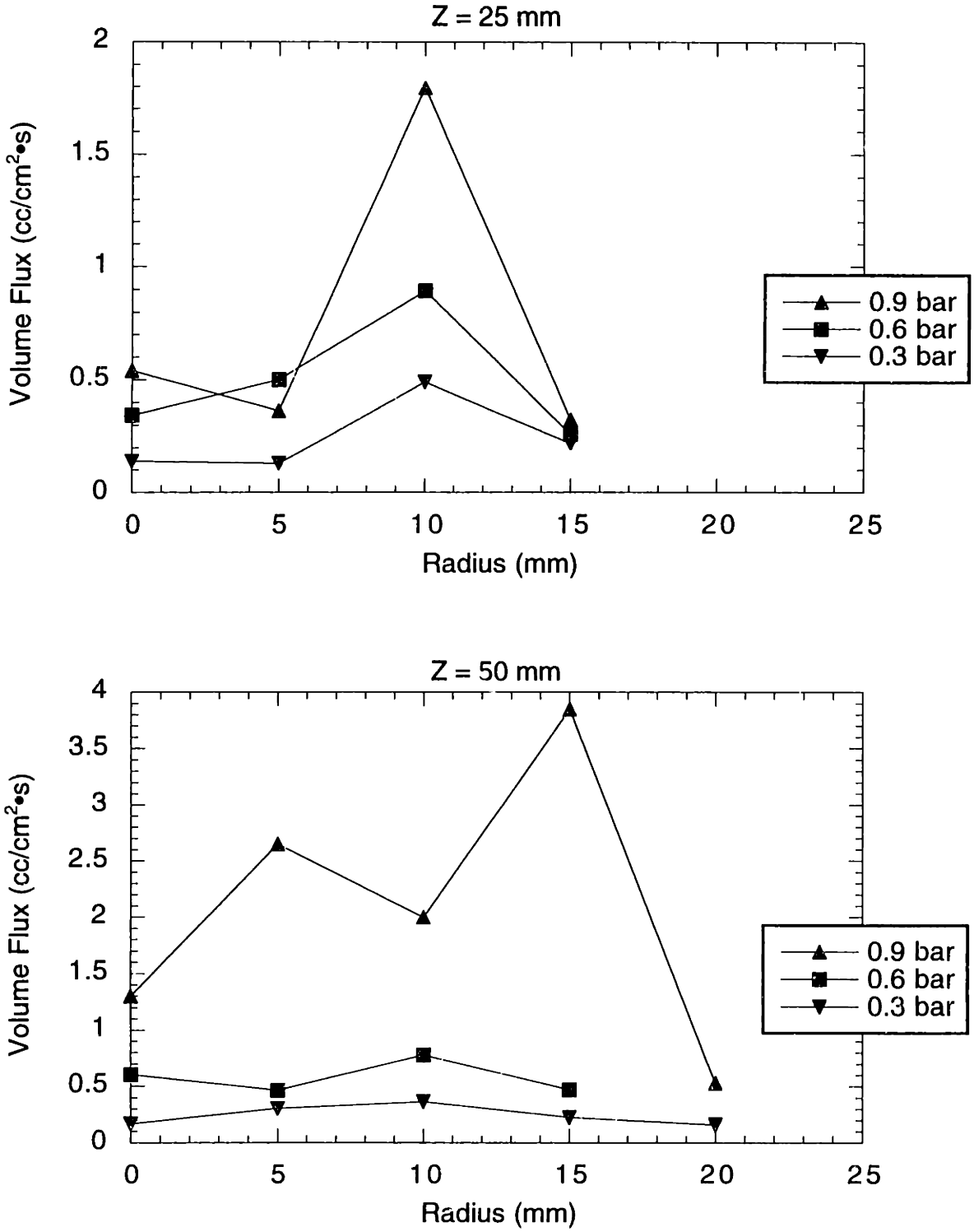

Figure 4.13: Spatial distributions of liquid volume flux at 90 °C. Open symbols are during fully developed injection only (DI), closed symbols are averaged over entire injection.

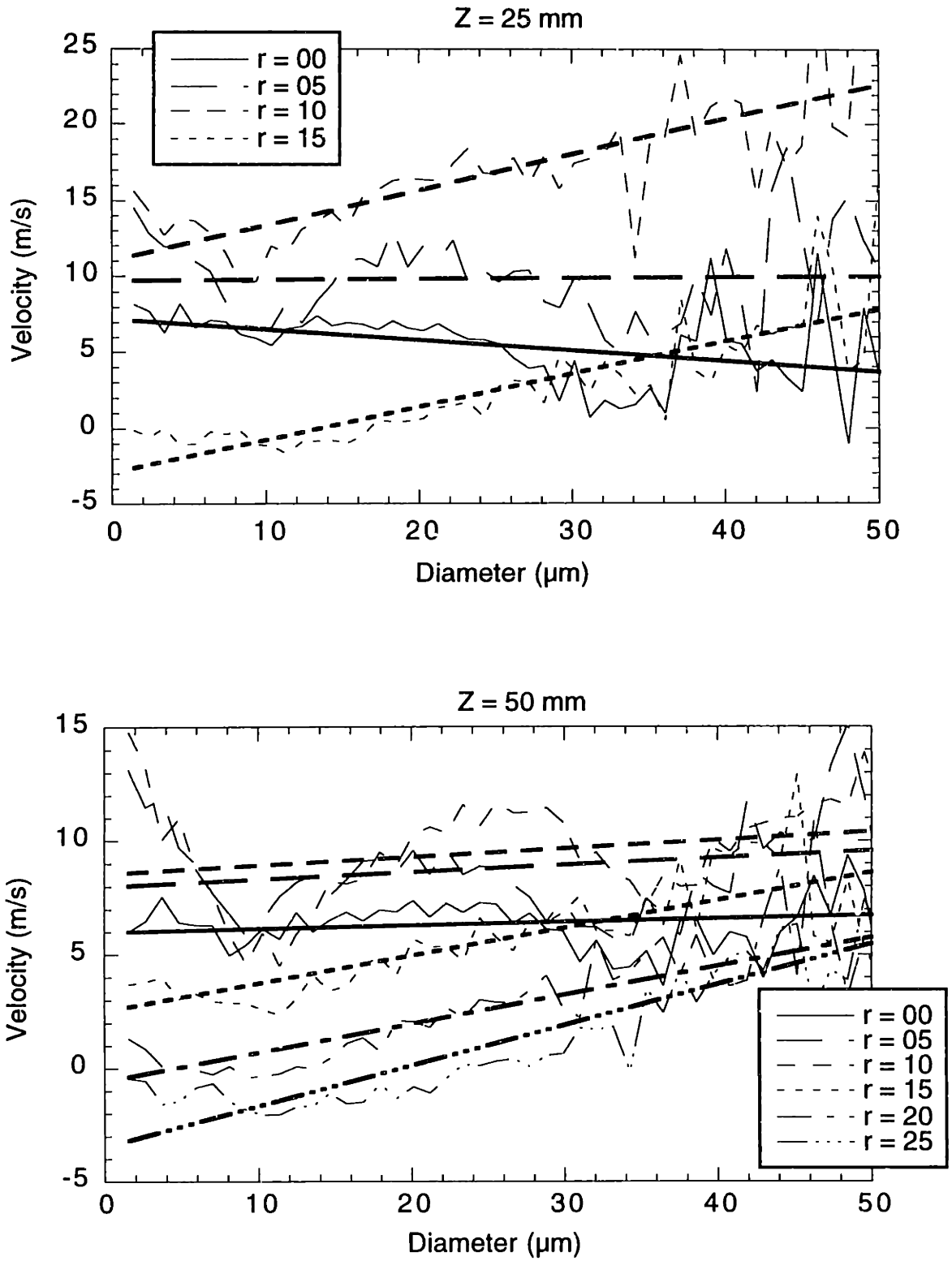

Figure 4.14: Average velocity as a function of diameter. P = 0.9 bar, T = 30 °C. Straight lines are linear fits to the data.

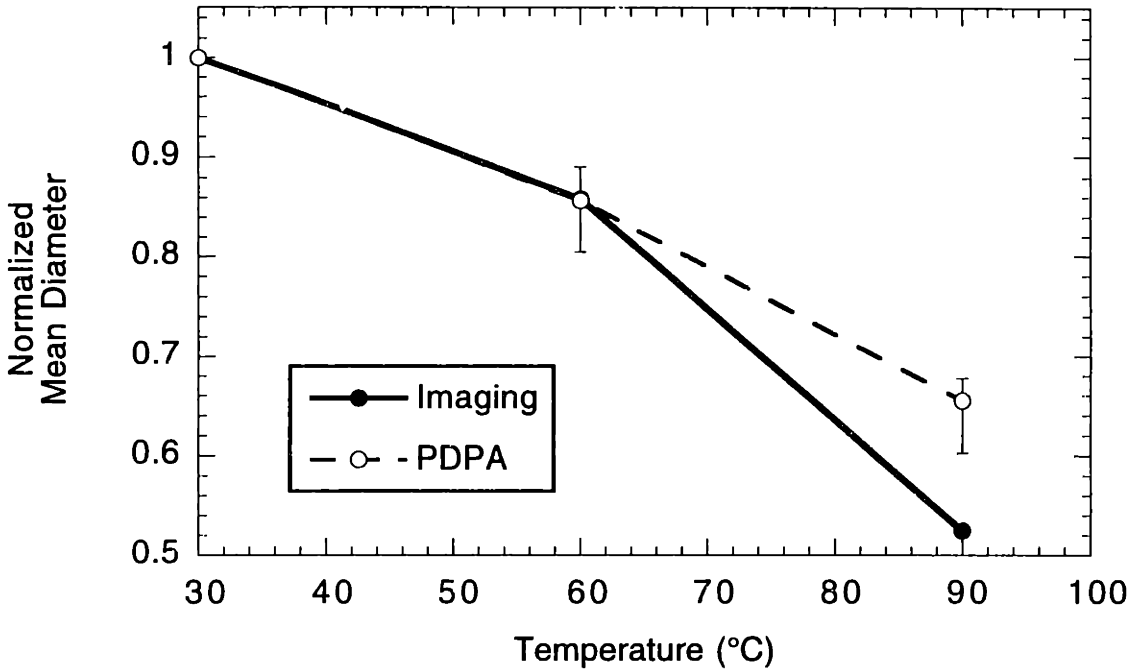

Figure 4.15: Comparison of droplet diameter reduction as measured by PDPA and imaging comparison. Chrysler injector, 0.3 bar intake pressure

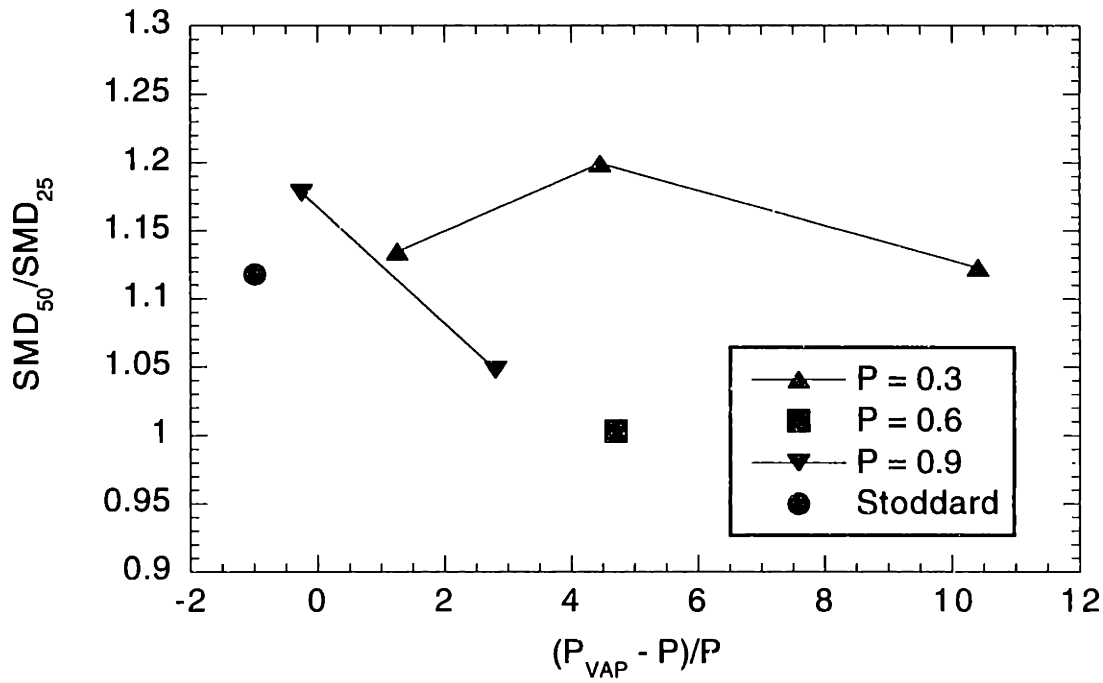

Figure 4.16: Plot of SMD increase against normalized excess vapor pressure. Indolene and Stoddard solvent, R = 10 mm.

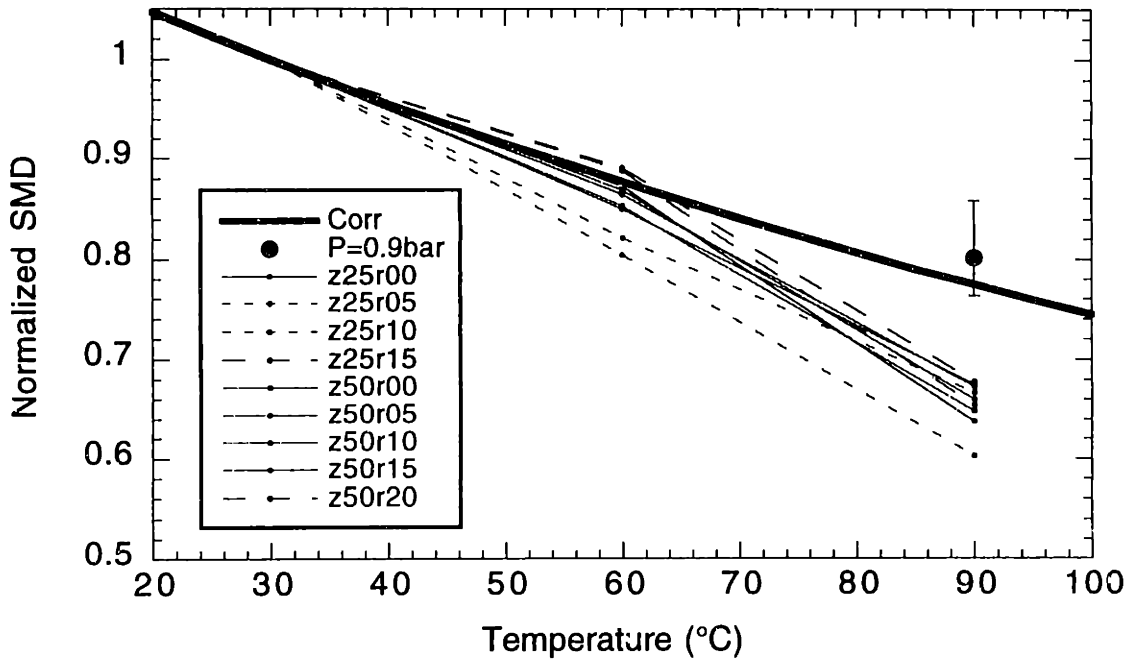

Figure 4.17: Comparison of change in SMD with temperature from PDPA and a correlation [47]. Indolene. Large point is at 0.9 bar, error bars represent scatter between measurement locations. Small points are at 0.3 bar, dashed lines represent case with different behavior.

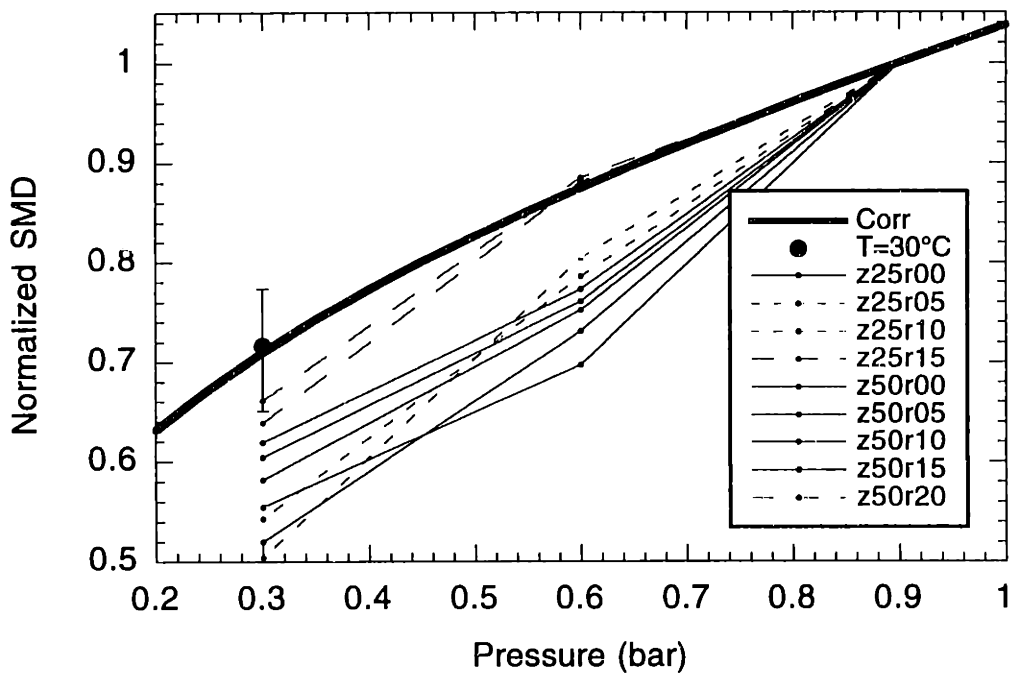

Figure 4.18: Comparison of change in SMD with pressure from PDPA and a correlation [47]. Indolene. Large point is at 30 °C, error bars represent scatter between measurement locations. Small points are at 90 °C, dashed lines represent case with different behavior.

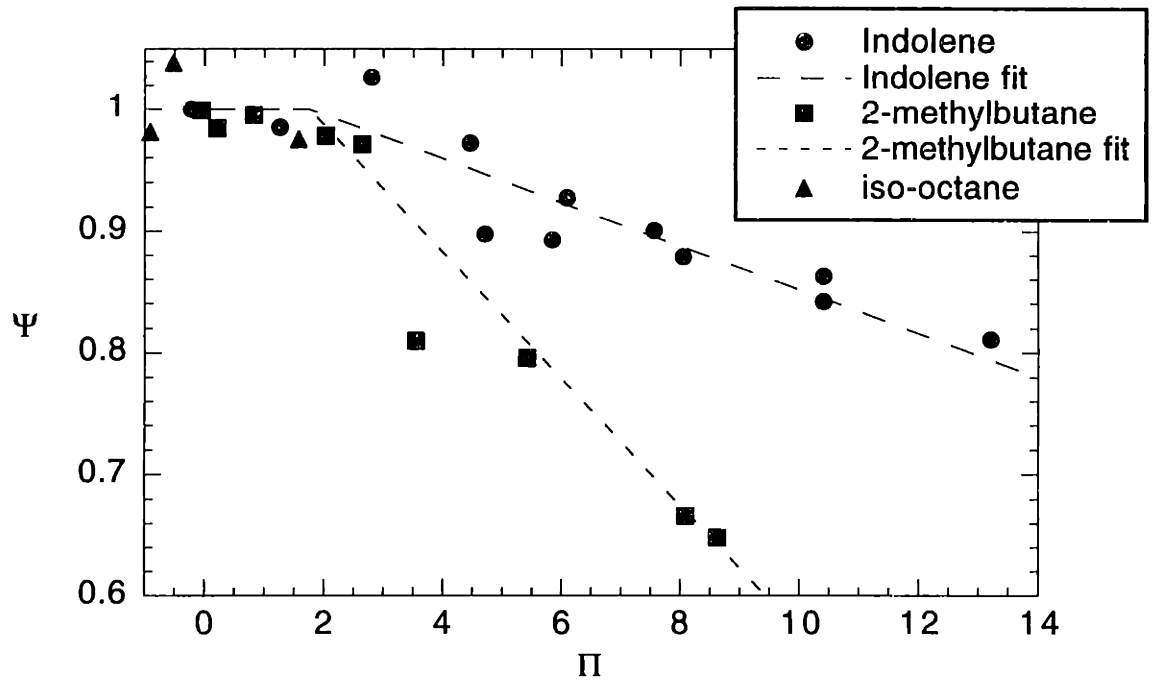

Figure 4.19: Superheat dependence of volatility-induced droplet size reduction. Data from Z = 50 mm.

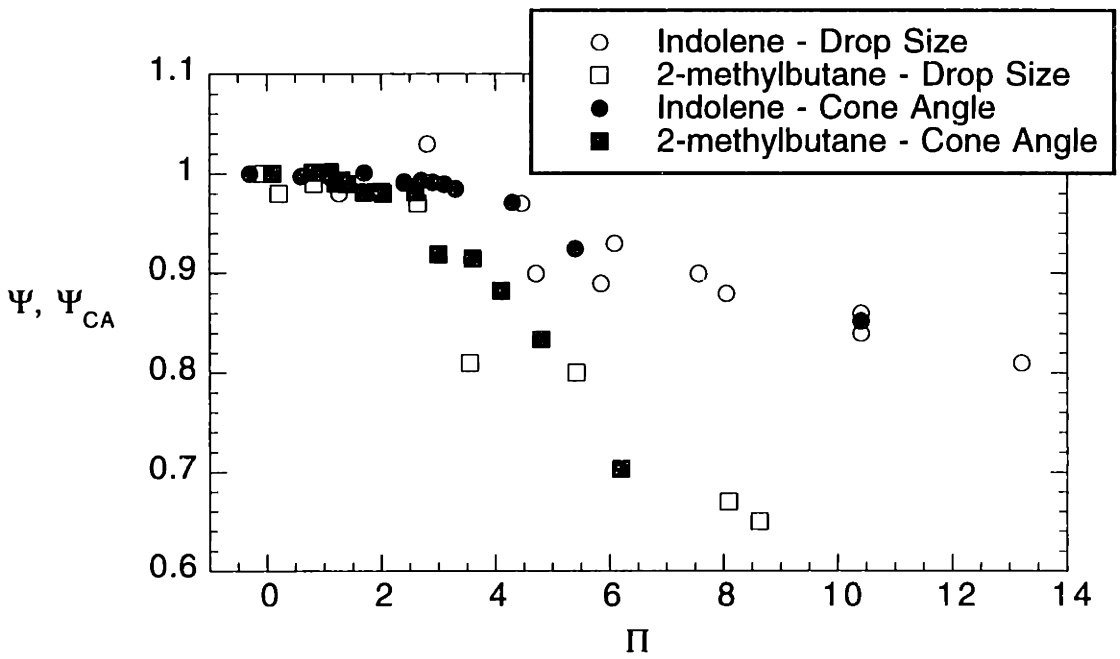

Figure 4.20: Comparison of SMD reduction predicted from initial cone angle increase with volatility-induced droplet size reduction.

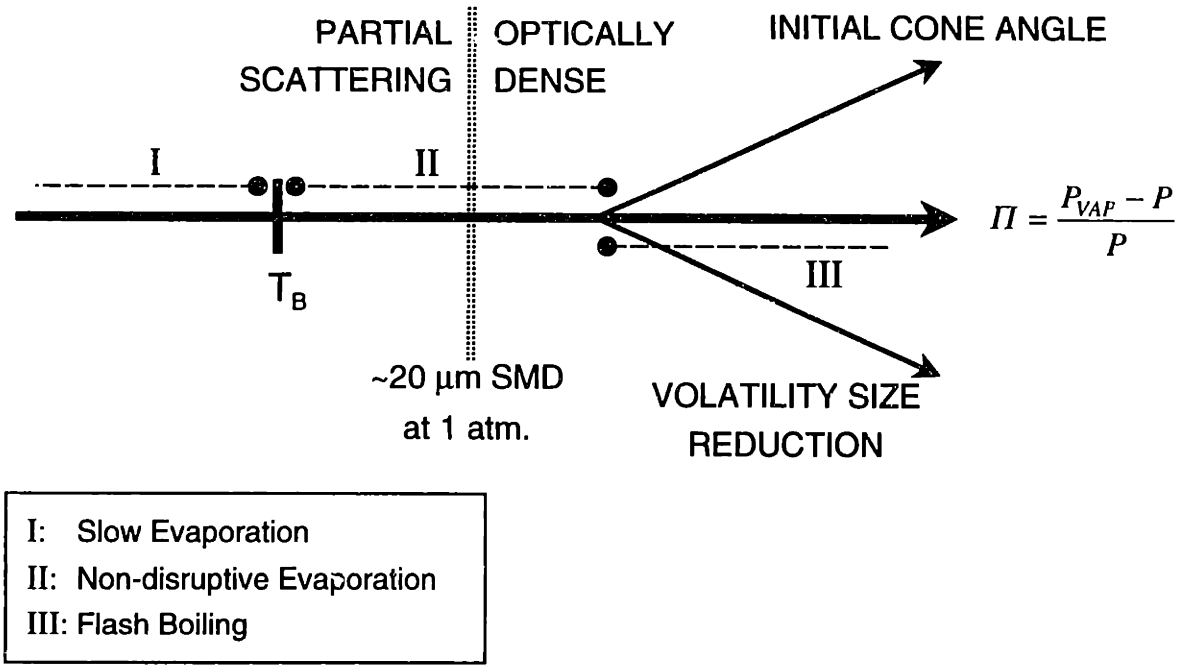

Figure 4.21: Schematic of spray regimes as a function of normalized excess vapor pressure.

CHAPTER 5

SPRAY MODELING

5.1 Model Description

To gain insight into the physics behind the observed changes in the spray structure, a computational model of the spray was investigated. The modeling software used was FIRE v7.0b produced by AVL LIST GmbH [54]. Access to the software, computing power, and initial model setup were supplied by the Advanced Engine Technology Group at DaimlerChrysler. The model consists of a standard Eulerian computational fluid dynamics representation of the gas phase. The liquid phase is added using a method termed the Discrete Droplet Method [55], in which liquid droplet parcels are tracked in a Lagrangian manner. Each parcel represents many droplets, since modeling the millions of individual droplets would be prohibitive. The parcels are introduced with initial values of position, size, velocity, temperature, and number of droplets per parcel. Coupling between the phases is two-way. Models for droplet breakup and coalescence are available but were not used in this work.

The evaporation sub-model used in FIRE was originally derived by Dukowicz [56]. The model is based on the following assumptions: spherical symmetry, quasi-steady gas-film around the droplet, uniform droplet temperature, uniform physical properties of surrounding fluid, and liquid-vapor thermal equilibrium at the droplet surface [54]. To solve the heat and mass transfer equations, a unity Lewis number is assumed and a single-droplet correlation is used to calculate the heat-transfer coefficient. The temperature used to calculate the fluid properties is the average of the local domain fluid temperature and the droplet surface temperature.

The computational domain is a cylinder 85 mm in diameter and 90 mm long, roughly the size of an engine cylinder. This domain is divided into a 50 by 50 by 50 grid, as shown in Figure 5.1. The smallest cells, under the injector, are 0.76-mm cubes. The injection occurs along the

axis of the cylinder from the top face. Droplet parcels are injected at a rate of 36 per 5 μs time step for a total of 12600 parcels per spray in the '2 ms' injection. The simulation begins 250 μs after the start of the injection time, representing the delay time in the actual injection. The first 400 time steps are at 5 μs increments, which encompasses the injection time. Another 100 time steps at 10 μs increments allowed observation of the decay of the spray structure. In some cases, shorter time steps were used at the beginning to increase the stability of the code.

As noted above, the primary inputs for the spray model are the initial values of position, size, velocity, temperature, and number of droplets per parcel. The initial position is randomly selected from around the injector orifice, which is located in the middle of the top face of the domain. The initial size of the droplets is determined by a probability distribution. As each parcel is injected, the diameter of the droplets it represents is chosen at random from the distribution. Three different primary diameter distributions were used. These distributions were produced from Gaussian profiles, which were adjusted to give particular values for SMD and DV_{90}. Parameters for these distributions are given in Table 5.1, and plots are shown in Figure 5.2. The first distribution was tailored to reproduce the PDPA data for a low-pressure low-temperature spray (0.3 bar, 30 °C). The second distribution was tailored after a low-pressure high-temperature spray (0.3 bar, 90 °C). The third was intended as an extension of the second to even smaller sizes. These three profiles will be referred to below by their SMD. The initial velocity of the droplet parcels is determined by the initial speed and cone angle. The initial speed, estimated from images of the penetration of the pre-spray under low-pressure cold conditions, initially peaks at 87 ms for 50 μs and ramps down to 81 ms from 200 μs on. The direction of each droplet parcel is randomly chosen between a defined inner and outer cone angle. Transient values of the initial outer cone angle were measured from images of a cold and a flash-boiling spray (0.3 bar, 30 and 90 °C). These profiles are shown in Figure 5.3. Since the initial cone angle of the flash-boiling spray proved difficult to measure, some of the points were estimated from the shape of the cold profile. These profiles are similar to those measured by

DaimlerChrysler for a similar injector [57]. The oscillations here are somewhat larger though, likely due to greater pressure transients in the fuel supply system ('rail dynamics'). The inner cone angle was taken to be 10 degrees less than the outer in most cases. In addition, a random perturbation velocity of up to 6.5% of the injection speed was added normal to the initial parcel direction. Droplet temperature, while consistent for all parcels at injection, was changed for the various tests. The number of droplets per parcel is determined by the instantaneous flow rate, the number of parcels, and droplet size for each parcel. The transient flow rate was set up with an initial overshoot and a slight decrease before closing. The profile is shown in Figure 5.4. All of these inputs, along with a listing of the desired sub-models and outputs are assembled into the spray input file, a sample of which is shown in Appendix 10.

This model was used for eight tests in which the droplet diameter distributions, the initial cone angle, and the volatility were varied. The computation time ranged from 31 to 72 CPU-hours running on an Origin 2000. Output files containing gas pressure, temperature, velocity, and composition, and droplet position, temperature, diameter were written for every 100 μs of spray time.

5.2 Spray Structure

5.2.1 Baseline Case

The baseline modeling case was designed to represent the cold low-pressure spray (0.3 bar, 30 °C), which was measured with the imaging and PDPA. Conditions for this case, as well as all the others, are shown in Table 5.2. All of these cases have a gas pressure of 0.3 bar. The low temperature is represented by the low fuel temperature and a low wall temperature (303 K). The 16-μm-SMD diameter distribution described above was used to simulate the PDPA results for these conditions. For a mid-volatility fuel, n-octane was used. The baseline case is referred to as O16 because of the n-octane fuel and the 16 μm SMD.

A full time series of this model is shown in Appendix 11 using images of droplets parcels, velocity vectors, liquid bulk density, equivalence ratio, and pressure all at the cut plane shown in Figure 5.1. The development of the model spray is much like the actual spray. The transient cone angle produces a concentrated pre-spray that penetrates ahead of the body of the spray. The droplet distributions show more droplets in the core of the spray than was expected from the imaging experiments, but these droplets represent little liquid mass since they have small diameters compared with the rest of the spray. This is confirmed by the liquid bulk density distributions, which appear quite hollow. Since the liquid density profiles best represent the PLIF imaging, comparisons with the PLIF development images in Appendix 7 are appropriate. The selected diameter distribution also appears appropriate since the downstream decrease in cone angle is similar to the imaging. This contraction of the spray is dependent on the drag on the droplets by the induced gas flows, and is therefore dependent on the droplet diameter. The low-pressure region in the core of the spray, which was mentioned early on, is very clear in the pressure profiles. The pressure profiles also show the formation and the downstream convection of the toroidal vortex outside the spray, which is often mentioned in the literature. This toroidal vortex, as well as the entrainment flow, can also be seen quite clearly in the velocity vector plot as well. The toroidal vortex is seldom seen in the current imaging experiments since it contains few droplets, as suggested by its absence in the liquid density profiles. The equivalence ratio plots show that the vapor distribution inside the spray cone is relatively uniform, but slightly higher along the axis. This agrees with the cold acetone profiles in Fig. 3.35, in which a higher concentration of vapor is observed along the spray axis.

The penetration of the baseline spray is shown as the solid curve in Figure 5.5 (O16). The penetration of the spray is determined by FIRE as the furthest droplet parcel. This penetration is, therefore, comparable to the visual method of determining the penetration from the images (Fig. 3.41). In fact, the model and the imaging measurements both show about 50

mm of penetration after 1 ms. Agreement should be good, though, since the initial velocity in the model was determined from similar imaging measurements.

The following sections discuss changes to the conditions of this case for comparison to the other modeling cases and the imaging and PDPA experiments. Three general changes are made to simulate effects seen in the flash boiling spray: decreased droplet size, vapor generation, and increased initial cone angle.

5.2.2 Droplet Diameter Decrease

One of the inputs to the model that was found to change substantially with operating conditions in the experiments was the mean droplet diameter. To determine how this aspect of the changes in the spray affects its structure, a case was modeled with a smaller mean diameter than the base case (O16). A comparison of profiles from the fully-developed sprays (2 ms ASOI) for these cases is shown in Figure 5.6. Similar observations could be made about the relationship between the wide-cone-angle cases (VGW10 and VGW8), but the difference is more obvious here.

The most obvious change with the decrease in droplet size is the decreased radial and axial penetration. The profiles show that, due to the greater contraction of the spray, its width is reduced by roughly 25%. The axial penetration of the pre-spray, which is plotted in Fig. 5.5, shows a 20% decrease. The axial penetration of the body of the spray, however, is only slightly reduced. This can be seen in the liquid density and the equivalence ratio profiles, as well as the location of the toroidal vortex apparent in the pressure profile. This decreased difference in the penetration rates of the pre-spray and main-spray, produces a structure in which the pre-spray does not separate significantly. This effect is consistent with observations of the imaging experiments as temperature was increased.

The details of each pair of profiles show some interesting effects as well. The droplets profile has a larger fraction of the droplets in the interior of the spray cone for the smaller SMD

case. This is reflected in the increased liquid density in the core of the spray. Due to the decreased width, the liquid density is also higher at the spray sheet. This is seen by the larger 'saturated' area, in which the density is higher than 1.8 kg-liquid/m^3. The image scale was not chosen to cover the full range, so that the details could be seen with a reasonably small number of contours. The vapor distribution is also affected by the decrease in width, as shown in the equivalence ratio profiles. The vapor-containing region is significantly smaller with the smaller SMD, but he concentration in the core is similar. This suggests that there is less evaporation in the case with smaller droplets. This effect is verified in the evaporation section below (Sec. 5.3). The pressure profiles show that the low-pressure zone in the core of the smaller-SMD spray is more confined, and the toroidal vortex is weaker. The weaker toroidal vortex is supported by the lower velocities around the vortex.

Overall, the greater interaction of the smaller droplets with the gas causes increased drag on the pre-spray and a greater contraction of the body of the spray. The decreased spray envelope results in a greater liquid density and a smaller vapor cloud.

5.2.3 Vapor Addition

The effect of vapor generation in the spray on its structure was studied through two methods of vapor addition. Since the evaporation model is relatively simplistic, flash boiling could not be modeled directly. Instead, vapor addition was achieved by the introduction of a second, more volatile spray. The two sprays were injected simultaneously, their droplet parcels intermixing. Details of the two sprays for the different cases are described in Table 5.2b. To better control the evaporation, a low volatility fluid, n-dodecane, was used for the primary spray. The 10-μm SMD droplet diameter distribution was used to simulate the low-pressure hot conditions described by the images and PDPA (0.3 bar, 90 °C). The vapor producing spray used n-heptane. The volume fraction of the fuel assigned to the vapor-producing spray was 25%. This represents a substantial amount of flash vaporization but is not unrealistic.

Two different methods were used to encourage the evaporation of the n-heptane sprays. The first method involved very small droplets (SMD < 4 μm) at a temperature just below their boiling point at this pressure. The small size was used to give the spray a large surface area to enhance evaporation. Because of instabilities in the code when the droplets slightly exceeded their boiling point, the temperature was set slightly below it. The droplets, therefore, evaporated gradually as they interacted with the hot chamber gasses (420 K). Figure 5.7 shows the mass of vapor evolved from the spray as a function of time normalized by the mass of n-heptane injected to that point in time. Unity on this plot represents the idealized case in which all of the injected n-heptane has evaporated, but none of the main spray (n-dodecane). This plot, therefore, represents how complete the vapor-addition is. The gradual-vapor-generation case described above (VG10) exhibits a rapid increase to about 0.8, but does not pass unity until after the end of injection (2 ms). This shows that some of the n-heptane droplets were not evaporating, which is supported by the fact that the penetration of n-heptane droplets was 70 to 80% of that of n-dodecane.

The second method of vapor generation involved superheating the n-heptane. The temperature was chosen by starting the both sprays at 90 °C. Then enough heat was transferred from the n-dodecane to the n-heptane to overcome its heat of vaporization. This allowed the n-heptane spray to vaporize in the first time step, yielding no penetration of vapor-generation spray. However, the curve for this case in Fig. 5.7 (VI10) does not reach unity immediately. This says that while no n-heptane droplets remain, it has not all been converted to vapor, suggesting that it may be condensing on the cooler n-dodecane droplets. In fact, there appears to be no differentiation between the two species in the vapor state. Therefore, it may be the case that when an n-dodecane droplet is surrounded by vapor, the vapor is assumed by the model to be n-dodecane vapor, which is well below its boiling point. At high enough concentrations, the vapor, which originated from n-heptane droplets may readily condense on n-dodecane droplets.

Figure 5.8 compares profiles from the two vapor addition cases described above with a case having only an n-dodecane spray (D10). The vapor mass fraction profile shows that the added vapor concentrates along the axis of the spray, approaching pure vapor near the injector. A column of vapor is consistent with the images of the hot spray of the acetone-doped fuel mixture. In addition, the vapor in the immediate addition case penetrates more quickly than in the other two cases. This faster penetration is also seen in the spray penetration plot in Fig. 5.5. The low evaporating case and the gradual-vapor-addition case (D10 and VG10) show nearly identical penetration profiles, while the immediate-vapor-addition case (VI10) shows a 10% higher penetration after 3 ms. Most of the lead by the immediate case, though, was gained before 1 ms. This initial penetration, higher than any of the other cases, is not consistent with the measurements of spray images described in Sec. 3.9.1, in which the penetration of the cold spray only falls behind later on because of the measurement technique losing track of the pre-spray. This suggests that the immediate-vapor-addition method may be too severe, at least early in the spray development.

The droplet distributions in Fig. 5.8 show that the exteriors of the three cases are similar, except for a decrease in width. The interior, on the other hand, shows a marked decrease in the number of droplets near the spray axis. This effect is seen more clearly in the liquid density profiles. With the immediate case, little liquid is seen in the core of the spray. This liquid density image of the immediate case actually has a number of features of the images of the flash-boiling sprays. About 15 mm downstream, the majority of the liquid contracts into a columnar structure, while some of the droplets maintain nearly the original cone angle. The vapor generation stretches the spray out, accentuating the shape. This spray would also appear hollow in the slit imaging tests (Sec. 3.8) due to the low number of droplets in the vapor core.

The pressure and velocity vector profiles show that the toroidal vortex is strengthened with the vapor addition, likely due to the narrower cone and higher velocities at the centerline.

The centerline axial velocities are shown more clearly in Figure 5.9. These are plots of distributions of the axial component of the velocity for the three cases described here.

One of the initial theories on the role of vapor generation was to create the increased initial cone angle observed in the images. The inability of this model to recreate that effect is likely due to one of three things. First, spatial resolution of the domain may be insufficient to model strong gas flows near the injector. Second, the radial velocity needed to push the droplets out to the side may be supplied by violent breakup, which is not modeled here. Third, evaporation may affect the flow in the orifice or the liquid sheet before breakup, which would effectively increase the initial cone angle at which the droplets are introduced. The effect of this possibility is explored in the next section.

In some ways, these three cases resemble the three evaporation cases described in Sec. 3.7 for the imaging experiments. The gradual-vapor-addition case has a high concentration of vapor in the core, but is not violent enough to significantly change the structure of the spray. The immediate-vapor-addition case then resembles the flash-boiling spray, with its narrow cylindrical shape, except for the lack of the increased initial cone angle.

5.2.4 Initial Cone Angle Increase

Since the modeling cases with vapor addition did not produce an increased initial cone angle, a few cases were run with an increased cone angle for the droplet introduction. As mentioned in the previous section, this is representative if the mechanism producing the increased cone angle occurs inside the injector or in the liquid sheet before breakup. The cone angle profile used is the upper one in Fig. 5.3. This was measured from the flash-boiling indolene spray images. The steady-state cone angle is 95 degrees.

Figure 5.10 shows the computed spray structures for these wide-cone-angle cases. The first case (VGW10) is analogous to the gradual-vapor-addition case in Fig. 5.8. The general structure is the same with the vapor core and toroidal vortex. The wide cone angle, however,

results in increased radial penetration and substantially decreased axial penetration. Figure 5.5 shows that the increase in cone angle reduced the penetration by about 20% after 3 ms (VG10 vs. VGW10). In the imaging experiments, the wider initial cone angle is accompanied by a rapid contraction keeping the overall width of the spray relatively small. In the modeling case, some contraction is observed in the liquid density profile, but not enough to be similar to the imaging experiments.

To encourage more contraction of the spray, the second case was run with a smaller droplet diameter distribution (VGW8). Compared with the previous case, this exhibits more contraction and, consequently, less radial penetration. However, it also reduces the axial penetration even further, as shown in Fig. 5.5.

Since the contraction in this case still did not appear sufficient, the third case in Fig. 5.10 was run with a larger difference between the inner and outer cone angles to enhance entrainment. Since only the outer cone angle can be measured from the images, it is possible that only a fraction of the droplets is thrown out to the larger cone angle. Therefore, this case was run with the wide outer cone angle and the inner cone angle from the standard case. Unfortunately, with the vapor-addition spray, this case proved to be highly unstable. This case was therefore run as an n-octane single spray (OT8). The profiles show a decreased radial penetration and an increased axial penetration. However, the spray is still too short and wide to resemble the images of the flash-boiling sprays.

A good representation of the flash-boiling sprays may require a wide or thick introductory cone angle with the immediate vapor-addition method. As shown in Fig. 5.8, the immediate vapor addition resulted in an increased axial penetration, which tended to draw out the spray giving it a thinner appearance. This is exactly the effect that is needed when a wide introductory cone angle is used. In addition, the mean droplet size may be significantly smaller in the early portion of the spray than at the PDPA measurement point, due to evaporation and/or coalescence.

5.3 EVAPORATION

The evaporation predicted by the spray model confirms some of the observations made of the spray profiles and shows a couple of effects that conflict with conventional wisdom developed from single-orifice sprays. The evaporation is shown in Figure 5.11 as the vapor mass normalized by the mass of fuel injected up to that time. The eight curves fall into two groupings separating the cases with vapor-generation sprays from those without. The vapor-addition curves quickly shoot up to about 20% as the n-heptane quickly evaporates. The curves are then relatively flat throughout injection since the n-heptane is evaporating as quickly as it is injected. The immediate-vapor-addition case (VI10) is slightly lower because the n-heptane was added by volume and its density is lower due to the higher temperature than in the other cases. The gradual-vapor-addition cases are noisy during injection due to an instability in the code that occurred whenever droplets were injected near their boiling point. In three or four consecutive time steps, few droplets would evaporate, followed by a large number evaporating in a single time step. After injection (> 2 ms), the three cases with 10-μm-SMD main sprays evaporated at nearly the same rate, while the 8-μm-SMD case (VGW8) evaporated more slowly due to its smaller penetration. After the initial transient in the vapor-addition cases evaporate at nearly the same rate as the n-dodecane spray (D10), suggesting that the n-dodecane in both situations is evaporating a nearly the same rate.

The effect of penetration on evaporation is shown more clearly in the n-octane cases. Contrary to intuition, the spray with the larger droplets (O16) evaporates much more quickly than the spray with smaller droplets (O8). This is due to the greater penetration of the coarser spray. The thick cone spray (OT8) also has a higher evaporation rate than the spray with the typical cone angle with the same droplet size distribution (O8), due to the greater radial penetration.

Another way to look at the evaporation is in its effect on the SMD of the spray. Figure 5.12 shows the SMD of the spray normalized by the SMD of the injected droplets for the cases without n-heptane droplets. The immediate-vapor-addition case (VI10) is included here because the n-heptane evaporated immediately. Except for initial transients, the mean droplet sizes decrease at a rate roughly proportional to the evaporation rate of the sprays. This is contrary to the conventional wisdom, which has the SMD increasing due to preferential evaporation of the smaller droplets. In the hollow-cone spray, however, the smaller droplets are drawn into the core of the spray. The gasses in the core of the spray are high in fuel vapor and cooler since they have been drawn through the spray sheet as well. The large droplets on the periphery are the ones that interact directly with the hot cylinder gasses. This supports the theory that the increase in SMD downstream measured with the PDPA is not due to preferential evaporation of the smaller droplets (Sec. 4.6.2). The immediate-vapor-addition case (VI10) has an initial increase likely due to the condensation of n-heptane discussed in Sec. 5.2.3.

Figure 5.13 shows a similar plot for the gradual-vapor-addition cases. Due to the rapid evaporation of the small n-heptane droplets, the curves rise quickly. After injection, the curves are nearly constant apparently because of a balance between the evaporation of the remaining n-heptane droplets and the SMD decrease due to evaporation of the main spray.

These results, in general, show that the location of a droplet, and consequently its environment, is more important than its diameter in determining its evaporation.

5.4 Conclusions

A computational fluid dynamics model with a spray sub-model was used to investigate the physics leading to the structure of the flash-boiling spray. Eight cases were run with changes to the inputs representing aspects of the flash-boiling spray. First, the mean droplet diameter was decreased to follow the PDPA measurements at low pressure and high temperature. Second,

rapid vapor production was added. Third, the outer cone angle was increased to match the imaging experiments.

The primary effect of the decreased droplet size was a decreased axial and radial penetration. The decreased axial penetration of the pre-spray agrees with the imaging experiments when droplet size is decreased due to increased temperature. The decreased width is consistent with imaging experiments of sprays with increasing temperature before the onset of flash boiling.

The vapor addition produced a column of vapor that runs down the axis of the spray increasing the gas velocity along the centerline. The column of vapor agrees with the hot spray images of the acetone-doped fuel mixtures (Sec. 3.7.4&5). When the vapor addition was immediately from the injector, rather than gradually within the spray, the gas velocities were increased sufficiently to cause increased penetration of the spray. This produced an elongated, columnar spray, which resembles the downstream structure of the flash-boiling sprays.

With the increased cone angle, even decreasing the SMD to 8 μm was insufficient to cause the contraction in the spray necessary to limit its radial penetration. The sprays, therefore, were too wide. Also, the axial penetration was too small. Therefore, since the increase in outer initial cone angle and the decrease in mean droplet size are known from the experiments, a high degree of vapor generation must be present to increase the axial penetration and elongate the spray. Since these high cone angles only occur at high levels of superheat, substantial vapor production is possible.

In addition, the evaporation characteristics shown in the model point out two interesting effects regarding the importance of the environment of the spray over its droplet diameter. First, the large-SMD spray, due to its greater penetration, was evaporating much more quickly than the small-SMD spray. Second, the SMD of the sprays decreased with evaporation, rather than increasing due to preferential evaporation of the smaller droplets, because the smaller droplets

are entrained into the interior of the spray where vapor concentrations are high and temperatures low.

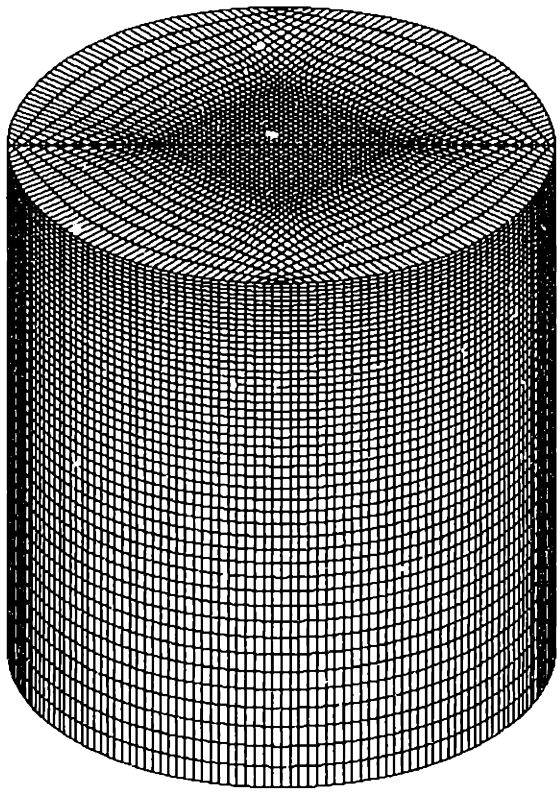

Figure 5.1: Grid divisions of computational domain. The horizontal line through the top face is the cut plane used for output of 2D profiles.

Table 5.1: Parameters of input droplet diameter distributions.

Main Spray	$y = e^{-a(x-b)^2}$ a	b	SMD (μm)	DV_{90} (μm)
1	0.009	8.5	16.3	25.0
2	0.027	6	10.2	15.4
3	0.040	5	8.4	12.6

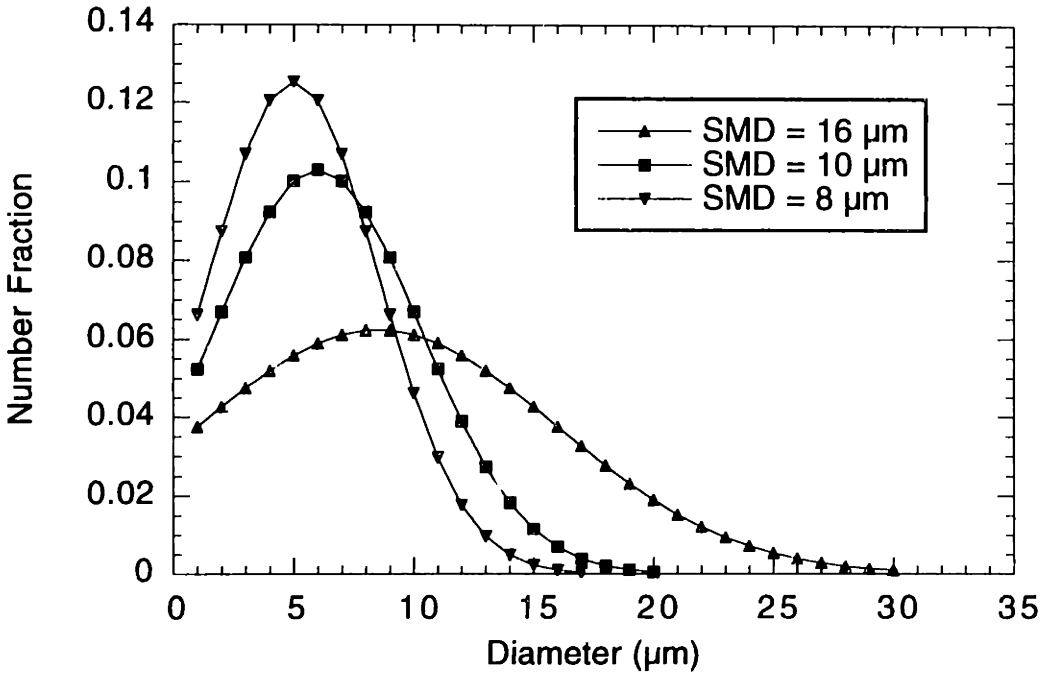

Figure 5.2: Histograms of primary-spray diameter distributions. Area under each curve is unity.

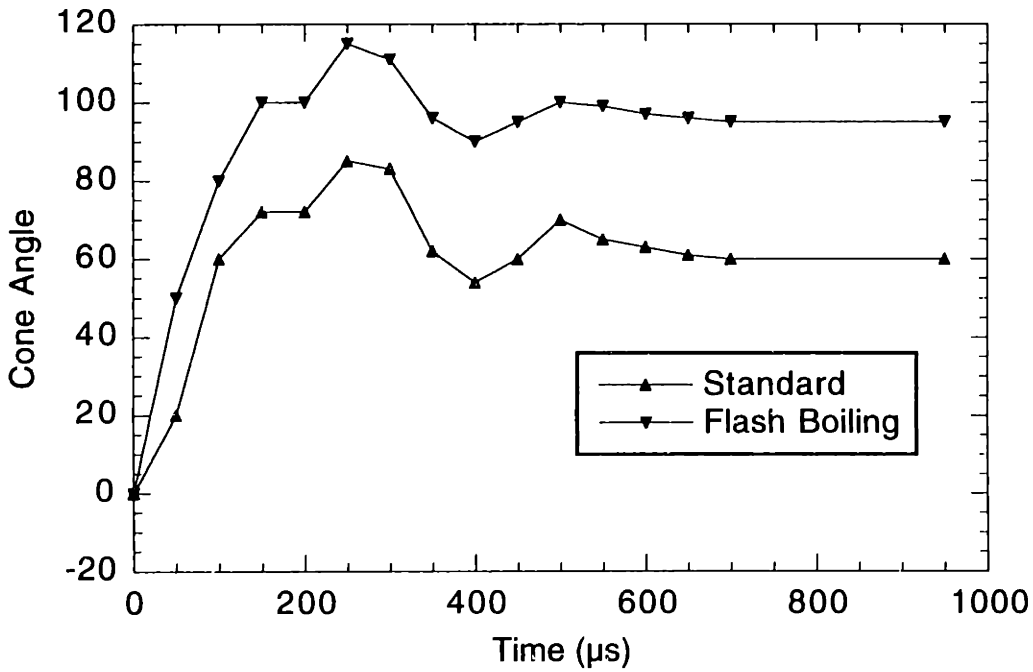

Figure 5.3: Plot of outer introductory cone angle during opening transient.

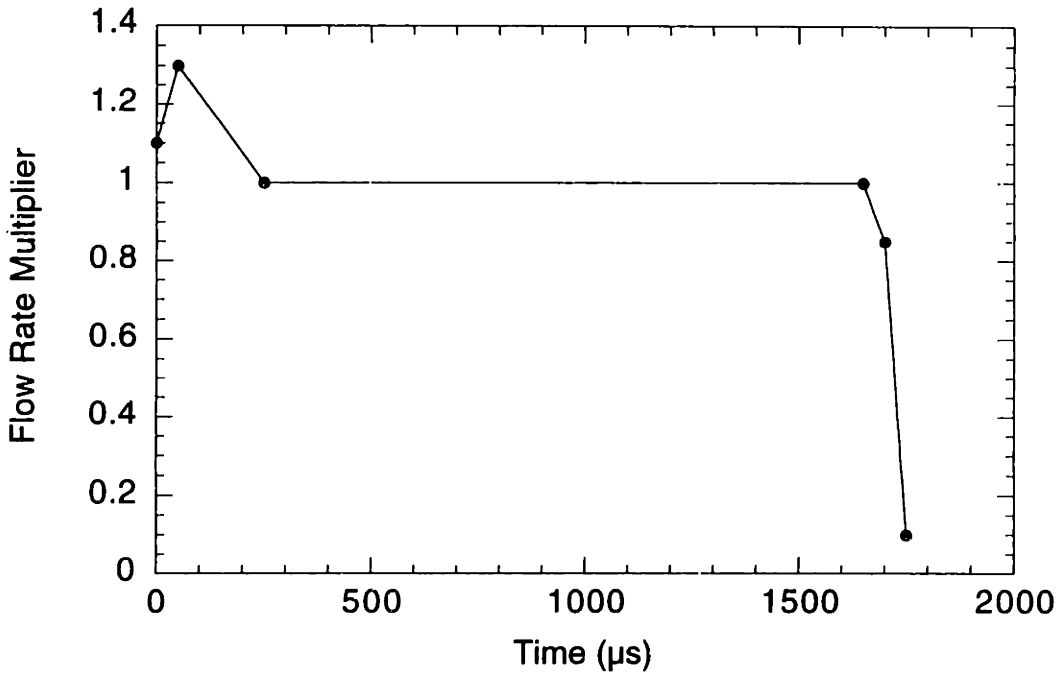

Figure 5.4: Flow rate multiplier as a function of time.

Table 5.2a: Modeling summary.

Test Name	File Name	Parameter Change	Cone Angle *(deg)*	Ovarall SMD *(μm)*	Computation Time *(CPU-hrs)*
O16	1	Baseline	50-60	16.3	31
O8	1b	Smaller SMD than O16	50-60	8.4	47
OT8	5	Thicker cone than O8	50-95	8.4	42
D10	2	Baseline for vapor addition	50-60	10.2	28
VI10	3	Vapor addition—immediate	50-60	10.2*	56
VG10	3b	Vapor addition—gradual	50-60	7.2	66
VGW10	4	Wider cone angle than VG10	85-95	6.7	72
VGW8	4b	Smaller SMD than VGW10	85-95	5.8	68

* due to immediate evaporation, n-heptane spray was not included in overall SMD calculation.

Table 5.2b: Modeling summary: spray quantities.

Test Name	Spray 1—Primary				Spray 2—Vapor Generating			
	Fuel	Q/Q_{TOT}	Temp. (K)	SMD (μm)	Fuel	Q/Q_{TOT}	Temp. (K)	SMD (μm)
O16	n-octane	1	303	16.3				
O8	n-octane	1	303	8.4				
OT8	n-octane	1	303	8.4				
D10	n-dodecane	1	363	10.2				
VI10	n-dodecane	0.75	333	10.2	n-heptane	0.25	463	3.3
VG10	n-dodecane	0.75	330	10.2	n-heptane	0.25	330	3.9
VGW10	n-dodecane	0.75	330	10.2	n-heptane	0.25	330	3.3
VGW8	n-dodecane	0.75	330	8.4	n-heptane	0.25	330	3.0

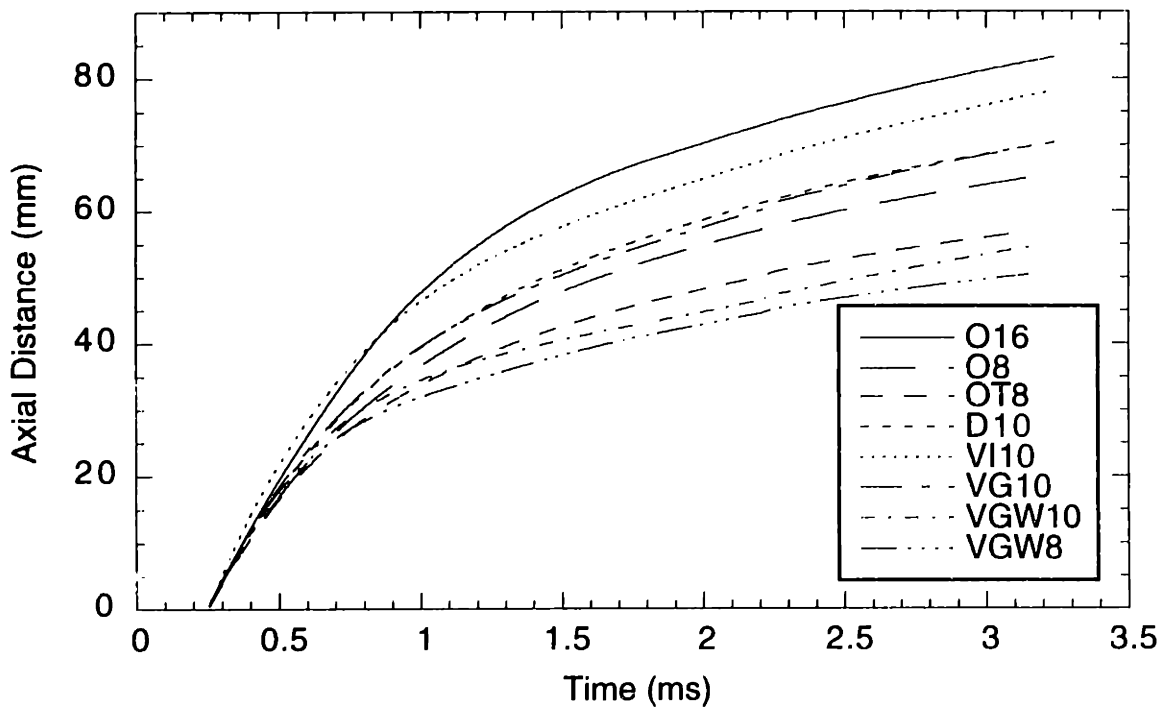

Figure 5.5: Axial penetration of leading edge of spray.

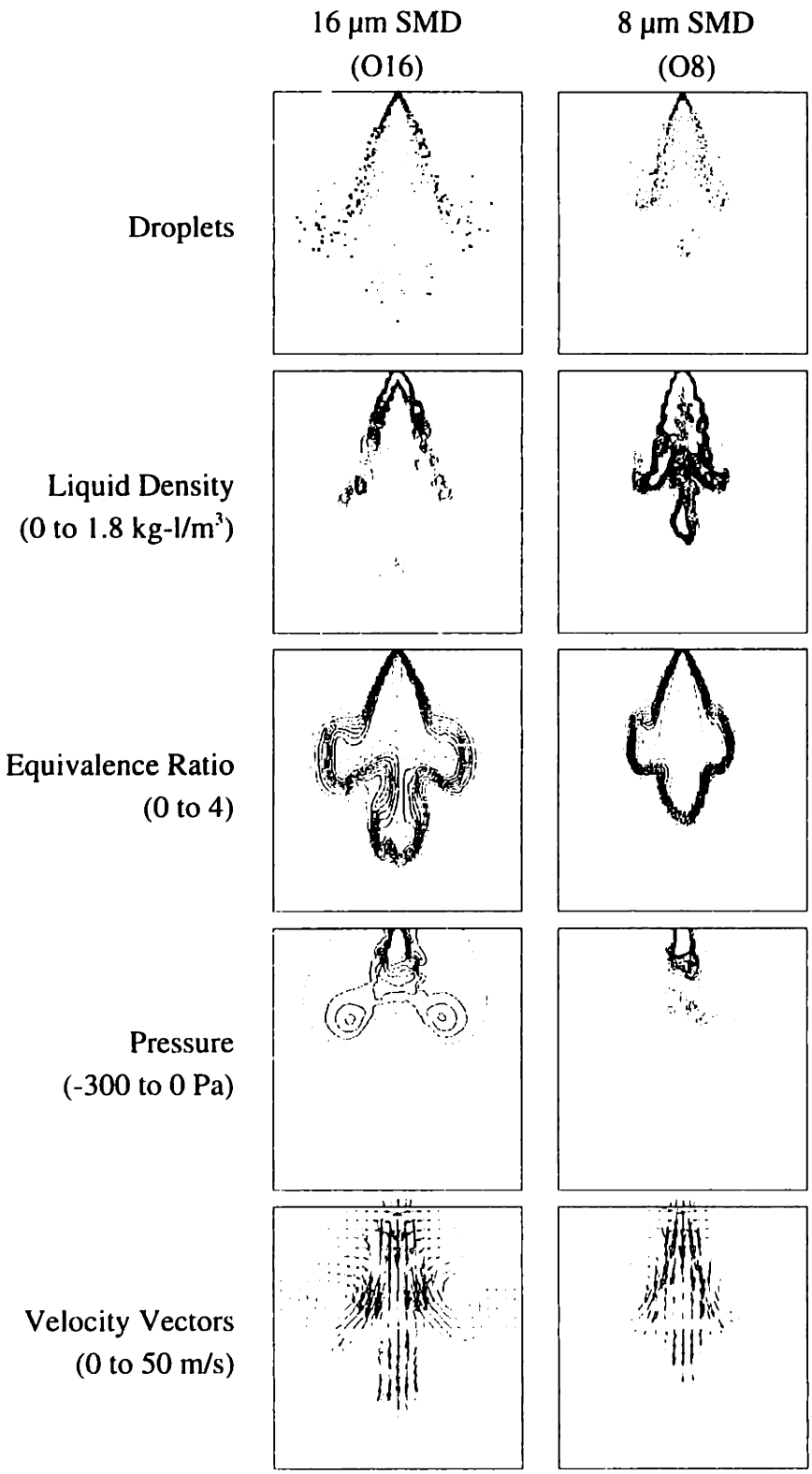

Figure 5.6: Effect of droplet diameter on spray structure. Comparison of case O16 and case O8 at 2 ms ASOI. Contour plots contain 11 contours separating 12 regions.

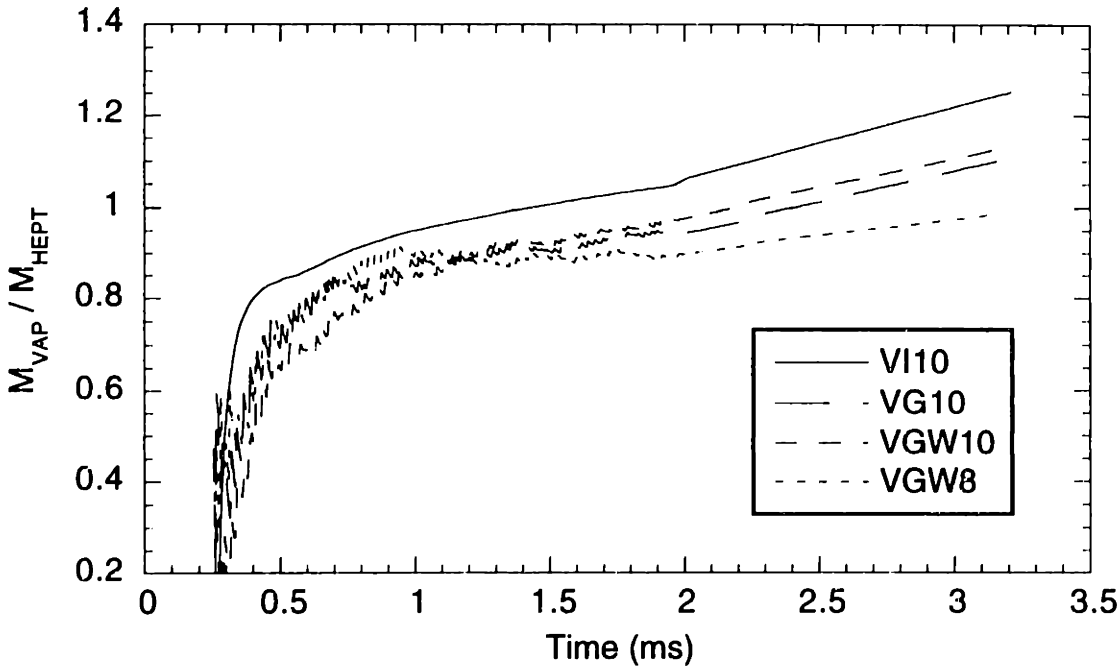

Figure 5.7: Vapor mass normalized by mass of heptane injected to that time for the four vapor-generation tests. Unity represents the idealized case in which all of the n-heptane has evaporated but none of the n-dodecane.

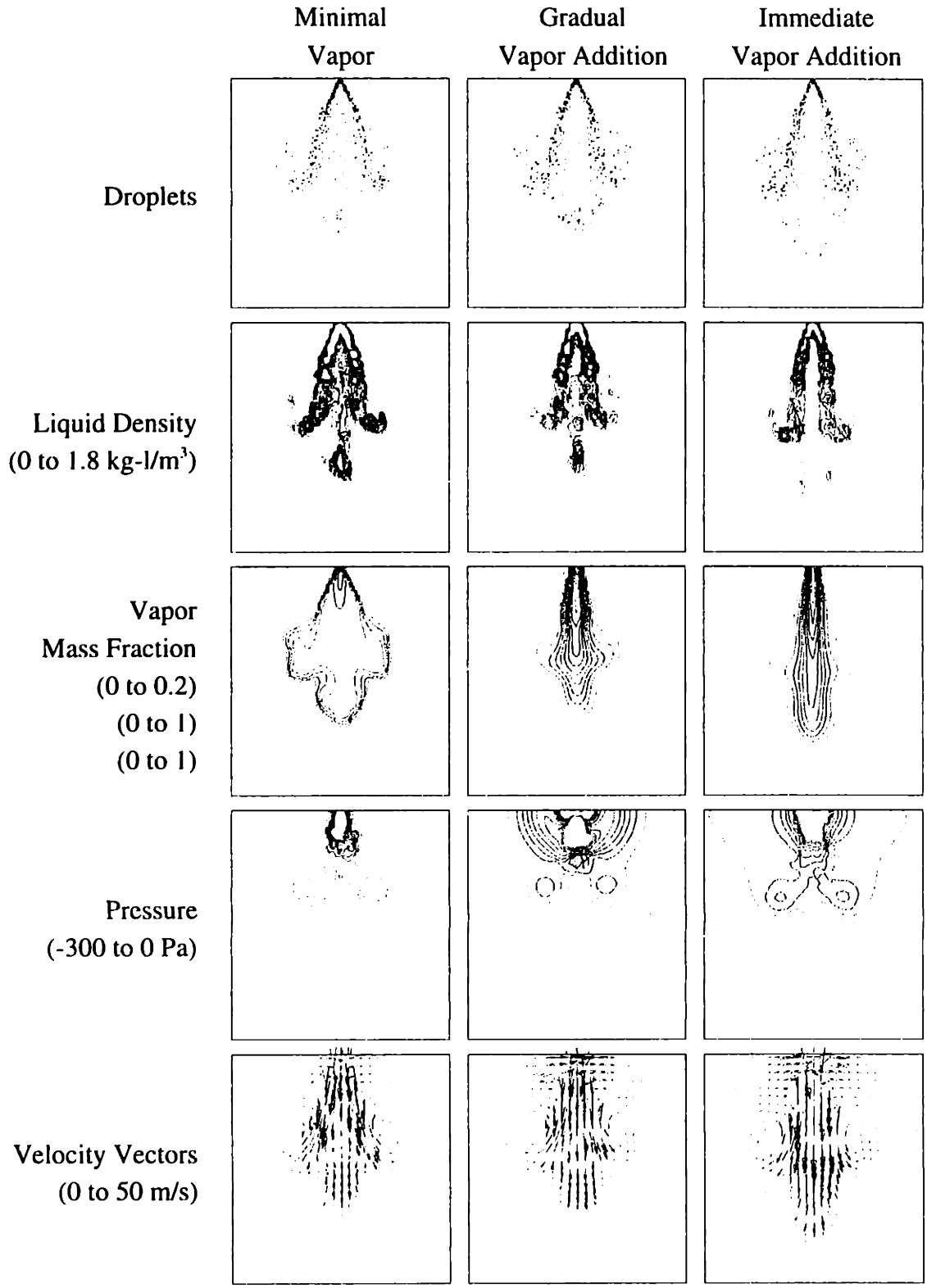

Figure 5.8: Effect of vapor generation on calculated spray structure. Comparison of cases D10, VG10, and VI10 at 2 ms ASOI. Contour plots contain 11 contours separating 12 regions.

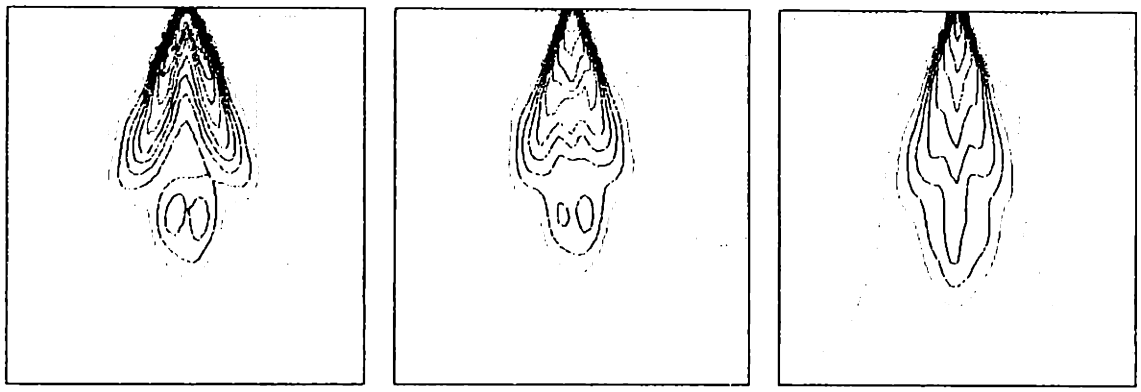

Minimal Vapor	Gradual Vapor Addition	Immediate Vapor Additon
D10	VG10	VI10
-59 to 6 m/s	-67 to 7 m/s	-100 to 9 m/s

Figure 5.9: Comparison of axial velocity profiles for vapor addition cases. Contour plots contain 11 contours separating 12 regions.

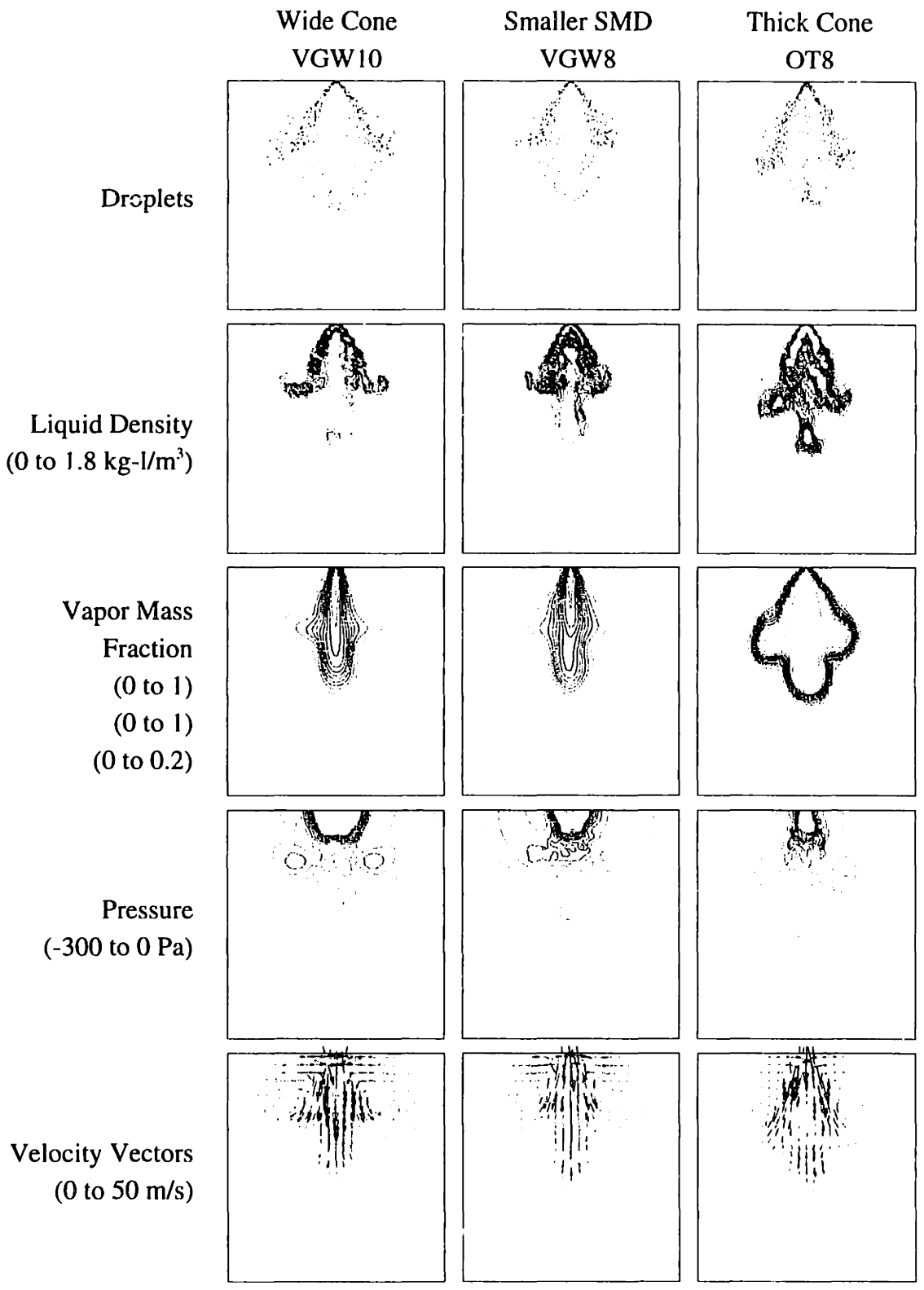

Figure 5.10: Comparison of calculated spray structures with increased introdutory cone angle. Contour plots contain 11 contours separating 12 regions.

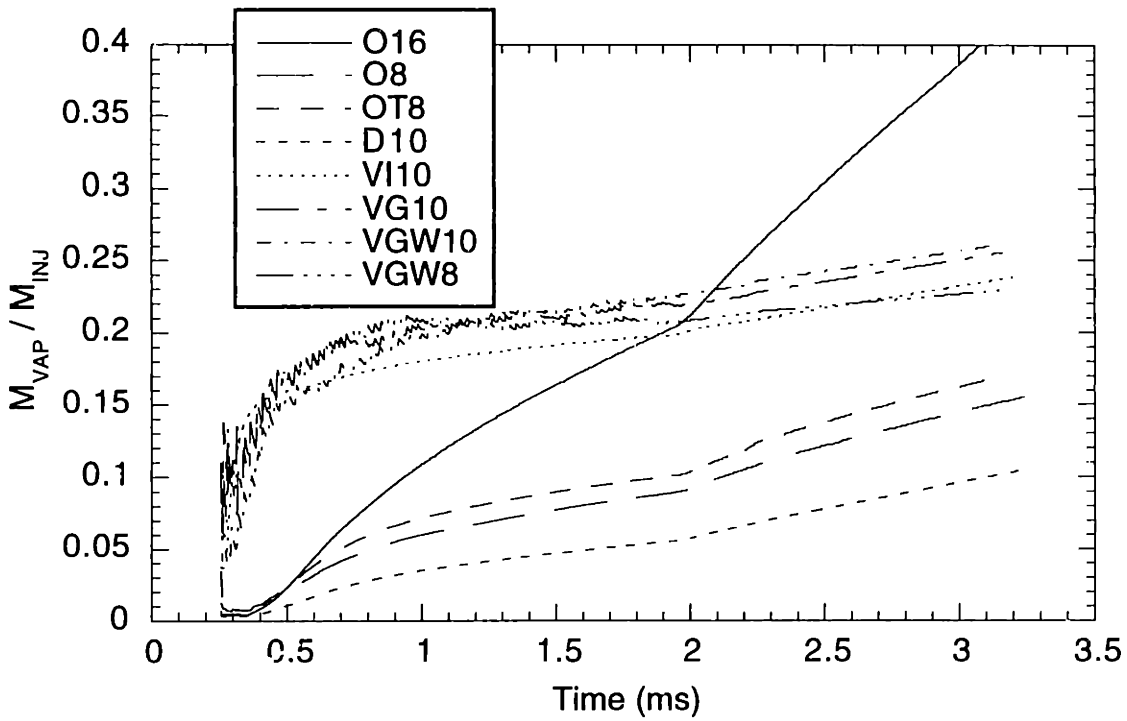

Figure 5.11: Vapor mass normalized by mass injected to that time. Injection ends at 2 ms.

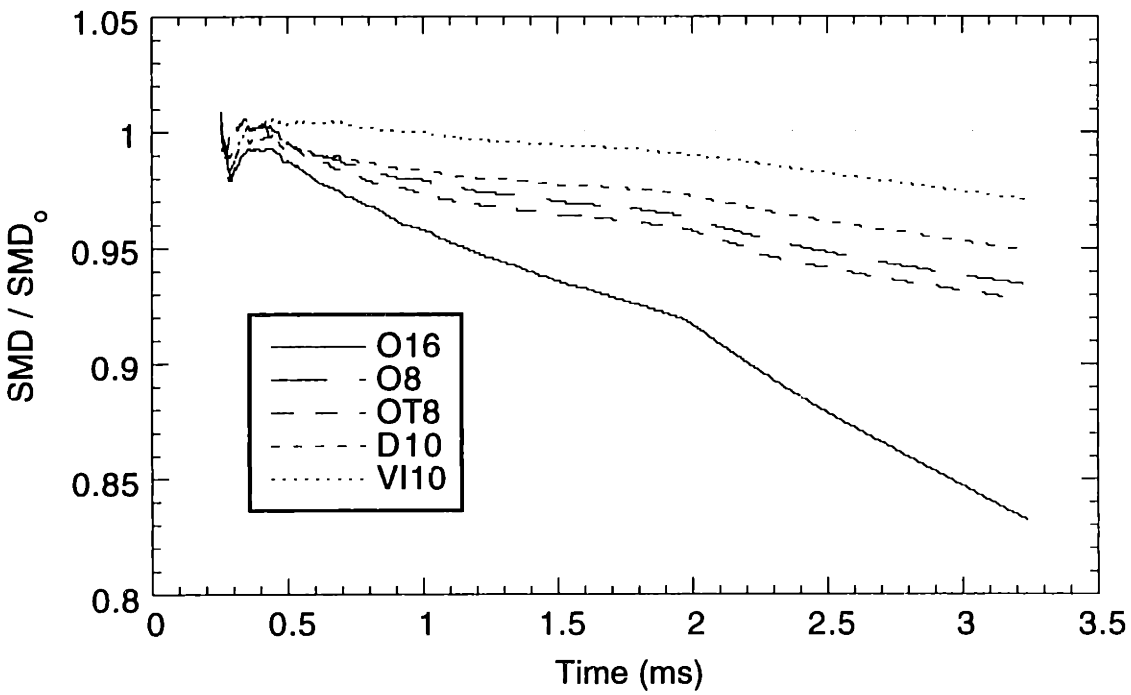

Figure 5.12: Sauter mean diameter of the spray normalized by value for the injected distribution.

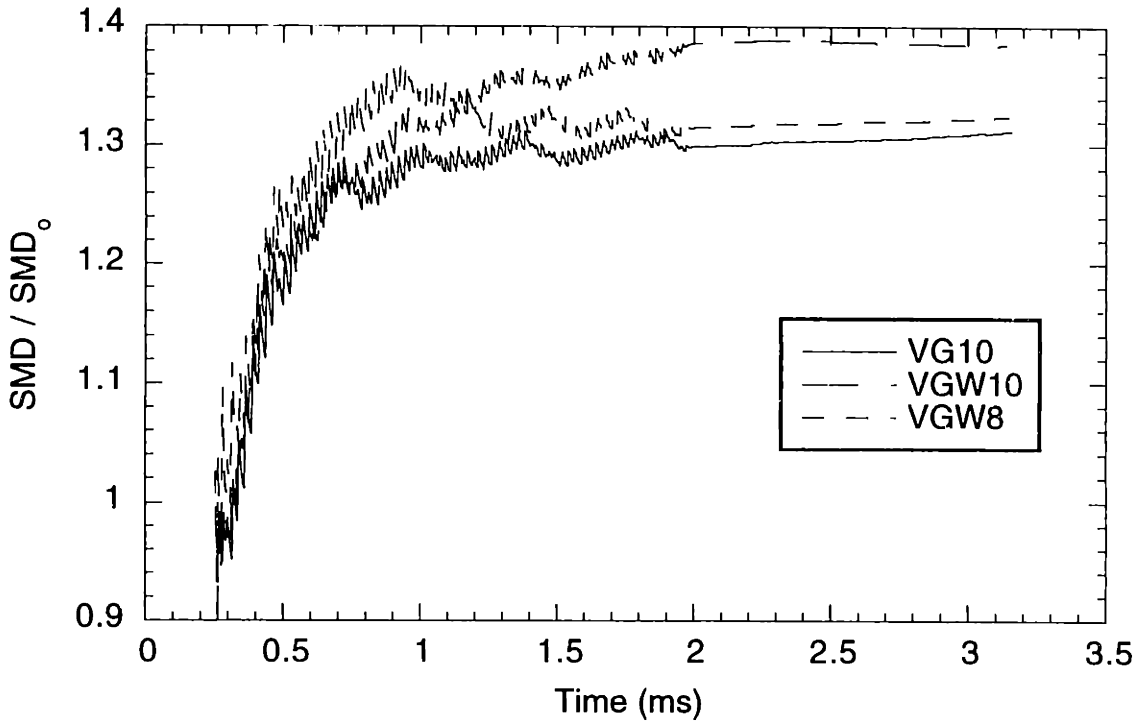

Figure 5.13: Sauter mean diameter of the spray of gradual-vapor-addition cases normalized by the value for the injected distribution.

CHAPTER 6

CONCLUSIONS

6.1 SPRAY STRUCTURE

In this study, the effects of engine operating conditions and fuel volatility on the spray from a pressure-swirl fuel injector were studied. The spray structure and droplet diameter distribution were observed over a wide range of engine temperatures and sub-atmospheric ambient pressures in an optically-accessible direct-injection spark-ignition engine. In addition, a 3D fluid dynamics and spray model was used to study the physics behind observed structural changes. The results of this work are summarized below.

1. Droplet mean diameter was found to decrease substantially with increasing fuel temperature and decreasing ambient density. Under conditions with a low potential for vaporization, the observed trends agree with published correlations for pressure-swirl atomizers covering this range of conditions ($P_A < 4$ bar).

2. Under conditions with a high potential for vaporization (low pressure, high temperature), an additional droplet size reduction mechanism was observed, which was associated with flash boiling or evaporation of the volatile components in the fuel. The predicted droplet diameter decrease due to the observed increase in initial cone angle is sufficient to explain this volatility-induced mechanism, suggesting that the vapor production increases the cone angle of the liquid sheet before breakup.

3. As conditions exceeded the boiling point of the fluid, rapid vaporization of light ends of the fuel was observed, resulting in a vapor core along the axis of the spray. This vapor core penetrated axially more quickly than the bulk of the droplets.

4. The spray penetration rate of the spray showed the following trends:
    a) The penetration rate of the pre-spray was higher under cold conditions than at hot conditions, due to the larger droplets. The penetration rate of the main spray was higher under hot conditions, however, due to the narrower shape of the spray and influence of the vapor production.
    b) The penetration rate was higher for low ambient pressure due to the lower drag on the droplets.
    c) The penetration rate was highest for early injection (90 °ATDCI) due to the bulk downward motion of the gasses. The penetration rate was the lowest for late injection timing (270 °ATDCI) due to the increased ambient density and bulk upward gas flow.
    d) The penetration rate was higher, on average, for light ends of the fuel due to the faster penetration of the vapor.
5. The width of the spray showed the following trends:
    a) The spray width was substantially larger under cold conditions due to the weaker interaction of the large droplets and the induced gas flows.
    b) The spray width was larger at low pressure due to the decreased influence of the gas flows.
    c) The spray width was largest for BDC injection. The width was smaller for early injection (90 °ATDCI) possibly due to the influence of the bulk downward flow. The width was smallest for late injection timing (270 °ATDCI) due to the increased ambient density.
    d) The spray width was larger, on average, for heavier ends of the fuel due to lighter ends being drawn to the axis of the spray when vaporized.
6. The droplet size was shown to increase further downstream. This effect was concluded to be due to coalescence, not preferential evaporation of the smaller droplets.

7. While flash boiling affected the spray throughout the spray development, similar stages of development were observed compared with the cold sprays. This suggests that the internal flows of the injector are not severely affected by the flash boiling.

8. Intake flows were shown to disrupt the spray structure for early injection (90 °ATDCI). The sprays injected at this timing also exhibited greater effects due to flash boiling. This is believed to be caused by decreased ambient pressure due to intake restrictions and increased ambient temperature due to the higher fraction of residual gas.

9. Recreation of the observed flash-boiling spray structure with the CFD model appears to require an increased initial cone angle, a very small droplet diameter distribution, and substantial vapor generation near the point of injection.

6.2 Diagnostic Concerns

In the process of this work, some insights have been gained into the operation of laser sheet imaging and phase-Doppler particle analysis with dense sprays. These observations are summarized below.

1. As the droplet size decreases for a fixed mass flow rate, the optical density of the spray increases. In the imaging experiments, this causes scattering of the laser sheet, which illuminates regions of the spray not aligned with the sheet. Since the intensity of the images corresponds to projection through the spray, the intensity in the interior regions of the spray increases.

2. In the extreme, when droplets are very small, light reaching the camera is no longer a projection through the spray. Instead, the light from the interior or back of the spray is significantly scattered before reaching the camera, resulting in a top-hat intensity profile for experiments imaging the droplets (Mie scattering, PLIF with low-volatility dopant). This

transition was shown to occur around an SMD of 20 μm for a spray at atmospheric ambient pressure.

3. PLIF images of primarily vapor, as in the case of flash boiling sprays with acetone dopant, appear as projections through the spray even when the droplets are very small (see Sec. 3.10). This effect is apparently due to the concentrating of the vapor in the core of the spray where the spray density is lower.

4. The PDPA measurements showed a 95% reduction in the number of droplets measured due to scattering when either the laser beams or the scattered light passed through the bulk of the spray. For measurements of the interior of the spray, both the laser beams and the scattered light pass through the spray sheet.

5. The majority of the droplets measured at locations interior to the spray with the PDPA were observed after the end of injection due to the excessive scattering during injection. This biasing resulted in a lower value for the mean velocity of droplets near the centerline.

6. The high optical density of the spray suggests that the use of any optical diagnostic to probe the interior of the spray cone would be difficult.

6.3 Impact on DISI Engines

The impact of these results on DISI engine design and operation is primarily through the changes in fuel distribution caused by the reduction in mean droplet diameter and vapor generation at high fuel temperatures and low ambient densities. Therefore, the impact is greatest under throttled, early-injection conditions in a warmed-up engine. Under these conditions, the droplets are very small and the spray is narrow. The lack of significant radial penetration, may inhibit the formation of a homogeneous charge in some cases. Despite the fact that the modeling suggests that the smaller-SMD sprays initially evaporate more slowly, later in the

cycle, as the spray interacts with the cylinder flows and the combustion chamber surfaces, the smaller-SMD spray should evaporate more quickly. The smaller droplets do appear to evaporate more quickly since the combustion was typically significantly less sooty under warmed-up conditions.

In addition, the decreased droplet diameter at increased temperature would greatly decrease the likelihood of wall wetting. Not only do the smaller droplets follow the gas flow more closely when interacting with a surface, but also the penetration of the pre-spray is greatly slowed at the increased temperature. At least for the Chrysler injector, the pre-spray appears to be of little concern at operating temperatures, since it does not separate from the body of the spray. The idea of purposefully heating the fuel is intriguing since the resulting smaller droplets may decrease wall wetting and decrease the number and size of droplets present at the time of the combustion. This has the potential of reducing hydrocarbon and particulate emissions during engine warm-up.

In general, cold bench tests and motored engine tests of the spray will misrepresent some aspects of the spray due to the larger droplets compared with the warmed-up engine. One method of reducing the differences would be to use a fluid that produces smaller droplets. The correlations shown in Sec. 4.6.7 can be used to estimate the mean droplet diameters produced by different fluids. For example, 2-methylbutane at room temperature produces droplet diameters similar to indolene at 100 °C.

6.4 Recommendations for Modeling

The modeling work described in Chapter 5 suggests a few points to consider when modeling pressure-swirl sprays under a variety of engine operating conditions.

1. The droplet diameter distribution varies significantly with fuel temperature and ambient density. The operating conditions covered in the PDPA experiments varied in SMD by

nearly a factor of three. The droplet diameter distribution has significant effects on axial and radial penetration as well as evaporation.

2. Rapid vapor production produces a vapor core in the spray and can influence the axial and radial penetration. Accurate representation of the vapor production would require an evaporation model for multi-component fuels that handles superheat of the fluid appropriately. In addition, significant flash boiling may be occurring inside the injector, the effects of which could not be modeled directly with the type of model used here. Artificial addition of vapor, such as that done in this work, appears to be most effective right at the injector tip.

3. Reproduction of the flash boiling spray structure requires an increased introductory cone angle for the droplets. A very small droplet diameter distribution and significant vapor generation were then found necessary to narrow the spray and increase the axial penetration to resemble the observations of the imaging experiments.

REFERENCES

1. Fraidl, G., Piock, W., and Wirth, M. "Gasoline Direct Injection: Actual Trends and Future Strategies for Injection and Combustion Systems," *SAE Paper* 960465 (1996).
2. Harada, J., Tomita, T., Mizuno, H., Mashiki, Z., and Ito, Y. "Development of Direct Injection Gasoline Engine," *SAE Paper* 970540 (1997).
3. Takagi, Y., Itoh, T., Muranaka, S., Iiyama, A., Iwairi, Y., Urushihara, T., and Naitoh, K. "Simultaneous Attainment of Low Fuel Consumption, High Output Power and Low Exhaust Emissions in Direct Injection SI Engines," *SAE Paper* 980149 (1998).
4. Houston, R. and Cathcart, G. "Combustion and Emissions Characteristics of Orbital's Combustion Process Applied to Multi-Cylinder Automotive Direct Injected 4-Stroke Engines." *SAE Paper* 980153 (1998).
5. Iwamoto, Y., Noma, K., Nakayama, O., Yamauchi, T., and Ando, H. "Development of Gasoline Direct Injection Engine," *SAE Paper* 970541 (1997).
6. Simko, A., Choma, M., and Repko, L. "Exhaust Emission Control by the Ford Programmed Combustion Process–PROCO," *SAE Paper* 720052 (1972).
7. Haslett, R.A., Monaghan, M.L., and McFadden, J.J. "Stratified Charge Engines," *SAE Paper* 760755 (1976).
8. Zhao, F., Lai, M., and Harrington, D.L. "A Review of Mixture Preparation and Combustion Control Strategies for Spark-Ignited Direct-Injection Gasoline Engines," *SAE Paper* 970627 (1997).
9. Scussel, A., Simko, A., and Wade, W. "The Ford PROCO Engine Update," *SAE Paper* 780699 (1978).
10. Jackson, N., Stokes, J., Whitaker, P., and Lake, T. "Stratified and Homogeneous Charge Operation for the Direct Injection Gasoline Engine – High Power with Low Fuel Consumption and Emissions," *SAE Paper* 970543 (1997).
11. Yang, J. and Anderson, R. "Fuel Injection Strategies to Increase Full-Load Torque Output of a Direct-Injection SI Engine," *SAE Paper* 980495 (1998).
12. Noma, K., Iwamoto, Y., Murakami, N., Iida, K., and Nakayama, O. "Optimized Gasoline Direct Injection Engine for the European Market," *SAE Paper* 980150 (1998).
13. Preussner, C., Döring, C. Fehler, S., and Kampmann, S. "GID: Interaction Between Mixture Preparation, Combustion System and Injector Performance," *SAE Paper* 980498 (1998).
14. Zhao, F., Yoo, J., Liu, Y., and Lai, M. "Spray Dynamics of High Pressure Fuel Injectors for DI Gasoline Engines," *SAE Paper* 961925 (1996).
15. Salters, D., Williams, P., Grieg, A., and Brehob, D. "Fuel Spray Characterization within an Optically Accessed Gasoline Direct Injection Engine Using a CCD Imaging System," *SAE Paper* 961149 (1996).

16. Shelby, M., VanDerWege, B., and Hochgreb, S. "Early Spray Development in Gasoline Direct-Injected Spark Ignition Engines," *SAE Paper* 980160 (1998).
17. Shiriashi, T., Nakayama, T., Nogi, T., and Ohsuga, M. "Effect of Spray Characteristics on Combustion in a Direct Injection spark Ignition Engine," *SAE Paper* 980156.
18. Parrish, S. and Farrell, P. "Transient Spray Characteristics of a Direct-Injection Spark-Ignited Fuel Injector," SAE Paper 970629 (1997).
19. Pontoppidan, M., Gaviani, G., Bella, G., and Rocco, V. "Direct Fuel Injection – A Study of Injector Requirements for Different Mixture Preparation Concepts," *SAE Paper* 970628 (1997).
20. Hoffman, J., Khatri, F., Martin, J., and Coates, S. "Mass-Related Properties of Atomizers for Direct-Injection SI Engines," *SAE Paper* 980500 (1998).
21. Hoffman, J., Eberhardt, E., and Martin J. "Comparison Between Air-Assisted and Single-Fluid Pressure Atomizers for Direct-Injection SI Engines Via Spatial and Temporal Mass Flux Measurements," *SAE Paper* 970630 (1997).
22. Davy, M., Williams, P., and Anderson, R. "Effects of Injection Timing on Liquid-Phase Fuel Distributions in a Centrally-Injected Four-Valve Direct-Injection Spark-Ignition Engine," *SAE Paper* 98FL-375 (1998).
23. Brown, R. and York, J. "Sprays Formed by Flashing Liquid Jets," *A.I.Ch.E. Jour.* Vol. 8, No. 2, pp. 149-153 (1962).
24. Lienhard, J. and Day, J. "The Breakup of Superheated Liquid Jets," *ASME J. Basic Eng.* Vol. 92, pp. 515-522 (1970).
25. Solomon, A., Rupprecht, S., Chen, L., and Faeth, G. "Flow and Atomization in Flashing Injectors," *Atom. and Spray Tech.* Vol. 1, pp. 53-76 (1985).
26. Zeigerson-Katz, M. and Sher, E. "Fuel Atomization by Flashing of a Volatile Liquid in a Liquid Jet," *SAE Paper* 960111 (1996).
27. Oza, R. and Sinnamon, J. "An Experimental and Analytical Study of Flash-Boiling Fuel Injection," *SAE Paper* 830590 (1983).
28. Senda, J., Nishikori, T., Tsukamoto, T., and Fujimoto, H. "Atomization of Spray under Low-Pressure Field from Pintle Type Gasoline Injector," *SAE Paper* 920382 (1992).
29. Senda, J., Hojyo, Y., and Fujimoto, H. "Modeling of Atomization Process in Flash Boiling Spray," *SAE Paper* 941925 (1994).
30. Adachi, M., McDonell, V., Tanaka, D., Senda, J., and Fujimoto, H. "Characterization of Fuel Vapor Concentration Inside a Flash Boiling Spray," *SAE Paper* 970871 (1997).
31. Aquino, C., Plensdorf, W., Lavoie, G., and Curtis, E. "The Occurrence of Flash Boiling in a Port Injected Gasoline Engine," *SAE Paper* 982522 (1998).
32. Shelby, M. "PLIF Investigation of the Fuel Distribution in Gasoline Direct Injection Fuel Sprays." Master's Thesis, Massachusetts Institute of Technology, June 1997.

33. Itoh, T., Kakuko, A, Hinushima, H., Urushiahara, T., Takagi, Y., Horie, K., Asano, M., Ogata, E., and Yamasita, T. "Development of a New Compound Fuel and Fluorescent Tracer Combination for Use with Laser Induced Fluorescence," *SAE Paper* 952465 (1995).
34. Fujikawa, T., Yoshiaki, H., and Akihama, K. "Quantitative 2-D Fuel Distribution Measurements in an SI Engine Using Laser-Induced Fluorescence with Suitable Combination of Fluorescence Tracer and Excitation Wavelength." *SAE Paper* 972944 (1997).
35. Lawrenz, W., Köhler, J., Meier, F., Stolz, W., Wirth, R., Bloss, W.H., Maly, R., Wagner, E., and Zahn, M. "Quantitative 2D LIF Measurements of Air/Fuel Ratios During the Intake Stroke in a Transparent SI Engine." *SAE Paper* 922320 (1992).
36. Hansen, A. and Lee, E. "Radiative and Nonradiative Transitions in the First Excited Singlet State of Symmetrical Methyl-Substituted Acetones." *J. Chem. Phys.*, Vol. 62, No. 1, pp. 183-189 (1975).
37. Goody, R. Principles of Atmospheric Physics and Chemistry. Oxford Press, New York, pp. 75-83, 1995.
38. Phase Doppler Particle Analyzer Installation Guide, Aerometrics, Inc., Release 3.0, 1987.
39. Bachalo, W. and Houser, M. "Development of the Phase/Doppler Spray Analyzer for Liquid Drop Size and Velocity Characterizations." AIAA-84-1199 (1984).
40. Dodge, L., Rhodes, D., and Reitz, R. "Drop-size Measurement Techniques for Sprays: Comparison of Malvern Laser-Diffraction and Aerometrics Phase/Doppler." *Appl. Opt.*, Vol. 26 No. 11, p. 2144-54 (1987).
41. Aerometrics Inc. Optical patternator.
42. Glaspie, C. DaimlerChrysler AETG, private communication.
43. Jakob, M. Heat Transfer. John Wiley &Sons, New York, pp. 262-3, 1949.
44. Green, D.W. Perry's Chemical Engineers' Handbook, (7th. ed.), McGraw-Hill, New York, pp. 13.16-13.26, 1997.
45. Himmelblau, D.M. Basic Principles and Calculations in Chemical Engineering, (6th. ed.). Prentice Hall, New Jersey, pp. 328,329, 1996.
46. Gmehling, J., Onken, U., and Rarey, J. Vapor-Liquid Equilibrium Data Collection: Ketones (Supplement 1), Chemistry Data Series, Vol. 1, Part 3b, DECHEMA, Germany, 1993.
47. Lefebvre, A. Atomization and Sprays. Hemisphere, New York pp. 165-222 (1989).
48. vanStralen, S. and Cole, R. Boiling Phenomena: Physicochemical and Engineering Fundamentals and Applications (Vol. 1). Hemisphere, Washington, pp. 89-94 (1979).
49. Owen, K. and Coley, T. Automotive Fuels Handbook. SAE, Warrendale, PA, pp. 564-6, 1990.
50. Annual Book of ASTM Standards: Section 5. American Society of Testing and Materials, 1996.

51. Fujikawa, T., Hattori, Y., and Akihama, K. "Quantitative 2-D Fuel Distribution Measurements in an SI Engine Using Laser-Induced Fluorescence with Suitable Combination of Fluorescence Tracer and Excitation Wavelength." *SAE Paper* 972944 (1997).
52. Heywood, J. Internal Combustion Engine Fundamentals. McGraw-Hill, New York, pp. 113, 1988.
53. Schetz. J. and Fuhs, A. Handbook of Fluid Dynamics and Fluid Machinery: Volume I. John Wiley & Sons, New York, pp. 156, 1996.
54. Spray User's Guide: FIRE Version 7. AVL LIST GmbH (1998).
55. Dukowicz, J. "A Particle-Fluid Numerical Model for Liquid Sprays." *J. Comp. Physics*, 35; pp. 229-253 (1980).
56. Dukowicz, J. "Quasi-Steady Droplet Change in the Presence Of Convection; Informal Report; Los Alamos Scientific Laboratory." LA7997-MS.
57. Glaspie, C., Jaye, J., Lawrence, T., Lounsberry, T., Mann, L., Opra, L., Roth, D., and Zhao, F. "Application of Design and Development Techniques for Direct Injection Spark Ignition Engines." *SAE Paper* 1999-01-0506 (1999).

APPENDIX 1
ENGINE CONTROLLER MODIFICATIONS

Skip-fire mode of the engine controller was designed to minimize warm-up of the engine during an experiment. To accomplish this, the engine is only fired for a limited number of cycles before each image and then motored while the camera transmits the image to the computer. Since the DI fuel system has no fuel storage mechanism, like port fuel injection, the fuel can be shut off and restarted on a cycle to cycle basis. This is preferable to turning off the spark on the motored cycles since no unburned fuel is sent into the exhaust.

Under continuous firing conditions, the camera is triggered every cycle. It then takes the image whenever it is ready. For skip-firing, the camera needs to be synchronized with the series of firing and motoring cycles. The previous version of the LabVIEW-based engine controller [1] was set up to deliver a pulse (Trigger Cycle) coincident with BDC of the desired cycle to a DCI counter. For more accurate timing, the camera system is triggered by the injection signal itself. In order to make the Trigger Cycle signal coincident with the injection signal, modifications to the controller were necessary.

First, the source of the Trigger Cycle counter (counter #9) was wired to the output of the Injection Duration counter (counter #8) rather than to the BDC input. Second, in order to allow the Trigger Cycle to coincide with the last fired cycle in each series, modifications to the software were necessary.

---

1. Shelby, M., "PLIF Investigation of the Fuel Distribution in Gasoline Direct Injection Fuel Sprays," Master's Thesis, Massachusetts Institute of Technology (1997).

APPENDIX 2
IMAGING SEQUENCING PROGRAM

The following is a sample DOS batch file used to program the PG200 for sequencing of PLIF images. See Princeton Instruments PG200 manual for explanation of commands.

```
c:\pg200\clearseq 2
c:\pg200\pgwidth 2 0.20 U
c:\pg200\pgsynmod 2 0 0
c:\pg200\pgtrgmod 2 1
c:\pg200\pgaux 2 396.00 U
c:\pg200\pgdelo 2 396.40 U
c:\pg200\pgdelay 2 400.00 U
c:\pg200\addseq 2
c:\pg200\pgaux 2 596.00 U
c:\pg200\pgdelo 2 596.40 U
c:\pg200\pgdelay 2 600.00 U
c:\pg200\addseq 2
c:\pg200\pgaux 2 796.00 U
c:\pg200\pgdelo 2 796.40 U
c:\pg200\pgdelay 2 800.00 U
c:\pg200\addseq 2
c:\pg200\pgaux 2 996.00 U
c:\pg200\pgdelo 2 996.40 U
c:\pg200\pgdelay 2 1000.00 U
c:\pg200\addseq 2
c:\pg200\pgaux 2 1196.00 U
c:\pg200\pgdelo 2 1196.40 U
c:\pg200\pgdelay 2 1200.00 U
c:\pg200\addseq 2
c:\pg200\pgaux 2 1596.00 U
c:\pg200\pgdelo 2 1596.40 U
c:\pg200\pgdelay 2 1600.00 U
c:\pg200\addseq 2
c:\pg200\pgaux 2 1996.00 U
c:\pg200\pgdelo 2 1996.40 U
c:\pg200\pgdelay 2 2000.00 U
c:\pg200\addseq 2
c:\pg200\pgaux 2 2396.00 U
c:\pg200\pgdelo 2 2396.40 U
c:\pg200\pgdelay 2 2400.00 U
c:\pg200\addseq 2
c:\pg200\pgaux 2 2796.00 U
c:\pg200\pgdelo 2 2796.40 U
c:\pg200\pgdelay 2 2800.00 U
c:\pg200\addseq 2
c:\pg200\pgaux 2 3196.00 U
c:\pg200\pgdelo 2 3196.40 U
c:\pg200\pgdelay 2 3200.00 U
c:\pg200\addseq 2
```

APPENDIX 3
PDPA SETUP SCREENS

The following are the copies of the setup screens for the PDPA system. The software version is 5.22.

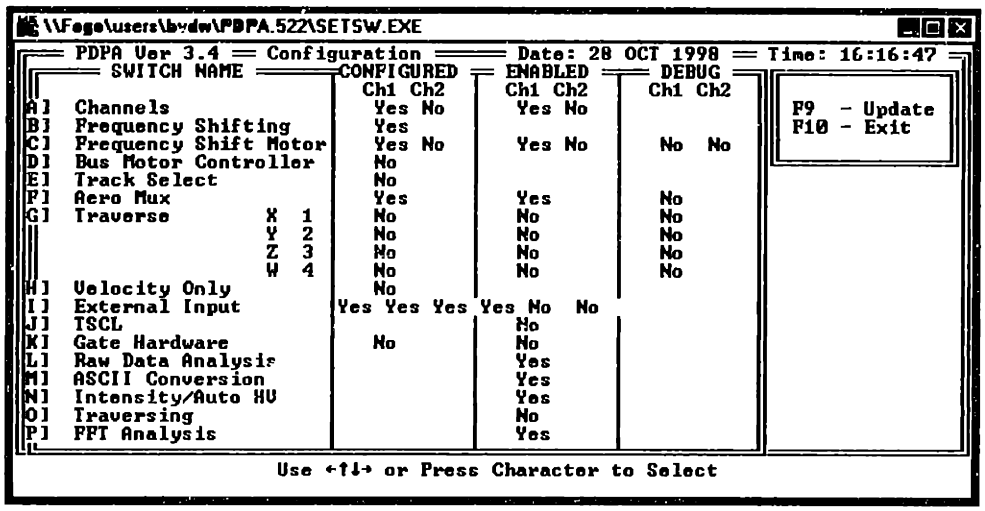

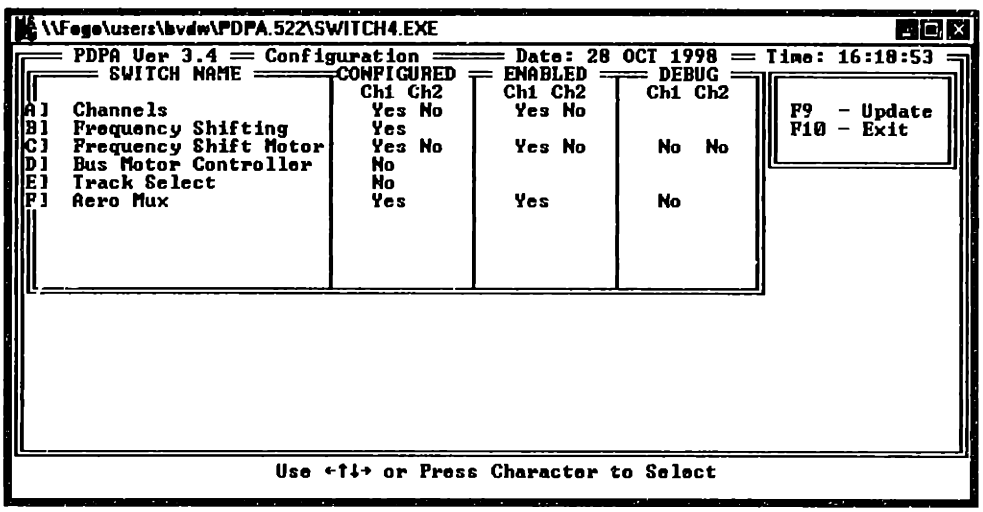

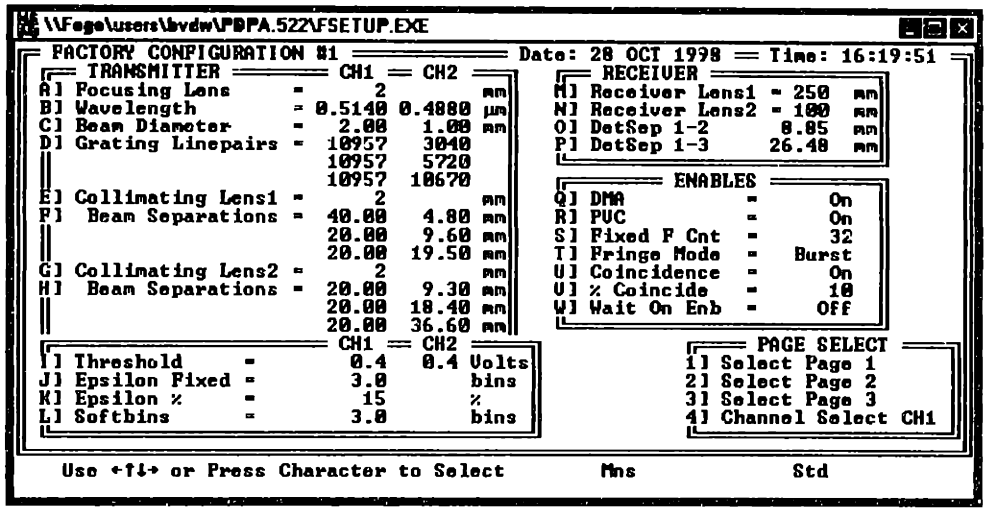
\\Fogo\users\bvdw\PDPA.522\FSETUP.EXE
FACTORY CONFIGURATION #1
Date: 28 OCT 1998
Time: 16:19:51
TRANSMITTER
CH1 CH2
A] Focusing Lens = 2 mm
B] Wavelength = 0.5140 0.4880 µm
C] Beam Diameter = 2.00 1.00 mm
D] Grating Linepairs = 10957 3040
10957 5720
10957 10670
E] Collimating Lens1 = 2 mm
F] Beam Separations = 40.00 4.80 mm
20.00 9.60 mm
20.00 19.50 mm
G] Collimating Lens2 = 2 mm
H] Beam Separations = 20.00 9.30 mm
20.00 18.40 mm
20.00 36.60 mm
RECEIVER
M] Receiver Lens1 = 250 mm
N] Receiver Lens2 = 100 mm
O] DetSep 1-2 = 8.85 mm
P] DetSep 1-3 = 26.48 mm
ENABLES
Q] DMA = On
R] PUC = On
S] Fixed F Cnt = 32
T] Fringe Mode = Burst
U] Coincidence = On
V] % Coincide = 10
W] Wait On Enb = Off
CH1 CH2
I] Threshold = 0.4 0.4 Volts
J] Epsilon Fixed = 3.0 bins
K] Epsilon % = 15 %
L] Softbins = 3.0 bins
PAGE SELECT
1] Select Page 1
2] Select Page 2
3] Select Page 3
4] Channel Select CH1
Use ←↑↓→ or Press Character to Select
Mns
Std

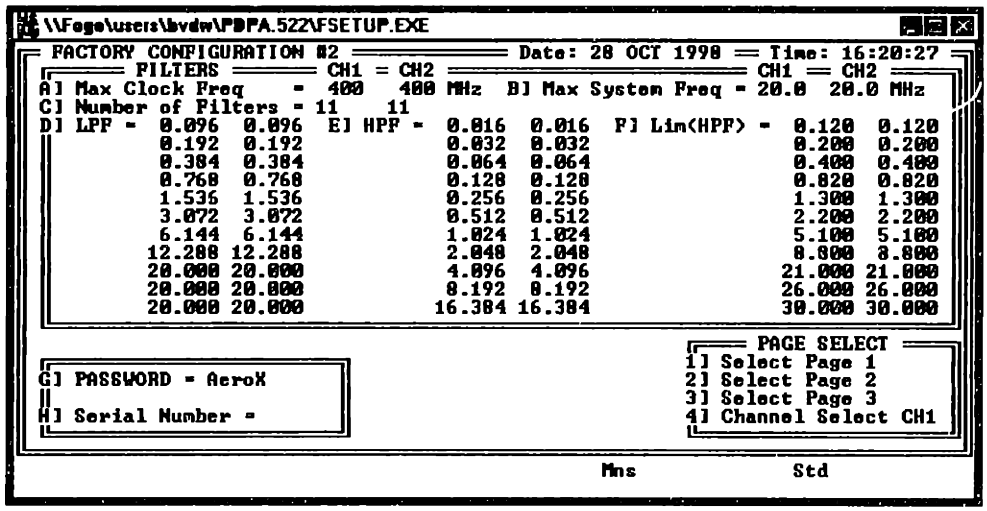
\\Fogo\users\bvdw\PDPA.522\FSETUP.EXE
FACTORY CONFIGURATION #2
Date: 28 OCT 1998
Time: 16:20:27
FILTERS
CH1 CH2
A] Max Clock Freq = 400 400 MHz
C] Number of Filters = 11 11
D] LPF = 0.096 0.096
0.192 0.192
0.384 0.384
0.768 0.768
1.536 1.536
3.072 3.072
6.144 6.144
12.288 12.288
20.000 20.000
20.000 20.000
20.000 20.000
E] HPF = 0.016 0.016
0.032 0.032
0.064 0.064
0.128 0.128
0.256 0.256
0.512 0.512
1.024 1.024
2.048 2.048
4.096 4.096
8.192 8.192
16.384 16.384
B] Max System Freq = 20.0 20.0 MHz
CH1 CH2
F] Lim(HPF) = 0.120 0.120
0.200 0.200
0.400 0.400
0.820 0.820
1.300 1.300
2.200 2.200
5.100 5.100
8.800 8.800
21.000 21.000
26.000 26.000
30.000 30.000
G] PASSWORD = AeroX
H] Serial Number =
PAGE SELECT
1] Select Page 1
2] Select Page 2
3] Select Page 3
4] Channel Select CH1
Mns
Std

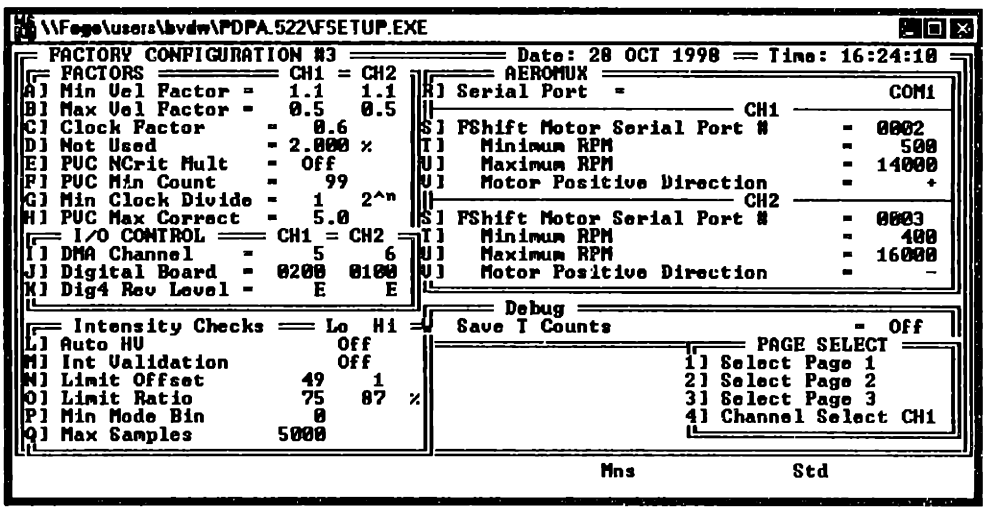
\\Fogo\users\bvdw\PDPA.522\FSETUP.EXE
FACTORY CONFIGURATION #3
Date: 28 OCT 1998
Time: 16:24:10
FACTORS
CH1 = CH2
A] Min Vel Factor = 1.1 1.1
B] Max Vel Factor = 0.5 0.5
C] Clock Factor = 0.6
D] Not Used = 2.000 %
E] PUC NCrit Mult = Off
F] PUC Min Count = 99
G] Min Clock Divide = 1 2^n
H] PUC Max Correct = 5.0
I/O CONTROL
CH1 = CH2
I] DMA Channel = 5 6
J] Digital Board = 0200 0100
K] Dig4 Rev Level = E E
Intensity Checks
Lo Hi
L] Auto HV Off
M] Int Validation Off
N] Limit Offset 49 1
O] Limit Ratio 75 87 %
P] Min Mode Bin 0
Q] Max Samples 5000
AEROMUX
R] Serial Port = COM1
CH1
S] FShift Motor Serial Port # = 0002
T] Minimum RPM = 500
U] Maximum RPM = 14000
V] Motor Positive Direction = +
CH2
S] FShift Motor Serial Port # = 0003
T] Minimum RPM = 400
U] Maximum RPM = 16000
V] Motor Positive Direction = -
Debug
Save T Counts = Off
PAGE SELECT
1] Select Page 1
2] Select Page 2
3] Select Page 3
4] Channel Select CH1
Mns
Std

APPENDIX 4
IMAGING EXPERIMENTAL LOG

The following pages contain data on all of the experiments for which PLIF and Mie scattering images were taken. Since the table is very large, it was separated into ten pages presented in an across-then-down order. Blank cells typically refer to data which is not applicable. Below is a listing of the column headings.

Table A4.1: Imaging experimental log column listing

No.	Column Description
1	Date of test
2	File name of images
3	Description of test
4	Scale of images
5	Number of frames in file
6	Injection timing
7	Image timing—'movie' if the image timing changed with each frame
8	Injector temperature
9	Head temperature
10	Injector
11	Fluorescent dopant
12	Ratio of fuel to dopant
13	Fuel
14	F-stop of camera lens
15	CCD cooler temperature
16	Intensifier gate duration
17	Delay between start of injection and intensifier gate—or explanation of movie sequence
18	Delay between start of injection and excimer laser signal
19	Delay between start of injection and CCD activation signal
20	Gain of intensifier
21	CCD exposure time
22	Laser energy—or power for argon-ion
23	Laser sheet width
24	Laser sheet height
25	Laser sheet location—always through center of injector
26	Injection duration
27	Skip fire settings—number skipped, number fired, number on which camera is triggered
28	Camshaft constants—EVO, IVO, EVC, IVC
29	Pressure data
30	Equivalence ratio—always near unity
31	Manifold absolute pressure

Appendix 4: Imaging F Experiment Log

Date	File Name	EXPERIMENT							FUEL/DOPANT				
		Description	Scale	Frames	Injection	Camera	Inj. T.	Head T.	Injector	Dopant	Doping	Fuel	F-stop	Cooler T
mo/day/yr	[type]		mm/pix		°ATCI	μsASOI	℃	℃	Make(angle)		vol. ratio		f/#	℃
8/26/97	di08261	Mistake—camera triggered of end of injection			60	3750		35 to 85°C	Zexel(60)	acetone	10:1	isooctane	5.6	0
8/27/97	di08271	Acetone warm-up; no transition observed			60	1000		35 to 95°C	Zexel(60)	acetone	10:1	isooctane	5.6	0
8/27/97	di08272	High-temp acetone warmup			60	1000		65 to 105°C	Zexel(60)	acetone	10:1	isooctane	8.0	0
8/28/97	di08281	Earlier timing acetone warmup			60	750		35 to 75°C	Zexel(60)	acetone	10:1	isooctane	11.0	0
8/28/97	di08282	Air introduced into fuel			60	1000		35 to 90°C	Zexel(60)	acetone	10:1	isooctane	11.0	0
9/3/97	di09031	More air - earlier camera timing			60	750		35 to 85°C	Zexel(60)	acetone	10:1	isooctane	11.0	0
9/3/97	di09032	Late injection			210	1000		35 to 80°C	Zexel(60)	3-pentanone	10:1	isooctane	11.0	0
9/4/97	di09041	Late injection - movie			210	movie			Zexel(60)	3-pentanone	10:1	isooctane	11.0	0
9/5/97	di09051	Very late injection - movie			270	movie		35 to 65°C	Zexel(60)	3-pentanone	10:1	isooctane	11.0	0
9/7/97	di09071	3-pentanone development movie			90	movie			Zexel(60)	3-pentanone	10:1	isooctane	11.0	0
9/7/97	di09072	3-pentanone warmup			60	1000		35 to 85°C	Zexel(60)	3-pentanone	10:1	isooctane	11.0	0
10/1/97	di10011	Old fuel system (no accumulator)			60	1000		35 to 95°C	Zexel(60)	acetone	10:1	isooctane	5.6	0
10/1/97	di10012	Earlier timing			60	750		35 to 95°C	Zexel(60)	acetone	10:1	isooctane	5.6	0
10/1/97	di10013	Later timing - image file lost			60	1250		35 to 95°C	Zexel(60)	acetone	10:1	isooctane	5.6	0
10/3/97	di10031	Low intake pressure			60	1000		40 to 75°C	Zexel(60)	acetone	10:1	isooctane	5.6	0
10/3/97	di10032	Ran to higher temp			60	1000		65 to 85°C	Zexel(60)	acetone	10:1	isooctane	5.6	0
10/3/97	di10033	Higher temp (2min after 17)			60	1000		85 to 102°C	Zexel(60)	acetone	10:1	isooctane	5.6	0
10/3/97	di10034	Midrange intake pressure			60	1000		60 to 100°C	Zexel(60)	acetone	10:1	isooctane	5.6	0
10/3/97	di10035	Return to normal intake pressure			60	1000		60 to 110°C	Zexel(60)	acetone	10:1	isooctane	5.6	0
11/23/97	di11231	Piston accum./oil contam—batch #1	0.104	10	90	1000		40 to 60°C	Zexel(60)	none		isooctane	5.6	0
11/23/97	di11232	cleaned window	0.104	10	90	1000			Zexel(60)	none		isooctane	5.6	0
11/23/97	di11233	Piston accum./oil contam—batch #2	0.104	10	90	1000			Zexel(60)	none		isooctane	5.6	0
11/23/97	di11234	retry	0.104	10	90	1000		60 to 90°C	Zexel(60)	none		isooctane	5.6	0
11/24/97	di11241	Vol. - hot/low pressure: laser too low	0.104	10	90	1000		95 to 105	Zexel(60)	acetone	10:1	isooctane	5.6	0
11/24/97	di11242	Volatility - hot/low pressure	0.104	10	90	1000			Zexel(60)	acetone	10:1	isooctane	5.6	0
11/24/97	di11243	Vol. - hot/low pressure: 8.0 fstop	0.104	10	90	1000		95 to 105	Zexel(60)	acetone	10:1	isooctane	8.0	0
11/24/97	di11244	Volatility - hot/med. pressure	0.104	10	90	1000		95 to 110	Zexel(60)	acetone	10:1	isooctane	8.0	0
11/24/97	di11245	Volatility - hot/high pressure	0.104	5	90	1000		95 to 110	Zexel(60)	acetone	10:1	isooctane	8.0	0
11/24/97	di11248	5 more frames	0.104	5	90	1000		95 to 105	Zexel(60)	acetone	10:1	isooctane	8.0	0
11/25/97	di11251	Vol. - high P / cold	0.104	5	90	1000		30 to 50	Zexel(60)	acetone	10:1	isooctane	8.0	0
11/25/97	di11252	5 more	0.104	5	90	1000		35 to 55	Zexel(60)	acetone	10:1	isooctane	8.0	0
11/25/97	di11253	Vol. - med P / cold	0.104	10	90	1000		30 to 60	Zexel(60)	acetone	10:1	isooctane	8.0	0
11/25/97	di11254	Vol. - low P / cold	0.104	10	90	1000		30 to 50	Zexel(60)	acetone	10:1	isooctane	8.0	0
12/1/97	di12011	Movie - low P / hot	0.104	20	90	movie		90 to 105	Zexel(60)	acetone	10:1	isooctane	8.0	0
12/1/97	di12012	try #2	0.104	20	90	movie		90 to 103	Zexel(60)	acetone	10:1	isooctane	8.0	0
12/1/97	di12013	Movie - low P / cold	0.104	20	90	movie		30 to 40	Zexel(60)	acetone	10:1	isooctane	8.0	0
12/1/97	di12014	background (no injection)	0.104	10	90	1000			Zexel(60)	none		none	8.0	0
12/1/97	di12015	Vol. - low P / cold	0.104	10	90	1000		30 to 40	Zexel(60)	acetone	10:1	isooctane	8.0	0
12/1/97	di12016	Movie2 - low P / cold	0.104	20	90	movie		30 to 45	Zexel(60)	acetone	10:1	isooctane	8.0	0
12/1/97	di12017	Movie3 - low P / cold	0.104	10	90	movie		30 to 45	Zexel(60)	acetone	10:1	isooctane	8.0	0
12/1/97	di12018	Movie3 - low P / cold	0.104	20	90	movie		35 to 50	Zexel(60)	acetone	10:1	isooctane	8.0	0
12/1/97	di12019	Movie2 - low P / hot	0.104	20	90	movie		90 to 100	Zexel(60)	acetone	10:1	isooctane	8.0	0
12/1/97	di12019a	Movie3 - low P / hot	0.104	20	90	movie		90 to 100	Zexel(60)	acetone	10:1	isooctane	8.0	0
12/3/97	di12031	Scattering - 0.3 bar / cold	0.104	10	90	1000		30 to 36	Zexel(60)	acetone	10:1	isooctane	2.8	0
12/3/97	di12032	Scattering - 0.3 bar / hot	0.104	10	90	1000		95 to 105	Zexel(60)	acetone	10:1	isooctane	2.8	0
12/3/97	di12033	Scat. Movie1 - 0.3 bar / hot	0.104	20	90	movie		90 to 105	Zexel(60)	acetone	10:1	isooctane	2.8	0
12/3/97	di12034	Scat. Movie2 - 0.3 bar / hot	0.104	20	90	movie		95 to 110	Zexel(60)	acetone	10:1	isooctane	2.8	0
12/3/97	di12035	Scat. Movie3 - 0.3 bar / hot	0.104	≈9	90	movie		90 to 100	Zexel(60)	acetone	10:1	isooctane	2.8	0
12/3/97	di12036	try #2	0.104	20	90	movie		95 to 115	Zexel(60)	acetone	10:1	isooctane	2.8	0
12/5/97	di12061	Scattering - 0.3 bar / cold / indolene	0.104	10	90	1000		30 to 40	Zexel(60)	none		indolene	2.8	0
12/6/97	di12062	LIF - 0.3 bar / cold / indolene	0.104	10	90	1000		35 to 45	Zexel(60)	none		indolene	11.0	0

Appendix 4: Imaging F Experiment Log

		CAMERA						LASER				ENGINE				OTHER	
Date	File Name	Gate Width	Gate Del	Laser Del	Cam. Del	Gain	Exposure	Laser E	Width	Height	Location	Inj. Dur.	Skip Fire	Spark	Cam	Eq. Ratio	MAP
mo/day/yr	*[].spe*	*µs*	*µs*	*µs*	*µs*	*%*	*sec*	*mJ*	*mm*	*mm*		*ms*	*sk:fr:trg*	*°ABCI*	*eo/io/ec/ic*	*lambda*	*bar*
8/26/97	dl08261	10	1000	999	998	90	0.05	*(20 kV)*	0.5	22	center of inj.	2.75	no	155	48/5/12/55	0.95	
8/27/97	dl08271	10	1000	999	998	90	0.05	*(20 kV)*	0.5	22	center of inj.	2.75	no	155	48/5/12/55	0.95	
8/27/97	dl08272	10	1000	999	998	90	0.05	*(20 kV)*	0.5	22	center of inj.	2.75	no	155	48/5/12/55	0.95	
8/28/97	dl08281	10	750	749	748	90	0.05	70	0.5	22	center of inj.	2.75	no	155	48/5/12/55	0.935	
8/26/97	dl08282	10	1000	999	998	90	0.05	70	0.5	22	center of inj.	2.75	no	155	48/5/12/55	0.93	
9/3/97	dl09031	10	750	749	748	90	0.05	70	0.5	22	center of inj.	2.75	no	155	48/5/12/55	0.938	0.55
9/3/97	dl09032	10	1000	999	998	90	0.05	70	0.5	22	center of inj.	2.75	no	165	48/5/12/55	0.975	0.55
9/4/97	dl09041	10	movie 350, 400, ... (-1,-2)			90	0.05	70	0.5	22	center of inj.	2.75	no	165	48/5/12/55		
9/5/97	dl09051	10	movie 350, 400, ... (-1,-2)			90	0.05	70	0.5	22	center of inj.	3.00	no	180	48/5/12/55		
9/7/97	dl09071	10	movie 350, 400, ... (-1,-2)			90	0.05	70	0.5	22	center of inj.	2.75	no	155	48/5/12/55		
9/7/97	dl09072	10	1000	999	998	90	0.05	70	0.5	22	center of inj.	2.75	no	155	48/5/12/55	0.935	0.55
10/1/97	dl10011	10	1000	999	998	90	0.05	70	0.5	22	center of inj.	2.70	no	155	48/5/12/55		0.5
10/1/97	dl10012	10	750	749	748	90	0.05	70	0.5	22	center of inj.	2.65	no	155	48/5/12/55		
10/1/97	dl10013	10	1250	1249	1248	90	0.05	70	0.5	22	center of inj.	2.60	no	155	48/5/12/55	0.95	0.54
10/3/97	dl10031	10	1000	999	998	90	0.05	70	0.5	22	center of inj.	1.70	no	155	48/5/12/55		0.34
10/3/97	dl10032	10	1000	999	998	90	0.05	70	0.5	22	center of inj.	1.70	no	155	48/5/12/55		
10/3/97	dl10033	10	1000	999	998	90	0.05	70	0.5	22	center of inj.	1.70	no	155	48/5/12/55	0.88	
10/3/97	dl10034	10	1000	999	998	90	0.05	70	0.5	22	center of inj.	2.15	no	155	48/5/12/55	0.88	0.43
10/3/97	dl10035	10	1000	999	998	90	0.05	70	0.5	22	center of inj.	2.65	no	155	48/5/12/55	0.99	0.56
11/23/97	dl11231	5	1000	997	996	90	0.05	70	0.5	22	center of inj.	2.80	no	155	48/5/12/55	0.98	0.53
11/23/97	dl11232	5	1000	997	996	90	0.05	70	0.5	22	center of inj.	2.80	no	155	48/5/12/55	0.96	0.56
11/23/97	dl11233	5	1000	997	996	90	0.05	70	0.5	22	center of inj.	2.80	no	155	48/5/12/55	0.96	0.57
11/23/97	dl11234	5	1000	997	996	90	0.05	70	0.5	22	center of inj.	2.80	no	155	48/5/12/55	0.95	0.57
11/24/97	dl11241	5	1000	997	996	90	0.05	70	0.5	22	center of inj.	1.65	no	155	48/5/12/55	0.93	0.36
11/24/97	dl11242	5	1000	997	996	90	0.05	70	0.5	22	center of inj.	1.65	no	155	48/5/12/55		0.36
11/24/97	dl11243	5	1000	997	996	90	0.05	70	0.5	22	center of inj.	1.65	no	155	48/5/12/55	0.93	0.36
11/24/97	dl11244	5	1000	997	996	90	0.05	70	0.5	22	center of inj.	3.55	no	155	48/5/12/55		0.63
11/24/97	dl11245	5	1000	997	996	90	0.05	70	0.5	22	center of inj.	5.30	no	155	48/5/12/55		0.89
11/24/97	dl11246	5	1000	997	996	90	0.05	70	0.5	22	center of inj.	5.30	no	155	48/5/12/55		0.89
11/25/97	dl11251	5	1000	997	996	90	0.05	70	0.5	22	center of inj.	5.30	no	155	48/5/12/55		0.89
11/25/97	dl11252	5	1000	997	996	90	0.05	70	0.5	22	center of inj.	5.30	no	155	48/5/12/55		0.89
11/25/97	dl11253	5	1000	997	996	90	0.05	70	0.5	22	center of inj.	3.55	no	155	48/5/12/55		0.61
11/25/97	dl11254	5	1000	997	996	90	0.05	70	0.5	22	center of inj.	1.65	no	155	48/5/12/55		0.35
12/1/97	dl12011	5	400...1200,350...450 (-3, -4)			90	0.05	70	0.5	22	center of inj.	1.65	10:10:10	155	48/5/12/55	0.95	0.36
12/1/97	dl12012	5	400...1200,350...450 (-3, -4)			90	0.05	70	0.5	22	center of inj.	1.65	10:10:10	155	48/5/12/55		
12/1/97	dl12013	5	350...1200 x50,rpt (-3, -4)			90	0.05	70	0.5	22	center of inj.	1.65	10:10:10	155	48/5/12/55		
12/1/97	dl12014	5	1000	997	996	90	0.05	70	0.5	22	center of inj.	1.65	10:10:10	155	48/5/12/55		
12/1/97	dl12015	5	1000	997	996	90	0.05	70	0.5	22	center of inj.	1.65	10:10:10	155	48/5/12/55		
12/1/97	dl12016	5	1250...2100 x50,rpt (-3, -4)			90	0.05	70	0.5	22	center of inj.	1.65	10:10:10	155	48/5/12/55		0.38
12/1/97	dl12017	5	2150...3000 x50,rpt (-3, -4)			90	0.05	70	0.5	22	center of inj.	1.65	10:10:10	155	48/5/12/55		
12/1/97	dl12018	5	2150...3000 x50,rpt (-3, -4)			90	0.05	70	0.5	22	center of inj.	1.65	10:10:10	155	48/5/12/55		0.36
12/1/97	dl12019	5	2150...3000 x50,rpt (-3, -4)			90	0.05	70	0.5	22	center of inj.	1.65	10:10:10	155	48/5/12/55		0.36
12/1/97	dl1201a	5	1250...2100 x50,rpt (-3, -4)			90	0.05	70	0.5	22	center of inj.	1.65	10:10:10	155	48/5/12/55		
12/3/97	dl12031	15	1000		996	90	0.05	*1.3 W*	0.5	40	center of inj.	1.65	10:10:10	155	48/5/12/55		
12/3/97	dl12032	15	1000		996	90	0.05	*1.5 W*	0.5	40	center of inj.	1.65	10:10:10	155	48/5/12/55		0.38
12/3/97	dl12033	15	350...1200 x50,rpt (-4)			90	0.05	*1.1 W*	0.5	40	center of inj.	1.65	10:10:10	155	48/5/12/55		
12/3/97	dl12034	15	1250...2100 x50,rpt (-4)			90	0.05	*1.5 W*	0.5	40	center of inj.	1.65	10:10:10	155	48/5/12/55		0.39
12/3/97	dl12035	15	1250...2100 x50,rpt (-4)			90	0.05	*1.5 W*	0.5	40	center of inj.	1.65	10:10:10	155	48/5/12/55		
12/3/97	dl12036	15	2150...3000 x50,rpt (-4)			90	0.05	*1.5 W*	0.5	40	center of inj.	1.65	10:10:10	155	48/5/12/55		
12/6/97	dl12051	15	1000		996	90	0.05	*1.5 W*	0.5	40	center of inj.	1.65	10:10:10	155	48/5/12/55		
12/6/97	dl12062	5	1000	997	996	90	0.05	70	0.5	22	center of inj.	1.65	10:10:10	155	48/5/12/55		

Appendix 4: Imaging F Experiment Log

Date	File Name	EXPERIMENT							FUEL/DOPANT				
		Description	Scale	Frames	Injection	Camera	Inj. T.	Head T.	Injector	Dopant	Doping	Fuel	F-stop	Cooler T
mo/day/yr	/type		mm/pix		°ATCI	μsASOI	℃	℃	Make(angle)		vol. ratio		f/#	℃
12/6/97	di12083	increased f-stop	0.104	10	90	1000		35 to 45	Zexel(60)	none		indolene	16.0	0
12/6/97	di12084	increased f-stop	0.104	10	90	1000		35 to 45	Zexel(60)	none		indolene	22.0	0
12/6/97	di12085	Scat. - 0.3 bar / cold / ind. / refocus	0.104	10	90	1000		30 to 40	Zexel(60)	none		indolene	2.8	0
12/6/97	di12086	Scattering - 0.3 bar / hot / indolene	0.104	10	90	1000		90 to 100	Zexel(60)	none		indolene	2.8	0
12/6/97	di12087	LIF - 0.3 bar / hot / indolene	0.104	10	90	1000		90 to 100	Zexel(60)	none		indolene	22.0	0
12/7/97	di12071	Scattering - 0.3 bar / hot / isooctane	0.104	10	90	1000		90 to 100	Zexel(60)	none		isooctane	2.8	0
12/7/97	di12072	try #2	0.104	10	90	1000		90 to 100	Zexel(60)	none		isooctane	2.8	0
1/20/98	di01201	3-pentanone LIF 0.3bar, cold / refocus	0.100	10	90	1000		35 to 45	Zexel(60)	3-pentanone	10:1	isooctane	8.0	0
1/20/98	di01202	3-pentanone LIF 0.3bar, hot	0.100	10	90	1000		90 to 100	Zexel(60)	3-pentanone	10:1	isooctane	8.0	0
1/20/98	di01203	3-pentanone LIF 0.3bar, hot (better)	0.100	10	90	1000		90 to 95	Zexel(60)	3-pentanone	10:1	isooctane	8.0	0
1/20/98	di01204	3-pentanone LIF 0.3bar, hot—windows dirty	0.100	10	90	1000		90 to 95	Zexel(60)	3-pentanone	10:1	isooctane	8.0	0
1/24/98	di01241	3-pent / cold / 0.3bar	0.100	10	90	1000		30 to 35	Zexel(60)	3-pentanone	10:1	isooctane	8.0	0
1/24/98	di01242	3-pent / cold / 0.6bar	0.100	10	90	1000		35 to 45	Zexel(60)	3-pentanone	10:1	isooctane	8.0	0
1/24/98	di01243	3-pent / cold / 0.9bar	0.100	10	90	1000		35 to 45	Zexel(60)	3-pentanone	10:1	isooctane	8.0	0
1/24/98	di01244	3-pent / hot / 0.3bar	0.100	10	90	1000		90 to 95	Zexel(60)	3-pentanone	10:1	isooctane	8.0	0
1/24/98	di01245	3-pent / hot / 0.6bar	0.100	10	90	1000		90 to 97	Zexel(60)	3-pentanone	10:1	isooctane	8.0	0
1/24/98	di01246	3-pent / hot / 0.9bar	0.100	10	90	1000		90 to 100	Zexel(60)	3-pentanone	10:1	isooctane	8.0	0
1/24/98	di01247	2-butanone / cold / 0.3bar	0.100	10	90	1000		30 to 35	Zexel(60)	2-butanone	10:1	isooctane	8.0	0
1/24/98	di01248	2-butanone / cold / 0.6bar	0.100	10	90	1000		35 to 45	Zexel(60)	2-butanone	10:1	isooctane	8.0	0
1/24/98	di01249	2-butanone / cold / 0.9bar	0.100	10	90	1000		35 to 45	Zexel(60)	2-butanone	10:1	isooctane	8.0	0
1/24/98	di0124a	2-butanone / hot / 0.3bar	0.100	10	90	1000		90 to 95	Zexel(60)	2-butanone	10:1	isooctane	8.0	0
1/24/98	di0124b	2-butanone / hot / 0.6bar	0.100	10	90	1000		90 to 100	Zexel(60)	2-butanone	10:1	isooctane	8.0	0
1/24/98	di0124c	2-butanone / hot / 0.9bar	0.100	10	90	1000		90 to 100	Zexel(60)	2-butanone	10:1	isooctane	8.0	0
3/28/98	di803281	Indolene LIF / hot / 0.3 bar	0.204	10	90	2000	80	100	Chrysler	none		indolene	32	0
3/28/98	di803282	Indolene LIF / hot / 0.5 bar	0.204	10	90	2000	80	100	Chrysler	none		indolene	32	0
3/28/98	di803283	Indolene LIF / hot / 0.7 bar	0.204	10	90	2000	80	95	Chrysler	none		indolene	32	0
3/28/98	di803284	Indolene LIF / hot / 0.9 bar	0.204	10	90	2000	80	90	Chrysler	none		indolene	32	0
3/28/98	di803285	Indolene LIF / hot / 0.8 bar	0.204	10	90	2000	80	90	Chrysler	none		indolene	32	0
3/28/98	di803286	Indolene LIF / hot / 0.6 bar	0.204	10	90	2000	80	90	Chrysler	none		indolene	32	0
3/28/98	di803287	Indolene LIF / hot / 0.4 bar	0.204	10	90	2000	80	90	Chrysler	none		indolene	32	0
5/4/98	m2mb26t	temp-controlled (outside engine)	0.069	10		2000	26		Chrysler	none		???	2.8	0
5/4/98	m2mb60t	temp-controlled (outside engine)	0.069	10		2000	60		Chrysler	none		???	2.8	0
5/4/98	m2mb70t	temp-controlled (outside engine)	0.069	10		2000	70		Chrysler	none		???	2.8	0
5/4/98	m2mb64t	temp-controlled (outside engine)	0.069	10		2000	64		Chrysler	none		???	2.8	0
5/4/98	m2mb80t	temp-controlled (outside engine)	0.069	10		2000	70		Chrysler	none		2-methylbutane	2.8	0
5/4/98	m2mb75t	temp-controlled (outside engine)	0.069	10		2000	80		Chrysler	none		2-methylbutane	2.8	0
5/4/98	m2mb85t	temp-controlled (outside engine)	0.069	10		2000	75		Chrysler	none		2-methylbutane	2.8	0
5/4/98	m2mb90t	temp-controlled (outside engine)	0.069	10		2000	85		Chrysler	none		2-methylbutane	2.8	0
5/4/98	m2mb62t	temp-controlled (outside engine)	0.069	10		2000	90		Chrysler	none		2-methylbutane	2.8	0
5/4/98	m2mb60b	temp-controlled (outside engine)	0.069	10		2000	62		Chrysler	none		2-methylbutane	2.8	0
5/4/98	m2mb50b	temp-controlled (outside engine)	0.069	10		2000	50		Chrysler	none		2-methylbutane	2.8	0
5/4/98	m2mb56t	temp-controlled (outside engine)	0.069	10		2000	56		Chrysler	none		2-methylbutane	2.8	0
5/4/98	m2mb54t	temp-controlled (outside engine)	0.069	10		2000	54		Chrysler	none		2-methylbutane	2.8	0
5/4/98	m2mb52t	temp-controlled (outside engine)	0.069	10		2000	52		Chrysler	none		2-methylbutane	2.8	0
5/4/98	m2mb48t	temp-controlled (outside engine)	0.069	10		2000	48		Chrysler	none		2-methylbutane	2.8	0
5/4/98	m2mb46t	temp-controlled / realligned laser	0.069	10		2000	46		Chrysler	none		2-methylbutane	2.8	0
5/4/98	m2mb54b	temp-controlled (outside engine)	0.069	10		2000	54		Chrysler	none		2-methylbutane	2.8	0
5/4/98	m2mb52b	temp-controlled (outside engine)	0.069	10		2000	52		Chrysler	none		2-methylbutane	2.8	0
5/4/98	m2mb51t	temp-controlled (outside engine)	0.069	10		2000	51		Chrysler	none		2-methylbutane	2.8	0
5/4/98	m2mb53t	temp-controlled (outside engine)	0.069	10		2000	53		Chrysler	none		2-methylbutane	2.8	0
5/4/98	m2mb50c	temp-controlled (outside engine)	0.069	10		2000	50		Chrysler	none		2-methylbutane	2.8	0

Appendix 4: Imaging F Experiment Log

		CAMERA						LASER				ENGINE				OTHER	
Date	File Name	Gate Width	Gate Del	Laser Del	Cam. Del	Gain	Exposure	Laser E	Width	Height	Location	Inj. Dur.	Skip Fire	Spark	Cam	Eq. Ratio	MAP
mo/day/yr	*ff.spe*	*µs*	*µs*	*µs*	*µs*	*%*	*sec*	*mJ*	*mm*	*mm*		*ms*	*sk:fr:trg*	*°ABCI*	*eo/io/ec/ic*	*lambda*	*bar*
12/6/97	dl12063	5	1000	997	996	90	0.05	70	0.5	22	center of inj.	1.65	10:10:10	155	48/5/12/55		
12/6/97	dl12064	5	1000	997	996	90	0.05	70	0.5	22	center of inj.	1.65	10:10:10	155	48/5/12/55		
12/6/97	dl12065	15	1000		996	90	0.05	*1.5 W*	0.5	40	center of inj.	1.65	10:10:10	155	48/5/12/55		
12/6/97	dl12066	15	1000		996	90	0.05	70	0.5	22	center of inj.	1.65	10:10:10	155	48/5/12/55		
12/6/97	dl12067	5	1000	997	996	90	0.05	*1.5 W*	0.5	40	center of inj.	1.65	10:10:10	155	48/5/12/55		
12/7/97	dl12071	15	1000		996	90	0.05	*1.4 W*	0.5	40	center of inj.	1.65	10:10:10	155	48/5/12/55	0.95	0.37
12/7/97	dl12072	15	1000		996	90	0.05	*1.4 W*	0.5	40	center of inj.	1.65	10:10:10	155	48/5/12/55		
1/20/98	dl01201	5	1000	999	998	90	0.05	70	0.5	22	center of inj.	1.65	10:10:10	155	48/5/12/55	0.94	0.38
1/20/98	dl01202	5	1000	999	998	90	0.05	70	0.5	22	center of inj.	1.65	no	155	48/5/12/55		
1/20/98	dl01203	5	1000	999	998	90	0.05	70	0.5	22	center of inj.	1.65	10:10:10	155	48/5/12/55		
1/20/98	dl01204	5	1000	999	998	90	0.05	70	0.5	22	center of inj.	1.65	10:10:10	155	48/5/12/55		
1/24/98	dl01241	5	1000	999	998	90	0.05	70	0.5	22	center of inj.	1.65	10:10:10	155	48/5/12/55		0.38
1/24/98	dl01242	5	1000	999	998	90	0.05	70	0.5	22	center of inj.	3.55	10:10:10	155	48/5/12/55		0.55
1/24/98	dl01243	5	1000	999	998	90	0.05	70	0.5	22	center of inj.	5.30	10:10:10	155	48/5/12/55		0.88
1/24/98	dl01244	5	1000	999	998	90	0.05	70	0.5	22	center of inj.	1.65	10:10:10	155	48/5/12/55		0.39
1/24/98	dl01245	5	1000	999	998	90	0.05	70	0.5	22	center of inj.	3.55	10:10:10	155	48/5/12/55		0.55
1/24/98	dl01246	5	1000	999	998	90	0.05	70	0.5	22	center of inj.	5.30	10:10:10	155	48/5/12/55		0.88
1/24/98	dl01247	5	1000	999	998	90	0.05	70	0.5	22	center of inj.	1.65	10:10:10	155	48/5/12/55		0.38
1/24/98	dl01248	5	1000	999	998	90	0.05	70	0.5	22	center of inj.	3.55	10:10:10	155	48/5/12/55		0.55
1/24/98	dl01249	5	1000	999	998	90	0.05	70	0.5	22	center of inj.	5.30	10:10:10	155	48/5/12/55		0.88
1/24/98	dl0124a	5	1000	999	998	90	0.05	70	0.5	22	center of inj.	1.65	10:10:10	155	48/5/12/55		0.37
1/24/98	dl0124b	5	1000	999	998	90	0.05	70	0.5	22	center of inj.	3.55	10:10:10	155	48/5/12/55		0.55
1/24/98	dl0124c	5	1000	999	998	90	0.05	70	0.5	22	center of inj.	5.30	10:10:10	155	48/5/12/55		0.87
3/28/98	dl803281	1	2000	1997	1996	90	0.05	100	0.5	full	center of inj.	2.40	10:10:10	155	48/5/12/55		0.3
3/28/98	dl803282	1	2000	1997	1996	90	0.05	100	0.5	full	center of inj.	4.00	10:10:10	155	48/5/12/55	0.95	0.5
3/28/98	dl803283	1	2000	1997	1996	90	0.05	100	0.5	full	center of inj.	5.60	10:10:10	155	48/5/12/55	0.97	0.7
3/28/98	dl803284	1	2000	1997	1996	90	0.05	100	0.5	full	center of inj.	7.20	10:10:10	155	48/5/12/55		0.9
3/28/98	dl803285	1	2000	1997	1996	90	0.05	100	0.5	full	center of inj.	6.40	10:10:10	155	48/5/12/55		0.8
3/28/98	dl803286	1	2000	1997	1996	90	0.05	100	0.5	full	center of inj.	4.80	10:10:10	155	48/5/12/55		0.6
3/28/98	dl803287	1	2000	1997	1996	90	0.05	100	0.5	full	center of inj.	3.20	10:10:10	155	48/5/12/55		0.4
5/4/98	m2mb26t	1	2000		1996	90	0.05	1.2 W	0.5	full	center of inj.						1
5/4/98	m2mb60t	1	2000		1996	90	0.05	1.1 W	0.5	full	center of inj.						1
5/4/98	m2mb70t	1	2000		1996	90	0.05	1.0 W	0.5	full	center of inj.						1
5/4/98	m2mb64t	1	2000		1996	90	0.05	1.0 W	0.5	full	center of inj.						1
5/4/98	m2mb80t	1	2000		1996	90	0.05	1.0 W	0.5	full	center of inj.						1
5/4/98	m2mb75t	1	2000		1996	90	0.05	1.0 W	0.5	full	center of inj.						1
5/4/98	m2mb85t	1	2000		1996	90	0.05	1.0 W	0.5	full	center of inj.						1
5/4/98	m2mb90t	1	2000		1996	90	0.05	1.0 W	0.5	full	center of inj.						1
5/4/98	m2mb62t	1	2000		1996	90	0.05	1.0 W	0.5	full	center of inj.						1
5/4/98	m2mb60b	1	2000		1996	90	0.05	1.0 W	0.5	full	center of inj.						1
5/4/98	m2mb50b	1	2000		1996	90	0.05	1.0 W	0.5	full	center of inj.						1
5/4/98	m2mb56t	1	2000		1996	90	0.05	1.0 W	0.5	full	center of inj.						1
5/4/98	m2mb54t	1	2000		1996	90	0.05	1.0 W	0.5	full	center of inj.						1
5/4/98	m2mb52t	1	2000		1996	90	0.05	1.0 W	0.5	full	center of inj.						1
5/4/98	m2mb48t	1	2000		1996	90	0.05	1.0 W	0.5	full	center of inj.						1
5/4/98	m2mb46t	1	2000		1996	90	0.05	1.0 W	0.5	full	center of inj.						1
5/4/98	m2mb54b	1	2000		1996	90	0.05	1.0 W	0.5	full	center of inj.						1
5/4/98	m2mb52b	1	2000		1996	90	0.05	1.0 W	0.5	full	center of inj.						1
5/4/98	m2mb51t	1	2000		1996	90	0.05	1.0 W	0.5	full	center of inj.						1
5/4/98	m2mb53t	1	2000		1996	90	0.05	1.0 W	0.5	full	center of inj.						1
5/4/98	m2mb50c	1	2000		1996	90	0.05	1.0 W	0.5	full	center of inj.						1

Appendix 4: Imaging F Experiment Log

Date	File Name	EXPERIMENT							FUEL/DOPANT				
		Description	Scale	Frames	Injection	Camera	Inj. T.	Head T.	Injector	Dopant	Doping	Fuel	F-stop	Cooler T
mo/day/yr	...\...\...		mm/pix		°ATDC	μsASOI	°C	°C	Make(angle)		vol. ratio		f/#	°C
5/4/98	m2mb100	temp-controlled (outside engine)	0.069	10		2000	100		Chrysler	none		2-methylbutane	2.8	0
5/4/98	m2mb100b	temp-controlled (outside engine)	0.069	10		2000	100		Chrysler	none		2-methylbutane	4.0	0
5/4/98	m2mb100c	temp-controlled (outside engine)	0.069	10		2000	100		Chrysler	none		2-methylbutane	2.8	0
5/4/98	m2mb30t	temp-controlled (outside engine)	0.069	10		2000	30		Chrysler	none		2-methylbutane	2.8	0
5/4/98	m2mb30b	temp-controlled (outside engine)	0.069	10		2000	30		Chrysler	none		2-methylbutane	2.8	0
5/6/98	find70	temp-controlled (outside engine)	0.069	10		1500	70		Chrysler	none		indolene	32	0
5/6/98	find90	temp-controlled (outside engine)	0.069	10		1500	90		Chrysler	none		indolene	32	0
5/6/98	find110	temp-controlled (outside engine)	0.069	10		1500	110		Chrysler	none		indolene	32	0
5/6/98	find120	temp-controlled (outside engine)	0.069	10		1500	120		Chrysler	none		indolene	32	0
5/6/98	find100	temp-controlled (outside engine)	0.069	10		1500	100		Chrysler	none		indolene	32	0
5/6/98	find80	temp-controlled (outside engine)	0.069	10		1500	80		Chrysler	none		indolene	32	0
5/6/98	find94	temp-controlled (outside engine)	0.069	10		1500	94		Chrysler	none		indolene	32	0
5/6/98	find96	temp-controlled (outside engine)	0.069	10		1500	96		Chrysler	none		indolene	32	0
5/6/98	find98	temp-controlled (outside engine)	0.069	10		1500	98		Chrysler	none		indolene	32	0
5/6/98	find92	temp-controlled (outside engine)	0.069	10		1500	92		Chrysler	none		indolene	32	0
5/6/98	find60	temp-controlled (outside engine)	0.069	10		1500	60		Chrysler	none		indolene	32	0
5/6/98	find30	temp-controlled (outside engine)	0.069	10		1500	30		Chrysler	none		Indolene	32	0
8/24/98	sascat0	beam profile / no spray /near center stroke	x	10		2000	30	30	Chrysler	none		stoddard	32	0
8/24/98	sascat1	beam profile / with spray /near center stroke	x	10		2000	30	30	Chrysler	none		stoddard	32	0
8/24/98	sascat2	beam profile / no spray / top of comb. chamber	x	10		2000	30	30	Chrysler	none		stoddard	32	0
8/24/98	sascat3	beam profile/ with spray / top of comb. ch.	x	10		2000	30	30	Chrysler	none		stoddard	32	0
8/24/98	scat01	into laser beam		10		2000	30	30	Chrysler	none		stoddard	8	0
8/24/98	scat02	into laser beam		10		2000	30	30	Chrysler	none		indolene	16	0
8/24/98	scat03	into laser beam		10		4000	30	30	Chrysler	none		indolene	16	0
9/2/98	di809021	movie with minimal airflow, 190°; cold	0.202	20	190	movie		30	Chrysler	none		indolene	22	0
9/2/98	di809022	movie with high airflow, 90°; cold	0.202	20	90	movie		40	Chrysler	none		indolene	22	0
9/2/98	di809023	movie with upward airflow, 270°; cold	0.202	20	270	movie		40	Chrysler	none		indolene	22	0
9/2/98	di809024	movie, low airflow, 135°; cold, dirty windows	0.202	20	135	movie		40	Chrysler	none		indolene	22	0
9/2/98	di809025	detailed movie of minimal flow; cold	0.202	20	179	movie		40	Chrysler	none		indolene	22	0
9/3/98	di809031	detailed movie of low upward flow, 45°; cold	0.202	20	225	movie		35	Chrysler	none		Indolene	22	0
9/3/98	di809032	movie of low upward flow; cold	0.202	20	225	movie		38	Chrysler	none		indolene	22	0
9/3/98	di809033	movie, low airflow, 135°; cold	0.202	20	135	movie		35	Chrysler	none		indolene	22	0
9/4/98	di809041	movie, minimal airflow; hot	0.202	20	179	movie	90	90	Chrysler	none		indolene	22	0
9/4/98	di809042	movie, max airflow, hot	0.202	20	90	movie	90	90	Chrysler	none		indolene	22	0
9/4/98	di809043	movie, upward flow, hot	0.202	20	270	movie	90	90	Chrysler	none		indolene	22	0
9/4/98	di809044	movie, slow upward flow, hot	0.202	20	225	movie	90	100	Chrysler	none		indolene	22	0
9/4/98	di809045	detailed movie, slow upward flow, hot	0.202	20	225	movie	90	100	Chrysler	none		indolene	22	0
9/4/98	di809046	detailed movie, max airflow, hot	0.202	20	90	movie	90	100	Chrysler	none		indolene	22	0
9/4/98	di809047	detailed movie, upward flow, hot	0.202	20	270	movie	90	100	Chrysler	none		indolene	22	0
9/14/98	di809141	movie, low flow, hot	0.202	20	135	movie	90	90	Chrysler	none		indolene	22	0
9/14/98	di809142	detailed movie, minimal flow, hot	0.202	20	179	movie	90	90	Chrysler	none		indolene	22	0
9/15/98	di809151	high pressure, late injection, cold, didn't fire	0.202	20	270	movie	30	30	Chrysler	none		indolene	22	0
9/18/98	di809181	high pressure, late injection, cold	0.202	8	270	movie	30	30	Chrysler	none		indolene	22	0
9/18/98	di809182	high pressure, BDC injection, cold	0.202	8	179	movie	30	30	Chrysler	none		indolene	22	0
9/18/98	di809183	high pressure, early injection, cold	0.202	8	90	movie	30	30	Chrysler	none		indolene	22	0
9/18/98	di809184	high pressure, late injection, hot	0.202	8	270	movie	90	90	Chrysler	none		indolene	22	0
9/18/98	di809185	high pressure, BDC injection, hot	0.202	8	179	movie	90	90	Chrysler	none		indolene	22	0
9/18/98	di809186	high pressure, early injection, hot	0.202	8	90	movie	90	90	Chrysler	none		indolene	22	0
9/18/98	di809187	full movie-but not to end of injection	0.202	8		movie			Chrysler	none		indolene	22	0
9/23/98	di809231	iso-octane reference spray (rinsed once)	0.202	10	179	2000	50	50	Chrysler	none		indolene	22	0
9/23/98	di809232	ALCB; acetone fuel mix, BDC injection, cold	0.202	11	179	movie	30	30	Chrysler	acetone	10:1	mix	8	-10

Appendix 4: Imaging F Experiment Log

		CAMERA						LASER				ENGINE				OTHER	
Date	File Name	Gate Width	Gate Del	Laser Del	Cam. Del	Gain	Exposure	Laser E	Width	Height	Location	Inj. Dur.	Skip Fire	Spark	Cam	Eq. Ratio	MAP
mo/day/yr	*[].spe*	*µs*	*µs*	*µs*	*µs*	*%*	*sec*	*mJ*	*mm*	*mm*		*ms*	*sk:fr:trg*	*°ABCI*	*eo/io/ec/ic*	*lambda*	*bar*
5/4/98	m2mb100	1	2000		1996	90	0.05	1.0 W	0.5	full	center of inj.						1
5/4/98	m2mb100b	1	2000		1996	90	0.05	1.0 W	0.5	full	center of inj.						1
5/4/98	m2mb100c	1	2000		1996	90	0.05	1.0 W	thnr	full	center of inj.						1
5/4/98	m2mb30t	1	2000		1996	90	0.05	1.0 W	0.5	full	center of inj.						1
5/4/98	m2mb30b	1	2000		1996	90	0.05	1.0 W	thckr	full	center of inj.						1
5/6/98	find70	1	1500	1997	1996	75	0.05	100	0.5	full	center of inj.						1
5/6/98	find90	1	1500	1997	1996	75	0.05	100	0.5	full	center of inj.						1
5/6/98	find110	1	1500	1997	1996	75	0.05	100	0.5	full	center of inj.						1
5/6/98	find120	1	1500	1997	1996	75	0.05	100	0.5	full	center of inj.						1
5/6/98	find100	1	1500	1997	1996	75	0.05	100	0.5	full	center of inj.						1
5/6/98	find80	1	1500	1997	1996	75	0.05	100	0.5	full	center of inj.						1
5/6/98	find94	1	1500	1997	1996	75	0.05	100	0.5	full	center of inj.						1
5/6/98	find96	1	1500	1997	1996	75	0.05	100	0.5	full	center of inj.						1
5/6/98	find98	1	1500	1997	1996	75	0.05	100	0.5	full	center of inj.						1
5/6/98	find92	1	1500	1997	1996	75	0.05	100	0.5	full	center of inj.						1
5/6/98	find60	1	1500	1997	1996	75	0.05	100	0.5	full	center of inj.						1
5/6/98	find30	1	1500	1997	1996	75	0.05	100	0.5	full	center of inj.						1
8/24/98	sascat0	1	2000	1997	1996	60	0.05	100	0.5	full	center of inj.						1
8/24/98	sascat1	1	2000	1997	1996	60	0.05	100	0.5	full	center of inj.						1
8/24/98	sascat2	1	2000	1997	1996	60	0.05	100	0.5	full	center of inj.						1
8/24/98	sascat3	1	2000	1997	1996	60	0.05	100	0.5	full	center of inj.						1
8/24/98	scat01	1	2000	1997	1996	60	0.05	100	0.5	full	center of inj.						1
8/24/98	scat02	1	2000	1997	1996	75	0.05	100	0.5	full	center of inj.						1
8/24/98	scat03	1	4000	3997	3996	75	0.05	100	0.5	full	center of inj.						1
9/2/98	di809021	1	400...7200 x400 (-3,-4)			90	0.05	100	0.5	full	center of inj.			155	48/5/12/55		0.3
9/2/98	di809022	1	400...7200 x400 (-3,-4)			90	0.05	100	0.5	full	center of inj.			155	48/5/12/55		0.3
9/2/98	di809023	1	400...7200 x400 (-3,-4)			90	0.05	100	0.5	full	center of inj.			155	48/5/12/55		0.3
9/2/98	di809024	1	400...7200 x400 (-3,-4)			90	0.05	100	0.5	full	center of inj.			155	48/5/12/55		0.3
9/2/98	di809025	1	350...1200 x50 +10k,15k (-3,-4)			90	0.05	100	0.5	full	center of inj.			155	48/5/12/55		0.3
9/3/98	di809031	1	350...1200 x50 +10k,15k (-3,-4)			90	0.05	100	0.5	full	center of inj.		10:10:10	155	48/5/12/55		0.3
9/3/98	di809032	1	400...7200 x400 (-3,-4)			90	0.05	100	0.5	full	center of inj.		10:10:10	155	48/5/12/55		0.3
9/3/98	di809033	1	400...7200 x400 (-3,-4)			90	0.05	100	0.5	full	center of inj.		10:10:10	155	48/5/12/55		0.3
9/4/98	di809041	1	400...7200 x400 (-3,-4)			90	0.05	100	0.5	full	center of inj.		10:10:10	155	48/5/12/55		0.3
9/4/98	di809042	1	400...7200 x400 (-3,-4)			90	0.05	100	0.5	full	center of inj.		10:10:10	155	48/5/12/55		0.3
9/4/98	di809043	1	400...7200 x400 (-3,-4)			90	0.05	100	0.5	full	center of inj.		10:10:10	155	48/5/12/55		0.3
9/4/98	di809044	1	400...7200 x400 (-3,-4)			90	0.05	100	0.5	full	center of inj.		10:10:10	155	48/5/12/55		0.3
9/4/98	di809045	1	350...1200 x50 +10k,15k (-3,-4)			90	0.05	100	0.5	full	center of inj.		10:10:10	155	48/5/12/55		0.3
9/4/98	di809046	1	350...1200 x50 +10k,15k (-3,-4)			90	0.05	100	0.5	full	center of inj.		10:10:10	155	48/5/12/55		0.3
9/4/98	di809047	1	350...1200 x50 +10k,15k (-3,-4)			90	0.05	100	0.5	full	center of inj.		10:10:10	155	48/5/12/55		0.3
9/14/98	di809141	1	400...7200 x400 (-3,-4)			90	0.05	100	0.5	full	center of inj.		10:10:10	155	48/5/12/55		0.3
9/14/98	di809142	1	350...1200 x50 +10k,15k (-3,-4)			90	0.05	100	0.5	full	center of inj.		10:10:10	155	48/5/12/55		0.3
9/15/98	di809151	1		-3	-4	90	0.05	100	0.5	full	center of inj.	3.0	15:5:5	180	48/5/12/55		0.9
9/18/98	di809181	1	400...2400 x400 (-3,-4)			90	0.05	100	0.5	full	center of inj.	5.3	15:5:5	155	48/5/12/55		0.9
9/18/98	di809182	1	400...2400 x400 (-3,-4)			90	0.05	100	0.5	full	center of inj.	7.2	15:5:5	155	48/5/12/55		0.9
9/18/98	di809183	1	400...2400 x400 (-3,-4)			90	0.05	100	0.5	full	center of inj.	7.2	15:5:5	180	48/5/12/55		0.9
9/18/98	di809184	1	400...2400 x400 (-3,-4)			90	0.05	100	0.5	full	center of inj.	7.2	15:5:5	180	48/5/12/55		0.9
9/18/98	di809185	1	400...2400 x400 (-3,-4)			90	0.05	100	0.5	full	center of inj.	7.2	15:5:5	180	48/5/12/55		0.9
9/18/98	di809186	1	400...2400 x400 (-3,-4)			90	0.05	100	0.5	full	center of inj.	7.2	15:5:5	180	48/5/12/55		0.9
9/18/98	di809187	1	400...2400 x400 (-3,-4)			90	0.05	100	0.5	full	center of inj.	7.2	15:5:5	180	48/5/12/55		0.9
9/23/98	di809231	1	400...2400 x400 (-3,-4)			90	0.05	100	0.5	full	center of inj.	2.6	3:10:10	155	48/5/12/55	1.0	0.3
9/23/98	di809232	0.2	2000	-3.6	-4	90	0.05	100	0.5	full	center of inj.	2.9	15:5:5	155	48/5/12/55		0.3

Appendix 4: Imaging F Experiment Log

Date	File Name	EXPERIMENT							FUEL/DOPANT				
		Description	Scale	Frames	Injection	Camera	Inj. T.	Head T.	Injector	Dopant	Doping	Fuel	F-stop	Cooler T
mo/day/yr	dl####		mm/pix		°ATCI	µsASOI	°C	°C	Make(angle)		vol. ratio		f/#	°C
9/23/98	dl809233	ALCE; acetone fuel mix, early injection, cold	0.202	11	90	movie	30	30	Chrysler	acetone	10:1	mix	4	-10
9/23/98	dl809234	ALCL; acetone fuel mix, late injection, cold	0.202	11	270	movie	30	30	Chrysler	acetone	10:1	mix	4	-10
9/23/98	dl809235	ALHE; acetone fuel mix, early injection, hot	0.202	11	90	movie	90	90	Chrysler	acetone	10:1	mix	4	-10
9/23/98	dl809236	ALHB; acetone fuel mix, BDC injection, hot	0.202	11	179	movie	90	90	Chrysler	acetone	10:1	mix	4	-10
9/23/98	dl809237	acetone fuel mix, late injection, hot	0.202	11	270	movie	90	90	Chrysler	acetone	10:1	mix	4	-10
9/23/98	dl809238	ALHL; ace mix, late, hot - higher f/#	0.202	11	270	movie	90	90	Chrysler	acetone	10:1	mix	5.6	-10
9/28/98	dl809281	ace mix, high P, BDC, cold	0.202	11	179	movie	30	30	Chrysler	acetone	10:1	mix	4	-10
9/28/98	dl809282	AHCE; ace mix, high P, early, cold	0.202	11	90	movie	30	30	Chrysler	acetone	10:1	mix	4	-10
9/28/98	dl809283	ace mix, high P, late, cold	0.202	10	270	movie	30	30	Chrysler	acetone	10:1	mix	4	-10
9/28/98	dl809284	AHCL; ace mix, high P, late, cold - higher f/#	0.202	10	270	movie	30	30	Chrysler	acetone	10:1	mix	5.6	-10
9/28/98	dl809285	AHCB; ace mix, high P. BDC, cold - higher f/#	0.202	11	179	movie	30	30	Chrysler	acetone	10:1	mix	5.6	-10
9/29/98	dl809291	ace mix, high P, late, cold	0.202	11	270	movie	30	30	Chrysler	acetone	10:1	mix	5.6	-10
9/29/98	dl809292	AHHB; ace mix, high P, BDC, hot	0.202	11	179	movie	90	90	Chrysler	acetone	10:1	mix	5.6	-10
9/29/98	dl809293	AHHE; ace mix, high P, early, hot	0.202	11	90	movie	90	90	Chrysler	acetone	10:1	mix	5.6	-10
9/29/98	dl809294	ace mix, high P, late, hot	0.202	11	270	movie	90	90	Chrysler	acetone	10:1	mix	5.6	-10
9/29/98	dl809295	AHHL; same, clean windows	0.202	11	270	movie	90	90	Chrysler	acetone	10:1	mix	5.6	-10
9/29/98	dl809296	ace mix, high P, 225, hot	0.202	11	225	movie	90	90	Chrysler	acetone	10:1	mix	5.6	-10
9/30/98	dl809301	CLCB; cyhx mix, BDC, cold	0.202	11	179	movie	30	30	Chrysler	cyclohexanone	10:1	mix	5.6	-10
9/30/98	dl809302	CLCE; cyhx mix, early, cold	0.202	11	90	movie	30	30	Chrysler	cyclohexanone	10:1	mix	5.6	-10
9/30/98	dl809303	CLCL; cyhx mix, late, cold	0.202	11	270	movie	30	30	Chrysler	cyclohexanone	10:1	mix	5.6	-10
9/30/98	dl809304	CLHB; cyhx mix, BDC, hot	0.202	11	179	movie	90	90	Chrysler	cyclohexanone	10:1	mix	5.6	-10
9/30/98	dl809305	CLHE; cyhx mix, early, hot	0.202	11	90	movie	90	90	Chrysler	cyclohexanone	10:1	mix	5.6	-10
9/30/98	dl809306	CLHL; cyhx mix, late, hot	0.202	11	270	movie	90	90	Chrysler	cyclohexanone	10:1	mix	5.6	-10
9/30/98	dl809307	CHHB; cyhx mix, high P, BDC, hot	0.202	11	179	movie	90	90	Chrysler	cyclohexanone	10:1	mix	5.6	-10
9/30/98	dl809308	CHHE; cyhx mix, high P, early, hot	0.202	11	90	movie	90	90	Chrysler	cyclohexanone	10:1	mix	5.6	-10
9/30/98	dl809309	cyhx mix, high P, late, hot	0.202	11	270	movie	90	90	Chrysler	cyclohexanone	10:1	mix	5.6	-10
9/30/98	dl80930a	CHHL; higher f/#	0.202	11	270	movie	90	90	Chrysler	cyclohexanone	10:1	mix	8.0	-10
9/30/98	dl80930b	CHCE; cyhx mix, high P, early, cold	0.202	11	90	movie	30	30	Chrysler	cyclohexanone	10:1	mix	5.6	-10
9/30/98	dl80930c	CHCB; cyhx mix, high P, BDC, cold	0.202	11	179	movie	30	30	Chrysler	cyclohexanone	10:1	mix	5.6	-10
9/30/98	dl80930d	cyhx mix, high P, late, cold	0.202	11	270	movie	30	30	Chrysler	cyclohexanone	10:1	mix	5.6	-10
9/30/98	dl80930e	CHCL; higher f/#	0.202	11	270	movie	30	30	Chrysler	cyclohexanone	10:1	mix	8.0	-10
10/2/98	dl810211	scattering/flow dist., BDC, cold	0.205	11	179	movie	30	30	Chrysler	none		indolene	16	-10
10/2/98	dl810212	scattering/flow dist., early, cold	0.205	11	90	movie	30	30	Chrysler	none		indolene	16	-10
10/2/98	dl810213	scattering/flow dist., early, hot	0.205	11	90	movie	90	90	Chrysler	none		indolene	22	-10
10/2/98	dl810214	scattering/flow dist., BDC, hot	0.205	11	179	movie	90	90	Chrysler	none		indolene	22	-10
1/6/99	dl901081	Mie scattering movie - cold	0.202	21	183	movie	30	30	Chrysler	none		indolene	2.8	-20
1/6/99	dl901082	Mie scattering movie - cold	0.202	21	183	movie	30	30	Chrysler	none		indolene	2.8	-20
1/6/99	dl901083	Mie scattering movie - med.	0.202	21	183	movie	60	60	Chrysler	none		indolene	2.8	-20
1/6/99	dl901084	Mie scattering movie - med.	0.202	21	183	movie	60	60	Chrysler	none		indolene	2.8	-20
1/6/99	dl901085	Mie scattering movie - hot	0.202	21	183	movie	90	90	Chrysler	none		indolene	2.8	-20
1/6/99	dl901086	Mie scattering movie - hot	0.202	21	183	movie	90	90	Chrysler	none		indolene	2.8	-20
1/8/99	dl901081	slit -4mm gap - 15mm down	0.202	10		movie	20	20	Chrysler	none		unknown	2.8	-20
1/8/99	dl901082	slit -4mm gap - 15mm down	0.202	10		movie	20	20	Chrysler	none		2-methylbutane	2.8	-20
1/8/99	dl901083	slit -4mm gap - 15mm down	0.202	10		movie	60	60	Chrysler	none		2-methylbutane	2.8	-20
1/8/99	dl901084	slit -4mm gap - 15mm down	0.202	10		movie	80	80	Chrysler	none		2-methylbutane	2.8	-20
1/8/99	dl901085	slit -4mm gap - 15mm down	0.202	10		movie	80	80	Chrysler	none		2-methylbutane	2.8	-20
1/8/99	dl901086	slit -4mm gap - 15mm down	0.202			8000	80	80	Chrysler	none		2-methylbutane	2.8	-20
1/9/99	dl901091	slit -2mm gap - 15mm down	0.202			8000	20	20	Chrysler	none		2-methylbutane	2.8	-20
1/9/99	dl901092	slit -2mm gap - 15mm down	0.202			8000	60	60	Chrysler	none		2-methylbutane	2.8	-20
1/9/99	dl901093	slit -2mm gap - 15mm down	0.202			8000	70	70	Chrysler	none		2-methylbutane	2.8	-20
1/9/99	dl901094	slit -2mm gap - 15mm down	0.202			8000	80	80	Chrysler	none		2-methylbutane	2.8	-20

Appendix 4: Imaging F Experiment Log

		CAMERA						LASER				ENGINE				OTHER	
Date	File Name	Gate Width	Gate Del	Laser Del	Cam. Del	Gain	Exposure	Laser E	Width	Height	Location	Inj. Dur.	Skip Fire	Spark	Cam	Eq. Ratio	MAP
mo/day/yr	*[].spe*	*µs*	*µs*	*µs*	*µs*	*%*	*sec*	*mJ*	*mm*	*mm*		*ms*	*sk:fr:trg*	*°ABCI*	*eo/io/ec/ic*	*lambda*	*bar*
9/23/98	di809233	0.2	400...3200	x400	+6,10 (-3.6,-4)	90	0.05	100	0.5	full	center of inj.	2.9	15:5:5	155	48/5/12/55		0.3
9/23/98	di809234	0.2	400...3200	x400	+6,10 (-3.6,-4)	90	0.05	100	0.5	full	center of inj.	2.9	15:5:5	180	48/5/12/55		0.3
9/23/98	di809235	0.2	400...3200	x400	+6,10 (-3.6,-4)	90	0.05	100	0.5	full	center of inj.	2.9	15:5:5	155	48/5/12/55		0.3
9/23/98	di809236	0.2	400...3200	x400	+6,10 (-3.6,-4)	90	0.05	100	0.5	full	center of inj.	2.9	15:5:5	155	48/5/12/55		0.3
9/23/98	di809237	0.2	400...3200	x400	+6,10 (-3.6,-4)	90	0.05	100	0.5	full	center of inj.	2.9	15:5:5	180	48/5/12/55		0.3
9/23/98	di809238	0.2	400...3200	x400	+6,10 (-3.6,-4)	90	0.05	100	0.5	full	center of inj.	2.9	15:5:5	180	48/5/12/55		0.3
9/28/98	di809281	0.2	400...3200	x400	+6,10 (-3.6,-4)	90	0.05	100	0.5	full	center of inj.	7.2	15:5:5	155	48/5/12/55		0.9
9/28/98	di809282	0.2	400...3200	x400	+6,10 (-3.6,-4)	90	0.05	100	0.5	full	center of inj.	7.2	15:5:5	155	48/5/12/55		0.9
9/28/98	di809283	0.2	400...3200	x400	+6,10 (-3.6,-4)	90	0.05	100	0.5	full	center of inj.	7.8	15:5:5	155	48/5/12/55	0.95	0.9
9/28/98	di809284	0.2	400...3200	x400	+6,10 (-3.6,-4)	90	0.05	100	0.5	full	center of inj.	7.8	15:5:5	155	48/5/12/55		0.9
9/28/98	di809285	0.2	400...3200	x400	+6,10 (-3.6,-4)	90	0.05	100	0.5	full	center of inj.	7.8	15:5:5	155	48/5/12/55		0.9
9/29/98	di809291	0.2	400...3200	x400	+6,10 (-3.6,-4)	90	0.05	100	0.5	full	center of inj.	7.8	15:5:5	180	48/5/12/55		0.9
9/29/98	di809292	0.2	400...3200	x400	+6,10 (-3.6,-4)	90	0.05	100	0.5	full	center of inj.	7.8	15:5:5	180	48/5/12/55		0.9
9/29/98	di809293	0.2	400...3200	x400	+6,10 (-3.6,-4)	90	0.05	100	0.5	full	center of inj.	7.8	15:5:5	180	48/5/12/55		0.9
9/29/98	di809294	0.2	400...3200	x400	+6,10 (-3.6,-4)	90	0.05	100	0.5	full	center of inj.	7.8	15:5:5	180	48/5/12/55		0.9
9/29/98	di809295	0.2	400...3200	x400	+6,10 (-3.6,-4)	90	0.05	100	0.5	full	center of inj.	3.0	15:5:5	180	48/5/12/55		0.9
9/29/98	di809296	0.2	400...3200	x400	+6,10 (-3.6,-4)	90	0.05	100	0.5	full	center of inj.	7.8	15:5:5	180	48/5/12/55		0.9
9/30/98	di809301	0.2	400...3200	x400	+6,10 (-3.6,-4)	90	0.05	100	0.5	full	center of inj.	2.7	15:5:5	155	48/5/12/55		0.3
9/30/98	di809302	0.2	400...3200	x400	+6,10 (-3.6,-4)	90	0.05	100	0.5	full	center of inj.	2.7	15:5:5	155	48/5/12/55		0.3
9/30/98	di809303	0.2	400...3200	x400	+6,10 (-3.6,-4)	90	0.05	100	0.5	full	center of inj.	2.7	15:5:5	180	48/5/12/55		0.3
9/30/98	di809304	0.2	400...3200	x400	+6,10 (-3.6,-4)	90	0.05	100	0.5	full	center of inj.	2.7	15:5:5	155	48/5/12/55		0.3
9/30/98	di809305	0.2	400...3200	x400	+6,10 (-3.6,-4)	90	0.05	100	0.5	full	center of inj.	2.7	15:5:5	155	48/5/12/55		0.3
9/30/98	di809306	0.2	400...3200	x400	+6,10 (-3.6,-4)	90	0.05	100	0.5	full	center of inj.	2.7	15:5:5	180	48/5/12/55		0.3
9/30/98	di809307	0.2	400...3200	x400	+6,10 (-3.6,-4)	90	0.05	100	0.5	full	center of inj.	7.5	15:5:5	180	48/5/12/55		0.9
9/30/98	di809308	0.2	400...3200	x400	+6,10 (-3.6,-4)	90	0.05	100	0.5	full	center of inj.	7.5	15:5:5	180	48/5/12/55		0.9
9/30/98	di809309	0.2	400...3200	x400	+6,10 (-3.6,-4)	90	0.05	100	0.5	full	center of inj.	7.5	15:5:5	180	48/5/12/55		0.9
9/30/98	di80930a	0.2	400...3200	x400	+6,10 (-3.6,-4)	90	0.05	100	0.5	full	center of inj.	7.5	15:5:5	180	48/5/12/55		0.9
9/30/98	di80930b	0.2	400...3200	x400	+6,10 (-3.6,-4)	90	0.05	100	0.5	full	center of inj.	7.5	15:5:5	170	48/5/12/55		0.9
9/30/98	di80930c	0.2	400...3200	x400	+6,10 (-3.6,-4)	90	0.05	100	0.5	full	center of inj.	7.5	15:5:5	180	48/5/12/55		0.9
9/30/98	di80930d	0.2	400...3200	x400	+6,10 (-3.6,-4)	90	0.05	100	0.5	full	center of inj.	7.5	15:5:5	180	48/5/12/55		0.9
9/30/98	di80930e	0.2	400...3200	x400	+6,10 (-3.6,-4)	90	0.05	100	0.5	full	center of inj.	3.0	17:3:3	180	48/5/12/55		0.9
10/21/98	di810211	0.2	400...3200	x400	+6,10 (-3.6,-4)	90	0.05	100	0.5	full	center of inj.	2.7	10:10:10	155	48/5/12/55		0.3
10/21/98	di810212	0.2	400...3200	x400	+6,10 (-3.6,-4)	90	0.05	100	0.5	full	center of inj.	2.7	10:10:10	155	48/5/12/55		0.3
10/21/98	di810213	0.2	400...3200	x400	+6,10 (-3.6,-4)	90	0.05	100	0.5	full	center of inj.	2.7	10:10:10	155	48/5/12/55		0.3
10/21/98	di810214	0.2	400...3200	x400	+6,10 (-3.6,-4)	90	0.05	100	0.5	full	center of inj.	2.7	10:10:10	155	48/5/12/55		0.3
1/6/99	di901061	1	400...4200	x200	-4	90	0.05	*1.5 W*	0.5	full	center of inj.	2.7	10:10:10	155	48/5/12/55		0.3
1/6/99	di901062	1.5	400...4200	x200	-4	90	0.05	*1.5 W*	0.5	full	center of inj.	2.7	10:10:10	155	48/5/12/55		0.3
1/6/99	di901063	1.5	400...4200	x200	-4	90	0.05	*1.5 W*	0.5	full	center of inj.	2.7	10:10:10	155	48/5/12/55		0.3
1/6/99	di901064	1.5	400...4200	x200	-4	90	0.05	*1.5 W*	0.5	full	center of inj.	2.7	10:10:10	155	48/5/12/55		0.3
1/6/99	di901065	1.5	400...4200	x200	-4	90	0.05	*1.5 W*	0.5	full	center of inj.	2.7	10:10:10	155	48/5/12/55		0.3
1/6/99	di901066	1.5	400...4200	x200	-4	90	0.05	*1.5 W*	0.5	full	center of inj.	2.7	10:10:10	155	48/5/12/55		0.3
1/8/99	di901081	1.5	400...4200	x200	-4	90	0.05	*1.5 W*	0.5	full	center of inj.	5.0					1
1/8/99	di901082	1.5	400...4200	x200	-4	90	0.05	*1.5 W*	0.5	full	center of inj.	5.0					1
1/8/99	di901083	1	400...4200	x200	-4	90	0.05	*1.5 W*	0.5	full	center of inj.	5.0					1
1/8/99	di901084	0.7	400...4200	x200	-4	90	0.05	*1.5 W*	0.5	full	center of inj.	5.0					1
1/8/99	di901085	0.5	400...4200	x200	-4	90	0.05	*1.5 W*	0.5	full	center of inj.	5.0					1
1/8/99	di901086	0.5	8000		-4	90	0.05	*1.5 W*	0.5	full	center of inj.	10.0					1
1/9/99	di901091	0.5	8000		-4	90	0.05	*1.3 W*	0.5	full	center of inj.	10.0					1
1/9/99	di901092	0.5	8000		-4	90	0.05	*1.5 W*	0.5	full	center of inj.	10.0					1
1/9/99	di901093	0.5	8000		-4	90	0.05	*1.5 W*	0.5	full	center of inj.	10.0					1
1/9/99	di901094	0.5	8000		-4	90	0.05	*1.5 W*	0.5	full	center of inj.	10.0					1

Appendix 4: Imaging F Experiment Log

Date:	File Name:	EXPERIMENT							FUEL/DOPANT				
		Description	Scale	Frames	Injection	Camera	Inj. T.	Head T.	Injector	Dopant	Doping	Fuel	F-stop	Cooler T
mo/da/yr	(type)		mm/pix		°ATCI	μsASOI	°C	°C	Make(angle)		vol. ratio		f/#	°C
1/9/99	dl901095	half spray - 15 mm down	0.202				70	70	Chrysler	none		2-methylbutane	2.8	-20
1/9/99	dl901096		0.202				80	80	Chrysler	none		2-methylbutane	2.8	-20
1/9/99	dl901097		0.202				80	80	Chrysler	none		2-methylbutane	2.8	-20
1/9/99	dl901098	slit - 2mm gap - 15mm down - thicker laser	0.202	5		8000	60	60	Chrysler	none		2-methylbutane	2.8	-20
1/9/99	dl901099	slit - 2mm gap - 15mm down - thicker laser	0.202	5		8000	80	80	Chrysler	none		2-methylbutane	2.8	-20
1/9/99	dl90109a	slit - 2mm gap - 15mm down - thicker laser	0.202	5		8000	25	25	Chrysler	none		2-methylbutane	2.8	-20
1/9/99	dl90109b	slit - 2mm gap - 15mm down - thicker laser	0.202	5		8000	25	25	Chrysler	none		2-methylbutane	2.8	-20
1/9/99	dl90109c	slit - 2mm gap - 15mm down - thicker laser	0.202	5		8000	60	60	Chrysler	none		2-methylbutane	2.8	-20
1/9/99	dl90109d	slit - 2mm gap - 15mm down - thicker laser	0.202	5		8000	80	80	Chrysler	none		2-methylbutane	2.8	-20
1/11/99	dl901111	backlit movie - larger field	0.112	20		movie	20	20	Chrysler	none		2-methylbutane	11	-20
1/11/99	dl901112	backlit movie - smaller field	0.049	10		8000	20	20	Chrysler	none		2-methylbutane	11	-20
1/11/99	dl901113	backlit movie - smaller field	0.049	10		8000	60	60	Chrysler	none		2-methylbutane	11	-20
2/11/99	dl902111	slit - 2mm gap - 15mm down	0.202	10		8000	30		Chrysler	none		2-methylbutane		-20
2/11/99	dl902112	slit - 2mm gap - 20mm down	0.202	10		8000	30		Chrysler	none		2-methylbutane		-20
2/11/99	dl902113	slit - 2mm gap - 25mm down	0.202	10		8000	30		Chrysler	none		2-methylbutane		-20
2/11/99	dl902114	slit - 2mm gap - 10mm down	0.202	10		8000	30		Chrysler	none		2-methylbutane		-20
2/11/99	dl902115	slit - 2mm gap - 10mm down	0.202	10		8000	60		Chrysler	none		2-methylbutane		-20
2/11/99	dl902116	slit - 2mm gap - 10mm down	0.202	10		8000	80		Chrysler	none		2-methylbutane		-20
2/11/99	dl902117	slit - 2mm gap - 25mm down	0.202	10		8000	80		Chrysler	none		2-methylbutane		-20
2/11/99	dl902118	slit - 2mm gap - 25mm down	0.202	10		8000	60		Chrysler	none		2-methylbutane		-20
2/11/99	dl902119	slit - 2mm gap - 15mm down	0.202	10		8000	60		Chrysler	none		2-methylbutane		-20
2/11/99	dl90211a	slit - 2mm gap - 15mm down	0.202	10		8000	80		Chrysler	none		2-methylbutane		-20
2/11/99	dl90211b	slit - 2mm gap - 20mm down	0.202	10		8000	80		Chrysler	none		2-methylbutane		-20
2/11/99	dl90211c	slit - 2mm gap - 20mm down	0.202	10		8000	60		Chrysler	none		2-methylbutane		-20

Appendix 4: Imaging F Experiment Log

		CAMERA						LASER				ENGINE				OTHER	
Date	File Name	Gate Width	Gate Del	Laser Del	Cam. Del	Gain	Exposure	Laser E	Width	Height	Location	Inj. Dur.	Skip Fire	Spark	Cam	Eq. Ratio	MAP
mo/day/yr	*[].spe*	*µs*	*µs*	*µs*	*µs*	*%*	*sec*	*mJ*	*mm*	*mm*		*ms*	*sk:fr:trg*	*°ABCI*	*eo/io/ec/ic*	*lambda*	*bar*
1/9/99	di901095	0.5			-4	90	0.05	*1.5 W*	0.5	full	center of inj.	10.0					1
1/9/99	di901096	0.5			-4	90	0.05	*1.5 W*	0.5	full	center of inj.	10.0					1
1/9/99	di901097	0.5			-4	90	0.05	*1.5 W*	0.5	full	center of inj.	10.0					1
1/9/99	di901098	0.5	8000		-4	90	0.05	*1.5 W*	3	full	center of inj.	10.0					1
1/9/99	di901099	0.5	8000		-4	90	0.05	*1.5 W*	3	full	center of inj.	10.0					1
1/9/99	di90109a	0.5	8000		-4	90	0.05	*1.5 W*	3	full	center of inj.	10.0					1
1/9/99	di90109b	0.5	8000		-4	90	0.05	*1.5 W*	0.5	full	center of inj.	10.0					1
1/9/99	di90109c	0.5	8000		-4	90	0.05	*1.5 W*	0.5	full	center of inj.	10.0					1
1/9/99	di90109d	0.5	8000		-4	90	0.05	*1.5 W*	0.5	full	center of inj.	10.0					1
1/11/99	di901111	0.5	400...2000	x200 +0	-4	90	0.05					10.0					1
1/11/99	di901112	0.5	8000		-4	90	0.05					10/0					1
1/11/99	di901113	0.5	8000		-4	90	0.05					10/0					1
2/11/99	di902111		8000		-4	90	0.05	*1.5 W*	3	full	center of inj.	10.0					1
2/11/99	di902112		8000		-4	90	0.05	*1.5 W*	3	full	center of inj.	10.0					1
2/11/99	di902113		8000		-4	90	0.05	*1.5 W*	3	full	center of inj.	10.0					1
2/11/99	di902114		8000		-4	90	0.05	*1.5 W*	3	full	center of inj.	10.0					1
2/11/99	di902115		8000		-4	90	0.05	*1.5 W*	3	full	center of inj.	10.0					1
2/11/99	di902116		8000		-4	90	0.05	*1.5 W*	3	full	center of inj.	10.0					1
2/11/99	di902117		8000		-4	90	0.05	*1.5 W*	3	full	center of inj.	10.0					1
2/11/99	di902118		8000		-4	90	0.05	*1.5 W*	3	full	center of inj.	10.0					1
2/11/99	di902119		8000		-4	90	0.05	*1.5 W*	3	full	center of inj.	10.0					1
2/11/99	di90211a		8000		-4	90	0.05	*1.5 W*	3	full	center of inj.	10.0					1
2/11/99	di90211b		8000		-4	90	0.05	*1.5 W*	3	full	center of inj.	10.0					1
2/11/99	di90211c		8000		-4	90	0.05	*1.5 W*	3	full	center of inj.	10.0					1

APPENDIX 5
SCATTERING CALCULATIONS

Scattering Intensity

This scattering analysis (adapted from Goody,1) begins with *Lambert's Law*

$$dI_\upsilon = -e_\upsilon n I_\upsilon d\ell \tag{A5.1}$$

which relates the change in radiant intensity of a light beam over an infinitesimal distance due to absorbing molecules to their density and extinction coefficient. Writing this equation in terms of the scattered light, and assuming no absorption and a single frequency:

$$\frac{dI_s}{d\ell} = snI \tag{A5.2}$$

The scattering efficiency is defined as

$$Q_s = \frac{s}{\pi r^2} \tag{A5.3}$$

The droplet size relative to the light wavelength is defined by x.

$$x = \frac{2\pi r}{\lambda} \tag{A5.4}$$

As the droplets become much larger than the wavelength of the light, the scattering efficiency, Q_s, approaches a constant value of 2:

$$Q_s \to 2 \quad \text{as} \quad x \to \infty$$

Also, for x greater than about 6, the scattering efficiency is oscillatory around 2. Therefore, for a sufficiently polydisperse spray, the scattering efficiency would average out to 2.

Therefore, for large x,

$$s = Q_s \pi r^2 \approx 2\pi r^2 \tag{A5.5}$$

---

1. Goody, Richard, Principles of Atmospheric Physics and Chemistry. Oxford Press, New York, pp. 75-83 (1995).

then,

$$\frac{dI_s}{d\ell} = 2\pi r^2 nI \propto r^2 n \tag{A5.6}$$

This equation shows the proportionality of the intensity of the scattered light to the total droplet surface area.

Next, assuming that a fixed amount of fluid is injected,

$$V = \frac{4}{3}\pi r^3 n \tag{A5.7}$$

Finally, the intensity of scattered light is inversely proportional to the droplet diameter for a fixed volume of fluid.

$$\frac{dI_s}{d\ell} = 2\pi r^2\left(\frac{3V}{4\pi r^3}\right)I = \frac{3VI}{2r} \propto \frac{1}{d} \tag{A5.8}$$

Since, as Eq. A#.6 showed, the scattering is proportional to the total droplet surface area, the appropriate mean diameter to use with Eq. A#.8 is the area mean diameter, D_{20}.

Angular Distribution

Most of the scattered light is concentrated into a strong forward peak [1], assuming multiple-scattering is not a concern. The edge of this peak is located at approximately:

$$x\sin(\theta) \approx 4 \tag{A5.9}$$

This results in a half-angle of the forward scattering peak of:

$$\theta \approx \sin^{-1}\left(\frac{4}{x}\right) = \sin^{-1}\left(\frac{4\lambda}{\pi d}\right) \tag{A5.10}$$

For a 10 μm droplet and the excimer laser, this results in:

$$\theta \approx \sin^{-1}\left(\frac{4(0.308\mu m)}{\pi(10\mu m)}\right) = 2.2° \tag{A5.10}$$

Nomenclature

d	droplet diameter
e	extinction coefficient per perticle
I	radiant intensity
I_s	scattered light radiant intensity
ℓ	path length
n	number density of particles
Q_s	scattering efficiency
r	droplet radius
s	scattering coefficient per particle
V	total liquid volume
x	scattering length scale
λ	light wavelength
λ	light frequency
θ	forward scattering peak half-angle

APPENDIX 6
LINEAR EQUATION SOLVER INPUT FILES

Below are the complete sets of equations solved for the bubble point calculations described in Sec. 3.3.1.3 and the T_{10} calculation in Sec. 3.5.

Bubble point: acetone / iso-octane

```
A12=0.8869
A21=2.1041
a1=7.11714
b1=1210.595
c1=229.664
a2=6.80304
b2=1252.59
c2=220.119

x1=.091
x2=.909

P=0.6*760
g1=exp(A12*(A21*x2/(A12*x1+A21*x2))^2)
g2=exp(A21*(A12*x1/(A12*x1+A21*x2))^2)
p1=10^(a1-b1/(T+c1))
p2=10^(a2-b2/(T+c2))
K1=g1*p1/P
K2=g2*p2/P

BP=K1*x1+K2*x2
BP=1
```

Bubble point: 2-butanone / iso-octane

```
A12=1.2317
A21=1.4248
a1=7.06356
b1=1261.34
c1=221.969
a2=6.80304
b2=1252.59
c2=220.119

x1=.091
x2=.909

P=0.6*760
g1=exp(A12*(A21*x2/(A12*x1+A21*x2))^2)
g2=exp(A21*(A12*x1/(A12*x1+A21*x2))^2)
```

```
p1=10^(a1-b1/(T+c1))
p2=10^(a2-b2/(T+c2))
K1=g1*p1/P
K2=g2*p2/P

BP=K1*x1+K2*x2
BP=1
```

Bubble Point: 3-pentanone / iso-octane

```
A12=0.9331
A21=0.9612
a1=7.02295
b1=1308.874
c1=214.036
a2=6.80304
b2=1252.59
c2=220.119

x1=.091
x2=.909

P=0.6*760
g1=exp(A12*(A21*x2/(A12*x1+A21*x2))^2)
g2=exp(A21*(A12*x1/(A12*x1+A21*x2))^2)
p1=10^(a1-b1/(T+c1))
p2=10^(a2-b2/(T+c2))
K1=g1*p1/P
K2=g2*p2/P

BP=K1*x1+K2*x2
BP=1
```

Ten percent evaporated temperature (T_{10}): acetone / iso-octane

```
A12=0.8869
A21=2.1041
a1=7.11714
b1=1210.595
c1=229.664
a2=6.80304
b2=1252.59
c2=220.119

z1=.091
z2=.909
P=1*760
0.1=V*(58.08*y1+114.231*y2)/(58.08*z1+114.231*z2)

g1=exp(A12*(A21*z2/(A12*z1+A21*z2))^2)
g2=exp(A21*(A12*z1/(A12*z1+A21*z2))^2)
p1=10^(a1-b1/(T+c1))
```

```
p2=10^(a2-b2/(T+c2))
K1=g1*p1/P
K2=g2*p2/P

F*z1 = L*x1+V*y1
F*z2 = L*x2+V*y2
y1=K1*x1
y2=K2*x2
x1+x2=1
y1+y2=1
F=1
```

APPENDIX 7
INDOLENE DEVELOPMENT IMAGES

On the following pages are PLIF images representing the development of indolene sprays at the six different conditions used in the PDPA experiments. The figure numbers for the different conditions are given in Table A7.1 below.

Table A7.1: Operating conditions for indolene development figures.

		Temperature (°C)		
		30	**60**	**90**
Intake Pressure (bar)	**0.3**	1	2	3
	0.6			4
	0.9	6		5

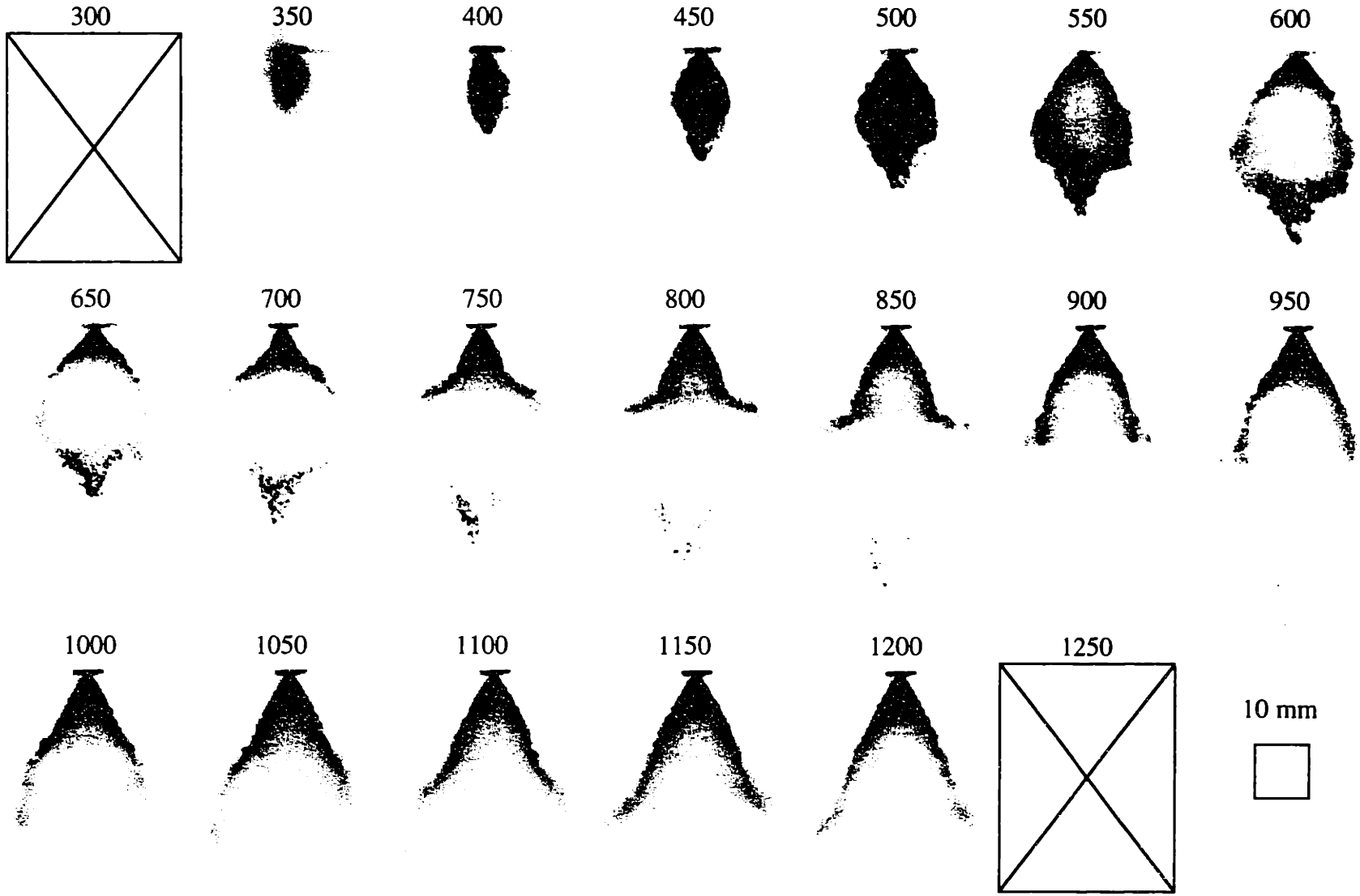

Figure A1.1: P = 0.3 bar / T = 30 °C Spray development sequence(300 to 1250 µs); Chrysler injector; PLIF; indolene.

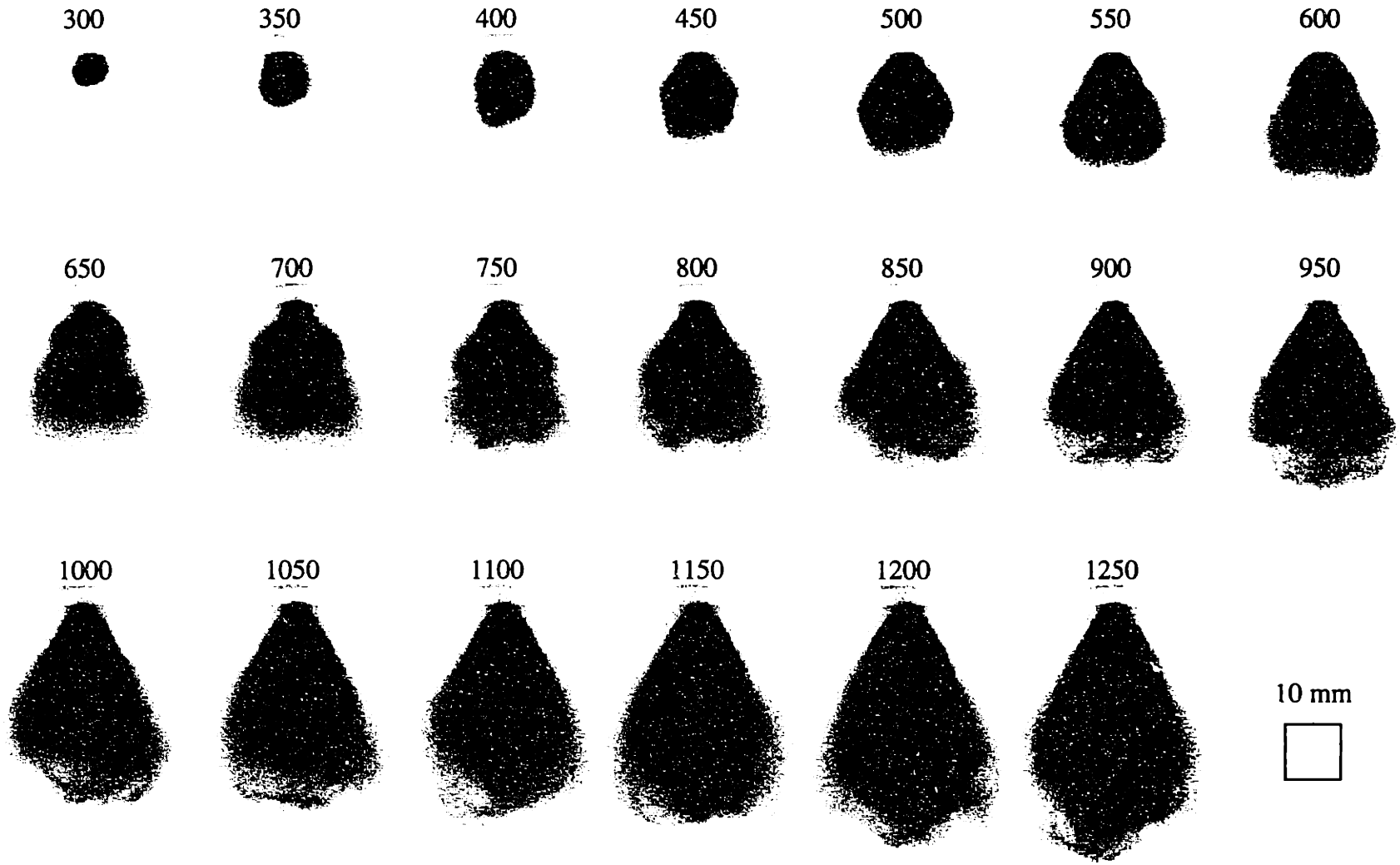

Figure A7.2: P = 0.3 bar / T = 60 °C Spray development sequence (300 to 1250 µs); Chrysler injector; PLIF; indolene.

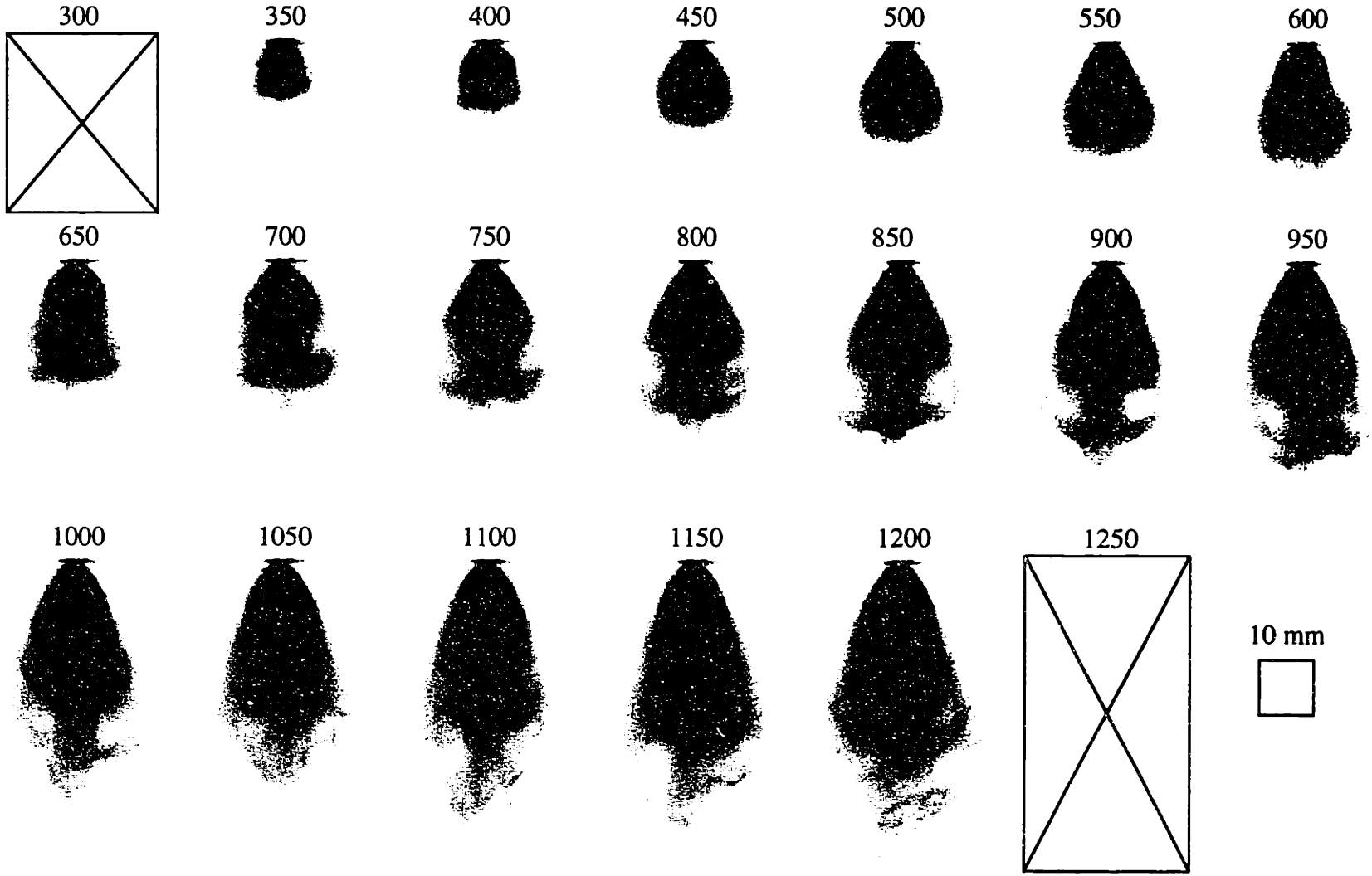

Figure A7.3: P = 0.3 bar / T = 90 °C Spray development sequence (300 to 1250 µs); Chrysler injector; PLIF; indolene.

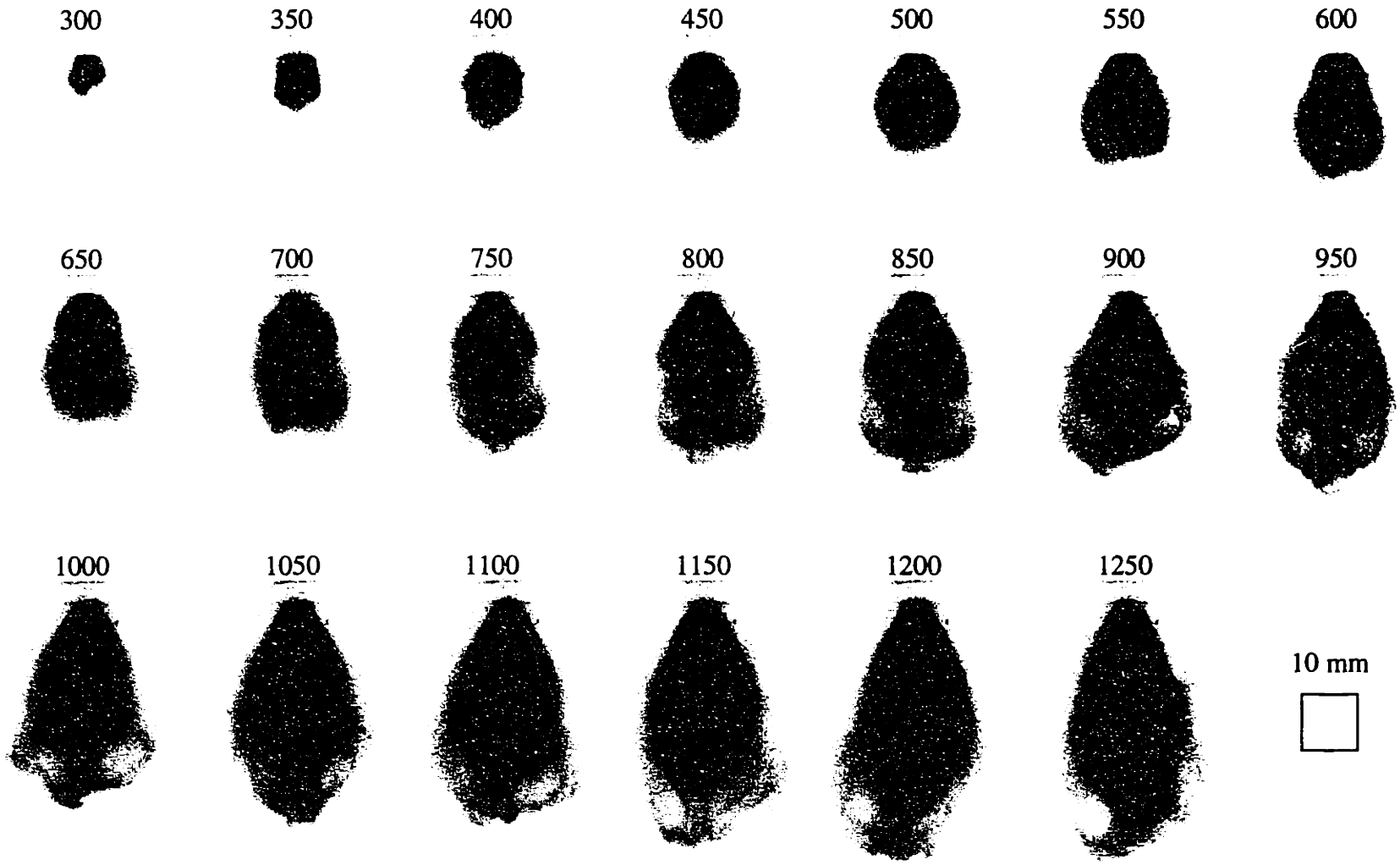

Figure A7.4: P = 0.6 bar / T = 90 °C Spray development sequence (300 to 1250 µs); Chrysler injector; PLIF; indolene.

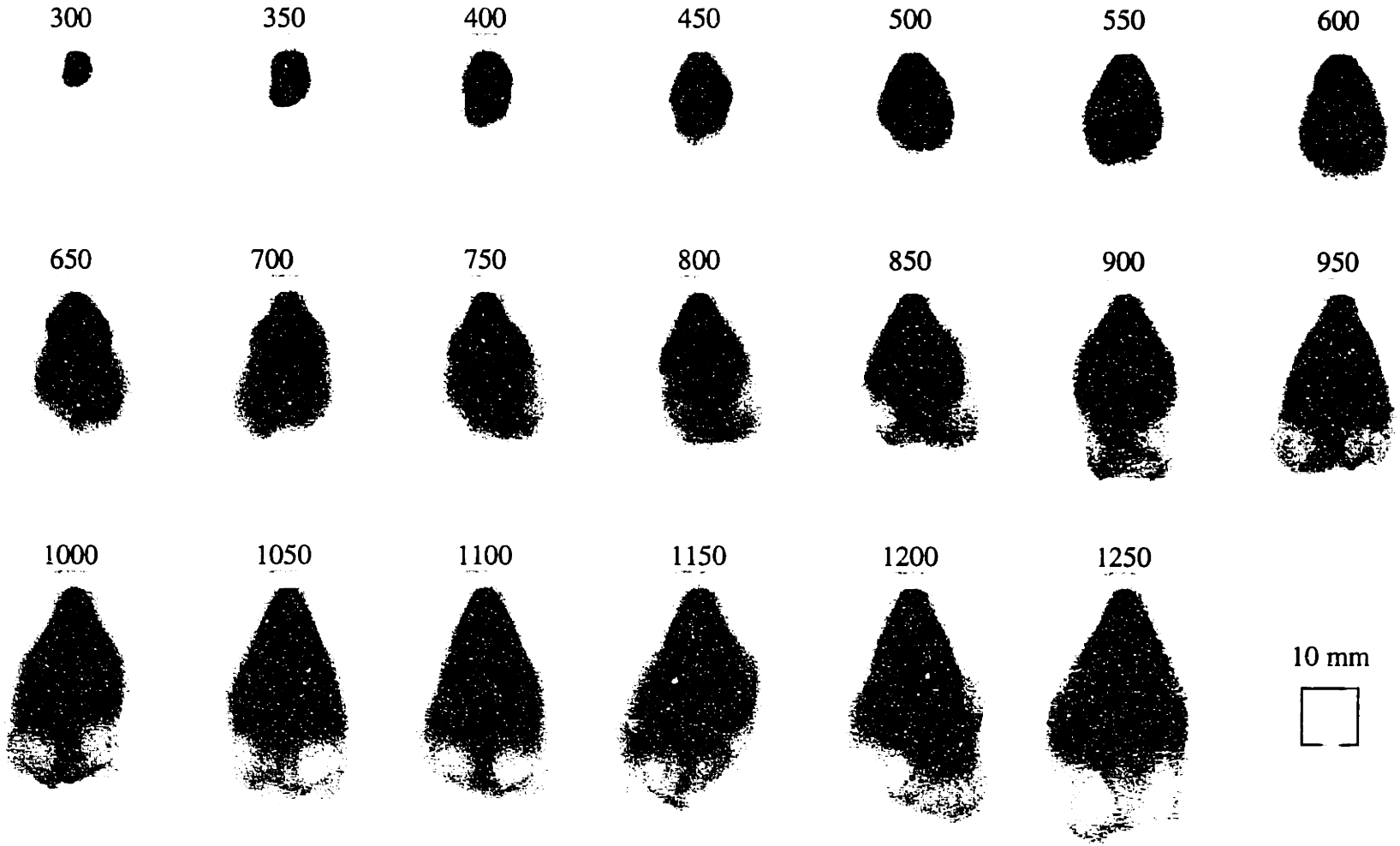

Figure A7.5: P = 0.9 bar / T = 90 °C Spray development sequence (300 to 1250 µs); Chrysler injector; PLIF; indolene.

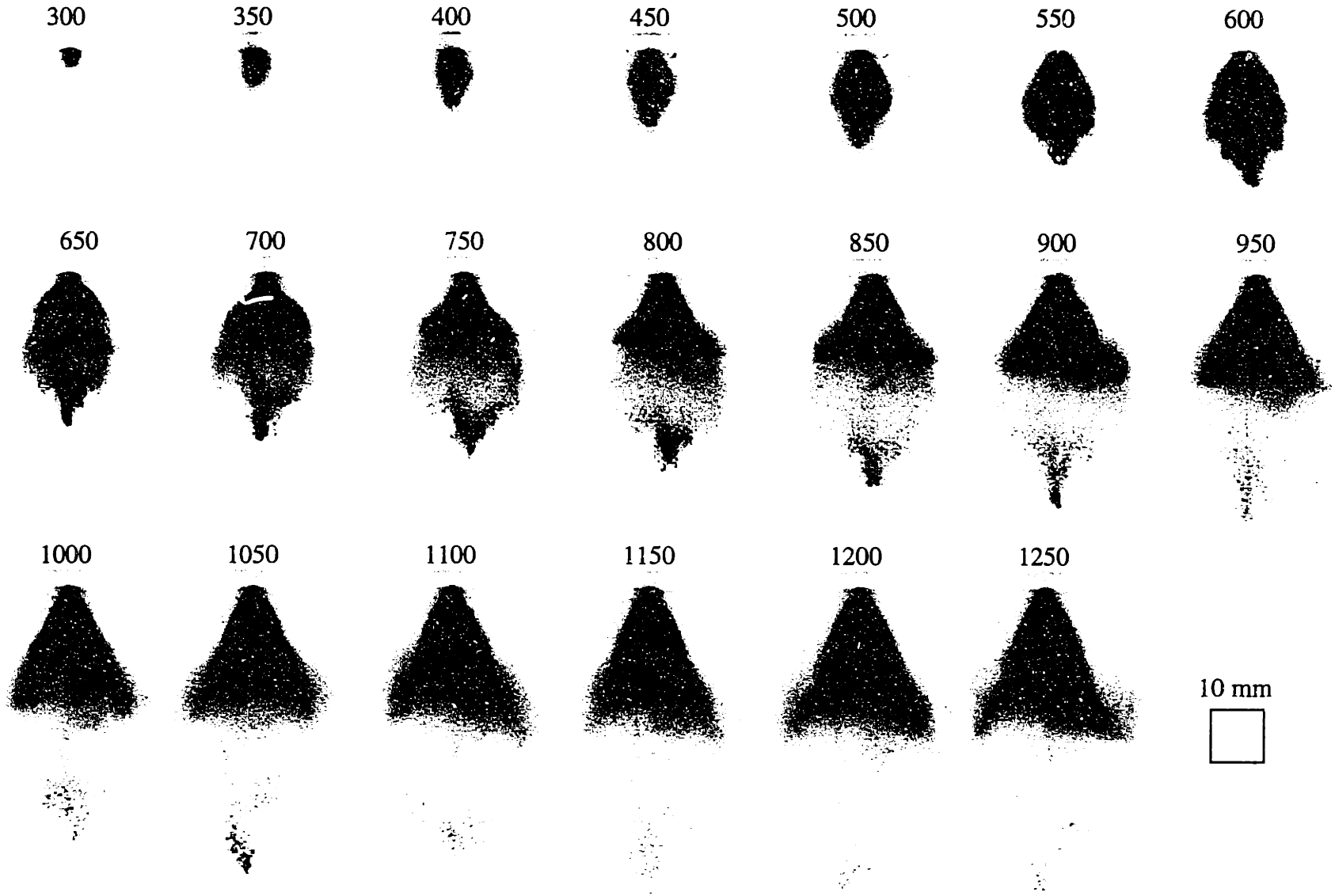

Figure A7.6: P = 0.9 bar / T = 30 °C Spray development sequence (300 to 1250 µs); Chrysler injector; PLIF; indolene.

APPENDIX 8
DATA MANIPULATION ALGORITHMS

Below are programs written for Matlab for manipulating both image and PDPA data.

Before each program is a description of its purpose.

A8.1 PLIF Calibration

Program used to extract the intensity profile from the reference image without beam expansion. Ten frames averaged, and then a number of rows averaged (Sec. 3.7.2.1).

```
fid=zeros(10,1);
fid(1)=fopen('c:\windows\desktop\refb1.bin','r');
fid(2)=fopen('c:\windows\desktop\refb2.bin','r');
fid(3)=fopen('c:\windows\desktop\refb3.bin','r');
fid(4)=fopen('c:\windows\desktop\refb4.bin','r');
fid(5)=fopen('c:\windows\desktop\refb5.bin','r');
fid(6)=fopen('c:\windows\desktop\refb6.bin','r');
fid(7)=fopen('c:\windows\desktop\refb7.bin','r');
fid(8)=fopen('c:\windows\desktop\refb8.bin','r');
fid(9)=fopen('c:\windows\desktop\refb9.bin','r');
fid(10)=fopen('c:\windows\desktop\refb10.bin','r');

sum=zeros(576,384);

for file=1:10
   file
   raw=fread(fid(file),[576,384],'ushort');
   sum=sum+raw;
end

line=fix(mean((sum(25:396,219:338))')./10);
plot(line)

fidout=fopen('c:\windows\desktop\refbline.txt','wt');
count=fprintf(fidout,'%5i\n',line);

fclose('all');
```

Program used to correct acetone vapor reference for absorption. Ten reference frames are averaged, background is subtracted, exponential factor is used to correct for absorption, and output image is written (Sec. 3.7.2.1).

```
b=.00142

fid=zeros(10,1);
fid(1)=fopen('c:\windows\desktop\refa1.bin','r');
fid(2)=fopen('c:\windows\desktop\refa2.bin','r');
fid(3)=fopen('c:\windows\desktop\refa3.bin','r');
fid(4)=fopen('c:\windows\desktop\refa4.bin','r');
fid(5)=fopen('c:\windows\desktop\refa5.bin','r');
fid(6)=fopen('c:\windows\desktop\refa6.bin','r');
fid(7)=fopen('c:\windows\desktop\refa7.bin','r');
fid(8)=fopen('c:\windows\desktop\refa8.bin','r');
fid(9)=fopen('c:\windows\desktop\refa9.bin','r');
fid(10)=fopen('c:\windows\desktop\refa10.bin','r');
fidbg=fopen('c:\windows\desktop\refbg.bin','r');
refbg=fread(fidbg,[576,384],'ushort');

sum=zeros(576,384);
for file=1:10
   file
   raw=fread(fid(file),[576,384],'ushort');
   sum=sum+raw;
end
rfaave=fix(sum./10);
clear sum

rfambg=rfaave-refbg;
neg=rfambg>=0;
rfambg=rfambg.*neg;
clear neg

rfacorr=rfambg+1;
for i=25:396
   cval=exp(b*(396-i));
   rfacorr(i,:)=rfacorr(i,:)*cval;
end

colormap(hot)
image(rfacorr'.*64./65535);
axis off

fidout=fopen('c:\windows\desktop\rfacorr.bin','w');
count=fwrite(fidout,rfacorr,'ushort')
fclose('all');
```

Program used to open PLIF image, subtract the background image, and normalize by the reference image (Sec. 3.7.2.1).

```
fiddi=fopen('c:\windows\desktop\lc180c28.bin','r');
di=fread(fiddi,[576,384],'ushort');
fidbg=fopen('c:\windows\desktop\refbg.bin','r');
bg=fread(fidbg,[576,384],'ushort');
fidcorr=fopen('c:\windows\desktop\rfacorr.bin','r');
rfacorr=fread(fidcorr,[576,384],'ushort');

dimbg=di-bg;
neg=dimbg>=0;
dimbg=dimbg.*neg;
clear neg

direl=dimbg./rfacorr;

lasercorr=mean(mean(direl(460:530,240:320)));
dicorr=direl./lasercorr;

colormap(hot)
image(dicorr'.*64);
axis off

fclose('all');
```

Program used to correct for dopant fluorescence yield and pressure, and to rescale the image. Output is written as an 8-bit image (Sec. 3.7.2.1).

```
fyratio=2.4;
temp=30;
range=0.6;

tcorr=1+0.0013*(temp-27)
correction=(255/range/fyratio/tcorr);
output=fix(dicorr*correction);
for i=1:576
   for j=1:384
      if output(i,j)>255
         output(i,j)=255;
      end
   end
end

fidout=fopen('c:\windows\desktop\lcc28.bin','w');
count=fwrite(fidout,output,'uchar')
fclose('all');
```

A8.2 Miscellaneous PLIF Programs

Program used to average ten image files.

```
fid=zeros(10,1);

fid(1)=fopen('u:\bvdw\LIFDATA\9902\raw\Z20T201.bin','r');
fid(2)=fopen('u:\bvdw\LIFDATA\9902\raw\Z20T202.bin','r');
fid(3)=fopen('u:\bvdw\LIFDATA\9902\raw\Z20T203.bin','r');
fid(4)=fopen('u:\bvdw\LIFDATA\9902\raw\Z20T204.bin','r');
fid(5)=fopen('u:\bvdw\LIFDATA\9902\raw\Z20T205.bin','r');
fid(6)=fopen('u:\bvdw\LIFDATA\9902\raw\Z20T206.bin','r');
fid(7)=fopen('u:\bvdw\LIFDATA\9902\raw\Z20T207.bin','r');
fid(8)=fopen('u:\bvdw\LIFDATA\9902\raw\Z20T208.bin','r');
fid(9)=fopen('u:\bvdw\LIFDATA\9902\raw\Z20T209.bin','r');
fid(10)=fopen('u:\bvdw\LIFDATA\9902\raw\Z20T2010.bin','r');

sum=zeros(576,384);

for file=1:10
   file

   raw=fread(fid(file),[576,384],'ushort');
   sum=sum+raw;
   clear raw
end

sum=fix(sum./10);
colormap(hot)
image(sum'.*64./65535);
axis off

fclose('all');
```

Program used to extract light extinction profile from back-lit images. Five frames are averaged for the image and five for the background, extinction is calculated point-wise assuming a dark charge of 750/64436, and output is written as a text file (Sec. 3.2.4).

```
fid=zeros(10,1);
fid(1)=fopen('u:\bvdw\LIFDATA\9901\ext_raw\ext601.bin','r');
fid(2)=fopen('u:\bvdw\LIFDATA\9901\ext_raw\ext602.bin','r');
fid(3)=fopen('u:\bvdw\LIFDATA\9901\ext_raw\ext603.bin','r');
fid(4)=fopen('u:\bvdw\LIFDATA\9901\ext_raw\ext604.bin','r');
fid(5)=fopen('u:\bvdw\LIFDATA\9901\ext_raw\ext605.bin','r');
fid(6)=fopen('u:\bvdw\LIFDATA\9901\ext_raw\ext606.bin','r');
fid(7)=fopen('u:\bvdw\LIFDATA\9901\ext_raw\ext607.bin','r');
fid(8)=fopen('u:\bvdw\LIFDATA\9901\ext_raw\ext608.bin','r');
fid(9)=fopen('u:\bvdw\LIFDATA\9901\ext_raw\ext609.bin','r');
fid(10)=fopen('u:\bvdw\LIFDATA\9901\ext_raw\ext6010.bin','r');
```

```
sum=zeros(576,384);
spray=zeros(576,384);
back=zeros(576,384);

for file=1:5
   file
   raw=fread(fid(file),[ 576,384] ,'ushort');
   sum=sum+raw;
   clear raw
end
spray=fix(sum./10);

sum=zeros(576,384);
for file=6:10
   file
   raw=fread(fid(file),[ 576,384] ,'ushort');
   sum=sum+raw;
   clear raw
end
back=fix(sum./10);

ext=(back-spray)./(back-750);

colormap(hot)
image(ext'.*64);

output=zeros(2,576);
output(1,:)=ext(:,100)';
output(2,:)=ext(:,380)';
fidout=fopen('u:\bvdw\lifdata\9901\ext_raw\ext60.txt','wt');
count=fprintf(fidout,'%6.4f   %6.4f\n',output);

fclose('all');
```

Program used to measure length and width of sprays in acetone/cyclohexanone PLIF images. Ten images are processed. A threshold intensity of 5000/65536 is used. Output is a two-column text file (Secs. 3.9.1 & 3.9.2).

```
fid=zeros(10,1);
fid(1)=fopen('c:\windows\desktop\di9.bin','r');
fid(2)=fopen('c:\windows\desktop\di10.bin','r');
fid(3)=fopen('c:\windows\desktop\di1.bin','r');
fid(4)=fopen('c:\windows\desktop\di2.bin','r');
fid(5)=fopen('c:\windows\desktop\di3.bin','r');
fid(6)=fopen('c:\windows\desktop\di4.bin','r');
fid(7)=fopen('c:\windows\desktop\di5.bin','r');
fid(8)=fopen('c:\windows\desktop\di6.bin','r');
fid(9)=fopen('c:\windows\desktop\di7.bin','r');
fid(10)=fopen('c:\windows\desktop\di8.bin','r');

spsize=zeros(10,2);
```

```
for fileno=1:10
   a=fread(fid(fileno),[ 576,384],'ushort');
   fileno

   area=a(48:387,25:370);
   neg=area>=5000;
   area=area.*neg;
   clear neg
   area(1:130,1:20)=zeros(130,20);
   area(211:340,1:20)=zeros(130,20);

   total=sum(sum(area));
   rowfrac=sum(area)./total;
   colfrac=sum(area')./total;
   wlimit=0.95;
   llimit=0.95;

   cumw=zeros(170,1);
   cuml=zeros(346,1);

   cumw(1)=colfrac(170)+colfrac(171);
   for i=2:170
      cumw(i)=cumw(i-1)+colfrac(171-i)+colfrac(170+i);
      if cumw(i)>wlimit & spsize(fileno,1)==0
         spsize(fileno,1)=i*2*0.202;
      end
   end
   cuml(1)=rowfrac(1);
   for i=2:346
      cuml(i)=cuml(i-1)+rowfrac(i);
      if cuml(i)>llimit & spsize(fileno,2)==0
         spsize(fileno,2)=i*0.202;
      end
   end
end

spsize
fidout=fopen('c:\windows\desktop\szchcl.txt','wt');
count=fprintf(fidout,'%6.4f %6.4f\n',spsize');
fclose('all');
```

A8.3 PDPA Processing Programs

Program used to create histograms versus time from raw data files. Ranges of parameters to accept are selected. Histograms of droplet rate, normalized droplet rate, average velocity, Sauter mean diameter, and volume flow rate are calculated. Number of droplets in each bin and the histograms are output in a text file (Sec. 4.3).

```
load u:\bvdw\pdpdata\rawfiles\p3t3\z25r00.txt
raw=z25r10;
clear z25r10;

rows=size(raw,1);

% column1 = diameter
% column2 = velocity
% column3 = fringe count
% column4 = time delay (external input)
% column5 = time interval
% column6 = run time

col=4;

range=zeros(2,6);

         %range( 1=min,2=max  ,   value  )
%diameter
range(1,1)=0   ;
range(2,1)=100 ;
%velocity
range(1,2)=-15 ;
range(2,2)=100 ;
%time delay
range(1,4)=0   ;
range(2,4)=10  ;
%run time
range(1,6)=0   ;
range(2,6)=300


nobins=40   ;

% initialize
hist=zeros(nobins,1);
avevel=zeros(nobins,1);
volume=zeros(nobins,1);
area=zeros(nobins,1);
count=0;

binsize=(range(2,col)-range(1,col))/nobins

for i=1:rows
   inrange(1)=raw(i,1)<range(2,1)&raw(i,1)>=range(1,1);
   inrange(2)=raw(i,2)<range(2,2)&raw(i,2)>=range(1,2);
   inrange(3)=raw(i,4)<range(2,4)&raw(i,4)>=range(1,4);
   inrange(4)=raw(i,6)<range(2,6)&raw(i,6)>=range(1,6);
```

```
    if  all(inrange)
        bin=1+fix( (raw(i,col)-range(1,col))/binsize );
        hist(bin)=hist(bin)+1;
        avevel(bin)=avevel(bin)+raw(i,2);
        volume(bin)=volume(bin)+raw(i,1)^3;
        area(bin)=area(bin)+raw(i,1)^2;
        count=count+1;
    end
end

time=raw(rows-1,6);

%  calculate output values
%       droplet rate
rate=hist/time;
%       normalized droplet rate
normrate=hist/count;
%       average velocity
avevel=avevel./hist;
%       Sauter Mean Diameter
sauter=volume./area;
%       volume flow rate
volflow=volume/time;

count
fraction=count/rows

x=[ (range(1,col)+binsize/2):binsize:(range(2,col)-binsize/2)];

plot(x,rate)
set(gca,'xlabel',text(0,0,'Time after SOI (ms)'))
set(gca,'ylabel',text(0,0,'Droplet Rate (/s)'))

output=zeros(nobins,6);
output(:,1)=hist;
output(:,2)=rate;
output(:,3)=normrate;
output(:,4)=volflow;
output(:,5)=avevel;
output(:,6)=sauter;

fidout=fopen('u:\bvdw\pdpdata\z25r10dv.txt','wt');
count=fprintf(fidout,'%5i %e %e %e %e %e\n',output');

fclose('all');
```

Program used for creating 3D plots of droplet rate histograms at four radial positions. Programs for five or six radial positions are an extension of this one (Sec. 4.3.3).

```
load u:\bvdw\pdpdata\hist\hp3t9\hz25r00.txt
load u:\bvdw\pdpdata\hist\hp3t9\hz25r05.txt
load u:\bvdw\pdpdata\hist\hp3t9\hz25r10.txt
load u:\bvdw\pdpdata\hist\hp3t9\hz25r15.txt

% column1 = hist
% column2 = rate
% column3 = normrate
% column4 = volflow
% column5 = avevel
% column6 = sauter

col=2;
fact=0.8;
tm=12;
rm=100*tm/15;

x=[ .15:.15:tm;.15:.15:tm;.15:.15:tm;.15:.15:tm] ';
y=[ zeros(1,rm);ones(1,rm)*5;ones(1,rm)*10;ones(1,rm)*15] ';

z=zeros(rm,4);
z(:,1)=hz25r00(1:rm,col)*fact;
z(:,2)=hz25r05(1:rm,col)*fact;
z(:,3)=hz25r10(1:rm,col)*fact;
z(:,4)=hz25r15(1:rm,col)*fact;
max(z)

plot3(x,y,z)
axis([ 0 12 0 15 0 15] )
title('P=0.9 T=30 Z=25')
xlabel('Time (ms)')
ylabel('Radial Position (mm)')
zlabel('Droplet Rate (#/ms)')
grid
whitebg
view(-35,25)
```

APPENDIX 9
DIAMETER AND VELOCITY HISTOGRAMS

The following plots show histograms of the number of droplets measured with the PDPA as a function of diameter and velocity. Each figure represents one of the six primary measurement points used in the PDPA study. The upper plot is the diameter histogram (as measured / not corrected). The lower plot is the velocity histogram. In each case, 5000 droplets were measured.

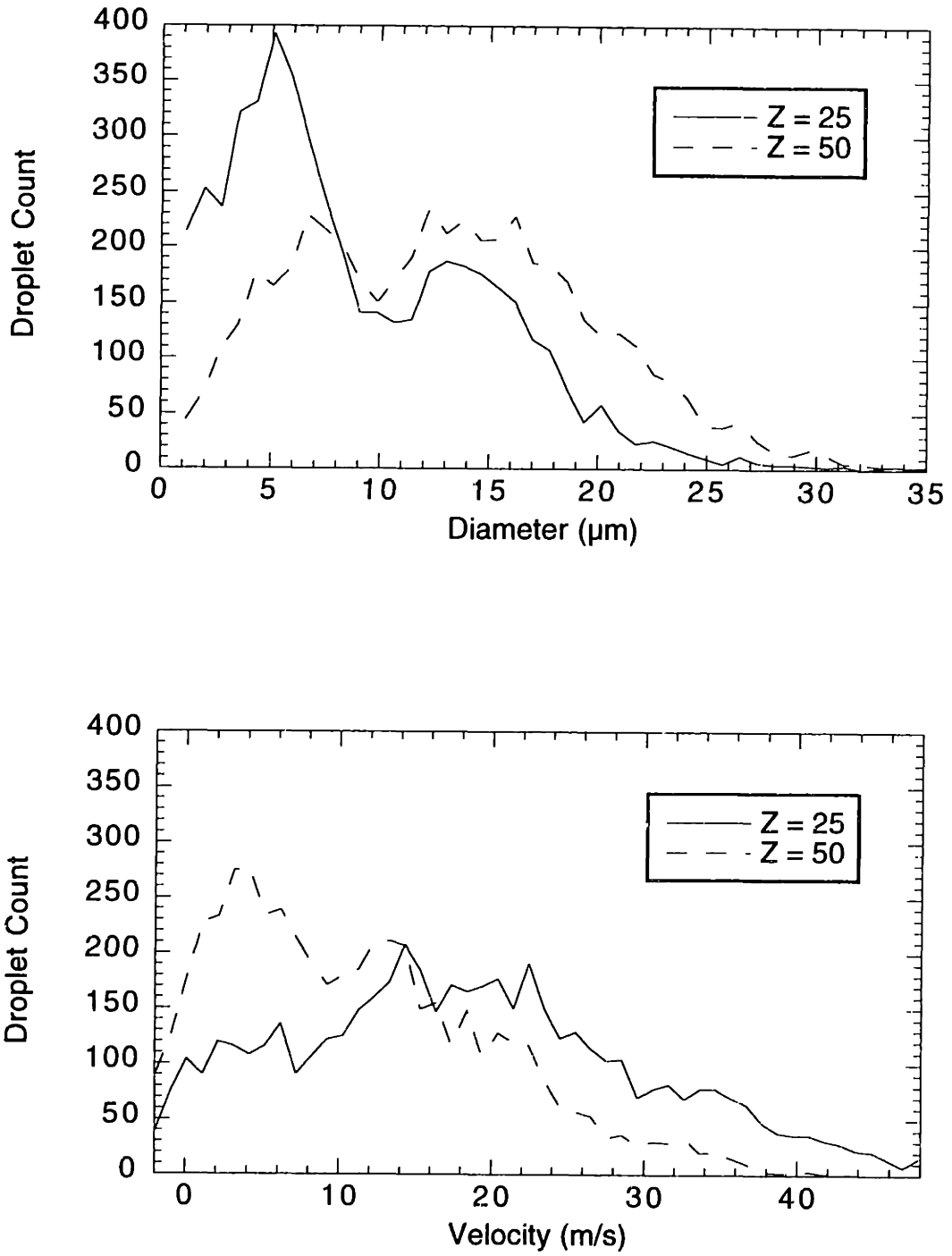

Figure A9.1: P = 0.3 bar / T = 30 °C Diameter and velocity histograms. 5000 total droplets measured, 50 bins.

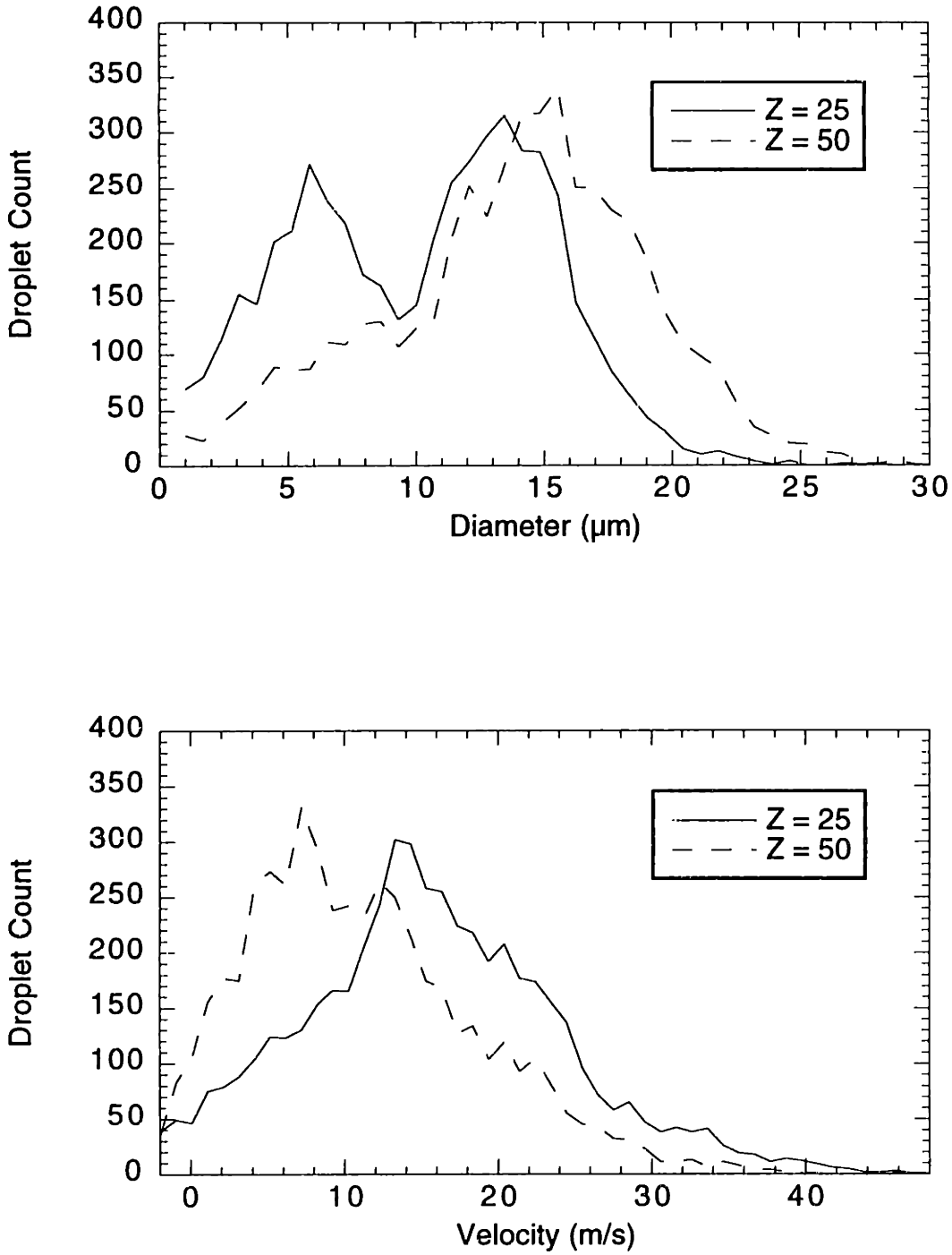

Figure A9.2: P = 0.3 bar / T = 60 °C Diameter and velocity histograms. 5000 total droplets measured, 50 bins.

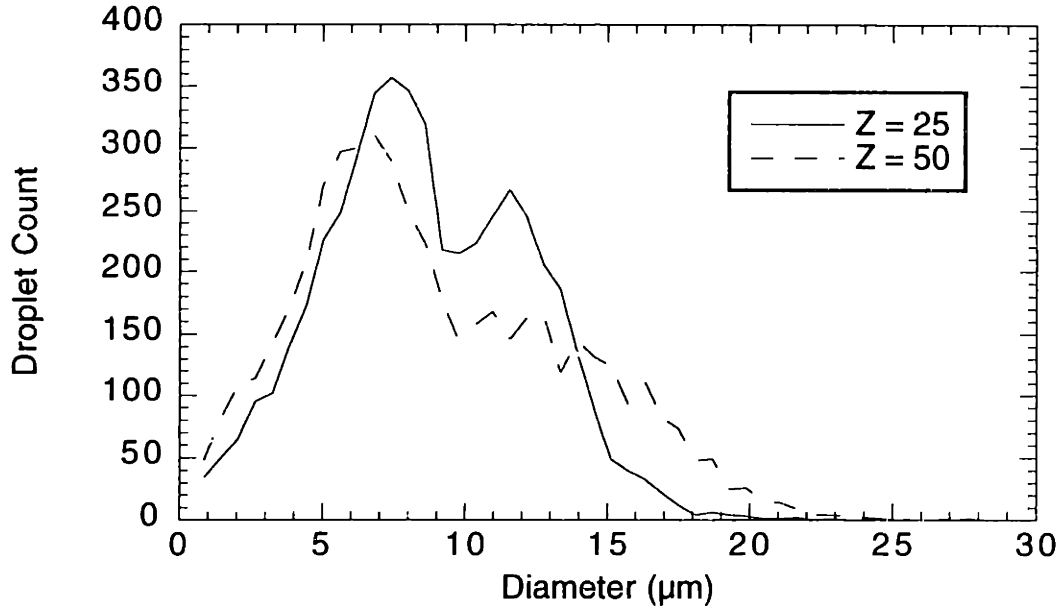

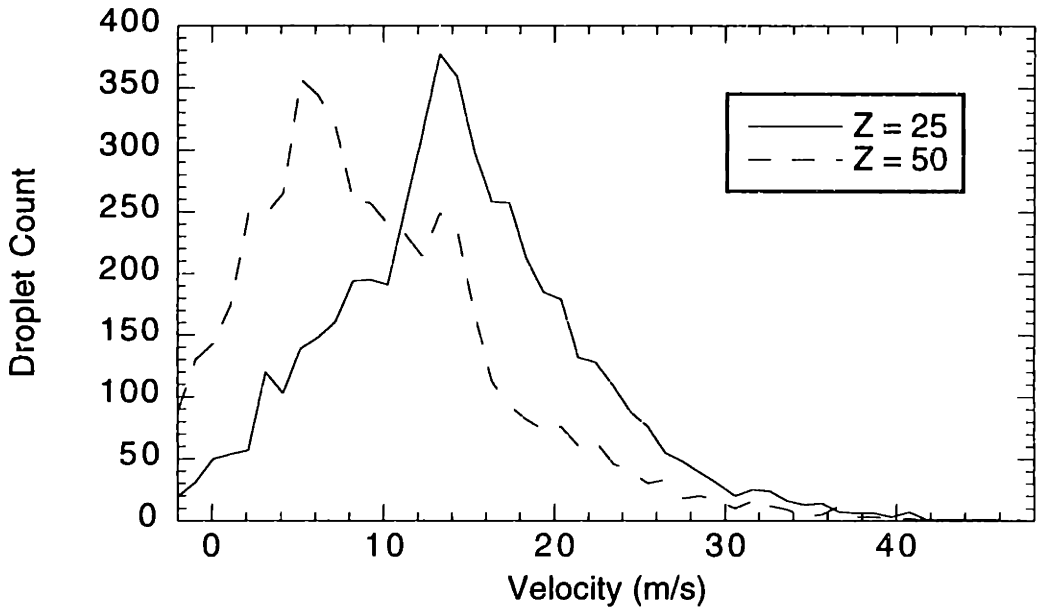

Figure A9.3: P = 0.3 bar / T = 90 °C Diameter and velocity histograms. 5000 total droplets measured, 50 bins.

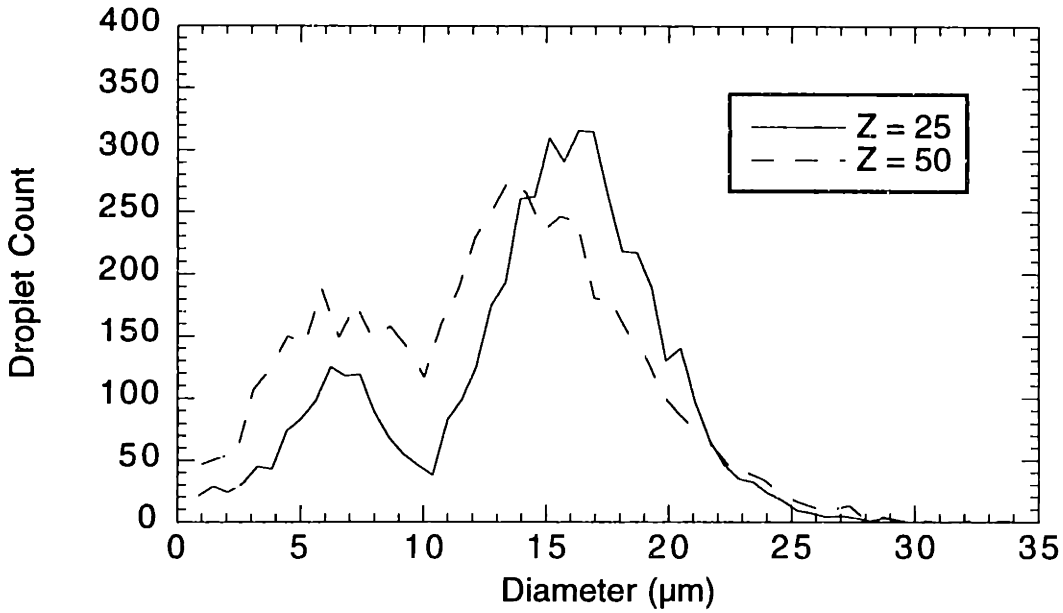

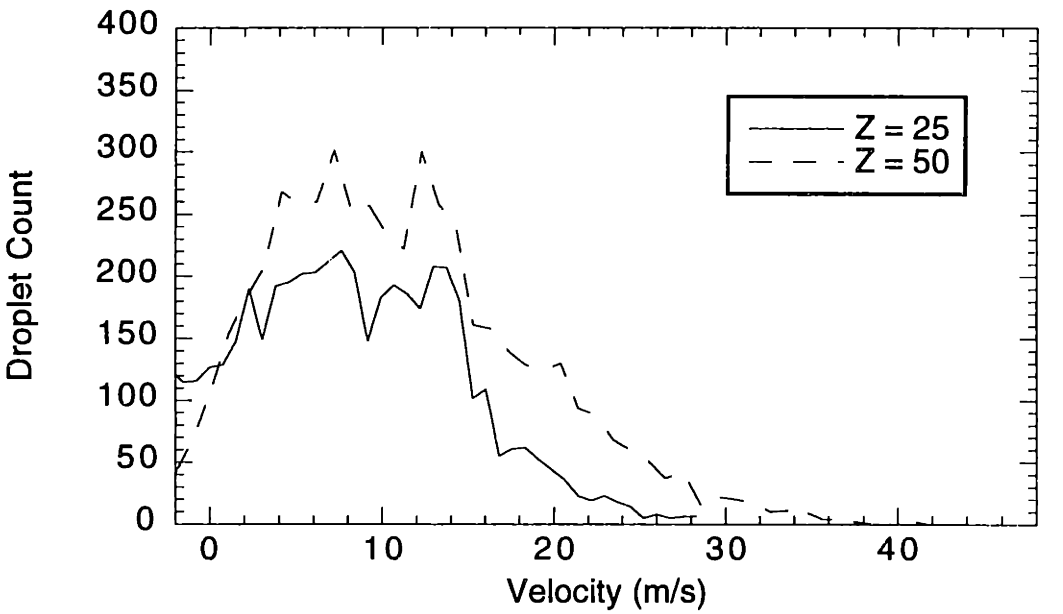

Figure A9.4: P = 0.6 bar / T = 90 °C Diameter and velocity histograms. 5000 total droplets measured, 50 bins.

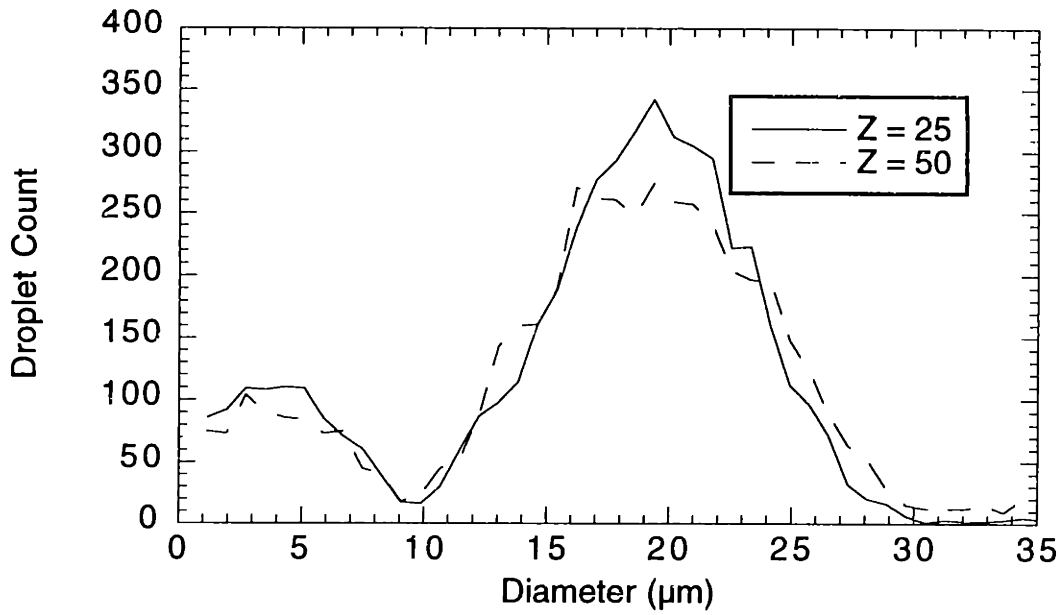

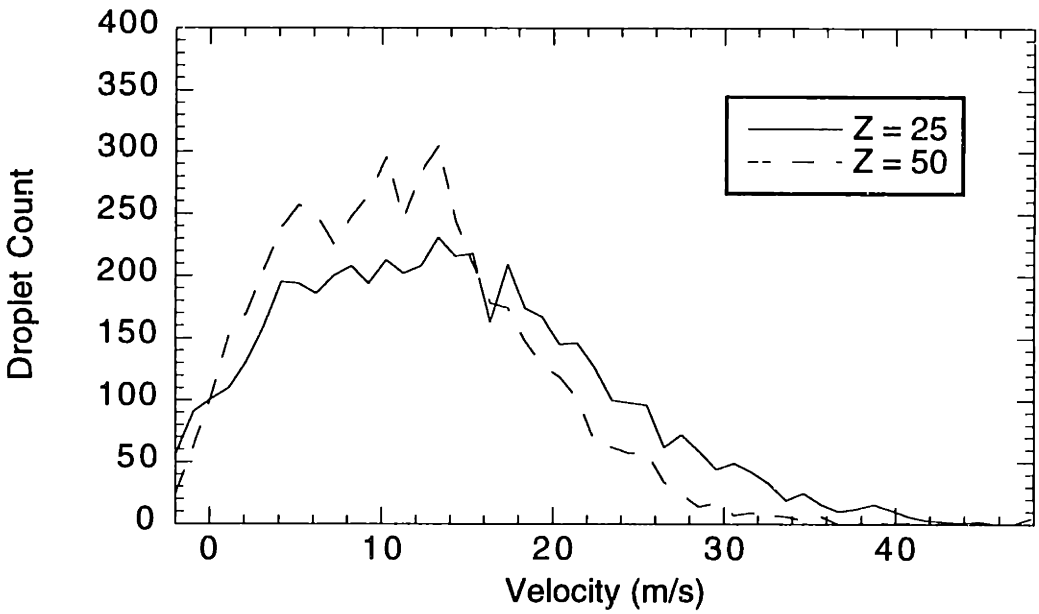

Figure A9.5: P = 0.9 bar / T = 90 °C Diameter and velocity histograms. 5000 total droplets measured, 50 bins.

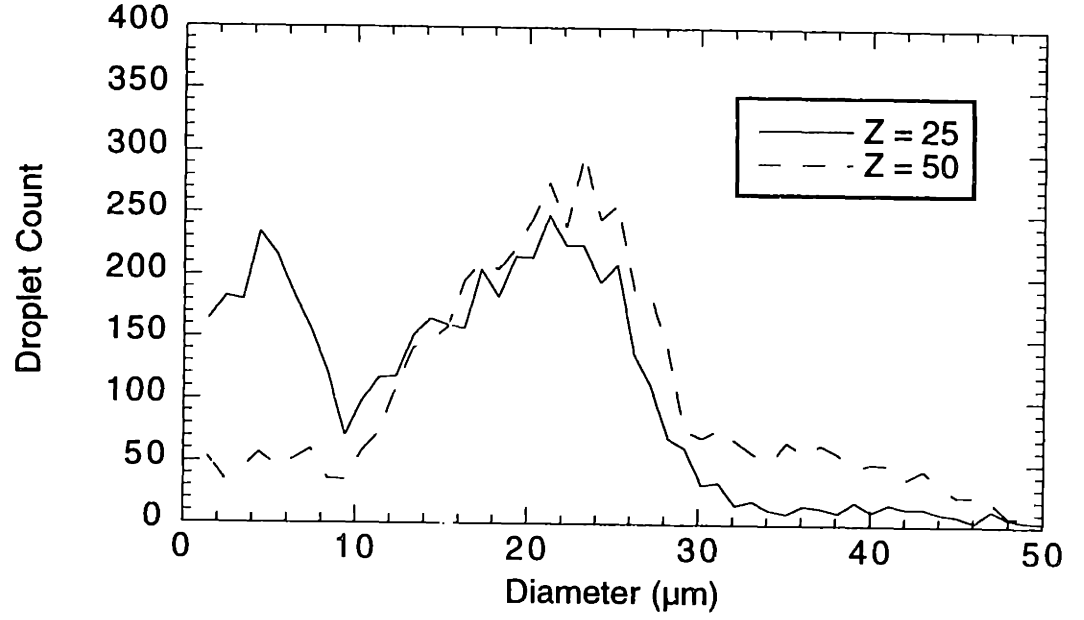

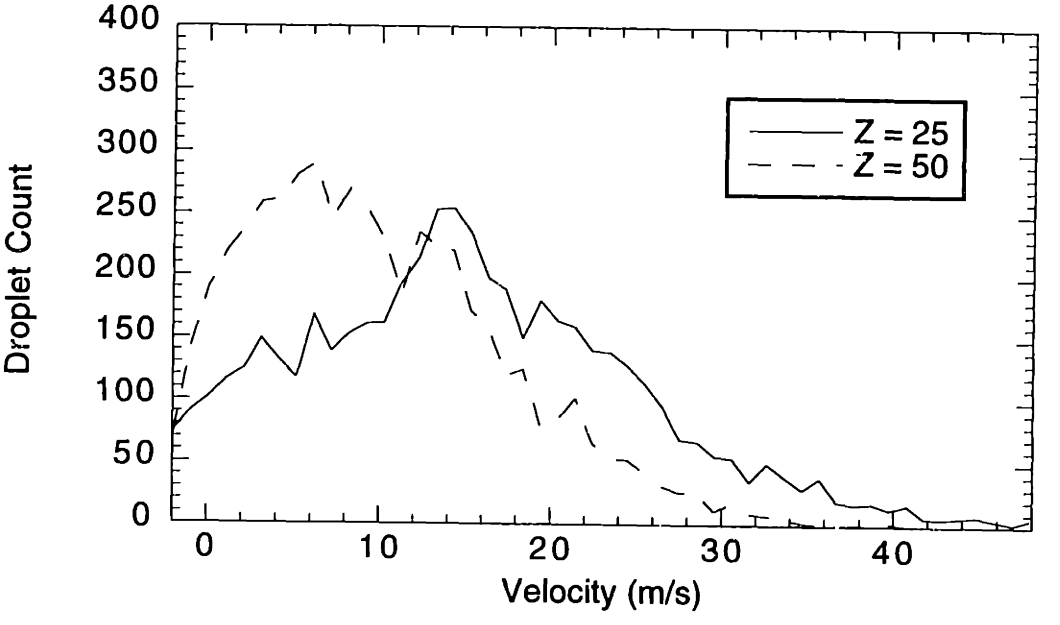

Figure A9.6: P = 0.9 bar / T = 30 °C Diameter and velocity histograms. 5000 total droplets measured, 50 bins.

APPENDIX 10
SPRAY MODEL INPUT FILES

Below are the spray input file and time management file from the base case (O16) from the modeling work with FIRE (Sec. 5.1).

Spray input file (.spr)

```
FIRE-V 7.0          FMT-SE  720 0
FIRE-V 7.0                                                  14-Jan-99 10:41:36

* ********************************************************************
* ****    General Input Data    ***********************************
* ********************************************************************
7.0 LINES=1 CALCULATION TASK (SPRAY/STREAKLINES)
* --------------------------------------------------------------------
**********************************************************
Spray
7.0 LINES=1 DROPLET INTRODUCTION OPTION
* --------------------------------------------------------------------
*  NOZZLE  ENTRAIN  FILE
* --------------------------------------------------------------------
    1       0       0
7.0 LINES=1 SPRAY OUTPUT FLAGS 1
* --------------------------------------------------------------------
*  LIFE   VELO   DIAM   DENS   TEMP   IMPI   PARC   HOLE
* --------------------------------------------------------------------
    0      0      1      0      1      0      0      0
7.0 LINES=1 SPRAY OUTPUT FLAGS 2
* --------------------------------------------------------------------
*  VAPO  USERFL  VOID   LIQM    D10    D30    D32    NOZ
* --------------------------------------------------------------------
    1      0      0      1      0      0      0      0
7.0 LINES=1 SPRAY OUTPUT FLAGS 3
* --------------------------------------------------------------------
*  WE     STO   TREL   NUMB   VRATE  HRATE  DRAGF  JETEN
* --------------------------------------------------------------------
    0      0      0      0      0      0      0      0
7.0 LINES=1 SPRAY OUTPUT FLAGS 4
* --------------------------------------------------------------------
*  IN_AR SPECTR  FLUCV  MAS_W DENS_W  TEM_W  THI_W  VAP_W
* --------------------------------------------------------------------
    0      0      0      0      0      0      0      0
7.0 LINES=1 SPRAY OUTPUT FLAGS 5
* --------------------------------------------------------------------
*  D32_W
* --------------------------------------------------------------------
    0
7.0 LINES=1 EULER LAGRANGE INTERACTION TERMS
* --------------------------------------------------------------------
*   U     V     W     M     H    TKE    ED    VOID
* --------------------------------------------------------------------
```

```
    1     1     1     1     1     0     0     1
7.0 LINES=1 SOLUTIONFLAGS
* ------------------------------------------------------------------
*   X-MOM  Y-MOM  Z-MOM  MASS  HEAT
* ------------------------------------------------------------------
    1      1      1      1      1
7.0 LINES=1 INTERPOLATIONMODE
* ------------------------------------------------------------------
    LINEAR
7.0 LINES=1 SUBMODELS
* ------------------------------------------------------------------
*   TURB_DISP    BREAKUP    INTERACTION    RAD_PERT   WALL_INTERACTION
* ------------------------------------------------------------------
    ENABLE       DISABLE      DISABLE      ENABLE       DISABLE
7.0 LINES=1 NUMBER OF PARCELS INTRODUCED PER TIMESTEP
* ------------------------------------------------------------------
*   N-SIZES  N-INTRO  N-CIRCD
* ------------------------------------------------------------------
     4        3        3
* ******************************************************************
* ****    Geometrical Input Data    ********************************
* ******************************************************************
7.0 LINES=1 NUMBER OF NOZZLES
* ------------------------------------------------------------------
    1
7.0 LINES=1 RADIAL PERTURBATION
* ------------------------------------------------------------------
*   FRACTION OF STARTVELOCITY
* ------------------------------------------------------------------
    6.500E-02
7.0 LINES=1 INJECTION START AND END TIME
* ------------------------------------------------------------------
*   T_START      T_END
* ------------------------------------------------------------------
    0.000e-04 1.750E-03
7.0 LINES=2 LOCATION OF NOZZLE
* ------------------------------------------------------------------
*   X_LOC       Y_LOC      Z_LOC
*   X_DIR       Y_DIR      Z_DIR     X_SYM     Y_SYM     Z_SYM
* ------------------------------------------------------------------
*   Static BOMB Position
    0.000E+00 0.000E+00 0.000E+00 0.000E+00 0.000E+00 0.000E+00
    0.000E+00 0.000E+00 1.000E+00 0.000E+00 0.000E+00 0.000E+00
7.0 LINES=1 NOZZLE DIAMETER AT HOLE
* ------------------------------------------------------------------
    0.00000
7.0 LINES=1 NUMBER OF NOZZLE HOLES
*  ------------------------------------------------------------------
    1
7.0 LINES=1 NUMBER OF HOLE VARIATIONS OUTER DIAMETER
* ------------------------------------------------------------------
    2
7.0 LINES=1 TIME - OUTER HOLE DIAMETER
* ------------------------------------------------------------------
    0.000E-04 1.750E-03
7.0 LINES=1 OUTER DIAMETER OF EACH HOLE
* ------------------------------------------------------------------
    4.572E-04 4.572E-04
7.0 LINES=1 NUMBER OF HOLE VARIATIONS INNER DIAMETER
* ------------------------------------------------------------------
    2
7.0 LINES=1 TIME - INNER HOLE DIAMETER
* ------------------------------------------------------------------
```

```
    0.000E-04 1.750E-03
7.0 LINES=1 INNER DIAMETER OF EACH HOLE
* ---------------------------------------------------------------------
    0.254E-04 0.254E-04
7.0 LINES=1 SPRAY ANGLE DELTA1 [ DEG]
* ---------------------------------------------------------------------
    0.00000
7.0 LINES=1 SPRAY ANGLE DELTA2 [ DEG]
* ---------------------------------------------------------------------
    0.00000
7.0 LINES=1 ANGLE OF CIRCUMFERENTIAL HOLE DISTRIBUTION [ DEG]
* ---------------------------------------------------------------------
    0.00000
* *********************************************************************
* ****    Droplet Input Data    ***************************************
* *********************************************************************
7.0 LINES=1 INJECTED FLUID
* ---------------------------------------------------------------------
    N-OCTANE
7.0 LINES=1 TOTAL FLUID VOLUME INJECTED [ M3]
* ---------------------------------------------------------------------
    1.936E-08
7.0 LINES=1 NUMBER OF STARTVELOCITY VARIATIONS
* ---------------------------------------------------------------------
    4
7.0 LINES=1 TIME - DROPLET STARTVELOCITY
* ---------------------------------------------------------------------
    0.000E-04 0.500E-04 2.000E-04 1.750E-03
7.0 LINES=1 START VELOCITY [ HOMOGENEOUS AT HOLE]
* ---------------------------------------------------------------------
* estimated for 5 MPa
    8.700E+01 8.700E+01 8.100E+01 8.100E+01
7.0 LINES=1 TEMPERATURE OF INJECTED FLUID
* ---------------------------------------------------------------------
* 30C = 303K;  60C = 333K;   90C = 363K
* Tb(n-octane)=360.1K
    303.000
7.0 LINES=1 NUMBER OF ELEMENTS FOR INJECTION RATE DIAGRAM
* ---------------------------------------------------------------------
    6
7.0 LINES=1 TIME - MASSFLOWRATE
* ---------------------------------------------------------------------
    0.000E-04 0.500E-04 2.500E-04 1.650E-03 1.700E-03 1.750E-03
7.0 LINES=1 INJECTION RATE DIAGRAMM
* ---------------------------------------------------------------------
    1.100E+00 1.300E+00 1.000E+00 1.000E+00 8.500E-01 1.000E-03
7.0 LINES=1 NUMBER OF HALF OUTER SPRAY CONE ANGLE VARIATIONS
* ---------------------------------------------------------------------
    16
7.0 LINES=2 TIME - HALF OUTER SPRAY CONE ANGLE
* ---------------------------------------------------------------------
 0.000E-04 0.500E-04 1.000E-04 1.500E-04 2.000E-04 2.500E-04 3.000E-04 3.500E-04
 4.000E-04 4.500E-04 5.000E-04 5.500E-04 6.000E-04 6.500E-04 7.000E-04 1.750E-03
7.0 LINES=2 HALF OUTER SPRAY CONE ANGLE[ DEG]
* ---------------------------------------------------------------------
 1.000E+00 1.000E+01 3.000E+01 3.600E+01 3.600E+01 4.250E+01 4.150E+01 3.100E+01
 2.700E+01 3.000E+01 3.500E+01 3.250E+01 3.150E+01 3.050E+01 3.000E+01 3.000E+01
7.0 LINES=1 NUMBER OF HALF INNER SPRAY CONE ANGLE VARIATIONS
* ---------------------------------------------------------------------
    16
7.0 LINES=2 TIME - HALF INNER SPRAY CONE ANGLE
* ---------------------------------------------------------------------
 0.000E-04 0.500E-04 1.000E-04 1.500E-04 2.000E-04 2.500E-04 3.000E-04 3.500E-04
```

```
 4.000E-04 4.500E-04 5.000E-04 5.500E-04 6.000E-04 6.500E-04 7.000E-04 1.750E-03
7.0 LINES=2 HALF INNER SPRAY CONE ANGLE[ DEG]
* ------------------------------------------------------------------
 0.000E+00 3.000E+00 2.500E+01 3.100E+01 3.100E+01 3.750E+01 3.650E+01 2.600E+01
 2.200E+01 2.500E+01 3.000E+01 2.750E+01 2.650E+01 2.550E+01 2.500E+01 2.500E+01
7.0 LINES=1 NUMBER OF ELEMENTS FOR SIZE AND PROBABILITY DISTR.
* ------------------------------------------------------------------
    30
7.0 LINES=4 DROPLET SIZE DISTRIBUTION
* ------------------------------------------------------------------
 1.000E-06 2.000E-06 3.000E-06 4.000E-06 5.000E-06 6.000E-06 7.000E-06 8.000E-06
 9.000E-06 1.000E-05 1.100E-05 1.200E-05 1.300E-05 1.400E-05 1.500E-05 1.600E-05
 1.700E-05 1.800E-05 1.900E-05 2.000E-05 2.100E-05 2.200E-05 2.300E-05 2.400E-05
 2.500E-05 2.600E-05 2.700E-05 2.800E-05 2.900E-05 3.000E-05
7.0 LINES=4 DROPLET PROBABILITY DISTRIBUTION
* ------------------------------------------------------------------
*** y=exp(-0.009(x-8.5)^2)
 3.757E+00 4.262E+00 4.748E+00 5.195E+00 5.583E+00 5.893E+00 6.109E+00 6.220E+00
 6.220E+00 6.109E+00 5.893E+00 5.583E+00 5.195E+00 4.748E+00 4.262E+00 3.757E+00
 3.254E+00 2.767E+00 2.311E+00 1.869E+00 1.528E+00 1.209E+00 9.396E-01 7.173E-01
 5.378E-01 3.960E-01 2.864E-01 2.035E-01 1.420E-01 9.727E-02
```

Time management file (.tim)

```
FIRE-V 7.0          FMT-SE  720 0
FIRE-V 7.0                                                  14-JAN-99 10:43:35

7.0 LINES=1 RUN MODE: STEADY(=-1), TIMESTEPS(=0), CRANKANGLE(=1)
       0
6.0 LINES=2 ENDTIMESTEP DELTA T
     400    5.0000E-06
     500    1.0000E-05
2.1 LINES=1 RESTART FLAG , REPEAT FLAG
       F    F
6.0 LINES=2 UNDERRELAXATION FACTOR MOMENTUM
    20     0.3000
    500    0.4000
6.0 LINES=2 UNDERRELAXATION FACTOR PRESSURE
    20     0.2000
    500    0.3500
6.0 LINES=2 UNDERRELAXATION FACTOR TKE
    20     0.4000
    500    0.5000
6.0 LINES=2 UNDERRELAXATION FACTOR DISSIPATION
    20     0.4000
    500    0.5000
6.0 LINES=2 UNDERRELAXATION FACTOR ENERGY
    20     0.3000
    500    0.4000
6.0 LINES=2 UNDERRELAXATION FACTOR MASS SOURCE
    400    0.9500
    500    1.0000
7.0 LINES=1 UNDERRELAXATION FACTOR VISCOSITY
    500    1.0000
```

```
6.0 LINES=2 DYNAMIC ADJUSTMENT OF UNDERRELAXATION (ON=1, OFF=0)
    350      0
    500      1
6.0 LINES=1 MAX ITERATIONS PER TIMESTEP
    500      50
6.0 LINES=3 MIN ITERATIONS PER TIMESTEP
    100      15
    400      10
    500      5
6.0 LINES=2 FLOW RESTART BACKUP OUTPUT
*     END     FLO    RST    BCK                                              *
      400     10      50    500
      500      5     100    500
6.0 LINES=1 OUTPUT PRESSURE
    500      1
6.0 LINES=1 OUTPUT VELOCITY
    500      1
6.0 LINES=1 OUTPUT DENSITY
    500      0
6.0 LINES=1 OUTPUT PASSIVE SCALAR
    500      0
6.0 LINES=1 OUTPUT TEMPERATURE
    500      1
6.0 LINES=1 OUTPUT VISCOSITY
    500      0
6.0 LINES=1 OUTPUT TURBULENCE
    500      0
6.0 LINES=1 OUTPUT VORTICITY
    500      0
6.0 LINES=1 OUTPUT Y PLUS
    500      0
6.0 LINES=1 OUTPUT ERROR
    500      0
6.0 LINES=1 TWO STAGE PRESSURE CORRECTION (ON=1, OFF=0)
    500      1
6.0 LINES=1 FLAGS FOR INCOMPRESSIBLE(=1),COMPRESSIBLE(=0)
    500      0
6.0 LINES=1 FLAGS FOR GLOBAL CONTINUITY (ON=1, OFF=0)
    500      0
6.2 LINES=1 SPECIES
*     AIR : O2N2 : GAS
      AIR
2.1 LINES=1 INITIAL VALUES OF BULK PRESSURE,DENSITY AND TEMPERATURE
*     PRESSURE [ Pa]    DENSITY [ kg/m3]    TEMPERATURE [ K]                  *
       0.300000E+05       0.000000E+00       4.2000000E+02
*7.0 LINES=1 INITIALIZATION VISCOSITY, SPECIFIC HEAT AND THERMAL CONDUCTIVITY
*    VISCOSITY [ kg/ms]      CP [ J/kgK]    TH. CONDUCT.[ W/mK]               *
*       1.915000E-05       9.982000E+02       2.541000E-02
2.1 LINES=1 TURBULENCE KINETIC ENERGY AND TURBULENCE LENGTH SCALE
*      TKE [ m2/s2]       TLS [ m]                                           *
      1.500000E-02     7.500000E-02
6.0 LINES=2 CONVERGENCE CRITERION
*     END     CONV.CRIT.                                                     *
      400    2.000000E-06
      500    2.000000E-05
3.1 LINES=1 START GEO LNK BND FLAG
*     GEOVALUE     LNKVALUE     BNDVALUE                                     *
       1.0000       1.0000       1.0000
6.0 LINES=1 SOLVE ENERGY (ON=1, OFF=0)
    500      1
6.0 LINES=1 SOLVE MOMENTUM U (ON=1, OFF=0)
    500      1
6.0 LINES=1 SOLVE MOMENTUM V (ON=1, OFF=0)
```

```
    500     1
6.0 LINES=1 SOLVE MOMENTUM W (ON=1, OFF=0)
    500     1
6.0 LINES=1 SOLVE PASSIVE SCALAR (ON=1, OFF=0)
    500     0
6.0 LINES=1 TURBULENCE MODEL RSM(=2) K-EPS(=1) LAMINAR(=0) INVISCID(=-1)
    500     1
6.0 LINES=1 DIFFERENCING SCHEME
    500    CTVD
6.2 LINES=1 MONITORING LOCATIONS: VELOCITY AND PRESSURE
*     END  VELOCITY  PRESSURE                                                *
      500  96218     35000
6.0 LINES=1 NUMBER OF MAX SOLVER ITERATIONS
*     END     U        V        W        P       TE       ED        H       PS  *
      500   100      100      100      100      100      100      100      100
6.0 LINES=1 NUMBER OF MIN SOLVER ITERATIONS
*     END     U        V        W        P       TE       ED        H       PS  *
      500    10       10       10       30       10       10       10       10
6.0 LINES=1 SOLVER TYPE
*     END     U        V        W        P       TE       ED        H       PS  *
    500   AUTO     AUTO     AUTO     AUTO     AUTO     AUTO     AUTO     AUTO
7.0 LINES=1 SOLVER TOLERANCE
*     END     U        V        W        P       TE       ED        H       PS  *
    500 0.10E+00 0.10E+00 0.10E+00 0.50E-01 0.10E+00 0.10E+00 0.10E+00 0.10E+00
6.0 LINES=1 BODYFORCE
*     END   ON/OFF    FORCE          X            Y            Z               *
    500     0     9.8100E+00   0.0000E+00   0.0000E+00  -1.0000E+00
2.1 LINES=7 FILENAMES
    AETG_bomb_v70p3.geo
    AETG_bomb_v70p3.lnk
    AETG_bomb_v70p3.bnd
    BVDW_1_base.flo
    BVDW_1_base.rst
    BVDW_1_base.bck
    BVDW_1_base.chk
4.0 LINES=1 SPRAY MODULE FILENAME
*  ACTIV. TS.  FILENAME                                                      *
       1       BVDW_1_base.spr
```

APPENDIX 11
MODEL TIME SEQUENCE

The following figure shows a time sequence of the base modeling case (O16). The first three steps of the sequence are not shown since little of the spray is visible. The five columns represent:

1. Droplets. A dot is drawn for each droplet parcel in the cut plane. The dot size is proportional to the droplet diameter.
1. Velocity Vectors. Arrows indicate the magnitude and direction of the gas velocity around the spray.
2. Liquid Density. Contours outline the areas of high bulk liquid density (kg-liquid/m^3). Saturated regions represent greater than 1.8 kg/m^3.
3. Equivalence Ratio. Contours outline the regions of high vapor concentration.
4. Pressure. Contours outline the regions of suppressed relative pressure. The saturated regions represent a suppression greater than 300 Pa.

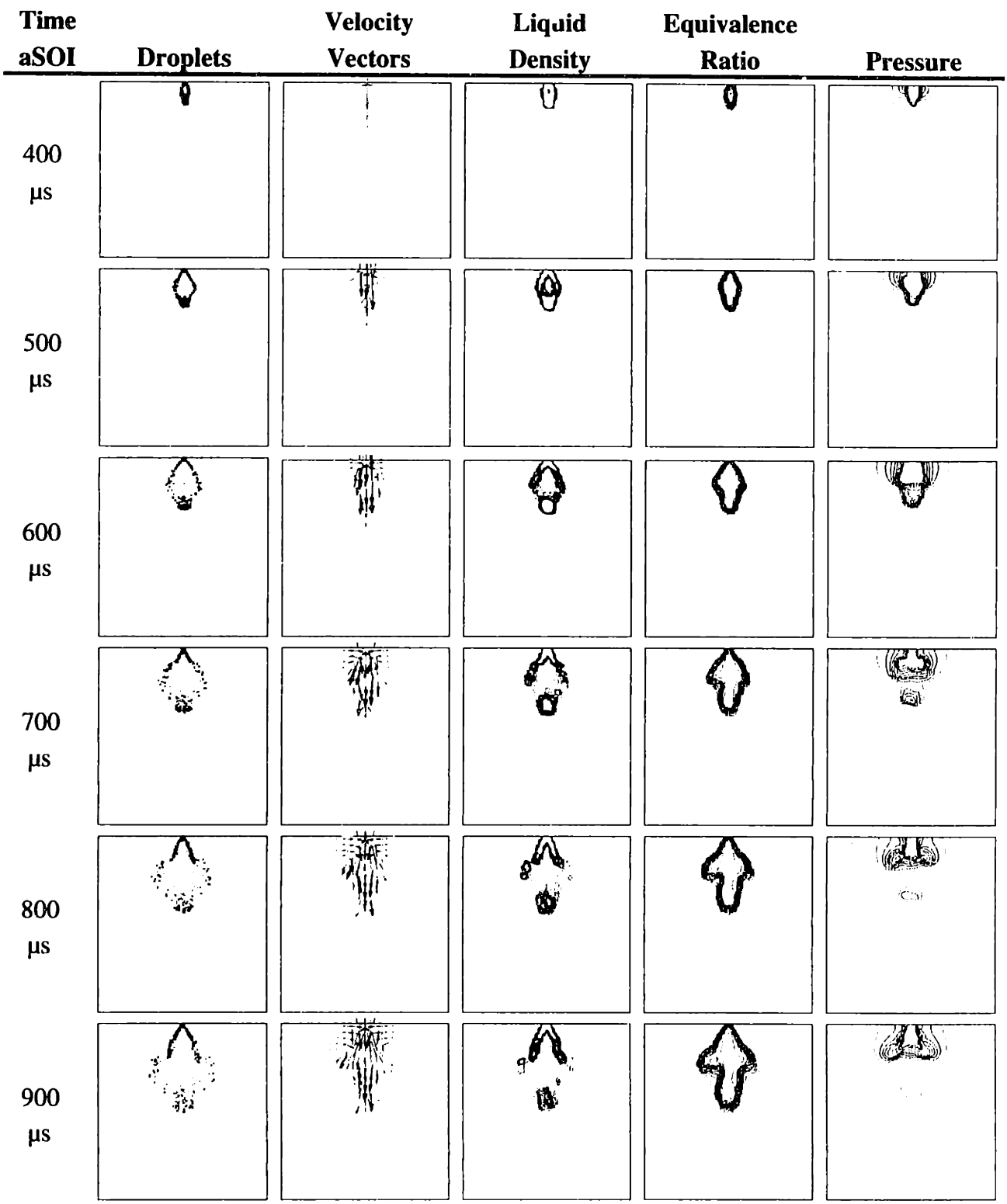

Figure A10a: Time sequence of model images for baseline test (O16). All images are on a cut-plane through the injector axis. Velocity vectors are scaled from 0 to 50 m/s. Contour plots contain 11 contours separating 12 regions with: liquid bulk density of 0 to 1.8 kg/m^3, fuel/air equivalence ratio of 0 to 4, and relative pressure of –300 to 0 Pa.

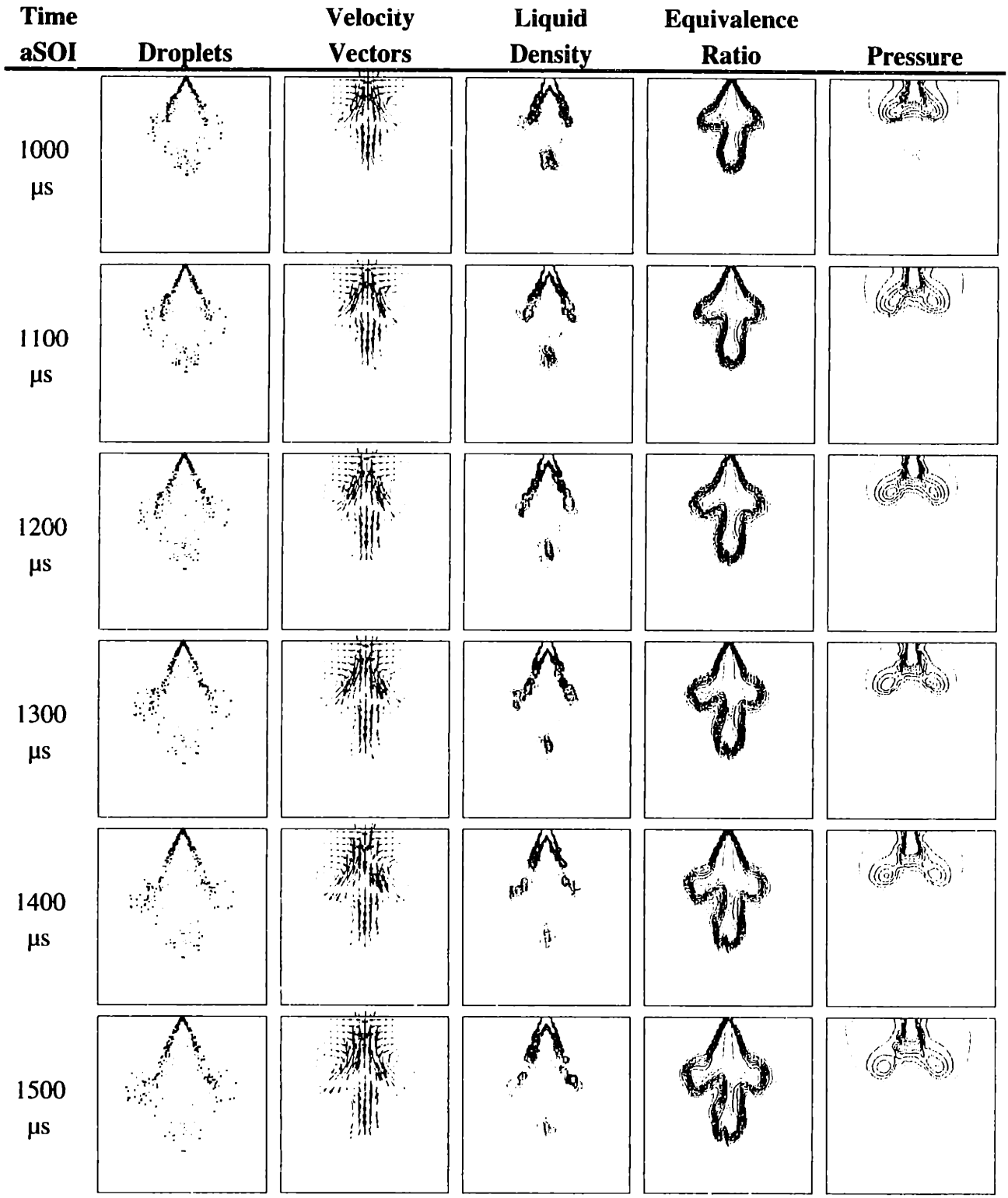

Figure A10b: Time sequence of model images for baseline test (O16). All images are on a cut-plane through the injector axis. Velocity vectors are scaled from 0 to 50 m/s. Contour plots contain 11 contours separating 12 regions with: liquid bulk density of 0 to 1.8 kg/m^3, fuel/air equivalence ratio of 0 to 4, and relative pressure of –300 to 0 Pa.

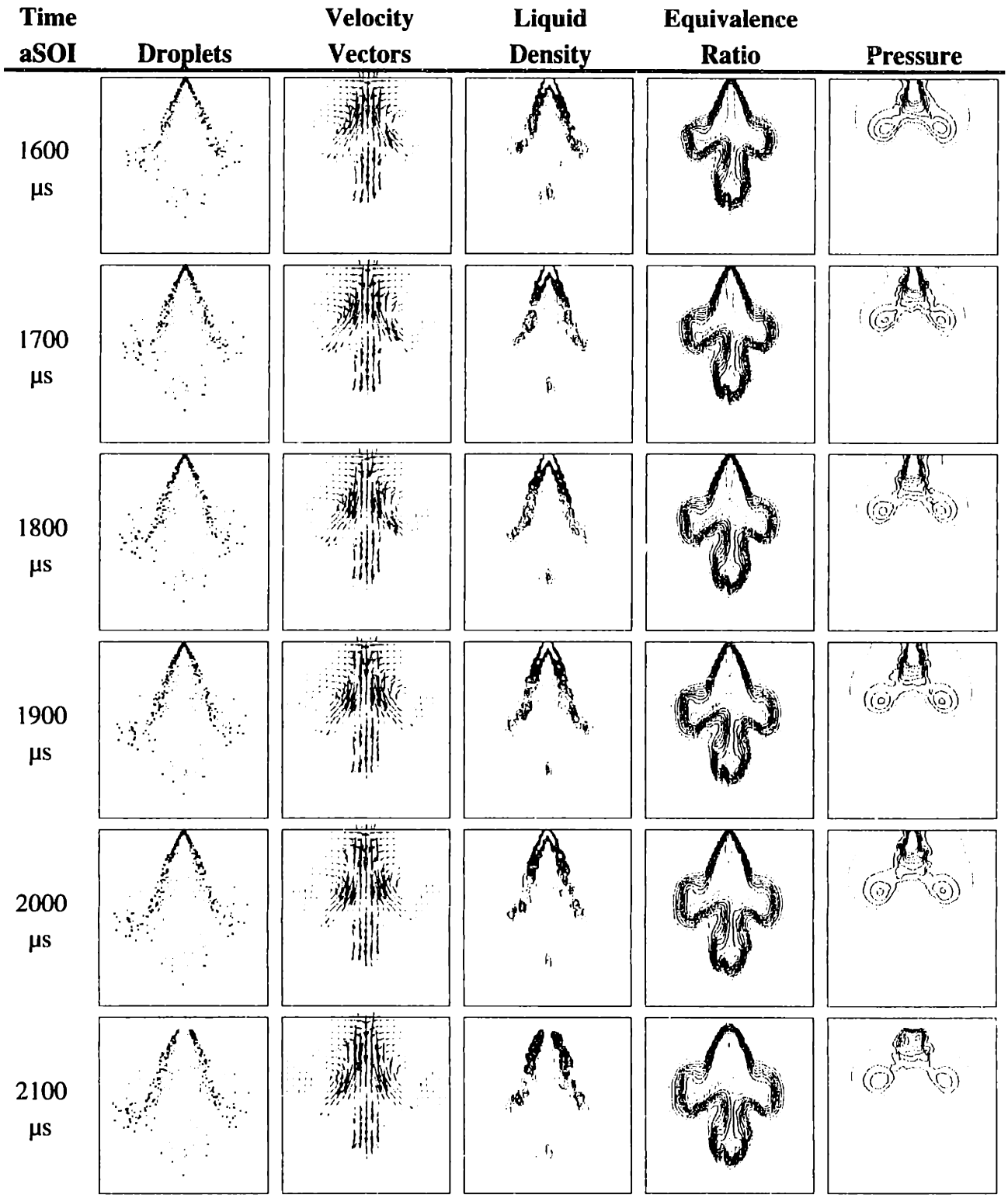

Figure A10c: Time sequence of model images for baseline test (O16). All images are on a cut-plane through the injector axis. Velocity vectors are scaled from 0 to 50 m/s. Contour plots contain 11 contours separating 12 regions with: liquid bulk density of 0 to 1.8 kg/m^3, fuel/air equivalence ratio of 0 to 4, and relative pressure of –300 to 0 Pa.

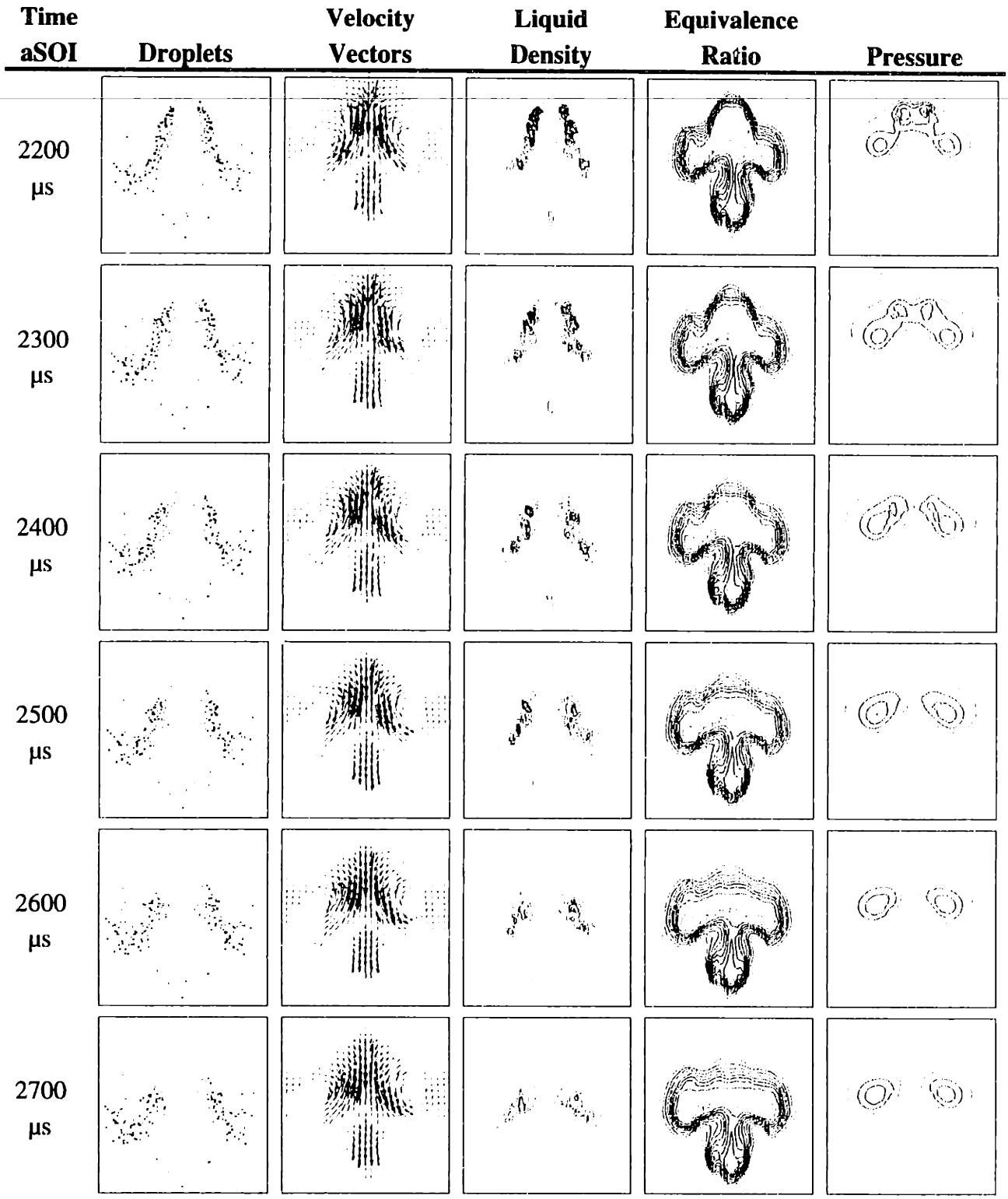

Figure A10d: Time sequence of model images for baseline test (O16). All images are on a cut-plane through the injector axis. Velocity vectors are scaled from 0 to 50 m/s. Contour plots contain 11 contours separating 12 regions with: liquid bulk density of 0 to 1.8 kg/m^3, fuel/air equivalence ratio of 0 to 4, and relative pressure of –300 to 0 Pa.

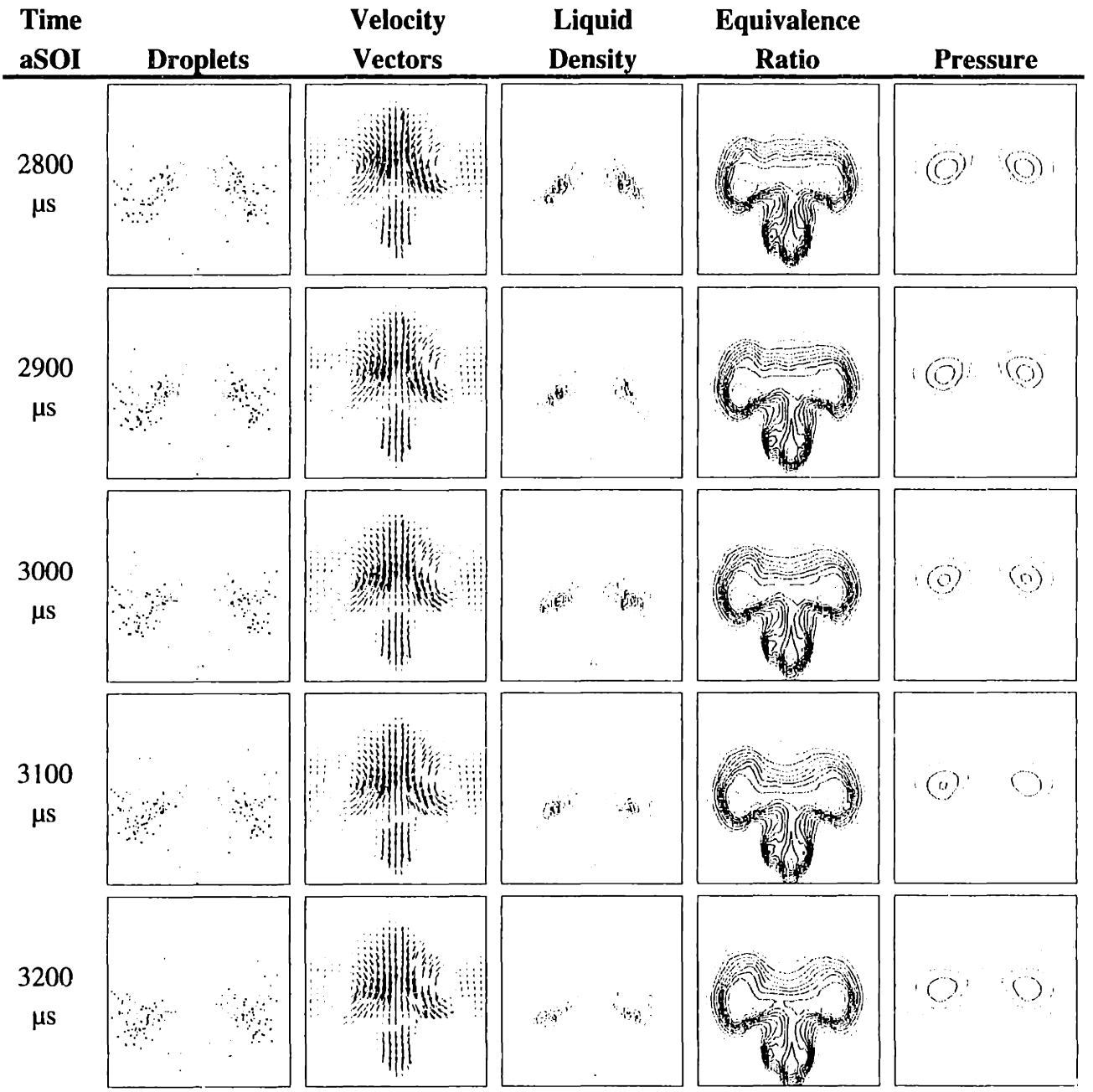

Figure A10e: Time sequence of model images for baseline test (O16). All images are on a cut-plane through the injector axis. Velocity vectors are scaled from 0 to 50 m/s. Contour plots contain 11 contours separating 12 regions with: liquid bulk density of 0 to 1.8 kg/m^3, fuel/air equivalence ratio of 0 to 4, and relative pressure of –300 to 0 Pa.